Thesis

Charge and Spin electrodynamics of SrTiO3 and EuTiO3 studied by optical spectroscopy

VAN MECHELEN, Jacobus Lodevicus Martinus

Abstract

This work is a threefold optical study of two perovskites: the very well known but still surprisingly intriguing SrTiO3 and its almost unexplored magnetic relative EuTiO3. A major extension to previous work is the very broad energy scale from the microwave to the ultra-violet region on which phenomena have been studied. Central in the thesis is the novel technique of time-domain spectroscopy in the THz range, a relatively unexplored range which clarifies and illustrates textbook phenomena of low energy physics. The thesis built up as follows. Chapter 1 introduces the theory of the interaction of light with matter and existing optical concepts needed in the following chapters. One part needs to be highlighted, it is a magnetic sum rule specially derived for the use in chapter 4, which relates the spectral weight of magnetic dipole transitions to the total magnetization of the system. Chapter 2 describes how SrTiO3 is tuned towards the formation of electron-phonon coupling by using chemical substitution of niobium as a control parameter. In chapter 3 it is shown that pristine SrTiO3 tuned by an external static electric field approaches a quantum ferroelectric state and shows an intriguing universal behavior below 20 K. Chapter 4 is [...]

Reference

VAN MECHELEN, Jacobus Lodevicus Martinus. *Charge and Spin electrodynamics of SrTiO3 and EuTiO3 studied by optical spectroscopy*. Thèse de doctorat : Univ. Genève, 2010, no. Sc. 4215

UNIVERSITÉ
DE GENÈVE

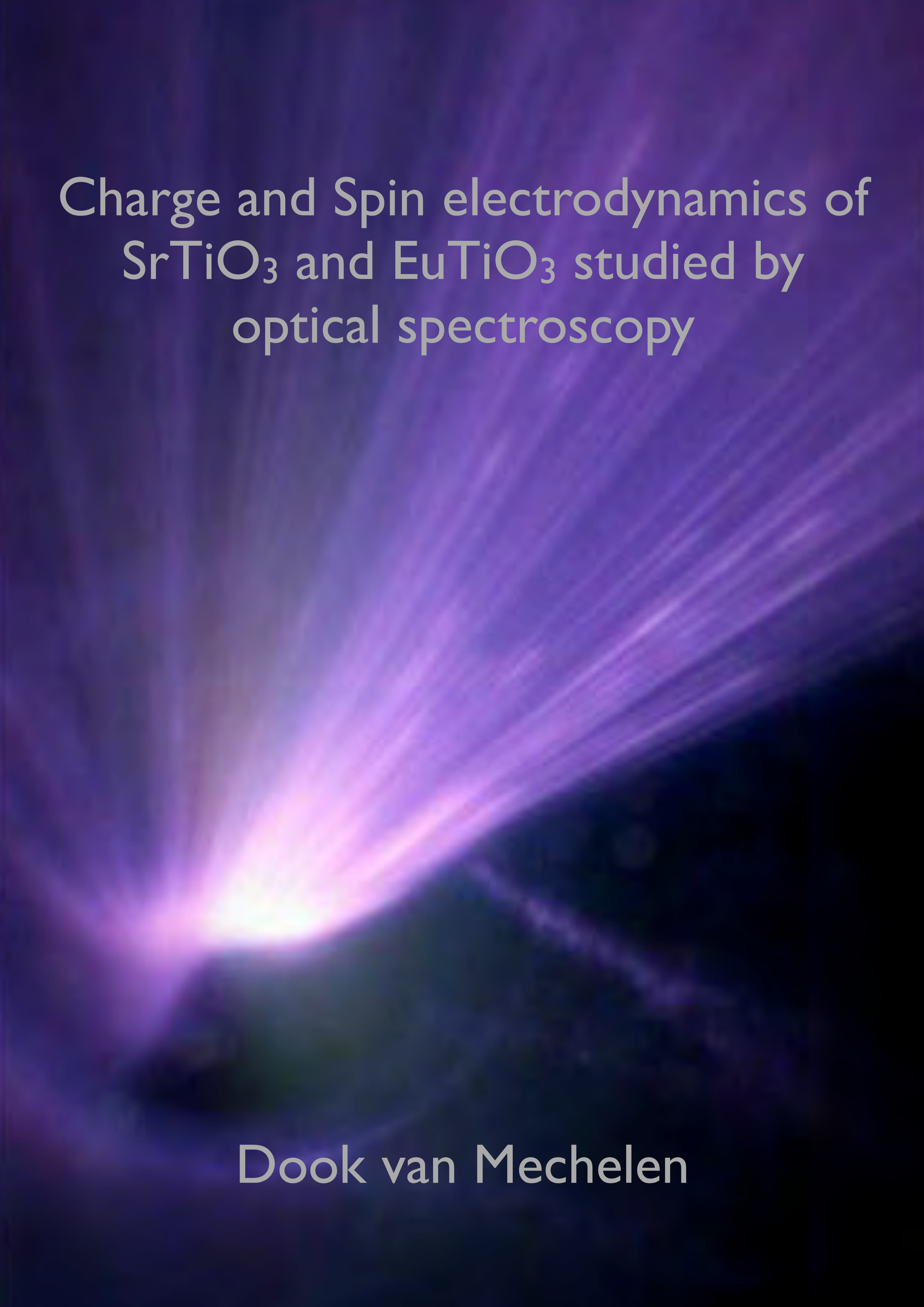

Charge and Spin electrodynamics of $SrTiO_3$ and $EuTiO_3$ studied by optical spectroscopy

Dook van Mechelen

UNIVERSITÉ DE GENÈVE
Département de Physique
de la Matière Condensée

FACULTÉ DES SCIENCES
Professeur D. van der Marel

Charge and Spin electrodynamics of $SrTiO_3$ and $EuTiO_3$ studied by optical spectroscopy

THÈSE

présenté à la Faculté des Sciences de l'Université de Genève
pour obtenir le grade de docteur ès Sciences, mention physique

par

Jacobus Lodevicus Martinus van Mechelen *dit* Dook
de
Utrecht (Pays-Bas)

Thèse n° 4215

GENÈVE
Imprimerie Harder, Genève
2010

UNIVERSITÉ
DE GENÈVE

FACULTÉ DES SCIENCES

Doctorat ès sciences
mention physique

Thèse de *Monsieur Jacobus Lodevicus Martinus VAN MECHELEN*

intitulée :

"Charge and Spin Electrodynamics of $SrTiO_3$ and $EuTiO_3$ Studied by Optical Spectroscopy"

La Faculté des sciences, sur le préavis de Messieurs D. VAN DER MAREL, professeur ordinaire et directeur de thèse, J.-M. TRISCONE, professeur ordinaire et Ch. RENNER, professeur ordinaire (Département de physique de la matière condensée), de Messieurs J. T. DEVREESE, professeur (Universiteit Antwerpen, Theorie van kwantumsystemen en complexe systemen, Antwerpen, Belgie), P. H. M. VAN LOOSDRECHT, professeur (University of Groningen, Zernike Institute for Advanced Materials, Groningen, The Netherlands) et J. LORENZANA, professeur (Università di Roma «La Sapienza», Dipartimento di Fisica, Roma, Italia), autorise l'impression de la présente thèse, sans exprimer d'opinion sur les propositions qui y sont énoncées.

Genève, le 20 mai 2010

Thèse - 4215 -

Le Doyen, Jean-Marc TRISCONE

N.B. - La thèse doit porter la déclaration précédente et remplir les conditions énumérées dans les "Informations relatives aux thèses de doctorat à l'Université de Genève".

Contents

Résumé en français

Les pérovskites réprésentent une classe d'oxydes intéressante dont les diverses propriétés électriques et magnétiques peuvent être modifiées par certains paramètres de réglage. Parmi ceux-ci sont le dopage chimique, la substitution d'isotopes, la pression, des champs électriques et magnétiques. Ce travail est une étude optique en trois parties sur deux pérovskites. Le premier, $\mathrm{SrTiO_3}$, reste très intriguant malgré le grand nombre d'études qui lui ont été consideré. Le second, $\mathrm{EuTiO_3}$, lui est apparenté mais magnétique et a été relativement peu etudié. Une extension importante des travaux précédents est l'échelle d'énergie étendue – des micro-ondes jusqu'aux ultraviolets – sur laquelle nous avons étudiés des phénomènes. Au centre de la thèse se situe la toute nouvelle technique de la spectroscopie THz dans le domaine du temps, une gamme relativement inexplorée qui clarifie et illustre des phenoménes de base dans la physique de basses énergies.

La thèse est composée ainsi. Le chapitre 1 présente la théorie de l'interaction de la lumière avec la matière et quelques concepts optiques nécessaires dans les chapitres suivants. Un aspect doit être souligné, c'est une règle de somme magnétique spécialement conçue pour l'utilisation dans le chapitre 4. Elle relie le poids spectral des transitions dipolaires magnétiques à l'aimantation totale du système. Le chapitre 2 décrit la façon dont $\mathrm{SrTiO_3}$ est accordé vers la formation d'une interaction entres les électron libres et des phonons en utilisant la substitution chimique de niobium comme paramètre de réglage. Une vaste étude des propriétés optiques et des propriétés de transport du $\mathrm{SrTi_{1-x}Nb_xO_3}$ dans la gamme $0.001 \leqslant x \leqslant 0.020$, pour des températures entre 7 K et 300 K et pour des énergies $0.3\ \mathrm{meV} < \hbar\omega < 7\,\mathrm{eV}$ a demontré la présence d'un pic de Drude qui est extraordinairement étroit à 7 K avec moins de 1 meV de large pour les dopages les plus faibles. La réduction du poids spectral de Drude révèle une masse renormalisée qui décroît légèrement de 2.5 à 1.5 avec le dopage, et qui est causée par le couplage électron-phonon. Le poids spectral manquant est retrouvé dans une série de bandes dans le moyen-infrarouge résultant de l'interaction électron-phonon. L'analyse optique du poids spectral rélève une *augmentation* inhabituelle de la masse en fonction de la température qui décroît avec le dopage. L'augmentation de la masse, la diminution de la mobilité et de la longueur de diffusion ainsi que le comportement de la résistivité statique en T^2, tous supportent l'idée d'un croisement d'un liquide polaronique à basse température vers un gaz polaronique à haute température. D'un point de vue théorique, nous interprétons les données expérimentales de la conductivité optique du $SrTiO_3$ dopé avec niobium en termes d'un gaz de grands polarons. L'approche théorique tient compte des effets à N corps, de l'interaction électron-phonon avec plusieurs branches de phonons LO, et de la dégénérescence et de l'anisotropie de la bande de conduction t_{2g} de Ti. Basé uniquement sur l'interaction de Frölich, notre théorie à N corps de grands polarons fournit une interprétation convaincante des spectres experimentaux de la conductivité optique du $SrTi_{1-x}Nb_xO_3$ sans aucun ajustement des paramètres matériels.

Le chapitre 3 décrit le comportement du mode mou ferroélectrique du $SrTiO_3$ sous l'influence d'un champ électrique extérieur. Nous avons effectué des mesures entre 2.8 K et 65 K pour des champs extérieurs jusqu'à 25 kV/cm. Le champs électrique est probablement un paramètre de réglage indirect qui lui induit un champs de tension qui est le véritable paramètre de réglage. En fonction du champs appliqué nous observons une transition de phase d'un état paraélectrique à un état ferroélectrique. Les mesures du mode mou ont permis de déterminer le paysage du potentiel anharmonique dans lequel le titane se situe. Notre approche classique ne tient pas en compte des fluctuations au point zéro importants et par conséquent le déplacement calculé de l'atome de titane est moyenné en temps, et le puit de potentiel est aplani comparé à la réalité. Un comportement universel a été observé à 3.4 kV/cm en dessous de 20 K pour un déplacement du Ti parallèle à la chaine Ti-O qui suggère la présence d'un point quantique critique entre l'état ferroélectrique et l'état paraélectrique.

Le chapitre 4 est consacré à l'influence d'un champ magnétique sur des propriétés optiques de faibles énergies du $EuTiO_3$. La nouvelle technique de l'ellipsométrie dans le domaine du temps dans la gamme des THz a été utilisée pour oberver une rotation de la polarisation de la radiation THz qui monte jusqu'à 340 deg $mm^{-1}T^{-1}$ pour le $EuTiO_3$ vierge. Cet effet gigantesque est causé par le dichroïsme des transitions dipolaires magnétiques entre les niveaux 4f de l'europium, qui sont séparés par l'effet Zeeman. Les électrons qui absorbent la radiation se mettent en résonance, ce qui est observé dans le spectre optique autour de 0.15 meV. Le poids spectral de cette résonance ferromagnétique n'est qu'un sixième du poids prévu par la règle de somme dérivée dans le chapitre 1. La raison de cette anomalie se trouve dans les spectres eux-mêmes: il y a d'autres transitions à plus haute énergie – de l'infrarouge lointain à l'infrarouge proche – qui doivent aussi être pris en compte dans le poids spectral total.

Globalement, la thèse montre la diversité des phenomènes de la physique moderne, soit la formation des polarons, la résonance magnétique et la ferroélectricité quantique, que l'on peut indépendamment induire et étudier dans des perovskites de titane, tout en réglant le paramètre de réglage approprié.

Introduction

Perovskites form an interesting class of oxide materials that often can be tuned towards versatile electric and magnetic properties using a given control parameter. Examples of this are chemical doping and isotope substitution but also parameters that do not affect the disorder in a system like hydrostatic pressure, electric fields and magnetic fields. In this way pioneering research on the perovskites resulted in exotic properties like superconductivity, colossal magneto-resistance and multiferroicity.

Optics itself is a very old technique which began with the development of lenses by the ancient Egyptians and Mesopotamians around 700 BC. Ever since it has shown its power for the study of solids e.g. by the fact that different degrees of freedom appear at different frequencies in an optical spectrum due to their distinct masses. In this way the absorption of relatively light free electrons shows up in the microwave to infrared region, the collective motion of atoms in the infrared and the absorption of bound electrons up to far in the x-ray region.

This work is a threefold optical study of two perovskites: the very well known but still surprisingly intriguing $SrTiO_3$ and its almost unexplored magnetic relative $EuTiO_3$. A major extension to previous work is the very broad energy scale from the microwave to the ultra-violet region on which phenomena have been studied. Central in the thesis is the novel technique of time-domain spectroscopy in the THz range, a relatively unexplored range which clarifies and illustrates textbook phenomena of low energy physics. The thesis built up as follows. Chapter 1 introduces the theory of the interaction of light with matter and existing optical concepts needed in the following chapters. One part needs to be highlighted, it is a magnetic sum rule specially derived for the use in chapter 4, which relates the spectral weight of magnetic dipole transitions to the total magnetization of the system. Chapter 2 describes how $SrTiO_3$ is tuned towards the formation of electron-phonon coupling by using chemical substitution of niobium as a control parameter. In chapter 3 it is shown that pristine $SrTiO_3$ tuned by an external static electric field approaches a quantum ferroelectric state and shows an intriguing universal behavior below 20 K. Chapter 4 is devoted to influence of a magnetic field on the low energy optical properties of $EuTiO_3$, which leads to a strong absorption due to the resonance of the electron spins, a so-called ferromagnetic spin resonance. Below we shortly describe each the Chapters 2 until 4.

II. Optical evidence of electron-phonon coupling in $SrTiO_3$

We have studied the optical and transport properties of $SrTi_{1-x}Nb_xO_3$ in the range $0.001 \leqslant x \leqslant 0.020$ for temperatures between 7 K and 300 K and for photon energies 0.3 meV $< \hbar\omega < 7\,\text{eV}$ and interpreted them with the support of LDA and tight-binding band structure calculations. We observe an unusually narrow Drude peak in electron doped $SrTiO_3$ at 7 K for charge carrier concentrations between 0.1% and 2% per unit cell, which is less than 1 meV for the lowest dopings. The suppression of the Drude spectral weight reveals a mass enhancement which slightly decreases with doping from 2.5 to 1.5, caused by the electron-phonon coupling. The missing spectral weight is recovered in a series mid-infrared side-bands resulting from the electron-phonon coupling interaction, traditionally associated with the polaronic nature of the charge carriers. The low temperature optical effective mass yields an intermediate electron-phonon coupling strength, $2.5 < \alpha < 4$, thus suggesting that the charge transport in electron doped $SrTiO_3$ is carried by large polarons.

With increasing temperature, the optical spectral weight analysis reveals an unusual mass *enhancement* which increases with doping. A possible crossover from a low temperature situation with large polarons to a high temperature case with small polarons has been suggested. This mass enhancement together with the decreasing mobility, the decreasing scattering length and the T^2 behavior of the DC resistivity all support the crossover from a low temperature polaron liquid to a high temperature polaron gas.

The experimental data of the optical conductivity of niobium doped $SrTiO_3$ are subsequently interpreted in terms of a gas of large polarons. The theoretical approach takes into account many-body effects, the electron-phonon interaction with multiple LO-phonon branches, and the degeneracy and the anisotropy of the Ti t_{2g} conduction band. Based on the Fröhlich interaction, our many-body large-polaron theory provides a convincing interpretation for the observed optical conductivity spectra of $SrTi_{1-x}Nb_xO_3$ *without* any adjustment of material parameters. In particular, the magnitudes of the calculated many-polaron optical conductivity spectra and of the experimental mid-infrared bands of the optical conductivity spectra of $SrTi_{1-x}Nb_xO_3$ are of the same order for all considered values of the doping parameters. The large-polaron model gives thus a convincing interpretation of the experimentally observed mid-infrared band of $SrTi_xNb_{1-x}O_3$.

III. Electro-optics of $SrTiO_3$

We have studied the effect of an external electric field on the dielectric properties of pristine $SrTiO_3$ by THz spectroscopy between 2.8 K and 65 K and for external fields below 25 kV/cm. The electric field is probably an indirect control parameter for $SrTiO_3$ and induces a strain field which is the relevant control parameter. As a function of the applied electric field we observe a transition from the paraelectric to the ferroelectric state. Based on the mode frequencies, we determine the anharmonic potential landscape of the Ti atom formed by the surrounding oxygens in-plane and out-of-plane. For large bias voltages, the Ti atom experiences the proximity of the O atom and the voltage vs. displacement curve becomes steep. The classical approach does not take into consideration the importance of zero-point fluctuations, which makes that the calculated displacement and potential energy are all *time averaged* values. The actual potential well is probably W shaped, although a static polarization in zero field is not adopted due to these quantum fluctuations. A scale invariant behavior is observed below 20 K at 3.4 kV/mm for a Ti motion along the Ti-O chain. This universality is manifested as a completely temperature independency below 20 K, and suggests the presence of a quantum critical point between the quantum ferroelectric state and the quantum paraelectric state.

IV. Magneto-optics of $EuTiO_3$

A time-domain study in the THz range on insulating $EuTiO_3$ has revealed the existence of a strong magnetic circular dichroism which manifests itself as a gigantic Faraday rotation of THz light up to 340 deg $mm^{-1}T^{-1}$. We have performed ellipsometric transmission measurements below 5.5 K in a magnetic field up to 1.6 T, from which we deduced the dielectric permittivity and the magnetic permeability for right and left handed circularly polarized light. Due to the spin-only character of $EuTiO_3$ the dichroism is present for *purely* magnetic dipole transitions inside the Zeeman split Eu 4f levels and shows up as a ferromagnetic spin resonance absorption for only one chirality. The ferromagnetic resonance energy is well described by the bare Zeeman energy without any corrections like demagnetization effects. The spectral weight of the resonance below 3.7 meV is only about a sixth of the expected spectral weight as described by the spin sum rule. It is very likely that magnetic dipole transitions between the crystal field split 4f levels are situated at higher energies, which could not be detected by the present measurement technique. Indications for this are the Faraday angle which is large and energy independent above the spin resonance and the ellipticity which increases towards higher energies. Both phenomena require the presence of a higher energy excitation which is dichroic.

Infrared reflectivity measurements on oxygen depleted $EuTiO_3$ show clear free carrier Drude absorption which is well separated from the lowest ferroelectric soft mode. A spectral weight analysis of $\sigma_1(\omega)$ has shown that the effective electron mass in $EuTiO_{3-x/2}$ with $x = 0.2\,\%$ is 3.1 ± 0.4 which is very similar to Nb doped $SrTiO_3$. This suggests that in the paramagnetic state, the charge carriers in $EuTiO_{3-x}$ are coupled in the same manner to the phonons as they are in $SrTi_{1-x}Nb_xO_3$.

In summary, this thesis demonstrates the diversity of phenomena in modern physics, be it the formation of polarons, magnetic spin-resonance or quantum ferroelectricity, that one can independently induce and study in titanate perovskites, just by tuning the appropriate control parameter.

Chapter 1

Introduction to optical spectroscopy

As an introduction to this thesis the first part of this chapter briefly revisits a number of subjects related to the interaction of light with matter that form the basis for the understanding and analysis of the experimental chapters. In the second part, a number of theoretical derivations are presented which are used for the data analysis in the following chapters. One deserves to be mentioned: a newly derived optical sum rule for magnetic dipole transitions, the so-called *spin sum rule*, presented in section 1.6.2. The final section of this chapter briefly discusses experimental issues involving THz time-domain spectroscopy.

1.1 The origin of the refractive index

The macroscopic space dependent and time dependent Maxwell equations can be written (in SI units) in their exact form

$$\nabla \cdot \mathbf{B} = 0 \tag{1.1}$$

$$\nabla \times \mathbf{E} = -\frac{\partial \mathbf{B}}{\partial t} \tag{1.2}$$

$$\nabla \cdot \mathbf{D} = \rho \tag{1.3}$$

$$\nabla \times \mathbf{H} = \frac{\partial \mathbf{D}}{\partial t} + \mathbf{J} \tag{1.4}$$

where **D** is the electric displacement field, ρ is the net charge density from an external source, **B** the magnetic field which is experienced by the electron (i.e., the magnetic induction), **E** the electric field of the electromagnetic radiation, **H** the magnetic field of the electromagnetic radiation and **J** the current density of free charges. In a medium the electric field induces a polarization of the present charges

$$P_i = \sum_j \chi_{ij} E_j + \sum_{jk} \gamma_{ijk} E_j E_k + \ldots \tag{1.5}$$

where i, j, k are different sites. We will restrict ourselves here to the linear response theory and thus only consider the first term. The relationship between the polarization and the magnetization and the above mentioned fields can then be written as

$$\mathbf{D} = \epsilon_0 \mathbf{E} + \mathbf{P} = \epsilon_0 \epsilon_r \mathbf{E} \tag{1.6}$$

$$\mathbf{H} = \frac{1}{\mu_0}\mathbf{B} - \mathbf{M} = \mu_0 \mu_r \mathbf{B} \tag{1.7}$$

$$\mathbf{J} = \sigma \mathbf{E} \tag{1.8}$$

where ϵ_0 and μ_0 are the static dielectric permittivity constant and the static magnetic permeability constant in free space, respectively, ϵ_r and μ_r the permittivity and permeability in a medium, respectively, and σ the conductivity. We deal here with the case of uncharged media, i.e., the external charge density $\rho = 0$. By taking the curl of Eqs. 1.2 and 1.4 and making use of the operator identity $\nabla \times (\nabla \times\ ) = \nabla(\nabla \cdot\ ) - \nabla^2$, the Maxwell equations lead to the wave equation for a transverse plane wave propagating in a medium,

$$\nabla^2 \mathbf{E} = \mu\epsilon \frac{\partial^2 \mathbf{E}}{\partial t^2} + \mu\sigma \frac{\partial \mathbf{E}}{\partial t} \qquad \nabla^2 \mathbf{B} = \mu\epsilon \frac{\partial^2 \mathbf{B}}{\partial t^2} + \mu\sigma \frac{\partial \mathbf{B}}{\partial t}. \tag{1.9}$$

Substituting the following form for (the electric part of) the plane wave

$$\mathbf{E} = \mathbf{E}_0\, e^{i(\mathbf{q}\cdot\mathbf{r} - \omega t)}, \tag{1.10}$$

where $\mathbf{E}_0$ is perpendicular to the wave vector $\mathbf{q}$, we obtain the non-trivial solution where all variables are frequency dependent,

$$q^2 = \frac{\omega^2}{c^2}\left[\epsilon_r + i\frac{\sigma}{\epsilon_0 \omega}\right]\mu_r. \tag{1.11}$$

We now define the complex refractive index $\tilde{n}$ as

$$q = \frac{\omega}{c}\,\tilde{n} \tag{1.12}$$

and further

$$\tilde{n}^2 = \tilde{\epsilon}\tilde{\mu} = (\epsilon_1 + i\epsilon_2)(\mu_1 + i\mu_2). \tag{1.13}$$

Analogy with Eq. 1.11 shows that ϵ_1 takes the role of the former ϵ_r in case $\tilde{\mu} = 1$. In a medium, ϵ_1 describes the dispersion and ϵ_2 the dissipation of an electric transition, similar to μ_1 and μ_2 of a magnetic transition.

1.2 Drude-Lorentz model

Electronic excitations in a solid can be described by a damped harmonic oscillator model which is called the Drude-Lorentz model. We first review the classical version and then briefly give some insights of the quantum mechanical one. Consider an electron with charge e and mass m bound to the nucleus which is assumed to have infinite mass compared to the electron. The equation of motion in the presence of an external magnetic field $\mathbf{B}$ can be written as

$$m\frac{d^2\mathbf{r}}{dt^2} + m\gamma\frac{d\mathbf{r}}{dt} + m\omega_0^2\mathbf{r} = -\frac{e}{c}\mathbf{v} \times \mathbf{B} + e\mathbf{E} \tag{1.14}$$

where the second term is the damping with damping constant γ, the third term the restoring force with ω_0 the characteristic frequency of the excitation, the fourth term the force due to the external magnetic field, and the last term the force on the electron due to the local electric field. In response to an ac electromagnetic field $\mathbf{E}(t) = \mathbf{E}_0\, e^{-i\omega t}$ we obtain the local polarization $\mathbf{p} = e\mathbf{r}$. With N the charge carrier density, the total polarization is

$$\mathbf{P} = N\langle\mathbf{p}\rangle = 4\pi\epsilon_0 N\alpha\mathbf{E}, \tag{1.15}$$

where α is the molecular polarizability. With $\mathbf{P} = \epsilon_0(\tilde{\epsilon}-1)\mathbf{E}$ we obtain the dielectric permittivity function for left ($-$) and right ($+$) handed circularly polarized light,

$$\tilde{\epsilon}_\pm(\omega) = 1 + \frac{\omega_p^2}{\omega_0^2 - \omega^2 - i\gamma\omega \mp \omega\omega_c} \tag{1.16}$$

where the oscillator strength $\omega_p^2 = Ne^2/(\epsilon_0 m)$ and the cyclotron frequency $\omega_c = eB/m$ [12]. With $\tilde{\epsilon}(\omega) = \epsilon_1(\omega) + i\epsilon_2(\omega)$ we get

$$\begin{aligned} \epsilon_1^\pm(\omega) - 1 &= \omega_p^2\frac{\omega_0^2 - \omega^2 \pm \omega\omega_c}{(\omega_0^2 - \omega^2 \pm \omega\omega_c)^2 + \gamma^2\omega^2} && (1.17) \\ \epsilon_2^\pm(\omega) &= \omega_p^2\frac{\gamma\omega}{(\omega_0^2 - \omega^2 \pm \omega\omega_c)^2 + \gamma^2\omega^2} && (1.18) \end{aligned}$$

Free electrons do not experience a restoring force and are allowed to freely move between the atoms, hence $\omega_0 = 0$ which results into the Drude model for metals. In general, an optical spectrum can be modeled using a series of terms like in Eq. 1.16 each corresponding to a specific resonance mode (plasmon, phonon, polaron, etc.). The total dielectric permittivity function then becomes a sum of one free electron and n bound electron contributions

$$\tilde{\epsilon}_\pm(\omega) = \epsilon_\infty + \frac{\omega_{p,e}^2}{\omega^2 - i\gamma_e\omega \mp \omega\omega_{c,e}} + \sum_{i=1}^{n}\frac{\omega_{p,i}^2}{\omega_{0,i}^2 - \omega^2 - i\gamma_i\omega \mp \omega\omega_{c,i}} \tag{1.19}$$

Since the ion mass is very large compared to the electron mass, the ionic cyclotron frequency is generally negligible.

In the preceding part, we derived the Drude-Lorentz formalism in a purely classical way. However, the same result is obtained quantum mechanically [2]. We will briefly revisit the key elements of the derivation (the units will be exceptionally in cgs), since they may show more insight than the classical variant.

The hamiltonian which describes a N electron system interacting with an electromagnetic wave can be written as the sum of an unperturbed term $\mathcal{H}_0$ and an interaction term $\mathcal{H}_i$.

$$\mathcal{H}_0 = \frac{1}{2m}\sum_{i=1}^{N}\mathbf{p}_i^2 + \sum_{i=1,j=1}^{N,M} V_j^0(\mathbf{r}_j - \mathbf{R}_j) + \frac{1}{2}\sum_{i=1,i'=1}^{N,N}\frac{e^2}{|\mathbf{r}_i - \mathbf{r}_{i'}|} \tag{1.20}$$

where the first term is the kinetic energy of the electrons with momentum $\mathbf{p}_i$, the second is the electron-lattice interaction due to the potential V_j^0 and the third term the electron-electron interaction. The interaction term is

$$\mathcal{H}_i = \frac{e}{2mc}\sum_{i=1}^{N}[\mathbf{p}_i\cdot\mathbf{A}(\mathbf{r}_i) - \mathbf{A}(\mathbf{r}_i)\cdot\mathbf{p}_i] + \frac{e}{m}\sum_{i=1}^{N}\mathbf{S}\cdot\mathbf{B}(\mathbf{r}_i) - e\sum_{i=1}^{N}\Phi(\mathbf{r}_i) \tag{1.21}$$

where the first term is the coupling of the electrons to the vector potential $\mathbf{A}(\mathbf{r}_i)$, the second term represents the coupling to the magnetic field $\mathbf{B}(\mathbf{r}_i)$ (see further section 1.5) and the third term describes an external scalar potential Φ as produced by an external charge. For the present discussion we will neglect the second and third term. We arrive at the Kubo formula for the optical conductivity when we proceed as follows. The total power that is dissipated in the system upon radiation is $P = \sigma_1 E^2$, so once we have the power, we obtain the real part of the optical conductivity and via the Kramers-Kronig relations also the imaginary part. P is determined by the probability that an incident photon excites an electron from one many body state $|s\rangle$ into another $|s'\rangle$ which is given by Fermi's Golden rule

$$W_{s\rightarrow s'} = \frac{2\pi}{\hbar^2}\left|\langle s'|\mathcal{H}_i|s\rangle\right|^2\ \delta(\omega - \omega_{s'} + \omega_s) \tag{1.22}$$

The interaction term, Eq. 1.21, can be reformulated in terms of the electrical current density $\mathbf{J}^{\mathrm{T}}(\mathbf{q})$ which gives

$$\mathcal{H}_i = -\frac{1}{c}\mathbf{J}^{\mathrm{T}}(\mathbf{q})\cdot\mathbf{A}^{\mathrm{T}}(\mathbf{q}) \tag{1.23}$$

Substituting Eq. 1.23 into Eq. 1.22 and summing over all initial occupied and final empty states yields the dissipated power P per unit time and volume. Since for transverse waves $\mathbf{E}^{\mathrm{T}} = i\omega\mathbf{A}^{\mathrm{T}}/c$ we obtain the real part of the optical conductivity expressed as a current-current correlation function

$$\sigma_1^{\mathrm{T}}(\mathbf{q},\omega) = \sum_s \frac{1}{\hbar\omega}\int dt\ \left\langle s\left|\mathbf{J}^{\mathrm{T}}(\mathbf{q},0)\,\mathbf{J}^{\mathrm{T}*}(\mathbf{q},t)\right|s\right\rangle e^{-i\omega t}, \tag{1.24}$$

which is the Kubo formula. It describes the fluctuations of the current in the ground state. For systems that obey Fermi statistics the Kubo formula changes to the Kubo-Greenwood formula [7]

$$\sigma_1(\omega) = \frac{\pi e^2}{m^2\omega}\left|\langle s'|p|s\rangle\right|^2\ D_{s's}(\hbar\omega) \tag{1.25}$$

where $\langle s'|p|s\rangle$ is the dipole matrix element and $D_{s's}$ the joint density of states. The Kubo formula (Eq. 1.24) can be used to derive the leading order metallic conductivity in a quantum mechanical fashion. The result is identical to what we obtained classically (cf. Eq. 1.16).

1.3 Kramers-Kronig relations

We obtained from the last section that the interaction of electromagnetic radiation with matter involves material specific properties, expressed in the dielectric permittivity function and the magnetic permeability function. These functions can be considered as a response function to a stimulus which is the electromagnetic radiation impinging on the material. If we imagine the response to be close to the spacial region where the light hits the material (i.e., in the local approximation) we can write for the response $X(t)$

$$X(t) = \int_{-\infty}^{\infty} G(t-t')\, f(t')\, dt' \tag{1.26}$$

where $G(t,t')$ is the response function and $f(t')$ is the stimulus. If we require that there is no response before the stimulus, or in other words if we require to system to be causal, then $G(t-t') = 0$ if $t < t'$ and Eq. 1.26 reduces to

$$X(t) = G(t-t_0) \tag{1.27}$$

In frequency space the response function becomes

$$G(\omega) = \int G(t-t')\, e^{i\omega(t-t')} dt \tag{1.28}$$

Assuming a complex frequency and integrating only over the upper half plane (due to causality) we get from Cauchy's theorem

$$G(\omega) = \frac{1}{i\pi}\, \mathcal{P} \int_{-\infty}^{\infty} \frac{G(\omega')}{\omega'-\omega}\, d\omega' \tag{1.29}$$

with $\mathcal{P}$ the principal value. Since $G(\omega)$ is a complex function, Eq. 1.29 relates its real to its imaginary part. This relationship states that if only one part (real or imaginary) of a complex observable has been measured (over a sufficiently broad frequency range), the other part can be deduced. These so-called Kramers-Kronig relations for the dielectric permittivity function can then be written as

$$\begin{aligned} \epsilon_1(\omega) - 1 &= \frac{1}{\pi}\, \mathcal{P} \int_{-\infty}^{\infty} \frac{\epsilon_2(\omega')}{\omega'-\omega}\, d\omega' && (1.30) \\ \epsilon_2(\omega) &= -\frac{1}{\pi}\, \mathcal{P} \int_{-\infty}^{\infty} \frac{\epsilon_1(\omega')-1}{\omega'-\omega}\, d\omega' && (1.31) \end{aligned}$$

and can identically be formulated for e.g. the magnetic permeability $\mu(\omega)$.

1.4 Fresnel equations

In the past sections we have seen that electromagnetic radiation interacts with matter. Here we will derive the amplitude and phase relations that exists for an electromagnetic plane wave impinging on the interface of two different media. A plane wave with frequency ω and wave vector $\mathbf{k}$ passes at $z = 0$ an interface that separates two media with ϵ, μ and ϵ', μ', respectively. The incident transverse plane wave (labelled i), characterized by

$$\mathbf{E} = \mathbf{E}_0 \, e^{i\mathbf{k}_i \cdot \mathbf{x} - i\omega t} \tag{1.32}$$

$$\mathbf{B} = \mathbf{B}_0 \, e^{i\mathbf{k}_i \cdot \mathbf{x} - i\omega t} \tag{1.33}$$

gets reflected and transmitted when it encounters the interface. In what follows, we label these two beams with r and t, respectively. The electric and magnetic fields of an electromagnetic wave traveling across an interface are subject to boundary conditions (as required by the Maxwell equations) which must be satisfied at all points of the interface at all times. The spatial and time variation of the incident, reflected and transmitted fields must be the same at $z = 0$, and thus

$$(\mathbf{k}_i \cdot \mathbf{x})_{z=0} = (\mathbf{k}_r \cdot \mathbf{x})_{z=0} = (\mathbf{k}_t \cdot \mathbf{x})_{z=0} \tag{1.34}$$

$$\omega_i = \omega_r = \omega_t \tag{1.35}$$

which states that all wave vectors lie in the same plane and the frequency of the wave is conserved. From which $k_i \sin\theta_i = k_r \sin\theta_r = k_t \sin\theta_t$ and since $k_i = k_r$ the angle of incidence is equal to the angle of reflection. Multiplying with c/ω_i gives Snell's law

$$\sqrt{\epsilon\mu}\,\sin\theta_i = \sqrt{\epsilon'\mu'}\,\sin\theta_t \tag{1.36}$$

which is the relationship among the phases of the incident, reflected and transmitted beam. If we apply now the amplitude boundary conditions which are (i) the normal components of $\mathbf{D}$ and $\mathbf{B}$ are continuous and (ii) the tangential components of $\mathbf{E}$ and $\mathbf{H}$ are continuous. We consider the situation of linearly polarized light for which $\mathbf{E}$ is perpendicular to the plane of incidence (s polarization). The boundary conditions for $\mathbf{E}$ and $\mathbf{H} = \mathbf{B}/\mu$ require

$$E_i + E_r = E_t \tag{1.37}$$

$$-\frac{B_i}{\mu}\cos\theta_i + \frac{B_r}{\mu}\cos\theta_r = -\frac{B_t}{\mu'}\cos\theta_t \tag{1.38}$$

which becomes with $\hat{\mathbf{k}} \times \mathbf{E} = v\mathbf{B}$ the Fresnel equations for s-polarized light

$$r_s = \left(\frac{E_r}{E_i}\right)_{\perp} = \frac{\cos\theta_i/Z_i - \cos\theta_t/Z_t}{\cos\theta_i/Z_i + \cos\theta_t/Z_t} \tag{1.39}$$

$$t_s = \left(\frac{E_t}{E_i}\right)_{\perp} = \frac{2\cos\theta_i/Z_i}{\cos\theta_i/Z_i + \cos\theta_t/Z_t} \tag{1.40}$$

where $Z = \sqrt{\mu/\epsilon}$ has the meaning of impedance if $\sigma = 0$ (i.e., for dielectrics). Similarly we can derive for **E** parallel to the plane of incidence (p polarization)

$$r_p = \left(\frac{E_r}{E_i}\right)_{||} = \frac{\cos\theta_i/Z_t - \cos\theta_t/Z_i}{\cos\theta_t/Z_i + \cos\theta_i/Z_t} \tag{1.41}$$

$$t_p = \left(\frac{E_t}{E_i}\right)_{||} = \frac{2\cos\theta_i/Z_i}{\cos\theta_t/Z_i + \cos\theta_i/Z_t} \tag{1.42}$$

For normal incidence there is no difference between s and p polarization. Moreover, if we assume the initial medium to be vacuum, then the transmission and (internal) reflection coefficients for a transverse electromagnetic plane wave can be written in their simplified form as

$$r = \frac{1-Z}{1+Z}, \qquad t_1 = \frac{2Z}{1+Z} \tag{1.43}$$

where $Z = Z_t$.

1.5 Magneto-optics

The hamiltonian of a solid with charge and spin degrees of freedom which interacts with an electromagnetic wave can be written as a sum of the unperturbed system $\mathcal{H}_0$ (given in Eq. 1.20) and the interaction with the electromagnetic wave $\mathcal{H}_i$ [10],

$$\mathcal{H}_i = \frac{1}{2m}\left[\mathbf{P} - q\mathbf{A}(\mathbf{R},t)\right]^2 + \frac{e}{m}\mathbf{S}\cdot\mathbf{B}(\mathbf{R},t) \tag{1.44}$$

where $\mathbf{A}(\mathbf{R},t)$ is the vector potential. During this linear interaction, the photon can transfer its angular momentum quantum $\hbar$ to the material in two different ways. In the absence of spin-orbit interaction, this is done either by (i) an electric (dipole) transition which is described by the first term in Eq. 1.44 as a transfer of the photon angular momentum to the orbital degree of freedom of the electron or (ii) by a magnetic (dipole) transition where the photon's angular momentum is transferred to the spin of the electron, given by the second term of Eq. 1.44. The ratio of the strengths of the two processes is equal to the wavelength over the Bohr radius, λ/a_0 and since $\lambda \gg a_0$ we conclude that in the dc to optical range the electric dipole transitions are always much stronger than the magnetic dipole transitions. Evaluating the first term of Eq. 1.44 within the hydrogen wave function eigenstates yields the electric dipole selection rules:

$$\Delta\ell = \pm 1 \tag{1.45}$$

$$\Delta m_\ell = \pm 1, 0 \tag{1.46}$$

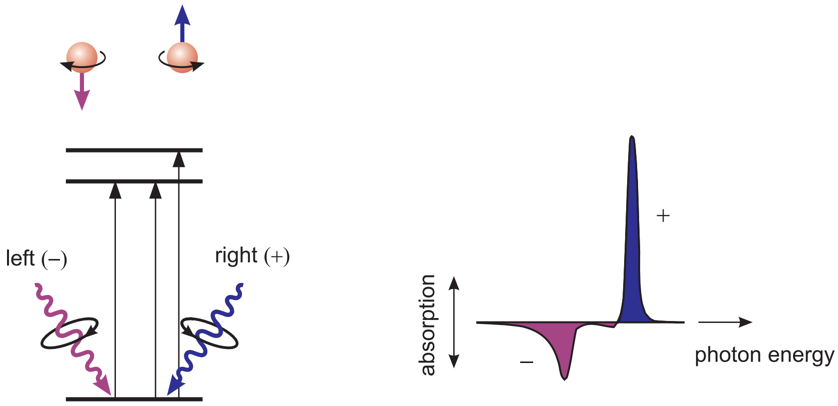

Figure 1.1: A cartoon of a dichroic optical process. The transition probabilities of right and left handed circularly polarized light are different, which causes one chirality to be more absorbed than the other.

and with the second term of Eq. 1.44 the magnetic dipole selection rules

$$\Delta\ell = 0 \tag{1.47}$$

$$\Delta m_\ell = \pm 1, 0 \tag{1.48}$$

$$\Delta m_s = \pm 1, 0 \tag{1.49}$$

These selection rules are important to describe the optical processes in solids. They imply that transitions are only allowed between orbitals that satisfy these rules. In general, when the polarization state of light contains two chiralities, each of them has a different probability to be absorbed, given by the selection rules. This can cause a fully polarization state dependent absorption, which is called dichroism. Fig. 1.1 schematically shows the process of purely spin dichroism. The two chiralities of the circularly polarized light have different transition probabilities for a certain transition. Therefore there is a net addition of spin angular momentum, which increases the total magnetization of the sample.

When the spin-orbit interaction is turned on, the good quantum numbers become ℓ and J, and the selection rules change to $\Delta\ell = 0$; $\Delta J = \pm 1, 0$ and $\Delta m_J = \pm 1, 0$. This makes the condition of angular momentum transfer less stringent and one can e.g. optically alter the spin state of a solid by only coupling to the first term of Eq. 1.44.

1.5.1 Polarization eigenstates in a magnetic field

In the derivation of the refractive index in section 1.1 we assumed a transverse electromagnetic wave that was linearly polarized without the presence of an external magnetic field. An external magnetic field or the presence of a nonzero spontaneous magnetization leads to a broken time reversal symmetry. Consequently, the dielectric permittivity and the magnetic permeability are not just scalars (as assumed in section 1.1), but are non reducible tensors. Exceptionally, we will consider that the magnetic permeability $\mu = \mu_0\mathbf{1}$, since it does not change the end result, but it significantly simplifies the derivation. We choose the magnetization parallel to the z axis, such that the permittivity tensor takes the form[1]

$$\epsilon(\mathbf{M},\omega) = \begin{vmatrix} \epsilon_{xx} & \epsilon_{xy} & 0 \\ -\epsilon_{xy} & \epsilon_{yy} & 0 \\ 0 & 0 & \epsilon_{zz} \end{vmatrix} \tag{1.50}$$

where all components depend on frequency and magnetization, are complex and satisfy the Onsager relations which state that the diagonal components are even functions of $\mathbf{M}$ and the off-diagonal components are odd functions of $\mathbf{M}$,

$$\epsilon_{ij}(-\mathbf{M},\omega) = \epsilon_{ji}(\mathbf{M},\omega) \tag{1.51}$$

Making use of the Maxwell equations 1.2 and 1.4 with $\mathbf{B} = \mu_0\mathbf{H}$ and putting $\sigma = 0$ for nonconducting media, we can substitute for an electromagnetic plane wave Eqs. 1.32-1.33 which results in a wave equation like we earlier obtained for a scalar dielectric function Eq. 1.9. Since the magnetization is parallel to the propagation vector $\mathbf{k} = k\hat{z} = \omega n\hat{z}/c$ the wave equation yields in matrix notation

$$\begin{pmatrix} k^2E_x \\ k^2E_y \\ 0 \end{pmatrix} = \frac{\omega}{c^2}\begin{pmatrix} \epsilon_{xx} & \epsilon_{xy} & 0 \\ -\epsilon_{xy} & \epsilon_{yy} & 0 \\ 0 & 0 & \epsilon_{zz} \end{pmatrix}\begin{pmatrix} E_x \\ E_y \\ E_z \end{pmatrix} \tag{1.52}$$

From which we get the index of refraction for an anisotropic medium

$$n_\pm^2 = \epsilon_{xx} \pm i\epsilon_{xy} \tag{1.53}$$

This result states that the polarization eigenstates for an anisotropic medium are circular, i.e., right and left handed. This means that in case we analyze optical spectra of anisotropic media or isotropic media in a magnetic field (which consequently then become anisotropic) it is more convenient to work with the eigenstates (circular polarization) then with linear polarization. The transformation from Cartesian to circular coordinates is for e.g. the transmission, permittivity and permeability

$$t_\pm = t_{xx} \pm it_{xy} \qquad \epsilon_\pm = \epsilon_{xx} \pm i\epsilon_{xy} \qquad \mu_\pm = \mu_{xx} \pm i\mu_{xy} \tag{1.54}$$

1.5.2 Faraday Effect

We showed that for an anisotropic medium (by itself or due to an external field) there is a spacial dispersion of the susceptibility and as a result the polarization

---

[1] The symmetry requires that the dielectric permittivity tensor is invariant under the operation of the group represented by matrix transformations that represent a rotation about the magnetization axis. This requires that some elements of the tensor vanish.

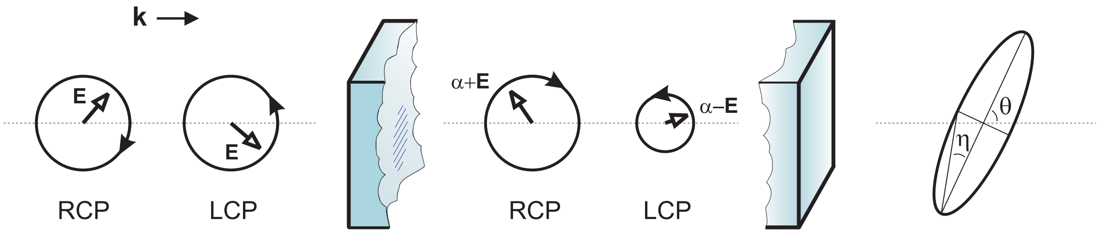

Figure 1.2: Two circularly polarized waves enter a material where (*i*) their mutual speed and (*ii*) the absorption for both is different which makes that the emerging wave is elliptically polarized.

eigenstates are circular. This generally implies that if linearly polarized light[2] is shed onto an anisotropic medium the polarization plane rotates gradually as the light beam proceeds [48]. In other words, the circularly polarized beams propagate with different refractive indices, n_+ and n_- and experience a different absorption. The first aspect creates a phase difference between them, whereas the second changes their mutual amplitudes. Consequently, the polarization state of the beam when both chiralities recombine on leaving the medium becomes elliptical, see Fig. 1.2. This circular dichroism phenomenon[3] is called the *polar* Faraday effect if the symmetry axis (i.e., the direction of the external magnetic field or the direction of the anisotropy field) is parallel to the propagation direction of the light. It is a *linear* magneto-optical effect and can thus be described by $\mathbf{M} = \chi\mathbf{H}$ without considering higher order terms. The ellipse can be characterized by the angle the major axis makes with respect to the polarization axis of the linearly polarized wave. The rotation angle per unit length is called the Faraday rotation $\theta_{\mathrm{F}}(\omega)$ and is given by the difference of the real parts of the indices of refraction [5]

$$\theta_{\mathrm{F}}(\omega) = \frac{\omega}{2c}\,\mathrm{Re}(n_+ - n_-), \tag{1.55}$$

with l the length of the transmission path. The quantity $(n_+ - n_-)$ can be expanded power series of the applied field H. For weak fields only the linear term is kept which results in the well-known formula for the Faraday rotation $\theta_F \simeq VHd$, with V the material dependent Verdet constant.[14] This relationship shows that to first order the rotation is linear with the applied field and the sample thickness d. The ellipticity per unit length of the transmitted wave $\eta_{\mathrm{F}}(\omega)$ which is defined as the ratio of the minor axis of the ellipse over the major one, is given by the difference of the imaginary parts of the indices of refraction

$$\eta_{\mathrm{F}}(\omega) = -\frac{\omega}{2c}\,\mathrm{Im}(n_+ - n_-). \tag{1.56}$$

---

[2] Linear polarized light can be thought of as being composed of two circular polarized beams: one rotating right or clockwise (+) and the other left or anti-clockwise (−) as viewed by the observer faced towards the light source.

[3] Generally referred to as *Magnetic Circular Dichroism*, but this is strictly speaking only appropriate if the nature of the transitions that generate the effect is magnetic.

Eqs. 1.55-1.56 indicate that both the rotation and the ellipticity increase with frequency. In the visible part of the spectrum rotation values of $10^4 - 10^6$ deg/cm are often encountered (e.g. for the ferromagnetic garnets) in magnetic fields less than 1 T, [5] whereas in the microwave region this is more of the order of 10^1 deg/cm below 1 T [15]. The rotation and ellipticity can also be obtained directly from the raw transmission data [21],

$$\theta_{\mathrm{F}}(\omega) = \frac{\arg(\mathcal{T}_+) - \arg(\mathcal{T}_-)}{2} \qquad \eta_{\mathrm{F}}(\omega) = \frac{|\mathcal{T}_-| - |\mathcal{T}_+|}{|\mathcal{T}_-| + |\mathcal{T}_+|} \tag{1.57}$$

where $\mathcal{T}_\pm$ is the transmission for RCP (+) and LCP (−) light.

1.5.3 Kerr Effect

Similar to the polar Faraday effect, there exists an equivalent for the reflected light of an anisotropic medium, the so-called polar Kerr effect (also called magneto-optical Kerr effect, MOKE). The Kerr rotation and ellipticity are,

$$\theta_{\mathrm{K}}(\omega) = -\mathrm{Im}\frac{n_+ - n_-}{n_+ n_- - 1} \qquad \eta_{\mathrm{K}}(\omega) = \mathrm{Re}\frac{n_+ - n_-}{n_+ n_- - 1}. \tag{1.58}$$

Notice that these properties opposite to the Faraday case are not proportional to the frequency. Kerr angles are generally very small, of the order of nano to micro degrees (e.g. Refs. [22] and [23]), although exceptions are EuO and EuSe with 7 and 10 degrees (between 1-5 eV), respectively [24].

1.6 Optical sum rules

In this section we will present optical sum rules for electric dipole transitions and also for pure magnetic dipole transitions, which are never reported before. Sum rules equate an integrated observable to a material dependent constant. They are of large practical use e.g. to verify the quality of the data but more importantly to find out (in)consistencies with the aimed theory.

1.6.1 Electric dipole transitions

The isotropic case

If an optical absorption spectrum for linearly polarized light consists solely of excitations that involve electric dipole transitions, then the sum of the spectral weights of all transitions is directly proportional to the ratio of the electron density N and the electron mass. This so-called optical Thomas Reiche Kuhn sum rule, or f sum rule, can be invoked from the Kramers-Kronig relations together with the Drude-Lorentz expression of the dielectric permittivity function in the high frequency limit. Hence $\omega \gg \omega_0$, $\omega \gg \omega_p$ and $\omega \gg \gamma$ which implies that all electrons (free and bound) respond as though they were free and $\epsilon_1(\omega) = 1 - \omega_p^2/\omega^2$. The Kramers-Kronig relation for ϵ_1 in the high frequency limit is

$$\epsilon_1(\omega) \approx 1 - \frac{2}{\pi\omega^2} \int_0^\infty \omega' \epsilon_2(\omega')\ d\omega' \tag{1.59}$$

which leads to the f sum rule

$$\frac{\pi}{2}\omega_p^2 = \int_0^\infty \omega\epsilon_2(\omega)\, d\omega. \tag{1.60}$$

This can be written as the f sum rule for the optical conductivity $\sigma_1(\omega)$

$$W \equiv \frac{\pi\epsilon_0}{2}\omega_p^2 = \int_0^\infty \sigma_1(\omega)\, d\omega = \frac{\pi N e^2}{2m}, \tag{1.61}$$

where W is the total spectral weight, N the charge carrier density and m the charge carrier mass.[4] The sum rule holds for all electric dipole transitions that involve charge. The Thomas Reiche Kuhn sum rule is the $k \to 0$ limit of the general Bethe sum rule [13]. For phonons with charge q_j and mass M_j the last term of Eq. 1.61 changes for instance to $\pi/2 \sum_j q_j^2/M_j$. As is extensively discussed in Chapter 2, with Eq. 1.61 one can deduce the effective charge carrier mass m^*/m by integrating just the free electron part of the optical conductivity. A sum rule which already inherently distinguishes between the coherent and incoherent part of the Drude spectral weight is the Devreese sum rule [16]

$$\frac{\pi N e^2}{2m^*} + \int_{\omega_L}^\infty \sigma_1(\omega) d\omega = \frac{\pi N e^2}{2m_b} \tag{1.62}$$

where the integral starts from the relevant longitudinal phonon frequency ω_L. m^* is the renormalized mass of the charge carriers and m_b is their band mass. This sum rule basically equates the spectral weight of the Drude peak (first term) and the mid-infrared band (second term) to the total spectral weight as expressed in Eq. 1.61.

The anisotropic case

In media that either have natural optical activity or induced anisotropy due to an external magnetic field, the polarization eigenstates are circular and the common f sum rule does not hold in the form of Eq. 1.61. This is because the dielectric permittivity tensor Eq. 1.50 and similarly the magnetic permeability tensor obey the Kramers-Kronig relations, but most dispersion relations involve the complex refractive index $\tilde{n}(\omega)$ which is a complicated function built up of

---

[4] The total spectral weight is often expressed in cgs units, and reads then $W = \omega_p^2/8$.

various elements of these tensors which generally does not obey these relations. However, a generalized Thomas Reiche Kuhn sum rule can be formulated [17] in terms of the optical conductivity for right and left handed circularly polarized light

$$W = \int_0^\infty \frac{\sigma_1^+(\omega) + \sigma_1^-(\omega)}{2}\, d\omega. \tag{1.63}$$

Let us explain why the f sum rule does not hold for each chirality individually by considering the Kuhn sum rule for the imaginary part of the index of refraction $\tilde{n}(\omega) = n(\omega) + i\kappa(\omega)$ [18, 19, 20]

$$\int_0^\infty [\kappa_+(\omega) - \kappa_-(\omega)]\, d\omega = 0. \tag{1.64}$$

Since the extinction coefficient $\kappa(\omega)$ is proportional to the rate of absorption, this sum rule states that the net transition rates for right and left handed circularly polarized light are equal. However, the oscillator spectral weights (which are proportional to the energies times the transition probabilities) are not equal and the standard form of the f sum rule (Eq. 1.61) does not apply to either mode separately. [17]

The first-moment circular-birefringence rule $\int_0^\infty \omega\, [n_+(\omega) - n_-(\omega)]\, d\omega = 0$ can be used with the Faraday rotation expressed in Eq. 1.55 to constitute a sum rule for the Faraday rotation $\theta_F(\omega)$ [17]

$$\int_0^\infty \theta_F(\omega)\, d\omega = 0. \tag{1.65}$$

1.6.2 Magnetic dipole transitions

The sum rules of the preceding part only consider electric dipole transitions. Sum rules also exist for the case of electric dipole transitions in the presence of a strong spin-orbit interaction, where transitions are neither pure electric dipole nor magnetic dipole like. However, for pure magnetic dipole transitions, to our knowledge, no optical sum rule existed before. It is important to notice that the Drude-Lorentz expressions do not hold for pure magnetic dipole transitions. The equivalent for the magnetic permeability is subject of the introduction of Chapter 4 but for completeness we repeat here the key elements. Like the equation of motion of the harmonic oscillator which described an electric dipole oscillator, we write for a magnetic dipole resonance the phenomenological Landau-Lifshitz-Gilbert equation of motion of the magnetization $\mathbf{M}$

$$\frac{d\mathbf{M}}{dt} = \gamma \mathbf{M} \times \mathbf{B} - \frac{\alpha}{|M|}\mathbf{M} \times \frac{d\mathbf{M}}{dt} \tag{1.66}$$

where $\gamma = g\mu_B\hbar^{-1}$ is the gyromagnetic ratio, g the Landé factor, $\mu_B = e\hbar/2m_e$ the Bohr magneton, $\alpha > 0$ is the Gilbert damping constant and $\mathbf{B}$ the magnetic field experienced by the electron. From Eq. 1.66 we obtain the magnetic susceptibility by substituting $\mathbf{B} = \mathbf{H}_0 + \mathbf{h}e^{i\omega t}$ and $\mathbf{M} = \mathbf{M}_0 + \mathbf{m}e^{i\omega t}$, which represent the sums of the the static part and the alternating ac component (needed to drive the system into resonance, see Chapter 4). Within the linear approximation (small ac power) this gives the components of the magnetic permeability tensor $\mu(\omega)$ in the circular representation

$$\mu^{\pm} = 1 + \frac{\omega_M}{(\omega_0 + i\Gamma) \mp \omega} = 1 + \frac{\omega_M(\omega_0 \mp \omega)}{(\omega_0 \mp \omega)^2 + \Gamma^2} - i\frac{\omega_M \Gamma}{(\omega_0 \mp \omega)^2 + \Gamma^2} \tag{1.67}$$

where Γ is the damping, $\omega_M = \mu_0 \gamma M$.[11] Similar as for the f sum rule, we take the limit of $\mu_1^{\pm}(\omega)$ for $\omega \gg \omega_0$ which gives

$$\lim_{\omega \gg \omega_0} \mu_1^{\pm}(\omega) = 1 \mp \frac{\omega_M}{\omega}. \tag{1.68}$$

Substitution in the Kramers-Kronig relation in the high frequency limit (cf. Eq. 1.59) gives the total magnetic spectral weight W

$$W = \int_0^{\infty} \mu_2^{\pm}(\omega)\, d\omega = \frac{\pi}{2}\omega_M = \frac{\pi}{2}\mu_0 \gamma M \tag{1.69}$$

which is the *optical spin sum rule* . Since the spin sum rule concerns just one specific circular polarization state, spectral weight analyses involving RCP and LCP spectra have thus to be done independently.

1.7 Transmission through a parallel plate

An electromagnetic wave incident on a parallel plate is partially reflected at the interface, partially transmitted and partially internally reflected. The part of the radiation that gets once (or more) internally reflected travels longer and thus also leaves the material later than the straight transmission. We derived in section 1.4 the Fresnel coefficients for the reflection and (straight) transmission at a vacuum-matter interface. For the opposite case of a matter-vacuum interface, the transmission coefficient changes to

$$t_2 = \frac{2}{1 + Z} \tag{1.70}$$

with $Z = \sqrt{\mu/\epsilon}$, whereas the amplitude reflection coefficient remains the same. For a plane wave (Eq. 1.32) with $k_i = \omega\tilde{n}/c$ the complex transmission of the part of the beam that is transmitted without any internal reflection, is

$$\mathcal{T}_1 = \frac{E_1}{E_0} = \frac{t_1 t_2\, e^{in\omega d/c}}{e^{i\omega d/c}} = \frac{4Z}{(1 + Z)^2}\, e^{i(n-1)\omega d/c} \tag{1.71}$$

where $n = \sqrt{\epsilon\mu}$ is the complex index of refraction (the previously used tilde will be omitted from now on), d is the thickness of the parallel plate. The transmission of the first beam that has been subject to internal reflections, i.e., the so-called *first echo*, is equal to

$$\mathcal{T}_2 = \frac{E_2}{E_0} = \frac{t_1 t_2\, r^2\, e^{3in\omega d/c}}{e^{i\omega d/c}} = \frac{4Z(1-Z)^2}{(1+Z)^4}\, e^{i(3n-1)\omega d/c} \tag{1.72}$$

The total transmission is given by the straight transmission $\mathcal{T}_1$ plus the sum of all internally reflected beams

$$\mathcal{T} = \sum_{i=1}^{\infty} \mathcal{T}_i = \frac{E}{E_0} = t_1 t_2\, \frac{e^{i(n-1)\omega d/c}}{1 - r^2\, e^{2in\omega d/c}} = \frac{4Z\, e^{i(n-1)\omega d/c}}{(1+Z)^2 - (1-Z)^2\, e^{2in\omega d/c}} \tag{1.73}$$

1.7.1 Direct inversion for the nonmagnetic case

From the experimentally measured transmission of a nonmagnetic material ($\mu = 1$), one can extract the dielectric permittivity function with Eqs. 1.71-1.73. These relations are not analytically invertible, but an inversion following an iterative approach converges fast for bulk thicknesses ($d \gtrsim 10^{-6}$ m). For the nonmagnetic case, the transmission and reflection coefficients t_1, t_2 and r (cf. Eqs. 1.43 and 1.70) can be written as

$$r = \frac{n-1}{n+1}, \qquad t_1 = \frac{2}{n+1}, \qquad t_2 = \frac{2n}{n+1} \tag{1.74}$$

The total complex transmission $\mathcal{T}(\omega)$ (Eq. 1.73) can then be directly inverted into the dielectric function, $\epsilon(\omega) = n(\omega)^2$ by the following iterative procedure:

$$\begin{aligned} n_{j+1}(\omega) = 1 \quad &+ \quad \frac{\ln\left[\mathcal{T}(\omega)\right] - \ln\left[4n_j(\omega)\right]}{i\omega d/c} \quad + \\ &+ \quad \frac{\ln\left\{\left[n_j(\omega)+1\right]^2 - \left[n_j(\omega)-1\right]^2 e^{2i\omega\, n_j(\omega) d/c}\right\}}{i\omega d/c} \end{aligned} \tag{1.75}$$

where the preceding 1 is coming from the phase term of the vacuum $e^{i\omega d/c}$. A similar expression can be formulated when only the straight transmission or the straight transmission and a certain number of echos have been measured.

1.7.2 Direct inversion for the magnetic case

A magnetic material is not only characterized by the dielectric permittivity function but also by the magnetic permeability function. This complicates the analysis of optical spectra of magnetic materials for which $\mu \neq 1$. Although the nonmagnetic case was not analytically solvable, the magnetic case is. The only

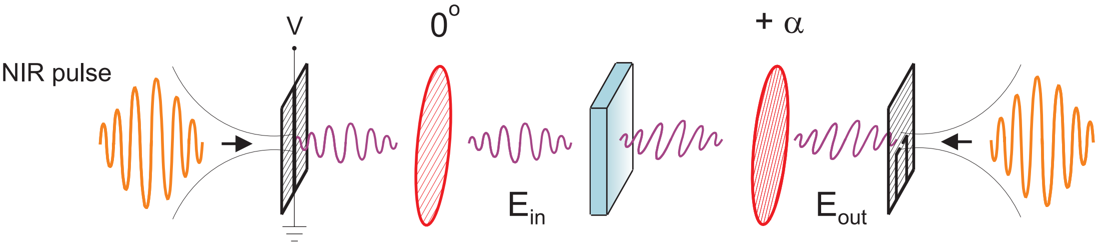

Figure 1.3: Schematic diagram showing the transmission line in the geometry as used in the analysis as described in the text. From left to right: a NIR pulse is focussed on a GaAs crystal which creates a linearly polarized THz pulse. To increase the degree of polarization a linear polarizer is placed in front of an anisotropic sample. On leaving the sample the polarization of the light has been changed to elliptical. With a rotatable polarizer is then possible to obtain the electric fields all over the ellipse. The linearly polarized light subsequently falls onto a GaAs receiver antenna and detection takes place when this event happens simultaneously with the arrival of the reference NIR pulse.

issue is that either the (complex) *straight* transmission $\mathcal{T}_1$ should be obtained for two different sample thicknesses or the (complex) straight transmission $\mathcal{T}_1$ and the transmission of the first echo $\mathcal{T}_2$ are separately obtained for one sample thickness.

In the following part we calculate the transmission of an isotropic sample in a magnetic field, and follow the cartoon diagram as depicted in Fig. 1.3. The electromagnetic wave is polarized in the x, y plane and propagates parallel to the magnetic field $\mathbf{H}_0$, i.e., along z. The polarization eigenstates of an isotropic sample in a magnetic field are circularly polarized. Since the absorption and dispersion of both chiralities is generally different, the incident linearly polarized light transforms into elliptically polarized light when leaving the sample. Subsequently the beam goes through a rotating linear polarizer and is finally projected onto a horizontally polarized detector along x. In order to find the transmission tensor from the measured complex transmission $\mathcal{T} = E_{\text{out}}^{\text{sample}}/E_{\text{out}}^{\text{ref}}$, we employ the Jones matrix formalism which describes the polarization of the optical field by the *amplitudes* in contrast to the Stokes-Müller formalism that treats their *intensities*. The state of polarization can be described by a Jones vector which contains the electric field components in the x and y direction

$$\begin{pmatrix} E_x \\ E_y \end{pmatrix} = \begin{pmatrix} X\, e^{i\phi_x} \\ Y\, e^{i\phi_y} \end{pmatrix} \tag{1.76}$$

The transformation of the polarization after transmission through an anisotropic material can be written as

$$\begin{pmatrix} E_x' \\ E_y' \end{pmatrix} = \hat{\mathcal{J}} \begin{pmatrix} E_x \\ E_y \end{pmatrix} = \begin{pmatrix} \mathcal{J}_{xx} & \mathcal{J}_{xy} \\ \mathcal{J}_{yx} & \mathcal{J}_{yy} \end{pmatrix} \begin{pmatrix} E_x \\ E_y \end{pmatrix} \tag{1.77}$$

where the 2×2 matrix $\hat{\mathcal{J}}$ is called the Jones matrix.[6] A linear horizontally aligned polarizer changes the polarization state of the light to linear. For this polarizer $\hat{\mathcal{J}}$ reads

$$\begin{pmatrix} 1 & 0 \\ 0 & 0 \end{pmatrix} \tag{1.78}$$

A linear polarizer at angle α is represented by

$$\begin{pmatrix} \cos^2\alpha & \cos\alpha\sin\alpha \\ \cos\alpha\sin\alpha & \sin^2\alpha \end{pmatrix} \tag{1.79}$$

The Jones matrix of the sample $\hat{\mathcal{T}}$ is in fact a 3×3 matrix, but since the z direction is not probed, it reduces to a 2×2 matrix, and becomes similar to the rotation and polarization operators

$$\hat{\mathcal{T}} = \begin{pmatrix} \mathcal{T}_{xx} & \mathcal{T}_{xy} \\ \mathcal{T}_{yx} & \mathcal{T}_{yy} \end{pmatrix} = \begin{pmatrix} \mathcal{T}_{xx} & \mathcal{T}_{xy} \\ -\mathcal{T}_{xy} & \mathcal{T}_{xx} \end{pmatrix} \tag{1.80}$$

where we applied the Onsager relation as mentioned before. A beam which is linearly polarized in the x, y plane can be written as

$$E_{\text{out}} = \frac{E_{\text{in}}}{\sqrt{2}} \begin{pmatrix} 1 \\ 0 \end{pmatrix}. \tag{1.81}$$

where E_{in} and E_{out} are defined in Fig. 1.3. Proper matrix multiplication in accordance to the geometrical setup in Fig. 1.3 results in

$$\mathcal{T} = \frac{E_{\text{out}}^{\text{sample}}}{E_{\text{out}}^{\text{ref}}} = \frac{\mathcal{T}_{xx}\cos^2\alpha - \mathcal{T}_{xy}\cos\alpha\sin\alpha}{\cos^2\alpha} = \mathcal{T}_{xx} - \mathcal{T}_{xy}\tan\alpha. \tag{1.82}$$

This shows that an ellipsometric measurement in which the polarizer angle α is varied provides the entire transmission tensor of Eq. 1.80. Since the polarization eigenstates are circularly polarized, it is convenient at this stage to pass from the Cartesian to the *circular* representation. The transmission for right and left circularly polarized light, $\mathcal{T}_+$ and $\mathcal{T}_-$ respectively, can be written as

$$\begin{aligned} \mathcal{T}_+ &= \mathcal{T}_{xx} + i\mathcal{T}_{xy} \\ \mathcal{T}_- &= \mathcal{T}_{xx} - i\mathcal{T}_{xy} \end{aligned} \tag{1.83}$$

Two different sample thicknesses

In the following we will assume the case for which the straight transmission of two identical samples of different thicknesses have been measured. The straight transmission $\mathcal{T}_1$ of an electromagnetic wave with frequency ω when passing once through a dielectric medium of thickness d_1 is given by Eq. 1.71. There are two of these equations, one for each chirality, but we have four complex unknowns, namely $\epsilon_+, \epsilon_-, \mu_+$ and μ_-, so two additional equations are needed. We obtain them by considering the straight transmission for a different thickness, say d_2. The index of refraction for each chirality is

$$n(\omega) \;=\; \sqrt{\epsilon(\omega)\mu(\omega)} \;=\; \frac{\ln \mathcal{T}_1^{d_1}(\omega) - \ln \mathcal{T}_1^{d_2}(\omega)}{i\omega(d_1 - d_2)/c} \tag{1.84}$$

where $\mathcal{T}_1^{d_1}$ and $\mathcal{T}_1^{d_2}$ are the transmissions corresponding to sample thickness d_1 and d_2, respectively. Now we have $n(\omega)$ we obtain $Z(\omega)$ through simple algebra. With $\xi = \mathcal{T}_1^{d_1}\, e^{-i\omega[n-1]\,d_1/c}$ we have

$$Z(\omega) = \frac{2 - \xi \pm 2\sqrt{1-\xi}}{\xi} \tag{1.85}$$

which brings us to the dielectric permittivity function and the magnetic permeability function for left and right circularly polarized light :

$$\epsilon_\pm(\omega) = n_\pm(\omega) Z_\pm(\omega) \qquad \mu_\pm(\omega) = \frac{n_\pm(\omega)}{Z_\pm(\omega)} \tag{1.86}$$

One sample thickness: making use of the 1^{st} echo

Suppose that a time-resolved transmission measurement has been carried out on a sample for which the index of refraction is sufficiently high that the straight transmission $\mathcal{T}_1$ can be separated from the first transmission pulse that has been subject to internal reflections in the sample, $\mathcal{T}_2$. We first have to obtain $Z(\omega)$ by putting $\zeta = \mathcal{T}_1^{3/2}\mathcal{T}_2^{-1/2}$ and $\phi_0 = e^{i\omega d/c}$ we get

$$Z(\omega) = \frac{2\phi_0^{-1} \pm \sqrt{4\phi_0^{-2} + \zeta^2}}{\zeta} \tag{1.87}$$

Substituting in Eq. 1.71 gives

$$n(\omega) \;=\; \sqrt{\epsilon(\omega)\mu(\omega)} \;=\; 1 + \frac{\ln \mathcal{T}_1(\omega) - \ln\left[4Z(\omega)\right] + 2\ln\left[Z(\omega)+1\right]}{i\omega d/c} \tag{1.88}$$

and similar to the previous case of two thicknesses we obtain with Eq. 1.86 the dielectric permittivity function $\epsilon_\pm(\omega)$ and the magnetic permeability function $\mu_\pm(\omega)$.

1.8 THz time-domain spectroscopy

The optical response of a material can be probed in several ways. If the beam of a monochromatic source is directed to a solid, the reflectivity and transmission can be obtained for a certain frequency. A point-like inversion towards the optical constants (ϵ, μ) is sometimes possible, but the information we obtain for a single frequency point is limited and in generally not enough to reveal the nature of excitations in a solid. A broad band frequency spectrum is obtained when the sample is illuminated with an electromagnetic wave with a well defined time or spectral dependence. In the first case, i.e., when using time domain spectroscopy, an ultra short electromagnetic pulse is sent to the sample where the pulse gets deformed (attenuated and delayed) according to the material parameters. The second way of measuring, frequency domain spectroscopy utilizes nowadays a Fourier transform technique for which the main beam is split and the response of a material is obtained as a function of the difference in path length between the two. Standard Fourier Transform Infrared Spectroscopy measures the transmission and/or the reflectivity. In case only the latter has been measured (e.g. for metals) than the Kramers-Kronig relations are needed to obtain the complex material parameters.

Since time-domain spectroscopy in the THz range is the measurement technique which is central in this thesis, we will describe it in some more extent. A titanium/sapphire laser emits ultrafast pulses with a wavelength of $\lambda = 800$ nm which are split in two beams. One beam impinges onto a photoconductive emitter consisting of a high mobility GaAs crystal on which two planar metal electrodes form an antenna supporting a large electric field across its surface, see Fig. 1.3. This generates charge carriers in the form of electron-hole pairs. The application of a bias voltage accelerates these charge carriers and forms a transient electric dipole which generates a short electromagnetic wave. The rise and fall of the transient current is on the time scale of one picosecond, therefore it generates a well-defined THz pulse front. For the spectrometer used for this thesis work (TPI 1000 from TeraView Ltd., Cambridge, UK) the width of the optical pulse is about 100 fs and the radiated THz pulse has thus a spectral bandwidth of the order of 3 THz [9]. For the detection an identical GaAs substrate is used. The incoming THz pulse causes a time dependent voltage across the gap between the two electrodes. This voltage is measured by shorting the gap with the second near-infrared pulse which has been delayed. The entire time-dependence of the THz pulse can be mapped out by changing the delay of this reference pulse. Please notice that THz time-domain spectroscopy measures the electric field $\mathbf{E}(t)$ which implies a complex response $\tilde{\mathbf{E}}(\omega)$ in frequency space. The Kramers-Kronig relations are therefore not required, although they can be used to verify causality and judge the quality of the data. The time average power of the THz radiation is 10 μW [25]. This leads with a THz pulse duration of 1 ps, a repetition rate of 80 MHz and a focal area of 3×3 mm^2 to a peak electric field of about 30 V/cm and a magnetic field of about 10 μT.

Fig. 1.4a shows an example of a time-domain spectrum which consists of a single pulse (black curve). When a material is placed in the transmission line we obtain a spectrum like the one for a thin plate of 94 μm SrTiO$_3$ (red and blue curve). A single pulse enters the sample where part of it passes straightly

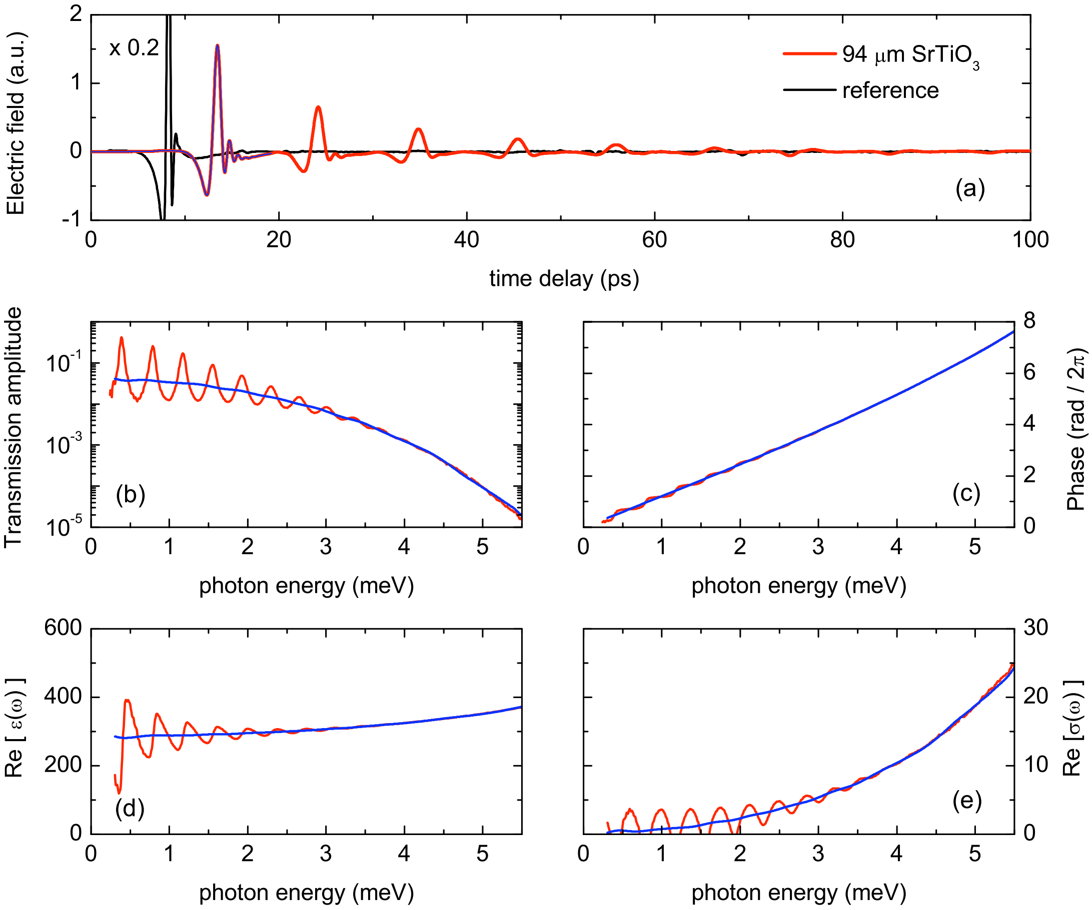

Figure 1.4: Panel (a) shows the time-domain THz spectrum of 94 μm thin SrTiO$_3$ at 298 K of the straight transmission (blue) and the transmission including all echos (red). The reference (scaled by a factor 0.2) is shown in black. After Fourier transformation the transmission amplitude and phase (panel b-c) are obtained for the entire time-domain spectrum (red) and only for the straight transmission (blue). Direct inversion of the complex transmission, as presented in section 1.7.1, gives the dispersion $\epsilon_1(\omega)$ and the conductivity $\sigma_1(\omega)$ in panel (d) and (e), respectively.

and the remaining part reflects internally and constitutes an ensemble of multiple pulses as a function of time. When the time-domain signal is Fourier transformed and divided by the Fourier transformed reference we obtain a complex transmission or in other words an amplitude and a phase (Fig. 1.4b-c). As described in section 1.7.1, we can invert the complex transmission to obtain the dielectric permittivity function (since $\mu = 1$ for $SrTiO_3$) and the conductivity as shown in Fig. 1.4d-e.

Bibliography

[1] E. Hecht, *Optics*, Addison-Wesley Longman, Inc. (1998).

[2] F. Wooten, *Optical Properties of Solids*, Academic Press, New York (1972).

[3] J.D. Jackson, *Classical Electrodynamics*, Wiley, New York (1975).

[4] M. Born and E. Wolf, *Principles of Optics*, University Press, Cambridge (1980).

[5] S. Sugano and N. Kojima (Eds.), *Magneto-optics*, Springer-Verlag (2000).

[6] H.G. Tompkins and E.A. Irene, *Handbook of Ellipsometry*, William Andrew Publishing−Springer (2005).

[7] M. Dressel and G. Grüner, *Electrodynamics of Solids*, Cambridge University Press (2002).

[8] Y. Toyozawa, *Optical Processes in Solids*, Cambridge University Press (2003).

[9] S.L. Dexheimer, *Terahertz Spectroscopy, principles and applications*, CRC Press (2008).

[10] C. Cohen-Tannoudji, B. Diu and F. Laloë, *Mécanique quantique*, Hermann, Paris (1973).

[11] B. Lax and K.J. Button, *Microwave Ferrites and Ferrimagnets*, McGraw-Hill book company, Inc (1962).

[12] Štefan Višňovský, *Optics in Magnetic Multilayers and Nanostructures*, CRC Press - Taylor and Francis, (2006).

[13] H. Bethe, Ann. Phys. (Leipzig) **5**, 325 (1930).

[14] H.S. Bennett and E.A. Stern, Phys. Rev **137**, A448 (1965).

[15] C.L. Hogan, Rev. Mod. Phys. **25**, 253 (1953).

[16] J.T. Devreese, L.F. Lemmens and J. Van Royen, Phys. Rev. B **15**, 1212 (1977).

[17] D.Y. Smith, Phys. Rev. B **13**, 5303 (1976).

[18] W. Kuhn, Z. Phys. Chem. B **4**, 14 (1929). Trans. Faraday. Soc. **26**, 293 (1930).

[19] L. Rosenfeld, Z. Phys. **52**, 161 (1928).

[20] E.U. Condon, Rev. Mod. Phys. **9**, 432 (1937).

[21] O. Morikawa, A. Quema, S. Nashima, H. Sumikura, T. Nagashima and M. Hangyo, J. Appl. Phys **100**, 033105 (2006).

[22] A. Kapitulnik, J. Xia, E. Schemm and A. Palevski, New J. of Phys. **11**, 055060 (2009).

[23] Y.K. Kato, R.C. Myers, A.C. Gossard and D.D. Awschalom, Science **306**, 1910 (2004).

[24] K.H.J. Buschow, *Handbook of Magnetic Materials, Volume 13*, pp. 379-381, Elsevier Science B.V., Amsterdam (2001).

[25] Teraview Ltd. Cambridge (UK), private communication (2010).

Chapter 2

Optical evidence of electron-phonon coupling in $SrTiO_3$

Electron-phonon coupling in the perovskites is a subject of much recent interest due to the controversy over its relevance in the phenomena of multiferroicity, ferroelectricity, superconductivity and colossal magnetoresistance [1, 2, 3, 4, 5]. Despite much progress, full understanding of the physics of electron-phonon coupling in perovskites is still lacking because of additional crystallographic complexities of many materials involved (breathing, tilting and rotational distortions, ferroelectric symmetry breaking), magnetism, complex electronic effects (strong correlations), and also because of the lack of high-accuracy spectroscopic measurements specifically designed to probe electron-phonon coupling. With this in mind, we have studied a prototypical perovskite oxide, $SrTi_{1-x}Nb_xO_3$ with $0 \leqslant x \leqslant 0.02$. Characterized by the threefold degeneracy of the conduction bands and the high lattice polarizability, electron doped $SrTiO_3$ provides a perfect opportunity for the study of electron-phonon coupling and polaron formation in an archetypal perovskite [44, 15].

2.1 Introduction to electron-phonon coupling

Free charge carriers coupled to bosons can mutually interact. If the bosonic field is represented by lattice excitations, i.e., phonons, the new quasi-particle that is formed is called a *polaron*. Pioneering work has been done by Lev Landau [38] which has been further elaborated by e.g. Pekar, Feynman and Fröhlich [56, 57, 58, 23, 59, 46]. The different coupling regimes are determined by the ratio of the electronic and bosonic energy scales, i.e., the Fermi energy E_F and energy of the relevant longitudinal phonon to which the electron couples, $\hbar\omega_{\mathrm{LO}}$. In case the electron is sufficiently free to move through the lattice (i.e., $E_F \gg \hbar\omega_{\mathrm{LO}}$) the quasi-particle can be seen as an electron dressed with the (slower) ionic deformation, which moves along with it. The lattice deformation is on the order of several unit cells and is thus long-ranged. This weak electron-phonon interaction is often called a large polaron. In the other limit, when $E_F \ll \hbar\omega_{\mathrm{LO}}$, the electron is almost pinned to one site where it deforms only its very local environment and creates a so-called small polaron. The motion of the electron goes in this case by hopping from one ionic potential well to the other. Such interactions are often strong and are consequently short ranged, generally on the order of one unit cell.

The interaction between the electrons and ions is energetically favorable and a new quasiparticle is created that has a lower ground state energy, E_p, than the sum of energies of the individual phonon and electron, called the polaron energy. As will be discussed in section 2.1.4 the electron can be decoupled from the phonons by exciting it above the ionic potential well, e.g. by illumination with (infrared) light. Another property of the new quasiparticle is that the interaction with the phonon bath increases the electron's effective mass. In the following we give a brief overview of the most common electron-phonon interactions and their signatures in an optical spectrum. Extensive reviews can be found in Refs. [24, 45, 43, 44, 41, 42].

2.1.1 Fröhlich interaction

The theory for electrons subject to a weak electron-phonon interaction, also called large polarons, has been initiated mainly by the work of Fröhlich [59]. A mobile electron is trapped by the attractive Coulomb potential of the positive ions which creates a new quasiparticle. One can describe the interaction of the electron and the ions (phonons) by the Fröhlich hamiltonian

$$H = \sum_{\mathbf{p}} \frac{p^2}{2m} c^\dagger_{\mathbf{p}} c_{\mathbf{p}} + \omega_0 \sum_{\mathbf{q}} a^\dagger_{\mathbf{q}} a_{\mathbf{q}} + \sum_{\mathbf{p},\mathbf{q}} \frac{M_0}{q\sqrt{V}} c^\dagger_{\mathbf{p}+\mathbf{q}} c_{\mathbf{p}} \left(a_{\mathbf{q}} + a^\dagger_{\mathbf{q}}\right) \tag{2.1}$$

$c^\dagger_{\mathbf{p}}$ and $c_{\mathbf{p}}$ are the creation and annihilation operators, respectively, of the electron with momentum $\mathbf{p}$ and $a^\dagger_{\mathbf{p}}$ and $a_{\mathbf{p}}$ of the phonon. V is the unit cell volume and M_0 contains the electron-phonon coupling strength α via

$$M_0^2 = 4\pi\alpha\hbar\sqrt{\hbar^3\omega_0^3/2m} \tag{2.2}$$

$$\alpha = \frac{e^2}{\hbar}\left(\frac{m}{2\hbar\omega_0}\right)^{1/2}\left(\frac{1}{\epsilon_\infty} - \frac{1}{\epsilon_0}\right) \tag{2.3}$$

where m is the band mass of the electron, ϵ_∞ the high frequency limit of the dielectric function and ϵ_0 the static dielectric constant. Generally, to simplify the problem this hamiltonian is evaluated for the problem of *one* electron with a dispersion less phonon, an Einstein mode. Furthermore, the only phonons to

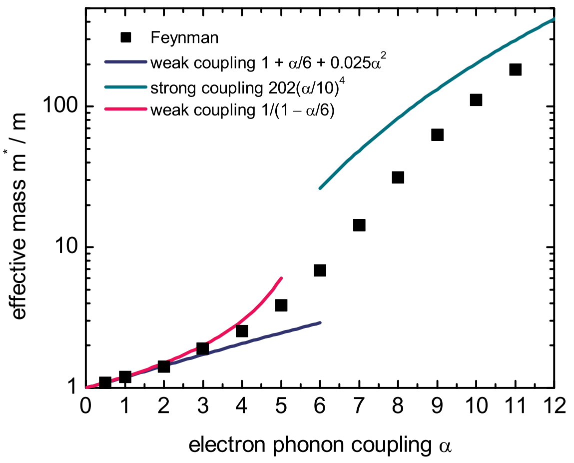

Figure 2.1: Relationship between the effective mass m^*/m and the electron-phonon coupling parameter α for the Feynman parameterization and compared to various limited-range coupling theories.

which the electron can couple are the longitudinal ones[1], so $\omega_0 = \omega_{\mathrm{LO}}$. The term in Eq. 2.3 which contains the difference between the reciprocal value of ϵ_∞ and ϵ_0 is due to the sum of the electronic and ionic polarizabilities resulting from the injection of an additional charge carrier. The range of coupling constants α for which the electron-phonon interaction is called weak and a large polaron forms is $0 \leqslant \alpha \leqslant 5$. The Fröhlich problem has been solved for different coupling ranges which results in various dependencies of the effective mass m^*/m_e and the polaron energy E_p as a function of α. In the weak coupling limit

$$E_p = -\alpha\hbar\omega_{\mathrm{LO}} \qquad\qquad m^*/m_e = 1 + \alpha/6, \tag{2.4}$$

and in the strong coupling limit

$$E_p \approx -0.1\alpha^2\hbar\omega_{\mathrm{LO}} \qquad\qquad m^*/m_e \approx 1 + \alpha^4/50. \tag{2.5}$$

The disadvantage of these expressions is that they are only valid is a narrow range of α. Fortunately, there exists an elaboration of the large polaron problem which holds even beyond the before mentioned range of α. In 1955, Feynman [23] applied the technique of path integrals to the polaron problem and within a variational approach obtained the effective mass m^* as a function of coupling parameter α, as graphically illustrated in Fig. 2.1.

2.1.2 Holstein interaction

With increasing electron-phonon strength, the electron becomes less and less free and is eventually trapped on the distance of about one lattice site. The polaron

---

[1] The transverse modes are characterized by $\partial\epsilon/\partial\omega_0 = \infty$ and do not contribute to the electrostatic potential created by the lattice distortion [48].

wave functions are identical on each lattice site and the periodicity of the lattice comes again into play like for the tight-binding model. These so-called small polarons[2] are often described by the Holstein hamiltonian [24]

$$H = t\sum_{j\delta} C^{\dagger}_{j+\delta}C_j + \sum_{\mathbf{q}} \omega_{\mathbf{q}} a^{\dagger}_{\mathbf{q}} a_{\mathbf{q}} + \sum_{j,\mathbf{q}} C^{\dagger}_j C_j \, e^{i\mathbf{q}\cdot\mathbf{R}_j} M_{\mathbf{q}} \left(a_{\mathbf{q}} + a^{\dagger}_{-\mathbf{q}}\right) \tag{2.6}$$

where C_j is the annihilation operator for a particle on site R_j. The summation δ is over the nearest neighbors. The third term is the Coulomb interaction between the electron and neighboring ions, which is described as a contraction or expansion of an ion at position $\mathbf{R}_j$ compared to its neighbors. The main difference with the Fröhlich hamiltonian (Eq. 2.1) is the first term which describes the (tight-binding-like) hopping of the electron together with the periodicity of the lattice.

In the strong coupling limit, the electron-phonon interaction prevails over the hopping term of Eq. 2.6, which is treated as a perturbation, and the electron becomes localized at the ion site. In the Holstein model, the amplitude of this perturbation is

$$t\,\langle f|X^{\dagger}_{j+\delta}X_j|i\rangle \tag{2.7}$$

where $|i\rangle$ and $|f\rangle$ are the phonon occupation numbers in the initial and final state, respectively. Since the number of phonons can change during the transition, Holstein distinguished processes where the phonon occupation in the initial and final state alter, so-called *non-diagonal* processes, and those where the amount of phonons do not change at all, the *diagonal* processes.[24] During a diagonal hopping event the electron keeps its phase coherence and if the non-diagonal processes are minor, then the tendency is to form energy bands, as in the Fröhlich model. The non-diagnonal processes on the other hand decrease the phase coherence and strengthen the (small) polaron formation and increase the effective mass (thereby flattening the energy bands).

In this hopping model, the rate of diagonal transitions decreases with increasing temperature, which means that the Fröhlich-type of electron-phonon coupling is rather found at low than at high temperatures.[24] At high temperatures the bandwidth decreases which means that the electrons are more and more localized. Another result from the Holstein model is that it predicts short wavelength phonons to be particularly important.

---

[2] As mentioned before the Fröhlich theory is generally used to describe weak electron-phonon interactions and the Holstein theory strong electron-phonon interactions, commonly referred to as large and small polarons, respectively. However, some literature utilizes within the Holstein theory an additional nomenclature as a function of coupling strength. They call relatively weak interactions described by the Holstein hamiltonian 'large' polarons and strong interactions 'small' polarons, which we will *not* follow in this work.

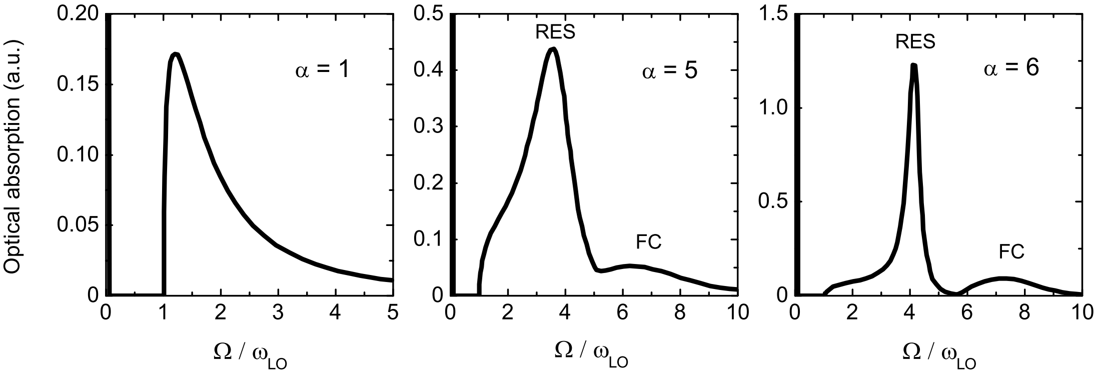

Figure 2.2: Polaron optical conductivity vs photon frequency for $\alpha = 1$ in the weak coupling approximation and for $\alpha = 5$ and 6 for the strong coupling approximation, from Refs. [27, 41]. The transition to the relaxed excited state (RES) and Franck-Condon (FC) band are indicated.

2.1.3 Many-polaron interaction

In the previous sections the electron-phonon problem was based on the interaction of a *single* electron with a bath of phonons. Although this is theoretically easier to treat it might not be very realistic since no single macroscopic material contains just one electron, or just one electron which couples while the others don't. The problem of a gas or liquid of polarons was first treated by Gurevich *et al.* [39] and later by Tempere and Devreese *et al.* [40], and will be subject of section 2.9 in comparison with the optical data on Nb doped $SrTiO_3$ which are presented in section 2.6.

2.1.4 Optical signatures of polarons

Devreese [41] calculated the optical absorption of a gas of large polarons in the weak coupling limit ($\alpha = 1$), which reduces to the one polaron absorption [27] as depicted in Fig. 2.2 at zero temperature. Visible are the unbroadened Drude absorption at frequency $\Omega = 0$ and a higher energy absorption with an onset at $\Omega = \omega_{\mathrm{LO}}$. Phonon energies are often on the order of tenths of eV, which makes the latter absorption to be in the mid-infrared range. In the weak coupling approximation, the absorption of a Fröhlich polaron is due to the absorption of a photon and the emission of a LO phonon which can only occur for $\Omega > \omega_{\mathrm{LO}}$. In the strong coupling limit, different processes come into play. A photon of high enough energy can promote the trapped electron to the continuum. In the mean time the lattice adapts itself to the presence of the electron. When the electron falls back its environment has changed to a so-called *relaxed excited state* (RES). This transition can also be seen as an excitation from one site to a neighboring site and has the energy

$$E_{\mathrm{RES}} = 0.065\alpha^2\hbar\omega_0. \tag{2.8}$$

When the energy of the incoming photon is larger than $E_{\mathrm{RES}} + \hbar\omega_0$ phonon assisted Franck-Condon transitions inside the new potential well can be made. In the optical spectrum this results is a side band consisting of discrete peaks at $n\hbar\omega_{\mathrm{LO}}$ with $n = 0, 1, 2\ldots$ Since in solids phonons form bands, the peaks are smeared out and form a multiphonon side band. The Franck-Condon transition with the highest probability has the energy

$$E_{\mathrm{FC}} = 0.141\alpha^2\hbar\omega_0 \tag{2.9}$$

In summary, the optical absorption spectrum of a large polaron in the strong coupling limit at zero temperature, as depicted in Fig. 2.2, shows a Drude peak at zero frequency, an onset at $\Omega = \omega_0$ and a multiphonon side band centered at several times the LO phonon frequency. On top of this, at the low energy side of the multiphonon side band there is a strong and narrow absorption peak due to a zero-phonon excitation to the relaxed excited state.

As mentioned before, one of the fingerprints of the presence of electron-phonon coupling is a mass renormalization of the electron. In the limit of a strong electron-phonon interaction, small polarons will be formed and the mass renormalization is expected to be large. The renormalized mass can be obtained by measuring the optical spectral weight of the Drude peak, which is equal to $\pi ne^2/(2m^*)$. Besides renormalizing the 'coherent' (Drude) part of the spectrum, the large polaron theory shows that the electron-phonon coupling is responsible for 'incoherent' contributions at higher energies, resulting in multiphonon absorption bands in the mid-infared range.

2.2 Introduction to SrTiO$_3$

Insulating SrTiO$_3$ is one of the best studied perovskite oxides and on a commercial level it has been a potential competitor of silicon for the semiconductor industry before the arrival of graphene due to its high mobility when it is slightly doped (up to 6000 cm^2/Vs). At room temperature SrTiO$_3$ is an optically transparent, cubic perovskite with lattice parameter of 3.905 Å. The Ti atoms are on the corners of the cube and each of them is surrounded by an oxygen octahedron (Fig. 2.3). The electron configuration is d^0 which makes SrTiO$_3$ a band insulator with a gap of about 3.2 eV. On lowering the temperature, a second-order displacive phase transition occurs at 105 K which doubles the unit cell and forms a tetragonal structure [49]. The transition involves a small rotation of the oxygen octahedra which is out-of-phase for adjacent octahedra in the (100) plane. Raman scattering experiments of Fleury *et al.* [37] have shown the complete softening of the zone boundary mode at 105 K and the appearance of two new modes below the transition. SrTiO$_3$ falls in the class of quantum paraelectric materials [1] which are characterized by the zero-point motion of the Ti atoms. Other

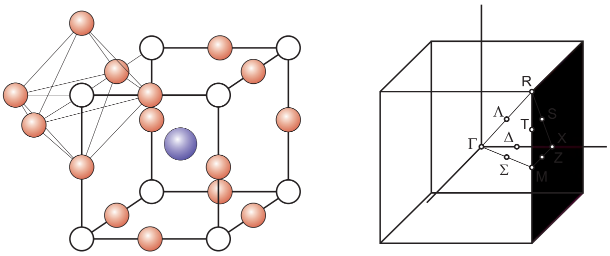

Figure 2.3: (a) Simple cubic perovskite crystal structure with around each corner Ti atom an octahedron of oxygen atoms. (b) First Brillouin zone for the simple cubic lattice.

materials in this class are $KTaO_3$, $CaTiO_3$ and $EuTiO_3$. On lowering the temperature, they show an approach towards a ferroelectric phase transition, which is eventually suppressed due to these quantum fluctuations [15] (together with the antiferrodistortive transition). For $SrTiO_3$ this is shown by the zone center optical mode E_u which partially softens from 11 meV at 300 K to 1.0 meV at 7 K [30]. The ferroelectric state can however be introduced by external stimuli or chemical substitution (Ba for Sr [60] or O^{18} for O^{16} [13] for instance). An example of an external stimulus is an externally applied dc electric field which modifies the position of the titanium atom, and which is the subject of Chapter 3.

$SrTiO_3$ can be electron doped by introducing Nb^{5+} at the Ti^{4+} site, La^{3+} at the Sr^{2+} site or by creating oxygen vacancies and hole doped by replacing Sc^{3+} or Zr^{3+} for Ti. At an electron doping concentration of 0.002 % charge carriers per unit cell an insulator to metal transition takes place at room temperature [14]. The visual appearence of $SrTiO_3$ changes with increasing doping from undoped colorless to yellowish and is dark gray for a 2 % Nb doped sample of 30 μm thick. All ways of chemical n-doping cause a superconducting state with a dome-shaped T_c vs. doping concentration between 0.003 % and 3 %. Maximum values of T_c occur around $x = 0.5\,\%$ per unit cell and are between 0.3 K [6] and 1.2 K [5]. STM measurements have shown evidence for two-band superconductivity in Nb-doped $SrTiO_3$ [51]. Because of the large dielectric constant, interband scattering between the two lowest conduction bands can be ignored, and both Fermi sheets contribute with a different order parameter. Another explanation for the superconductivity is the formation of bipolarons which are charged bosons and can condensate into a superfluid-like state.[50]

Pioneering work on electron-phonon coupling in $SrTiO_3$

Since the early 1960s $SrTiO_3$ has been thought of as an ideal model compound to study electron-phonon coupling. Pioneering work by Barker [7] shows the optical reflectivity of oxygen depleted $SrTiO_3$ in the far and mid-infrared range. His fitting procedure requires the presence of a mid-infrared band around 0.25

eV. A similar absorption can be observed in first reported transmission measurements by Calvani *et al.* [14] but due to the limited spectral range a complete picture of the mid-infrared absorption is absent. To decide about the presence and the type of electron-phonon formation a broad band spectrum is required, such that knowledge can be obtained about the coherent and incoherent part. However, the presence of a strong soft mode at slightly higher energies than a modest coherent Drude peak complicates this study. A reliable determination of the Drude absorption which would lead to a determination of the mass renormalization is thus impossible without having measured both features, which at low temperatures are all below 5 meV. In the previous literature, no consensus was reached about the presence and the nature of the electron-phonon coupling [7, 8, 82, 11, 12, 13, 14, 15, 16, 18].

2.3 Band structure

2.3.1 Local-density approximation

First principles calculations were performed by Dr. Igor I. Mazin (Naval Research Laboratory, Washington D.C., USA) using the Linear Augmented Plane Wave method as implemented in the WIEN2k code [35] and the generalized gradient approximation for the exchange-correlation potential in the form proposed by Perdew *et al.* [36]. Calculations have been performed in the high-temperature perovskite structure ($a = 3.905$ Å) as well as in the low-temperature tetragonal structure (group no. 140, I4/mcm, $a = 5.529$ Å, $c = 7.824$ Å, $\mathrm{O}_x = 0.244$). Optimizing the O position in the calculations yields $\mathrm{O}_x = 0.223$ which indicates that even zero-point fluctuations substantially reduce the average distortion, as expected. Nb doping was simulated in the virtual crystal approximation, changing the nuclear charge of Ti from 22 to $22 + x$, or that of Sr from 38 to $38 + x$ (the results did not change, proving that this is a good approximation in the considered range of dopings).

Most calculations were performed with the value of RK_{max} (the radius of the muffin tin multiplied by the plane wave cut off) equal to 7 for the wavefunction expansion, and $RG_{\mathrm{max}} = 14$ for the charge density expansion; calculations with $RK_{\mathrm{max}} = 8$ and $RG_{\mathrm{max}} = 16$ did not show a discernible difference. Fermi-surface integrals were evaluated using the k-point meshes up to $28 \times 28 \times 28$. The plasma frequencies were evaluate as the Fermi-surface averages of the squared Fermi velocities. The Fermi velocities and optical matrix elements were calculated using the WIEN2k optics package. The accuracy of the Fermi velocities was tested (in the cubic case) by numerical differentiation of the energy eigenvalues. Our first principles results show a substantially weaker effect of the tetragonality compared to the semi-empirical calculations of Mattheiss [28] (less than 4 meV splitting of the otherwise degenerate states at Γ, compared to ~ 20 meV). This in fact resolves

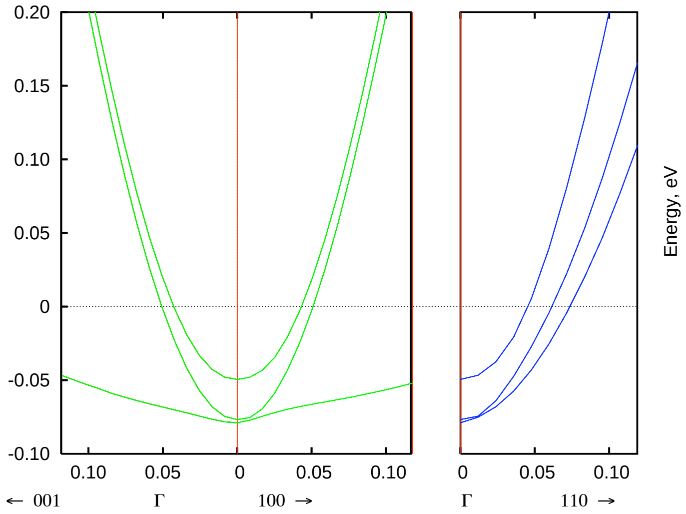

Figure 2.4: Blow-up of the electronic structure in the tetragonal phase near the Γ point (units of the wave vectors are inverse bohrs), at 2% doping. The Fermi level is indicated by the dotted line.

a long-standing controversy between the band structure of Ref. [28] and the de Haas-Van Alphen measurements of Gregory *et al.* [29].

Fig. 2.4 shows the bottom of the band structure of electron doped $SrTiO_3$ at a doping level of 2% charge carriers per unit cell. Visible are the three Ti 3d conduction bands which are split by the crystal field and by the spin-orbit interaction so that the three t_{2g} levels become occupied when the material is electron-doped by substituting pentavalent Nb for tetravalent Ti. A remarkable property of the $SrTiO_3$ band structure is the quasi 2 dimensionality of the bands. Fig. 2.4 shows a two-dimensional view from which can be seen that each band has two directions of strong curvature and one which is almost flat. This makes it like three canals crossing each other at the Γ-point. The ratio of the heavy and light masses is approximately 27, as discussed later (cf. section 2.7.2).

The exotic Fermi surface of electron doped $SrTiO_3$ is depicted in Fig 2.5. With increasing electron concentration, one first fills the lowest t_{2g} band which gives rise to a starfish-like Fermi surface. There are arms in the ±[100], ±[010] and ±[001] directions, which sum up to six in total and not four as previous work reported [28, 29]. As mentioned above, the second band is about 5 meV higher. When this one is partly filled (above $\sim 0.08\,\%$ per unit cell) it gives rise to an almost isotropic ball-shaped Fermi surface within the starfish-shaped outer one. At the center of the Brillouin zone, the Fermi surface consists thus of two disjoint sheets, with a very different electron mobility.

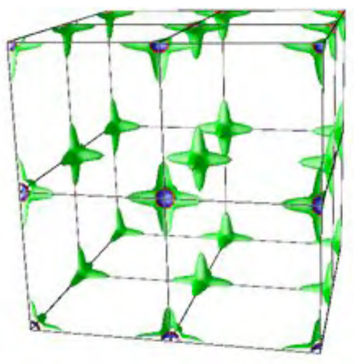

Figure 2.5: Fermi surface of the high-symmetry phase at 2% doping, showing the large anisotropy of the lowest band (at 9.7% doping this Fermi surface sheet undergoes a topological transition).

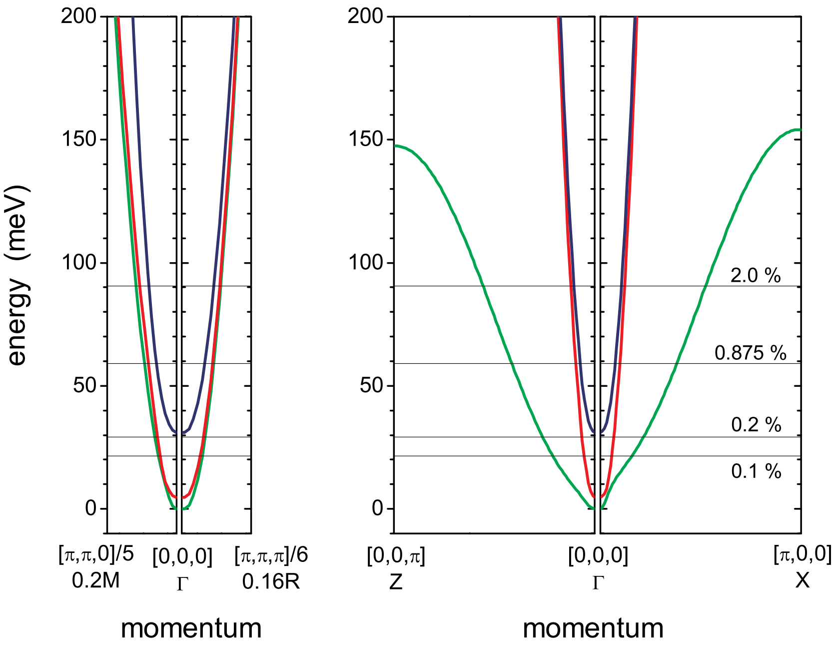

Figure 2.6: Electronic band structure based on the tight-binding approximation fitted to the LDA band structure of electron doped SrTiO$_3$ near the Γ point. The Fermi energy is indicated by horizontal black lines for several doping concentrations.

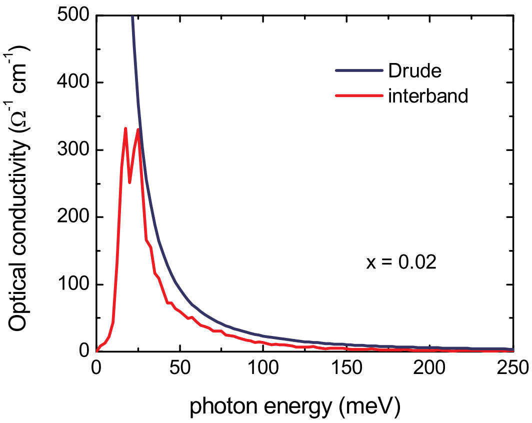

Figure 2.7: The optical conductivity $\sigma_1(\omega)$ of $\mathrm{SrTi}_{1-x}\mathrm{Nb}_x\mathrm{O}_3$ for $x = 0.02$ at 20 K obtained from the tight-binding band structure. Indicated are the partial conductivities of the intraband (Drude) and interband transitions.

2.3.2 Tight-binding approximation

The LDA calculation of the SrTiO_3 band structure is a heavy calculation and gives little direct understanding of the physical parameters of the doped SrTiO_3 system. It is therefore preferable to calculate the electronic band structure using a simpler tight-binding approximation. Since the purpose is to get understanding of the conduction band bottom close to the $\Gamma = [0,0,0]$ point, we take only *d*-*d* interactions into account of the Ti xy, xz and yz orbitals. The multiband *d*-*d* Hamiltonian in real space for a well defined quantum number J can then be written as

$$H^{dd} = H_{d0} + H_{tdd} + H_h \tag{2.10}$$

$$H_{d0} = \sum_{\alpha i\gamma} \varepsilon_d^0 \, d^\dagger_{\alpha i\gamma} d_{\alpha i\gamma} \tag{2.11}$$

$$H_{tdd} = \sum_{\alpha i\gamma,\alpha' i'\gamma'} t^{dd}_{\alpha i\gamma,\alpha' i'\gamma'} \, d^\dagger_{\alpha i\gamma} d_{\alpha' i'\gamma'} \; + \; \text{h.c.} \tag{2.12}$$

where $d^\dagger_{\alpha i\gamma}$ is the creation operator of an electron in the 3d orbital γ at Ti site i in the α-th unit cell. H_{d0} is the bare level energy of the Ti 3d orbital, H_{tdd} the *d*-*d* hybridization term and H_h denotes the crystal field ζ and spin-orbit interaction ξ. $t^{dd}_{\alpha i\gamma,\alpha' i'\gamma'}$ is the nearest-neighbor hopping term which can be expressed in terms of the Slater-Koster parameters t_σ and t_π [67].

The Hamiltonian can be written in *k*-space form by using the Bloch-electron operator

$$d^\dagger_{\mathbf{k},i\gamma} = \frac{1}{\sqrt{N}} \sum_\alpha e^{i\mathbf{k}\cdot\mathbf{R}_\alpha} d^\dagger_{\alpha,i\gamma} \tag{2.13}$$

where **k** labels the wave vector in the first Brillouin zone. After evaluation of the nearest-neighbor hopping terms Eq. 2.10 becomes in matrix notation

$$H = \sum_{\mathbf{k}} d^{\dagger}_{\mathbf{k},i\gamma}\ \hat{T}(\mathbf{k})\ d_{\mathbf{k},i\gamma} \tag{2.14}$$

with

$$\hat{T}(\mathbf{k}) = \begin{pmatrix} 0 & \xi/2 & \xi/2 \\ \xi/2 & 0 & \xi/2 \\ \xi/2 & \xi/2 & \zeta_z \end{pmatrix} + t_\sigma \begin{pmatrix} 1-\cos k_x a & 0 & 0 \\ 0 & 1-\cos k_y a & 0 \\ 0 & 0 & 1-\cos k_z a \end{pmatrix}$$
$$+\, t_\pi \begin{pmatrix} 2-\cos k_y a-\cos k_z a & 0 & 0 \\ 0 & 2-\cos k_x a-\cos k_z a & 0 \\ 0 & 0 & 2-\cos k_x a-\cos k_y a \end{pmatrix}$$

Diagonalization provides the energy eigenstates and permits to map out the band structure close to $\mathbf{k} = \mathbf{0}$, where the bands have to very good approximation a parabolic character. In order to have the same degree of precision as the LDA calculation, the tight-binding band structure has been fitted to the low-energy part of the LDA band structure based on the Wien code. The following set of parameters produces all fine structures near the band bottom: $t_\pi = -1.23$ meV, $t_\sigma = -70$ meV, $\xi = 18.8$ meV and the crystal field parameter in the z-direction $\zeta_z = -6.7$ meV. Fig. 2.6 shows the resulting band structure for different directions in $\mathbf{k}$-space. The Fermi energies corresponding to electron concentrations of SrTi$_{1-x}$Nb$_x$O used in the experimental part of this chapter are indicated by horizontal black lines. It should be noticed that for the lowest doped samples only the two lowest t$_{2g}$ bands are filled, whereas for the two highest doped samples all three t$_{2g}$ bands play a role. The optical conductivity can be calculated by considering the current operator $\mathcal{J}$ which is defined by the conservation law of electron number, given by

$$\mathcal{J} = \sum_{\mathbf{k}} d^{\dagger}_{\mathbf{k},i\gamma}\ \hat{\mathcal{J}}(\mathbf{k})\ d_{\mathbf{k},i\gamma} \tag{2.15}$$

and

$$\hat{\mathcal{J}}(\mathbf{k}) = e\nabla_{\mathbf{k}}\hat{T}(\mathbf{k}). \tag{2.16}$$

The Kubo formula (cf. Eq. 1.24) gives the optical conductivity $\sigma_1(\omega)$ trough the current-current correlation function, and is shown at 20 K in Fig. 2.7. The total $\sigma_1(\omega)$ is composed of intraband and interband transitions in the x and z direction. The interband transitions between the split t$_{2g}$ levels give a sharp structure centered around 20 meV.

Fig. 2.8a shows the Fermi energy E_F as a function of doping at 20 K. As a function of temperature the chemical potential μ increases and thus the k-space region that is occupied by electrons increases also. Since each of the three bands has a heavy direction which becomes filled upon increasing temperature, one expects also an average mass increase. Fig. 2.8b shows the average band mass as a function of temperature, which is highly constant and changes only about 1 % between 20 K and 300 K.

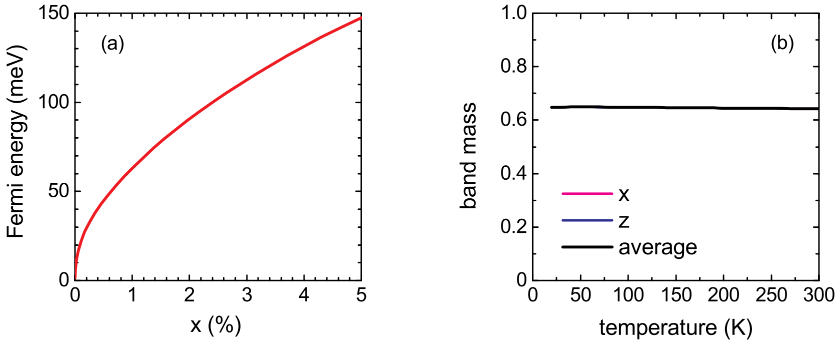

Figure 2.8: (a) Doping dependence of the Fermi energy. (b) Temperature dependence of the band mass (relative to m_e) for $x = 1\,\%$ in the x and z direction and the average value.

2.4 Sample preparation

Nb doped $SrTiO_3$ single crystals ((100) face) of 5×5 mm^2, double side polished, are commercially obtained from Crystec (Berlin). Nominal doping concentrations as specified by the company are 0, 0.1 %, 0.2 %, 1.0 % and 2.0 % Nb per unit cell. The as-obtained thicknesses are all 50 ± 10 μm, with exception of the 2% sample. For the optical measurements, in order to obtain a measurable transmission in spectral ranges with a relatively large absorption, some of the samples have been chemically etched thinner by attacking both surfaces with a NH_4F buffered HF solution. The solution has been heated to $50-60$ °C and put in a bath of water of the same temperature which vibrates ultrasonically. This bath is essential since otherwise the etching is inhomogeneous and so-called etch pits develop in the sample. Etching rates are a strong function of temperature and HF concentration. Rates that are utilized are typically $1-10$ μm per hour. The thicknesses of all measured samples in different spectral ranges are listed in Table 2.1.

2.5 Thermodynamic and transport properties

2.5.1 DC Hall effect

The DC Hall effect has been measured for the Nb doped samples as mentioned in the previous section. The contacts are made by ultrasonic wire bonding and connected in a Van der Pauw configuration [53] for magnetic fields ranging between -2.0 and 2.0 T and between 300 K and 7 K. The Hall coefficient as a function of applied magnetic field is very linear for $x \geqslant 0.2\%$. Only at 7 K tiny non-linear effects are visible for $x = 0.1\,\%$. Fig. 2.9 shows the electron carrier density as a function of temperature for all samples. Dashed horizontal lines indicate the nominal value as specified by the supplier. At 7 K the Hall charge carrier densities of the 4 samples are: 0.105%, 0.196%, 0.875% and 2.00%, which is within 12

Table 2.1: Thickness values of the entire set of SrTi$_{1-x}$Nb$_x$O$_3$ samples in different spectral ranges and for different temperatures T.

x (%)	spectral range (meV)	T (K)	thickness (μm)
0	0.3 - 7000	7 - 300	60
	0.6 - 12	7	27.5
0.1	0.3 - 12	300	41
	0.9 - 12	7	11.3
	2 - 7000	7 - 300	50
0.2	0.3 - 12	300	43
	0.9 - 12	7	7.8
	2 - 7000	7 - 300	57
	100 - 600	7 - 300	37
0.9	4 - 7000	7 - 300	52
2.0	4 - 700	7 - 300	537
	850 - 7000	7 - 300	30

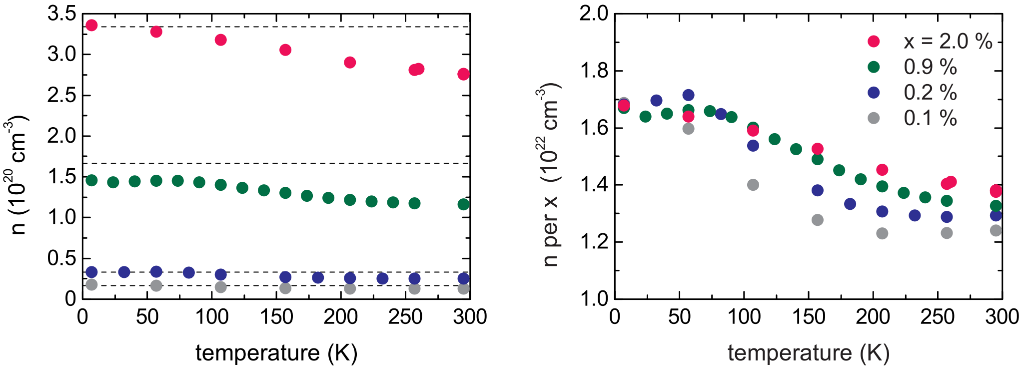

Figure 2.9: Left panel: Temperature dependence of the electron carrier density n for all considered Nb doped SrTiO$_3$ samples. Horizontal dashed lines indicate the nominal Nb concentration as provided by the crystal supplier. Right panel: Temperature dependence of the electron carrier density n normalized to the 7 K value.

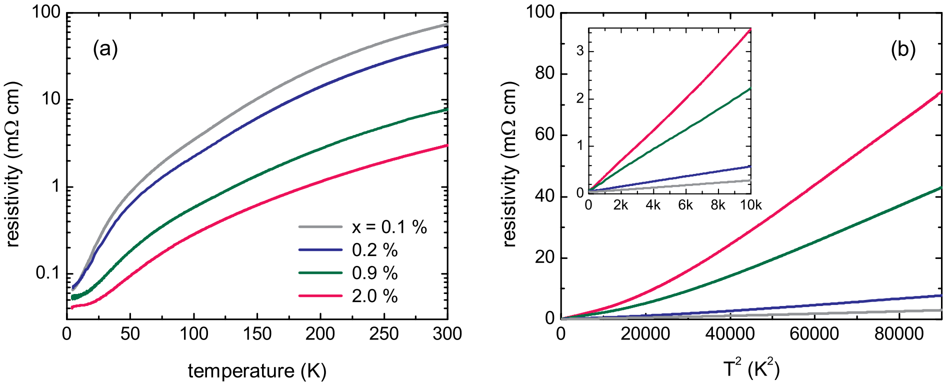

Figure 2.10: (a) Temperature dependence of the DC resistivity of $\mathrm{SrTi}_{1-x}\mathrm{Nb}_x\mathrm{O}_3$ for $x = 0.1\,\%, 0.2\,\%, 0.9\,\%$ and $2.0\,\%$; (b) resistivity vs T^2, the inset shows the resistivity vs T^2 below 100 K.

% of the Nb concentration specified by the supplier (0.1%, 0.2%, 1.0% and 2.0%, respectively, Crystec, Berlin). The right panel of Fig. 2.9 shows the temperature dependence of the charge carrier density normalized to the 7 K value. Notice the decreasing Hall number with increasing temperature and the tendency to saturate at higher temperature which gets stronger towards lower doping. This temperature dependence is counter intuitive since impurity electrons could become less mobile at low temperatures which would suggest a decreasing rather than an increasing carrier density.

The Nb concentration at room temperature has been measured by wavelength dispersive x-ray diffraction spectrometry (WDS) for the two highest doped samples. This technique is similar to EDX where a $10\,\mu$m diameter electron beam bombards a macroscopic sample volume of several microns deep from which characteristic X-rays are emitted. The enhanced accuracy of WDS as compared to EDX is due to the fact that for WDS the detector counts for each individual x-ray wavelength whereas for EDX a broad band spectrum is recorded at once. The precision of the WDS apparatus (JEOL JXA-8800M Electron Microprobe) is estimated at $0.04\,\%$. The Nb concentration of nominally $1\,\%$ and $2\,\%$ doped samples are $0.80\,\%$ and $1.96\,\%$ respectively. In this chapter, the charge carrier concentrations as measured by the Hall effect will be used, and the samples will be assigned by their low temperature Hall effect charge carrier concentration, i.e., $0.1\,\%, 0.2\,\%, 0.9\,\%$ and $2.0\,\%$.

2.5.2 DC resistivity

The DC resistivity has been measured between 300 K and 4 K in a Van der Pauw configuration [53]. Contacts have been made by ultrasonic wire bonding (20 μm thick Si doped Al wire). Fig. 2.10a shows the resistivity of Nb doped SrTiO_3 vs. temperature T which demonstrates that all samples are metallic in

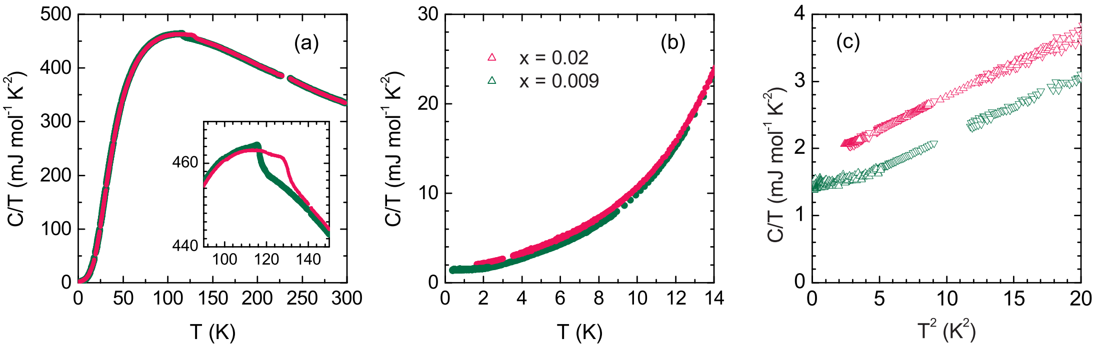

Figure 2.11: Temperature dependence of the specific heat C_p divided by temperature of SrTi$_{1-x}$Nb$_x$O$_3$ for $x = 0.9\,\%$ and $2.0\,\%$. (a) Global view below 300 K, the inset shows a detail between 90 K and 150 K; (b) detailed view below 14 K; (c) C_p/T vs T^2 between 0.38 K and 4.5 K.

the considered range. Fig. 2.10b shows the resistivity versus the temperature squared. A T^2 behavior can be observed for all dopings in two temperature ranges: 100 K $\lesssim T$ and 200 K $\lesssim T < 300$ K. Generally, the resistivity of a metal has a Fermi liquid T^2 dependence at low temperatures and becomes linear in T well above the Debye temperature Θ_D (roughly 500 K for SrTiO$_3$) because the phonon population increases directly proportional with T. The low temperature T^2 behavior points to electron-electron scattering and is due to the fact that the amount of scattering events is linear with T and the distance to the Fermi level also varies linear with T. For the same reason polaron-polaron scattering should also have a T^2 behavior, contrary to standard electron-phonon scattering which goes as T^5 [66].

2.5.3 Specific heat

Specific heat measurements have been carried out as a function of temperature and are displayed in Fig. 2.11. C_p for $x = 0.009$ and $x = 0.020$ is shown below 300 K. The inset of Fig. 2.11a shows the temperature of the antiferrodistortive phase transition, which appears to be strongly dependent on doping. For systems that obey Fermi-Dirac statistics, the specific heat has a linear term due to electronic excitations (Fermi statistics) and a T^3 term due to sound degrees of freedom,

$$c_v = \gamma T + AT^3. \tag{2.17}$$

The $T = 0$ offset in a plot of c_v/T vs T^2 therefore directly gives the coefficient γ. The linear term of the specific heat only appears below 5 K, and is shown in Fig. 2.11c. Fits to the data reveal $\gamma = 1.25$ mJ mol^{-1}K^{-2} and $\gamma = 1.82$ mJ mol^{-1}K^{-2} for 0.9 % and 2.0 %, respectively. From the coefficient γ one can obtain

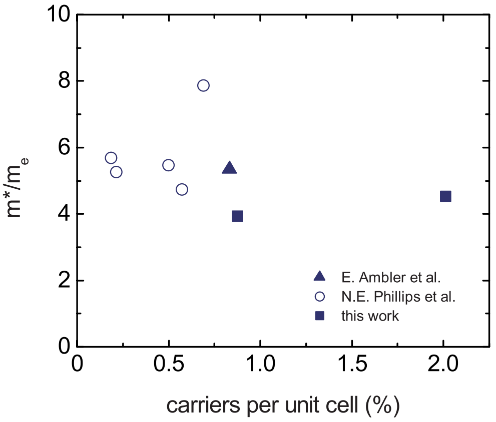

Figure 2.12: Specific heat effective mass m_D^*/m_e as a function of the carrier density of electron doped $SrTiO_3$.

the density of states at the Fermi level by

$$N(E_F) = \frac{3\gamma}{2\pi^2 k_B^2}. \tag{2.18}$$

$N(E_F)$ is proportional to the electronic density-of-states mass m_D, which in turn is related to the band masses m_x, m_y and m_z of the three degenerate t_{2g} bands by [65]

$$m_D = (m_x m_y m_z)^{1/3}. \tag{2.19}$$

m_D represents the geometrical average of the band masses in the three directions. The coefficient γ provides thus the specific heat effective mass $m_D^* = 3.93 m_b$ for 0.9 % and $m_D^* = 4.54 m_b$ for 2.0 %. These values agree with previous measurements by Ambler *et al.* [54] and Phillips *et al.* [55] and are plotted in Fig. 2.12. The specific heat mass renormalization will be discussed together with the optical effective mass in section 2.7.2.

2.6 Optical measurements

We have measured the optical reflectivity and transmission of double side polished, 5 × 5 mm^2 ((100) face) single crystals of $Sr_{1-x}Nb_xTiO_3$ between 300 K and 7 K in the range from 0.3 meV to 7 eV using time-domain THz spectroscopy (TPI spectra 1000, TeraView Ltd. - Cambrigde, UK), Fourier transform infrared spectroscopy and photometric IR-UV spectroscopy. To obtain a detectable transmission we have used for each composition several samples of different thickness (8 – 60 μm), adopted to the spectral range and value of the optical transmission (see Table 2.1). As mentioned before, the Hall carrier concentrations x are 0.105%, 0.196%, 0.875% and 2.00% at 7 K. Compared to earlier measurements [7, 13, 16, 14, 18], we expand the lower limit of the spectral range from

1.2 meV [13] to 0.3 meV and consider a fine grid temperature dependence with intervals of 4 K.

Optical reflectivity has been measured between 300 K and 7 K using a Bruker IFS 113v Fourier-transform spectrometer at normal incidence in the range 4 - 700 meV. The detectors were a Si bolometer operating at 1.6 K for the spectral range 2 - 12 meV and at 4.2 K for the spectral range 9 - 85 meV. In the mid-infrared, for photon energies 75 - 800 meV, we used both a DTGS and a liquid nitrogen cooled MCT detector. Samples are cooled down and warmed up at a typical pressure of 10^{-6} mbar in a home-build cryostat which has the unique, but essential feature that the sample position is quasi static as a function of temperature. At room temperature, a ~ 0.3 μm gold layer is *in situ* evaporated on the sample surface. A temperature dependent measurement of this layer allows to obtain the temperature dependent reflectivity of the studied sample.

In the mid-infrared range, the sample thickness is of the same order as the wavelength and consequently Fabry-Pérot interference fringes appear in the raw reflectivity spectrum if the absorption is small. In order to facilitate fitting, we removed the interference pattern from the as-measured reflectivity by Fourier filtering, but fitted the relation between the fringe number and the frequency of the maximum to get a reliable value of $\sigma_2(\omega)$. Since the intensity of the interference pattern decreases with increasing absorption, this procedure could only be done for the undoped sample, for which 300 periods with a maximum intensity of 20% could be distinguished. Note that the mid-infrared reflection for $x = 0$ in Fig. 2.13 is much larger than for $x > 0$, which is due to the fact that the reflection on the back side of the sample contributes substantially to the total reflectivity. This reflectivity has been appropriately modeled in the analysis which gives $\sigma(\omega)$ (section 2.7.1).

2.6.1 Reflectivity in the infrared

Fig. 2.13 shows the reflectivity of SrTi$_{1-x}$Nb$_x$O$_3$ for $0 \leqslant x \leqslant 0.02$ at 7 K and 300 K. In the infrared region we observe three polar phonons at room temperature: the lowest-energy TO1 phonon around 11 meV (the previously mentioned ferroelectric soft mode) is the Slater mode corresponding to the vibration of Ti cations against the oxygen octahedra; the TO2 phonon around 22 meV represents the vibrations of the Sr cation against the TiO$_6$ octahedra and the highest frequency TO4 phonon around 70 meV represents the bending of the oxygen octahedra. The low energy part of the spectrum is mainly determined by the ferroelectric TO1 mode which softens differently for each doping concentration with decreasing temperature as can be seen from the inset of panel (b). Above the phonon region (i.e., the Reststrahlenband), the data show a sharp plasma edge at 0.10 eV for undoped SrTiO$_3$ which broadens and shifts to higher energy with increasing doping. The bare plasma frequencies for the $x = 0.9\,\%$ and $x = 2.0\,\%$ samples are 0.36 and 0.54 eV respectively. Although, due to screening the actual plasma

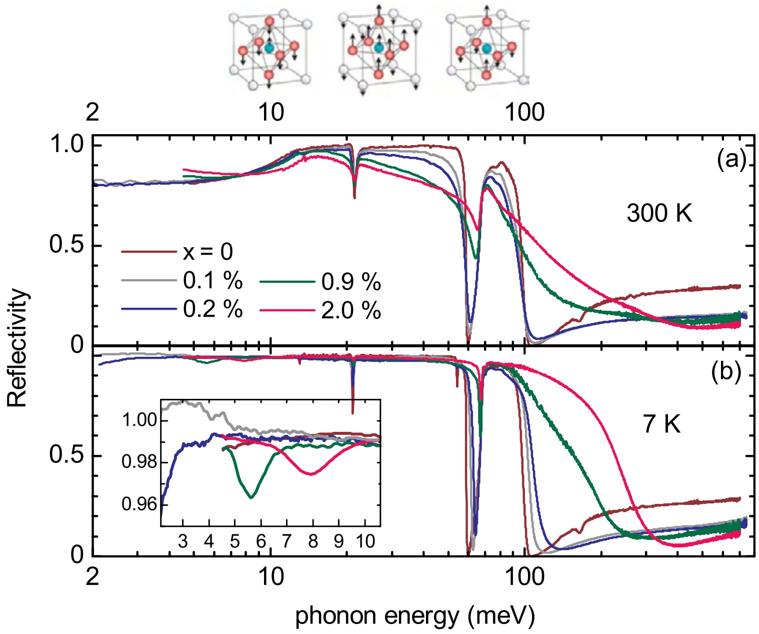

Figure 2.13: Reflectivity data in the infrared (a) at 300 K, (b) at 7 K. The inset in (b) shows the reflectivity below 10 meV. Cartoons show the individual TO phonon movements, after Ref. [71].

resonance frequencies are a factor $\sqrt{\epsilon_\infty} = 2.3$ smaller, and occur at 0.16 and 0.23 eV, which can be recognized in the experimental reflectivity spectra as the upper frequency limit of the reflectivity edge. Undoped $SrTiO_3$ also shows an absorption around 0.17 eV which is, in agreement with its tiny strength, a bi-phonon.

2.6.2 Transmission in the infrared and visible

The transmission of $SrTi_{1-x}Nb_xO_3$ has been measured with a Bruker 66v FTIR spectrometer equipped with a SiC Globar source and a wide range MCT detector between 100 - 900 meV and a Varian Cary 5000 spectrophotometer equipped with a deuterium arc lamp (3.3 - 6.5 eV) and a tungsten-halogen lamp (1.55 - 3.3 eV) and InGaAs and PdS detectors between 0.5 - 6.5 eV. Fig. 2.14 shows the transmission of $SrTi_{1-x}Nb_xO_3$ at 7 K and 300 K between 0.1 eV and 3.5 eV. Fabry-Pérot interference finges, similar to the ones previously mentioned for the reflectivity data, have been removed by Fourier filtering and their frequency dependence is separately fitted. For low doped samples, the infrared transmission is mainly determined by a strong and broad absorption around $0.2 - 0.4$ eV. For high doped samples, the transmission in this range was unmeasurably low and could only be detected above $\sim$ 0.8 eV. With increasing photon energy, a weak absorption around 2.5 eV can be observed which is due to the interband transition between the Ti t_{2g} and e_g levels. Around $3.2 - 3.3$ eV the fundamental band gap

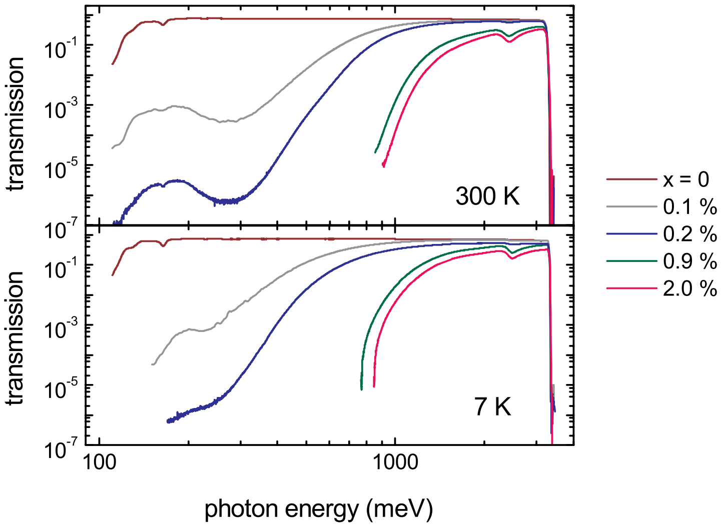

Figure 2.14: Transmission data of SrTi$_{1-x}$Nb$_x$O$_3$ at 7 K and 300 K in the infrared and visible spectral range.

shows up in the spectra as an abrupt decrease of transmission.

2.6.3 Transmission in the THz range

Optical transmission in the range between 0.3 and 12 meV has been recorded between 7 and 300 K by THz time-domain spectroscopy using a TPS spectra 1000 (TeraView Ltd.). The pressure in the sample compartment is typically 10^{-1} mbar, low enough that water absorption does not perturb the transmission spectra. Nb doped SrTiO$_3$ samples have been cooled down in a commercial Janis ST-100 helium flow cryostat. It turned out to be essential to seal the samples with nontransparent glue (silver paste) at the circumference of the sample holder transmission hole in order to prevent parasite transmission of long wavelength light. Fourier transformation of the intensity of the transmitted electric field as a function of delay time gives the transmission amplitude $|t(\omega)|^2$ and phase $\varphi(\omega)$ (Fig. 2.15). The steps in the phase – as well as the peaks in the amplitude – are characteristic for the internal Fabry-Pérot resonances, each of which gives a phase shift of π radians. On cooling down the soft optical phonon mode moves into the THz frequency domain, and thinner samples were needed to obtain a measurable transmission (see Table 2.1). In order to get a reliable transmission value of the order of 10^{-7} at 7 K, the long-wavelength stray radiation (e.g. due to reflections inside the cryostat) has been separately measured *in situ* and subtracted from the total recorded electric field. The device that allowed for this is a flat metallic shutter which is placed in front of the sample and has a reflection coefficient $R \sim 1$, much like SrTiO$_3$ in the THz range at low temperatures. The amount of stray light is thus similar when the shutter is open and closed. The shutter makes

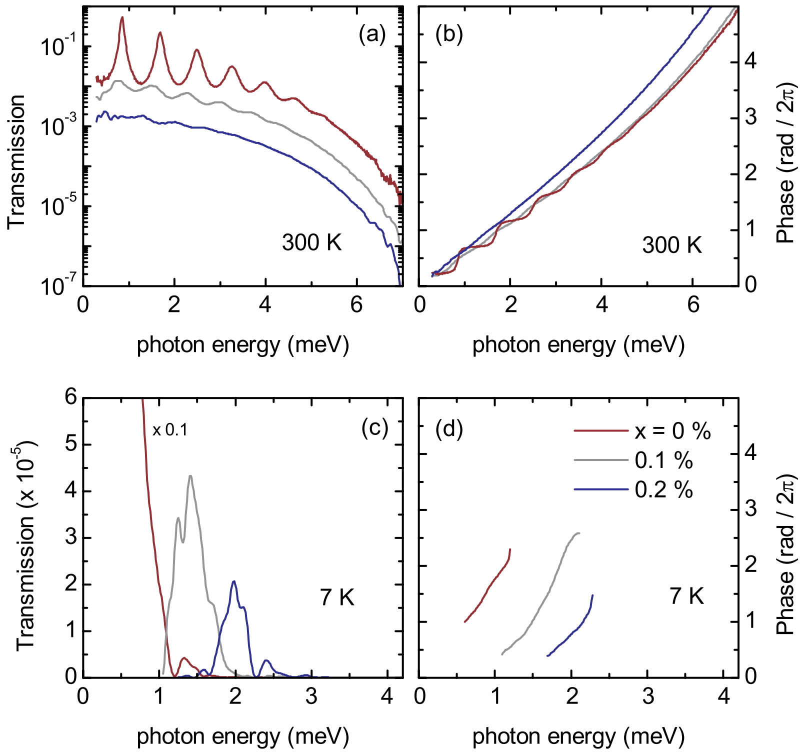

Figure 2.15: THz transmission phase and amplitude at 300 K and 7 K for samples with doping concentrations of $x = 0\%$, 0.1% and 0.2%. Both the peaks in the amplitude and the steps in the phase in (a,b) are signatures of Fabry-Pérot interference.

a magnetically induced guided vertical movement upwards to cover the sample, which operates down to liquid helium temperatures.

At 7 K the transmission spectra of low doped SrTiO$_3$ are dome shaped (see Fig. 2.15c). The absence of transmission below 1 meV is a clear manifestation of a Drude absorption due to free carriers. The low transmission on the high energy side is due to the absorption of the ferroelectric soft mode. The complex transmission $t(\omega)$ has been directly inverted into the dielectric function, $\epsilon(\omega) = \epsilon_1(\omega) + i\epsilon_2(\omega)$, by applying the iterative approach as written in Eq. 1.75 of section 1.7.1.

The lower limit of the spectral range is for our samples determined by the diffraction limit of the sample holder aperture and is also dependent on the amount of transmission. For example, at 300 K for the sample with $x = 0.1\%$ reliable data can be obtained down to 0.3 meV, whereas at 7 K the very low transmission pushes this threshold up to 1.0 meV.

2.7 The low temperature case

In this section we present a spectral weight analysis based on the optical conductivity obtained from the earlier presented optical data. Since traditionally strong electron-phonon coupling is predicted to be present at low temperatures, we first consider first the case of 7 K. The temperature dependence will be discussed in section 2.8.

2.7.1 The optical conductivity

The dielectric permittivity function $\epsilon(\omega) = \epsilon_1(\omega) + 4\pi i\sigma_1(\omega)/\omega$ of Nb doped SrTiO$_3$ in the range from 0.3 meV and 7 eV has been deduced from the experimentally obtained data in the following way. The real and imaginary part of $\epsilon(\omega)$ by inversion of the Fresnel equations of transmission and phase (below 12 meV for the samples with $x = 0,\ 0.001$ and 0.002), inversion of the Fresnel equations of reflection and transmission coefficients (above 0.1 eV), and from Kramers-Kronig analyzes of the reflectivity spectra ($2 - 80$ meV) with Drude-Lorentz fits [36] to aforementioned reflectivity, transmission and phase spectra up to 7 eV, and ρ_{DC}.

Fig. 2.16 shows the optical conductivity $\sigma_1(\omega)$ as a function of doping at 7 K and 300 K. The gap of SrTiO$_3$ is revealed as the sharp onset of the optical conductivity at 3.3 eV in all samples. The absorption peak at 2.4 eV, with intensity proportional to the charge carrier density, reveals optical excitation of the doped t_{2g} states to the empty e_g states. The only subgap contributions to the optical conductivity of undoped SrTiO$_3$ (Fig. 2.16) are the three infrared active phonons at 11.7, 21.8 and 67.6 meV (at room temperature). The lowest one exhibits a strong red shift upon cooling, and saturates at about 2.3 meV at 7 K. Upon doping this mode hardens for all temperatures, reaching 8.5 meV at

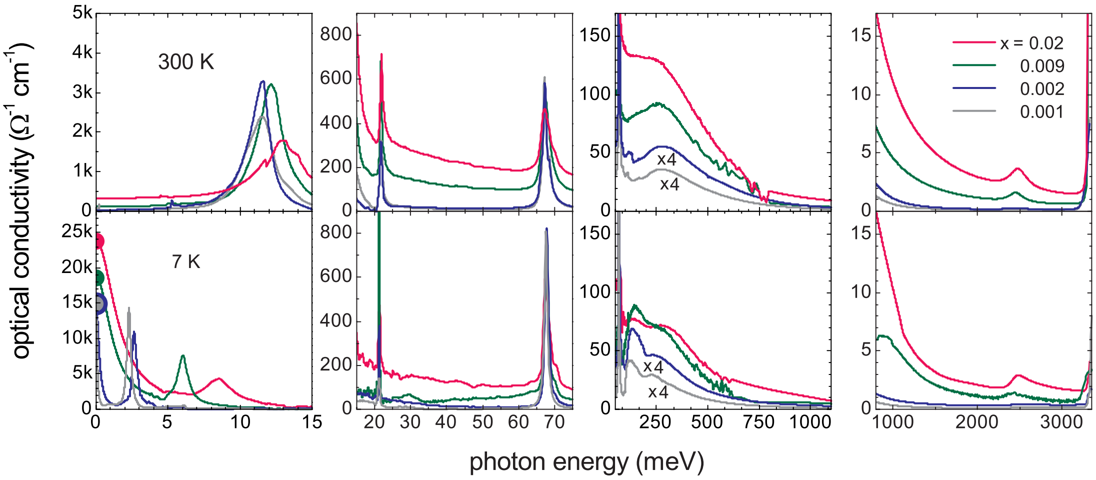

Figure 2.16: The optical conductivity of $\mathrm{SrTi}_{1-x}\mathrm{Nb}_x\mathrm{O}_3$ for $x = 0.001$, 0.002, 0.009 and 0.02 at 300 K (top) and 7 K (bottom), together with the DC conductivity (dots). For clarity the spectral windows corresponding to the extreme infrared, far infrared, mid infrared and visible range are displayed with different magnifications.

7 K at 2% doping. A more detailed discussion of the phonon behavior follows in section 2.8.1. For the present discussion, the most important effect of substituting Nb is to dope electrons, which yields a clearly distinguishable Drude peak, which is broad at 300 K but gets extremely narrow (< 1 meV) at low temperatures, as shown in Fig. 2.16. This unusually narrow Drude peak is the coherent part of the polaronic conduction in n-doped SrTiO_3 as will be argued below. For the 0.9% and 2% doped samples, the metallic conductivity is directly visible from the increase of the reflectivity below the soft optical phonon (see Fig. 2.13). In addition we observe a broad asymmetric mid-infrared absorption which increases with doping, confirming the result of Calvani *et al.* [14]. This band evolves into a double peak structure when the temperature is lowered to 7 K (Fig. 2.16). First principles LDA calculations (cf. section 2.3.1) and tight-binding calculations demonstrate that interband transitions within the t_{2g} manifold is about an order of magnitude too weak to account for the observed intensity (Fig. 2.7). We will argue below that the observed lineshape can be understood as a multiphonon sideband of the free carrier (Drude) response.

2.7.2 Charge carrier mass enhancement

As mentioned before, the effective mass of the charge carriers m^* can be obtained by analyzing the Drude spectral weight. In Fig. 2.17 we show the spectral weight $W(\omega)$, defined as

$$W(\omega_c) \equiv \int_0^{\omega_c} \sigma_1(\omega) d\omega. \tag{2.20}$$

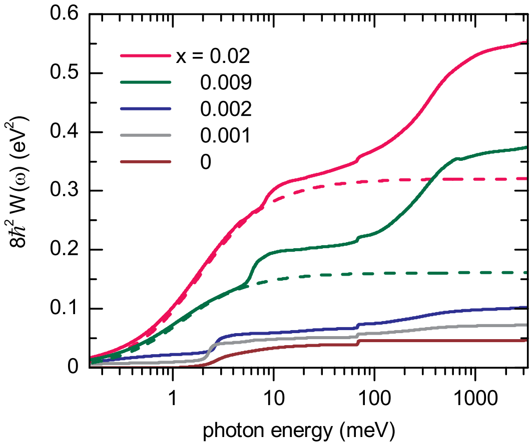

Figure 2.17: The integrated optical spectral weight of SrTi$_{1-x}$Nb$_x$O$_3$ as a function of photon energy and relative to the charge carrier concentration, at 7 K. The Drude spectral weight is separately shown for $x = 0.9\%$ and $x = 2\%$ (dashed lines).

The electronic contribution $8W(\infty) = \omega_p^2 = 4\pi ne^2/m$, where e and m are the free electron charge and mass, and n is the electron density. The contribution of the infrared phonons manifests itself in $W(\omega)$ as steps, *e.g.* at 6.0 meV in the 0.9% doped sample (Fig. 2.17). Such a strong phonon close to the Drude peak requires experimental data that extend beyond the soft phonon frequency. (*i*) The $\epsilon_1(\omega)$ and $\epsilon_2(\omega)$ data below 3 meV measured by time-domain THz spectroscopy (for $x = 0.001$ and 0.002) and (*ii*) far-infrared reflectivity (above 2 meV for $x = 0.001$ and 0.002, and above 4 meV for $x = 0.009$ and 0.02) are crucial for the separation of the spectral weight in the Drude peak from the large contribution by the soft phonon mode. This is particularly important for the lower doped samples, where the Drude spectral weight is one order of magnitude smaller than the spectral weight of the soft optical mode.

For the two lowest dopings we apply the partial sum rule (Eq. 2.20) with cutoff frequencies $\hbar\omega_c = 1.5$ meV (0.1%) and 2.0 meV (0.2%), which are larger than the Drude relaxation rate but below the soft phonon (see Fig. 2.16) [20], yielding $\hbar\omega_p = 111 \pm 18$ meV and 157 ± 23 meV, respectively, shown by the red squares in Fig. 2.18. For the two highest doped samples $\hbar\omega_p = 399 \pm 53$ meV and 562 ± 61 meV for $x = 0.009$ and 0.02 respectively. The mass renormalization of the charge carriers can be obtained by defining it as the ratio of the mid-infrared plus the Drude spectral weight and the Drude spectral weight: $m^*/m = (W_{\text{mir}} + W_{\text{Drude}})/W_{\text{Drude}}$. We observe a twofold mass enhancement, *i.e.*, $m^*/m = 2.0 \pm 0.3$ for the low charge carrier densities considered in the present study (Fig. 2.18, inset). The calculated LDA band mass $m_b \approx 0.63m_e$, which implies $m^*/m_b = 3.0 \pm 0.4$. The analysis is based on a large amount of spectra taken during different measurement runs and the total errorbar is calculated from the statistical average. Within the limits of the errorbar, the inset of Fig. 2.18

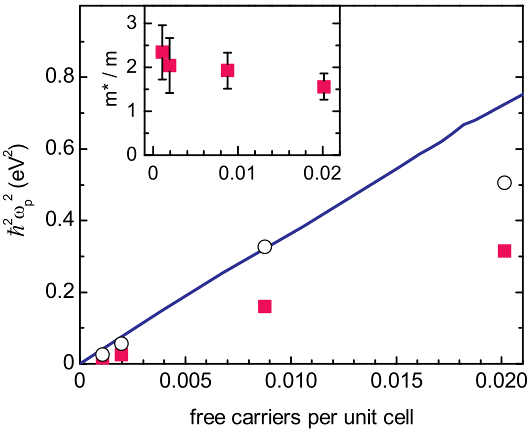

Figure 2.18: Experimental plasma frequency at 7 K derived from the spectral weight of the Drude peak (squares) together with that from the band structure calculations (solid line) as a function of the free carrier concentration (from Hall effect). The circles display the total electronic spectral weight at 3 eV. The inset shows the corresponding effective carrier mass $m^*/m = (W_{\text{mir}} + W_{\text{Drude}})/W_{\text{Drude}}$.

shows that there is a slight mass decrease with doping. Such a decrease can be understood as due to a screening upon increasing the doping which effectively decreases the electron-phonon coupling parameter and thus the observed mass.

Other experimental techniques that can measure mass renormalizations are thermopower [64], cyclotron resonance [65] and specific heat, of which the latter has been presented in section 2.5.3. The mass which has been deduced from the linear part of the C/T vs. T^2 curve provided an effective mass $m_D^* = 5 \pm 1$ as shown in Fig. 2.12. At first glance it seems to be different from the optical mass renormalization of Fig. 2.18. However, the specific heat measures the density-of-states mass m_D (see Eq. 2.19) and optics measures

$$\frac{1}{\bar{m}_b} = \frac{1}{3}\left(\frac{1}{m_x} + \frac{1}{m_y} + \frac{1}{m_z}\right) \tag{2.21}$$

which is an average over all occupied states. With a mass ratio of 27 between the heavy and light bands, the optical equivalent of the specific heat mass becomes 2.5±0.5, very similar to the optical mass. Recent ARPES measurements [72] have shown a weak kink structure in the electronic dispersion which they attribute as a weak electron-phonon coupling to the lowest TO1 mode. They reveal a mass renormalization due to this mode only of $m^*/m \sim 1.3$ which would correspond to $\alpha \approx 1.8$, much larger than the predicted value of 0.01 [70]. The reported overall mass renormalization for $x = 0.01$ is about 2.2, also very close to our optical mass.

For $0.001 \leqslant x \leqslant 0.02$, the band-structure value of the Fermi energy, E_F, ranges from 0.02 to 0.1 eV, relative to the bottom of the lowest t_{2g} band, which coincides with the energy of the relevant longitudinal optical phonon, $\hbar\omega_{\text{LO}} =$

0.10 eV [21, 22] (for $x = 0$). This is a difficult parameter range to describe theoretically where none of the usual approximations, *i.e.*, $\hbar\omega_{\mathrm{LO}}/E_F \ll 1$ nor $\hbar\omega_{\mathrm{LO}}/E_F \gg 1$ are applicable. However, the energy of this longitudinal mode is a strong function of temperature and doping, such that at 7 K it increases to 0.20 eV at 0.9 % and attains 0.28 eV at 2 % (cf. Fig. 2.26). We thus consider for the present discussion the latter limit, appropriate for all dopings and all considered temperatures. It takes as a starting point the model of a single polaron [23, 24], characterized by the coupling constant α. Within a variational approximation, Feynman [23] deduced the relation $m^*(\alpha)$ valid in the range $0 < \alpha < 12$, as mentioned in section 2.1.1. Applying Feynman's relation to the experimental m^* values, we obtain for the lowest doped sample a value $3 < \alpha < 4$, in excellent agreement with the value $\alpha = 3.6$ from the Fröhlich model in a polar medium with multiple optical phonon branches (see section 2.9). With increasing doping α decreases slightly towards $2 < \alpha < 3$.

The optical conductivity shows a broad absorption band between 0.1 and 1 eV (Fig. 2.16). The f-sum rule, $8W(\infty) = \omega_p^2$, is almost satisfied at 3 eV (Fig. 2.18), demonstrating that the intensity in this mid-infrared band compensates to a large extent the deficit of Drude spectral weight. Such spectral weight redistribution between the 'coherent' (Drude) and the 'incoherent' (mid-infrared) contributions of the optical conductivity suggests that the mass enhancement reflects coupling of electrons to bosonic degrees of freedom, most probably phonons. A spectral shape similar to the observed mid-infrared band at 300 K (Fig. 2.16) was calculated by Emin [25], who considered the photo-ionization spectrum out of the potential well formed by the lattice deformation of the polaron. Upon cooling, the maximum of this band remains between 200 and 350 meV, and at 7K an additional peak emerges on the low-energy side with a maximum varying from 120 (0.1%) to 140 meV (2%). Devreese *et al.* [27] have numerically found a broad mid-infrared band with (for intermediate couplings) a peak at lower energies. They explain it as a multiphonon band and the peak as a relaxed state of an electron optically excited within the polaronic potential well. The model predicts the maxima of the two bands to be at $0.065\alpha^2\hbar\omega_{\mathrm{LO}}$ and $0.14\alpha^2\hbar\omega_{\mathrm{LO}}$ (cf. section 2.1.4). With $\alpha \approx 4$ this corresponds to 110 meV and 230 meV, consistent with the experimentally observed positions (Fig. 2.16). In section 2.9 the experimentally obtained optical conductivity that has been presented in this section is compared to the optical conductivity obtained from a many large polaron model.

2.8 Temperature dependence

2.8.1 The optical conductivity and dielectric permittivity

In the preceding section we presented the optical data on Nb doped SrTiO$_3$ at 7 K and 300 K and described the analysis to obtain the renormalized optical mass

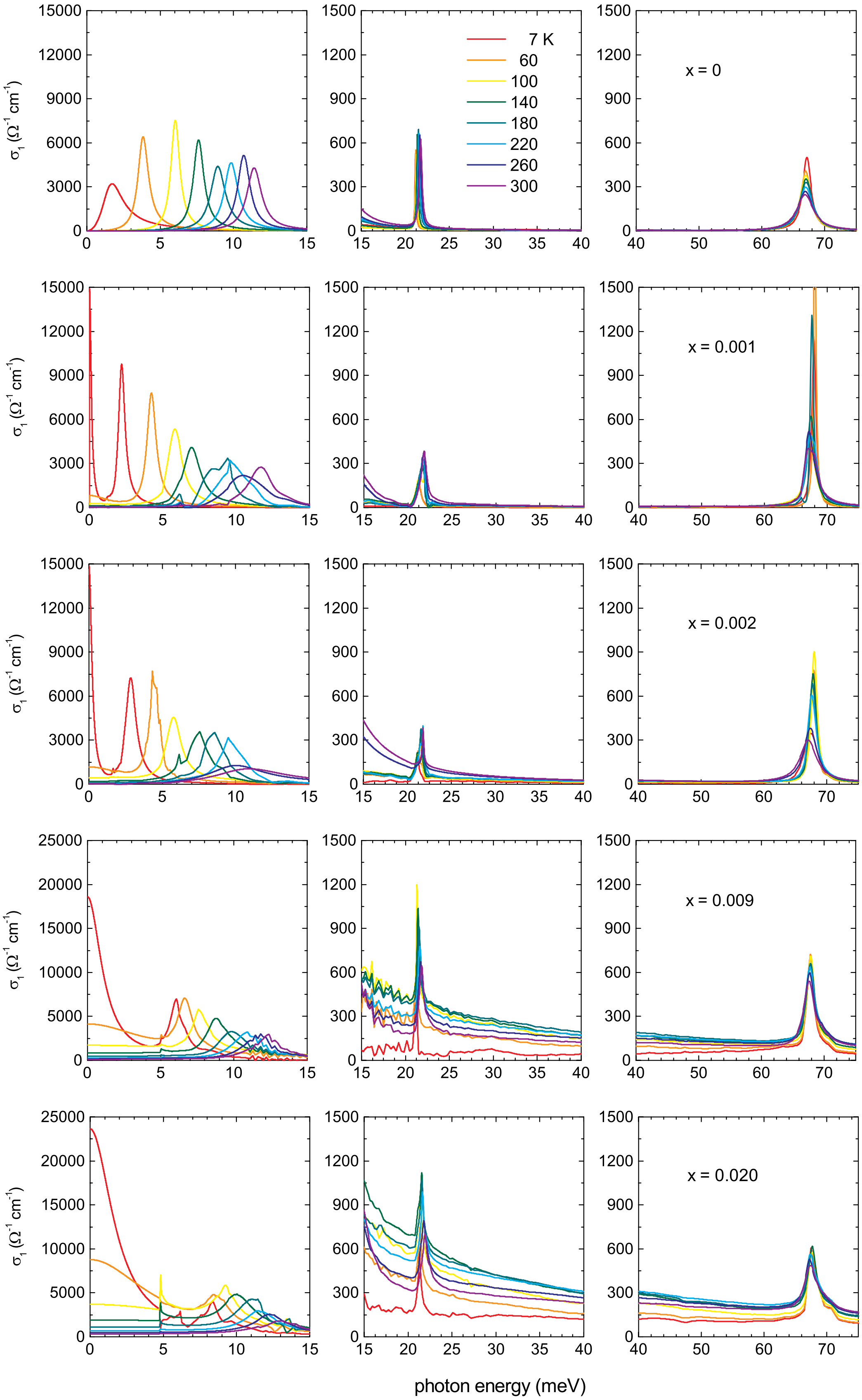

Figure 2.19: The optical conductivity of $SrTi_{1-x}Nb_xO_3$ for x = 0, 0.001, 0.002, 0.009 and 0.02 for selected temperatures for photon energies between 0 and 75 meV.

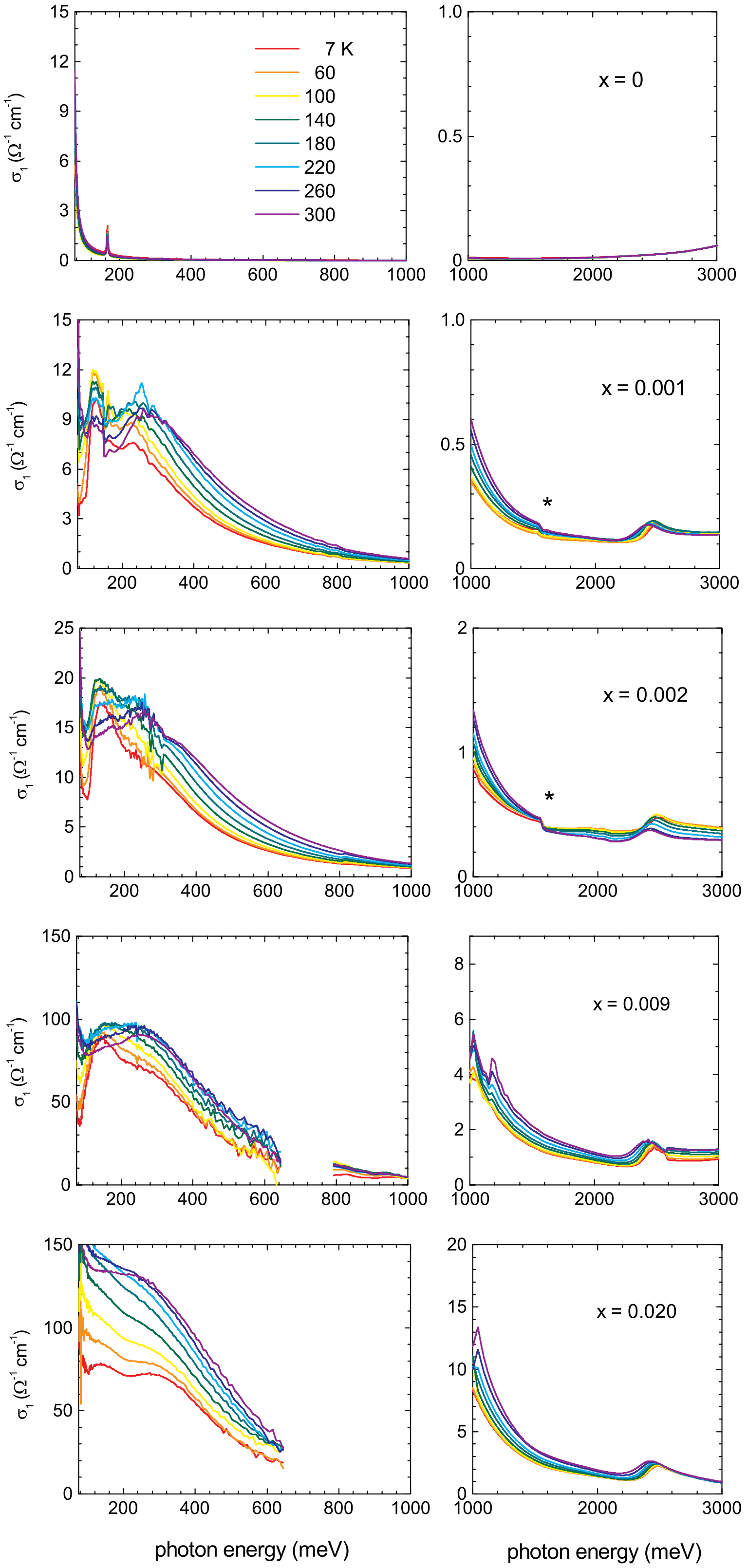

Figure 2.20: The optical conductivity of SrTi$_{1-x}$Nb$_x$O$_3$ for $x = 0$, 0.001, 0.002, 0.009 and 0.02 for selected temperatures for photon energies between 75 meV and 3.0 eV. The * indicates a change of the source in the Varian Cary 5000 spectrometer (see section 2.6.2).

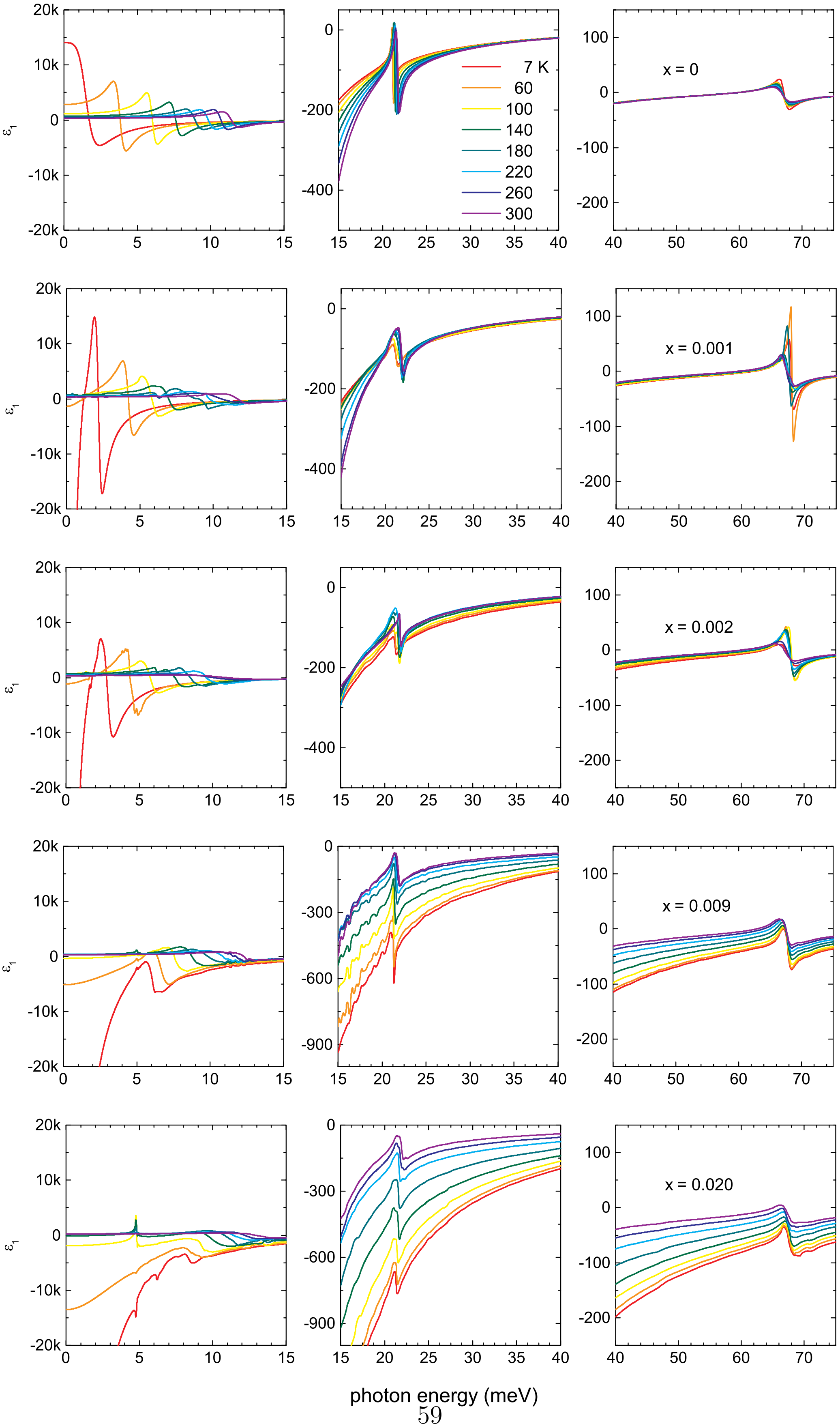

Figure 2.21: The real part of the dielectric permittivity of $SrTi_{1-x}Nb_xO_3$ for $x = 0$, 0.001, 0.002, 0.009 and 0.02 for selected temperatures for photon energies between 0 and 75 meV.

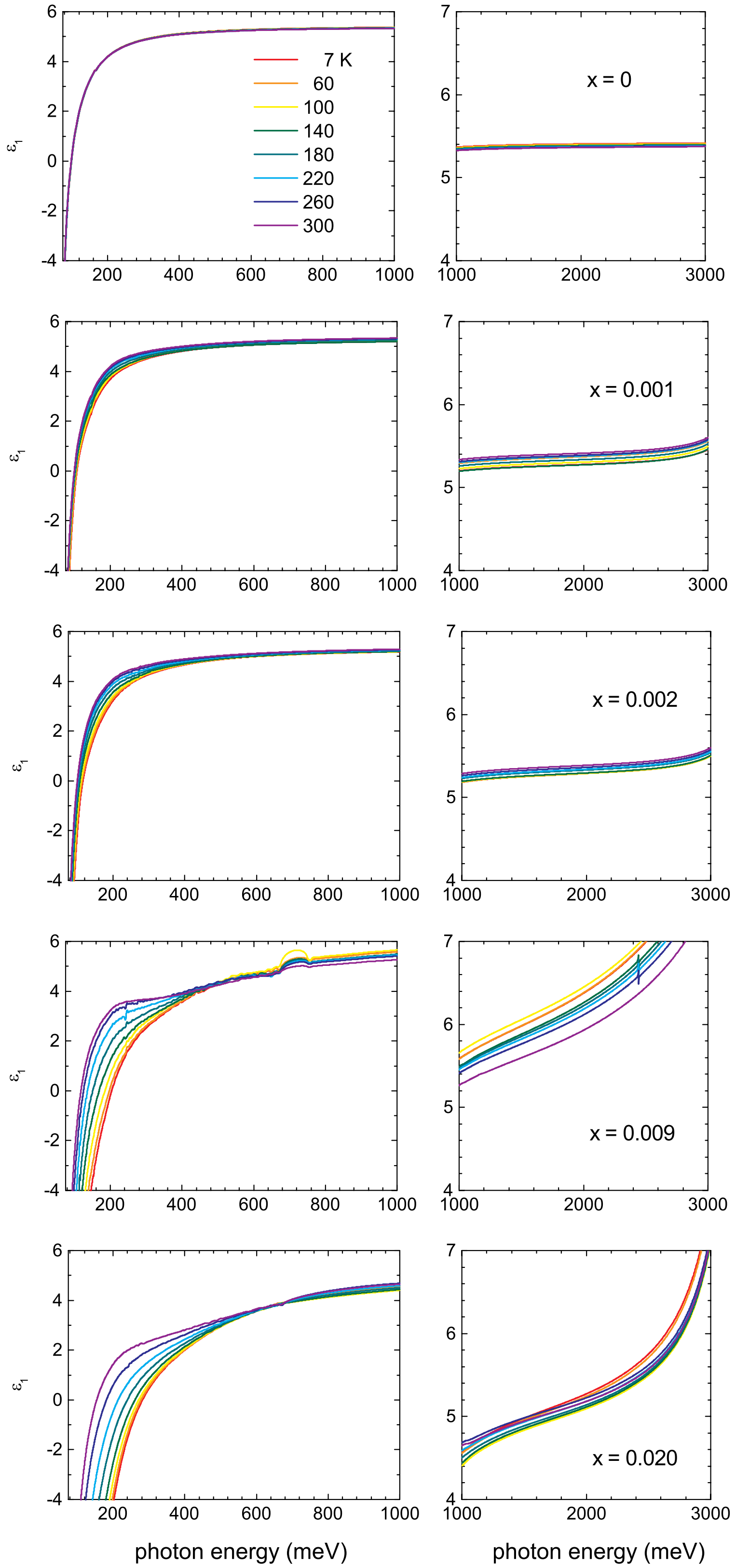

Figure 2.22: The real part of the dielectric permittivity of SrTi$_{1-x}$Nb$_x$O$_3$ for $x = 0$, 0.001, 0.002, 0.009 and 0.02 for selected temperatures for photon energies between 75 meV and 3.0 eV.

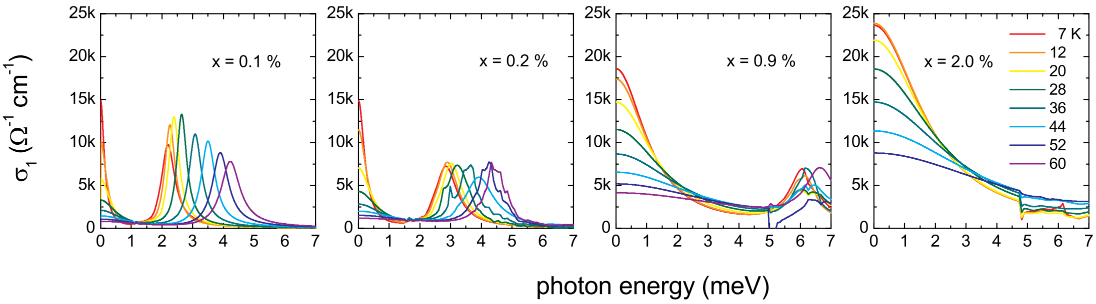

Figure 2.23: The optical conductivity of SrTi$_{1-x}$Nb$_x$O$_3$ for x = 0.001, 0.002, 0.009 and 0.02 for selected temperatures below 60 K for photon energies up to 7 meV.

at 7 K. In the following we extent the considered temperatures and perform the same analysis for the optical mass. Figs. 2.19-2.20 and Figs. 2.21-2.22 show the optical conductivity $\sigma_1(\omega)$ and the dielectric permittivity $\epsilon_1(\omega)$, respectively, of SrTi$_{1-x}$Nb$_x$O$_3$ for selected temperatures between 7 K and 300 K and for photon energies $0 \leqslant \hbar\omega \leqslant 3$ eV.

Drude peak

Starting from the lowest energies Fig. 2.19 shows a peak in σ_1 centered around zero photon energy which is due to intraband (Drude) transitions. At room temperature it is broad and structureless and is basically only a free carrier background to the optical conductivity, but below 50 K it sharpens and gets extremely narrow for the lowest doped sample (see Fig. 2.23). Fig 2.24 shows the scattering time τ obtained from Drude-Lorentz fits to the optical data. Also plotted are the scattering length $\ell = v_F\tau$ and the DC electron mobility $\mu_{\mathrm{DC}} = \sigma_{\mathrm{DC}}/n_{\mathrm{Hall}}e$. They all show the same trend: an increase below 50 K which grows with decreasing x, in agreement with Ref. [64]. Notice that the scattering length of Nb doped SrTiO$_3$ for $x = 0.001$ is 300 nm at the lowest temperature, whereas typical scattering lengths in metals are on the order of $1 - 10$ Å. A similar mobility below 40 K has been reported for n-doped BaTiO$_3$, where the decrease towards higher temperatures was attributed to the scattering of free electrons from acoustical and longitudinal or transverse optical phonons [62].

TO and LO phonons

The optical properties for photon energies between the Drude peak and the mid-infrared band are mainly characterized by three transverse optical phonons (see also section 2.6.1) that show a distinct temperature dependence on cooling. The lowest of them, the ferroelectric soft mode, is the strongest of the three and is easily recognizable by the huge ϵ_1 which increases up to about $1.5 \cdot 10^4$ at 7 K for undoped SrTiO$_3$ (Fig. 2.21). This mode softens with decreasing temperature

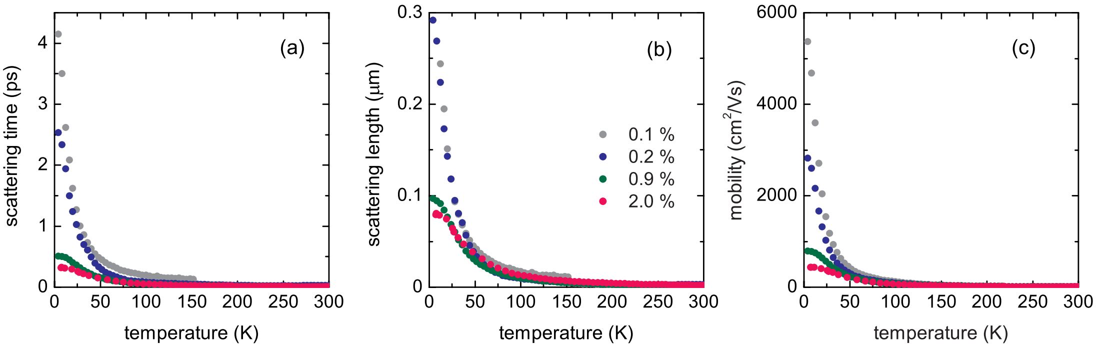

Figure 2.24: The experimental temperature dependence of (a) the scattering time obtained from $\sigma_1(\omega)$ (b) the scattering length and (c) the mobility obtained from σ_{DC} and n_{Hall} of $\mathrm{SrTi}_{1-x}\mathrm{Nb}_x\mathrm{O}_3$.

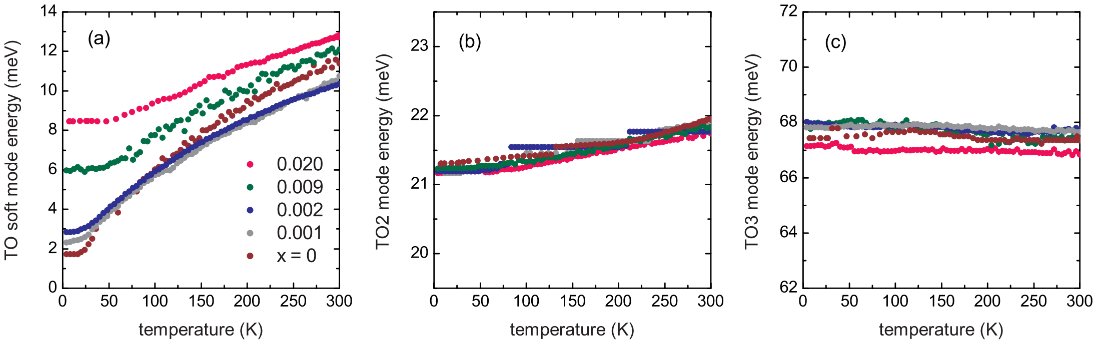

Figure 2.25: Experimental temperature dependence of the three TO modes of $\mathrm{SrTi}_{1-x}\mathrm{Nb}_x\mathrm{O}_3$. The limited resolution of the fitting procedure causes steps as can be observed in (b).

by an amount which strongly depends on the Nb doping as can been read off from Fig. 2.25, in agreement with Ref. [13]. It has been argued in the past that quantum fluctuations prevent the mode from complete softening and thus SrTiO_3 from becoming ferroelectric [15, 69]. However, the quantum fluctuations should disappear when an impurity like Nb is introduced. Fig. 2.25a shows that upon doping the mode hardens at low temperature, but also the temperature independent plateau extents to higher temperature with increasing x, which is not reconcilable with the occurrence of quantum fluctuations. It is however certain that upon Nb doping the soft mode energy becomes stabilized and one moves away from the ferroelectric state.

The higher energy TO modes have little temperature dependence: the one around 22 meV softens by about 1 meV , and the mode around 68 meV hardens by a very small amount of less than 0.2 meV.

Above the highest TO mode, the zero-crossing of $\epsilon_1(\omega)$ correspond to the energy of the highest LO phonon close to the Γ-point. As described in the in-

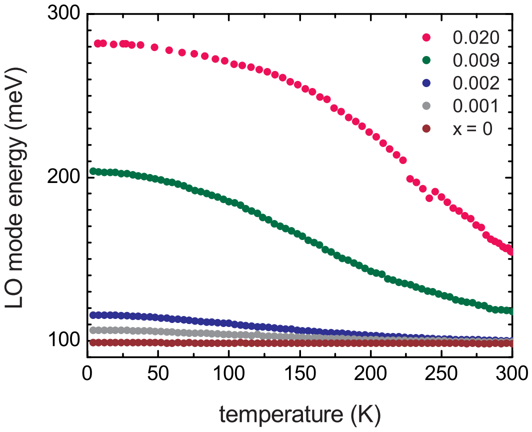

Figure 2.26: Temperature dependence of the highest longitudinal optical mode of $SrTi_{1-x}Nb_xO_3$, obtained from the zero-crossings of $\epsilon_1(\omega)$.

troduction of this chapter, the LO phonons couple to the electrons. Eagles [70] derived the polaron coupling constants α for the three TO modes in $SrTiO_3$ with increasing TO energy : 0.01, 0.50, 1.83. This implies that the zero-crossing of $\epsilon_1(\omega)$ is the right parameter to look at to directly see any renormalization due to electron-phonon coupling. Fig. 2.26 shows the temperature dependence for the considered doping concentrations. While for $x \leqslant 0.2\,\%$ this mode is to good approximation temperature independent, it rapidly rises for higher dopings, as earlier reported by Gervais *et al.* [13]. Without any plasmon-phonon coupling, the energy of this mode would remain invariant.

The spectral weight $W(\omega)$, defined trough Eq. 2.20, implies in the limit $\omega \to \infty$ the identity

$$W(\infty) \equiv \sum_j \frac{\pi n_j q_j^2}{2m_j} \tag{2.22}$$

where the summation is over all types of particles in the solid (electrons and nuclei) characterized by their density n_j, charge q_j and mass m_j. If, in the case of an ionic insulator, we truncate the integration at a frequency Ω_c below the onset of the interband transitions, the quantity $W(\Omega_c)$ should correspond to a sum over $\pi n_j q_j^2/2m_j$ where q_j and m_j are the charge and the mass of the ions of the material provided that the rigid-ion model works. Applying the righthand side of Eq. 2.22 to $SrTiO_3$, the rigid ion model result is $8\hbar^2 W(\Omega_c) = 0.0143$ eV^2. In Fig. 2.17 we can read off the value for pristine $SrTiO_3$ for $\hbar\omega > 70$ meV where $W(\omega)$ has become constant. This experimental value is in fact $8\hbar^2 W_{vib} = 0.0464$ eV^2, i.e., 3 times larger than the prediction based on the rigid ion model. The situation is reminiscent of the transition metal monosilicides and IV-VI semiconductors [63]. In those systems the large optical phonon spectral weight has been understood from the resonance aspect of the chemical bond, whereby electronic charge is dynamically redistributed between bonds during the vibration of an optical mode.

Optically weak phonons become effectively ‘charged’ by this mechanism. This leads us to an important observation that the coupling to interband transitions of the soft phonon is responsible for about 70% of the high static dielectric constant, and thereby for the paraelectric susceptibility of pristine SrTiO$_3$.

Mid-infrared band

In the mid-infrared range (Fig. 2.20[3]) we observe for all samples a smooth transition from the broad band structure at room temperature to a double peak shape at low temperature. In the preceding section we explained the low-energy peak as due to on-site excitations within the polaronic potential well and the broader band due to Franck-Condon transitions. The temperature dependence of the entire mid-infrared conductivity is remarkable: with increasing temperature the strength of the 120 meV peak grows up to about 100-140 K, and then decreases without completely disappearing at room temperature. The overall conductivity level does not change much for $0.1 < \hbar\omega < 0.3$ eV and shows a gradual decrease above this range, following a $\omega^{-5/2}$ behavior above 0.5 eV. This picture is similar for the three lowest doped samples.[4] However, $x = 0.02$ is different: on warming up the low temperature double peak structure becomes increasingly indistinguishable and the overall conductivity level doubles. It could be argued that the nature of the mid-infrared peaks (and particularly the one at 120 meV) is due to (*i*) interband transitions between the non-degenerate t$_{2g}$ levels or (*ii*) interband transitions between possible impurity levels and the bottom of the t$_{2g}$ band. Fig. 2.7 shows the optical conductivity as calculated with the tight-binding model presented in section 2.3.2. Interband transitions between the spin-orbit split t$_{2g}$ levels are visible around 25 meV, which is quite beyond the energy range of the experimentally observed mid-infrared peaks. Nevertheless, the calculated spectral weight for $x = 0.02$ corresponds very well to the experimental spectral weight of the peak at 120 meV. This suggests that the 120 meV peak is a *phonon-assisted* interband transition between the t$_{2g}$ levels, where again the $\hbar\omega_{\mathrm{LO}} = 0.1$ eV phonon is involved. To discuss the second option, when undoped pristine SrTiO$_3$ is electron doped, localized impurity levels will be formed for very low electron concentrations just below the conduction band. The insulator-to-metal transition is achieved at the moment when this impurity level merges with the conduction band and carriers become free to move. The 120 meV peak grows proportionally with the Nb concentration and corresponds to about 0.05 impurity level per Nb atom. At low temperatures, all charge carriers should end up

---

[3] It should be mentioned that Fig. 2.16 relies on mid-infrared transmission data taken with a DTGS detector, whereas the transmission data for Fig. 2.20 is taken with a liquid nitrogen cooled MCT detector, which has a significant better signal to noise ratio.

[4] The apparent fine structure on $\sigma_1(\omega)$ for $x = 0.001$ in the mid-infrared range for all temperatures is artificial. It has been verified that it is not due to Fabry-Pérot interference. A similar measurement did not reproduce the structure.

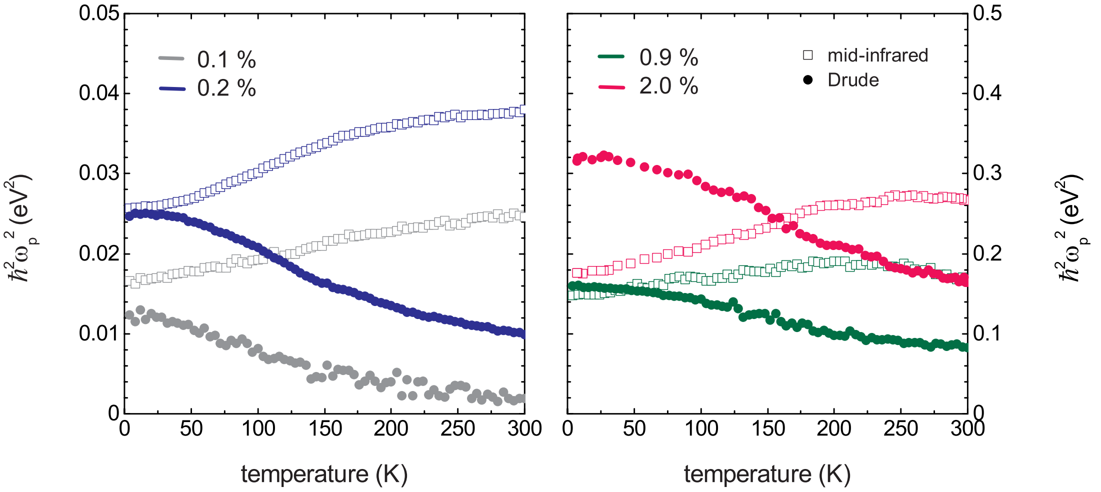

Figure 2.27: Experimental temperature dependence of the spectral weight of both the Drude peak (circles) and the mid-infrared band (squares) for $x = 0.1\ \%, 0.2\ \%, 0.9\ \%$ and $x = 2.0\ \%$.

in these donor levels. This means that the intensity of the 120 meV peak should have been 20 times higher than we observe and the Drude peak should entirely disappear. A remaining possibility is impurity levels due to e.g. oxygen vacancies or cluster formation of Nb. However, both scenarios are not compatible with the strength of the peak which is proportional to the Nb doping. Finally, the 120 meV peak can also be due to on-site transitions inside the polaronic potential well, as theoretically predicted within the single polaron model. The fact that we observe an increasing strength of this peak with decreasing doping would be a manifestation of the approach towards the single polaron limit (cf. section 2.9).

2.8.2 Temperature dependent optical mass

Fig. 2.27 shows the temperature dependence of the spectral weight of both the Drude peak and the mid-infrared band, obtained in the way as described in section 2.7.2. For all doping concentrations our data show a gradual increase of the mid-infrared spectral weight with increasing temperature, as earlier observed by Ref. [14], of about a factor 1.5. At the same time, we see a decrease of the Drude spectral weight by about a factor two for the highest doped samples which increases for lower dopings. The total electronic spectral weight slightly decreases upon increasing temperature, very similar to the Hall constant (cf. Fig. 2.9).

The temperature dependent Drude and mid-infrared spectral weight yield the temperature dependence of the optical effective mass by $m^*/m = (W_{\mathrm{mir}} + W_{\mathrm{Drude}})/W_{\mathrm{Drude}}$, as shown in Fig. 2.28. At 7 K we already noticed a minor decrease with doping (see Fig. 2.18). As a function of temperature, the optical mass grows by an amount which is strongly dependent on the doping concentration.

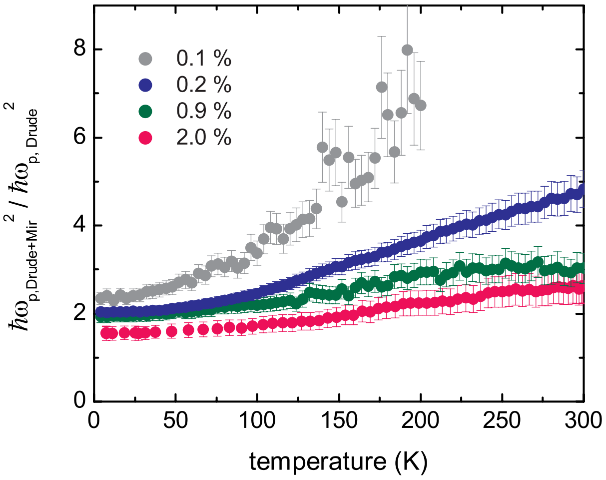

Figure 2.28: Experimental temperature dependence of the effective mass m^*/m obtained from the ratio of the total (Drude and mid-infrared) spectral weight and the Drude spectral weight for $x = 0.1\,\%, 0.2\,\%, 0.9\,\%$ and $2.0\,\%$.

At low doping of $x = 0.1\,\%$ we observe a reliable increase from $2.3m_b$ up to about $7m_b$ at 200 K, whereas for the $2\,\%$ doped sample m^*/m only increases from 1.6 to 2.2 at 200 K. A rapid increase of the effective mass has been reported earlier by Gervais *et al.* [13] for Nb doped SrTiO$_3$, based on the temperature dependence of the plasma frequency. He reports an average mass increase of a factor 2.9 between 78 K and 300 K for $0.006 \leqslant x \leqslant 0.015$. An increasing mass is compatible with the decreasing electron mobility as measured by dc transport (Fig. 2.24), although it is opposite to the expectation that thermal fluctuations undo the self-trapping and reduce the effective mass [30, 31]. At a fixed temperature (e.g. 200 K) the mass strongly increases for decreasing x, as would be expected for the approach to the single polaron limit. But is this really the origin of the increasing mass?

With increasing temperature also the Fermi energy increases and the heavy electron branch of the t$_{2g}$ bands becomes more and more filled. Since the ratio of the heavy and the light branches is approximately 27, this might be the origin of the observed renormalization. Within the tight-binding model, we calculated the band mass dependence on temperature (Fig. 2.8) which displays a minor decrease and shows that filling of the heavy electron band does not play a role at all. The reason for this is the little phase space the heavy band occupies in the entire Brillouin zone.

If the mass increase is due to an effectively increasing electron-phonon coupling strength due to the fact that the coupling becomes the less and less screened, then not only a decrease of the Drude weight is expected but also an increase of the mid-infrared spectral weight. In addition, the polaron energy is expected to shift to higher energies in agreement with the coupling constant α and thus the observed effective mass. An increase of the mid-infrared spectral weight has been observed, but the polaron energy almost does not vary with doping (see Fig. 2.20). Eagles calculated the renormalized mass for a system where small and large polarons coexists and the population small polarons increases with temperature. He reports values of the density-of-states mass of $6m_e, 6.5m_e$ and $22m_e$ at 0, 78 and 300 K, respectively.[12] This mass increase has the same temperature trend and magnitude as we observe for the lowest doped samples in Fig. 2.28.

An effective mass which increases with temperature has been explained by Kabanov and Ray with a two-fluid model of delocalized carriers and localized polarons pinned to impurity sites [32]. However, in this model the Hall coefficient depends strongly on temperature and becomes completely suppressed at low temperatures, in contradiction to the almost constant Hall coefficient of our Nb-doped STO crystals (see section 2.5.1). While Ciuchi *et al.* [33] have demonstrated that the polaron radius *decreases* when the temperature is increased, the authors maintain that the polaron mass will decrease with increasing temperature. The Holstein model on the other hand (cf. section 2.1.2) predicts a mass increase with temperature due to the increasing importance of so-called non-diagonal processes. These transitions do not keep phase coherence, flatten the polaron bands and therefore pave the way for small polaron formation. With increasing temperature, a crossover from larger to smaller polarons is thus to be expected.

Theoretical work until now has concentrated on the properties of a single polaron, while the important (but quite difficult) problem of the polaron liquid remains to be solved. An alternative explanation considers the *collective* nature of a polaron liquid. In this respect we conjecture that in its ground state the electron-phonon interacting system forms a homogeneous fluid which is uniformly accelerated by an external electric field, without excitation of the vibrational degrees of freedom. Since the charge fluid is no longer uniform at finite T due to thermal charge density excitations, its translation upon applying an electric field becomes increasingly hindered by coupling to the lattice vibrations when we increase the temperature, resulting in a reduced Drude spectral weight and an increase of the mid-infrared spectral weight. The relevant temperature scale for this to occur is the Fermi temperature, is about 250 K for the 0.1 % doped sample and less than 1000 K for the highest doped sample. The aforementioned process whereby a polaron will escape from its self-trapped potential will occur on the (higher) energy scale of the polaron binding energy, i.e., approximately 2000 K.

2.9 Many-body large polaron optical conductivity

In the preceding sections we presented the optical conductivity spectra of Nb doped $SrTiO_3$. We observed a renormalized coherent Drude peak and two mid-infrared multiphonon side bands. The energies of these side bands correspond well to the predicted values within the theory of *single* large polarons. Also, the decay of $\sigma_1(\omega)$ at high frequencies goes like $\omega^{-5/2}$ which is typical for large polaron behavior, opposite to a Gaussian decrease for small polarons. As already mentioned in the introduction, a one-polaron theory has limited validity since there are many more electrons in a solid, and a many-electron approach is thus certainly more appropriate. To understand the shape and the intensity of the mid-infrared band of the experimental optical conductivity spectra of SrTi$_{1-x}$Nb$_x$O$_3$, Prof. J.T. Devreese and Dr. S.N. Klimin from the University of Antwerp have calculated the large-polaron optical conductivity spectra for SrTi$_{1-x}$Nb$_x$O$_3$ using the model for the optical conductivity of a large-polaron gas developed in Ref. [73] as published in Ref. [78]. The model has been adapted to take into account (*i*) multiple LO-phonon branches [74] (*ii*) the degeneracy and (*iii*) the anisotropy of the conduction band in SrTi$_{1-x}$Nb$_x$O$_3$. These adaptations from a very general model to the specific case of SrTiO$_3$ are necessary to match the experimental data.

The starting point for the treatment of a many-polaron system is the Fröhlich Hamiltonian

$$\begin{aligned} H =& \sum_{\mathbf{k}} \sum_{\sigma=\pm 1/2} \frac{\hbar^2 k^2}{2m_b} c^{+}_{\mathbf{k},\sigma} c_{\mathbf{k},\sigma} + \sum_{\mathbf{q}} \sum_{j=1}^{n} \hbar\omega_{L,j} a^{+}_{\mathbf{q},j} a_{\mathbf{q},j} + U_{e-e} \\ &+ \frac{1}{\sqrt{V}} \sum_{\mathbf{q}} \sum_{j=1}^{n} \left(V_{\mathbf{q},j} a_{\mathbf{q},j} \sum_{\mathbf{k}} \sum_{\sigma=\pm 1/2} c^{+}_{\mathbf{k}+\mathbf{q},\sigma} c_{\mathbf{k},\sigma} + \mathtt{h.c.} \right), \end{aligned} \tag{2.23}$$

where $c^{+}_{\mathbf{k},\sigma}$ ($c_{\mathbf{k},\sigma}$) are the creation (annihilation) operators for an electron with momentum $\mathbf{k}$ and with the spin z-projection σ, $a^{+}_{\mathbf{q},j}$ ($a_{\mathbf{q},j}$) are the creation (annihilation) operators for a phonon of the j-th branch with the momentum q, $\omega_{L,j}$ are the LO-phonon frequencies (approximated here as non-dispersive), and V is the volume of the crystal. The polaron interaction amplitude $V_{\mathbf{q},j}$ is [75]

$$V_{\mathbf{q},j} = \frac{\hbar\omega_{L,j}}{q} \left(\frac{4\pi\alpha_j}{V} \right)^{1/2} \left(\frac{\hbar}{2m_b\omega_{L,j}} \right)^{1/4}, \tag{2.24}$$

where α_j is a dimensionless partial coupling constant characterizing the interaction between an electron and the j-th LO-phonon branch. The electron-electron interaction is described by the Coulomb potential energy

$$U_{e-e} = \frac{1}{2} \sum_{\mathbf{q}\neq 0} \frac{4\pi e^2}{\varepsilon_\infty q^2} \sum_{\mathbf{k},\mathbf{k}',\sigma,\sigma'} c^{+}_{\mathbf{k}+\mathbf{q},\sigma} c^{+}_{\mathbf{k}'-\mathbf{q},\sigma'} c_{\mathbf{k}',\sigma'} c_{\mathbf{k},\sigma}. \tag{2.25}$$

Optical phonons in SrTiO$_3$ show a considerable dispersion (see e.g. Ref. [76] and references therein). The effect of the phonon dispersion is a broadening of the polaron optical conductivity band. However, for SrTiO$_3$ the dispersion of the optical phonons that contribute to the optical polaron conductivity is only a few percent of $\omega_{L,j}$ and is thus very small compared to the characteristic width of the polaron band. Therefore, in the present treatment, we apply the approximation of non-dispersive phonons.

The coupling constants α_j are obtained by comparing the expression for the amplitudes of the electron-phonon interaction $V_{\mathbf{q},j}$ in terms of the dielectric function of the lattice $\epsilon(\omega)$ to Eq. 2.24.[78] One obtains a set of linear equations for the coupling constants α_j ($j = 1, \ldots, n$). Knowledge of the band mass, of the electronic dielectric constant ε_∞ and of the LO- and TO-phonon frequencies is sufficient to determine the coupling constants α_j (see Table 2.2) taking into account mixing between different optical-phonon branches.

Table 2.2: Optical-phonon frequencies and partial coupling constants of Nb doped SrTiO$_3$. Phonon energies are in meV.

x T	0.1% 7 K	0.1% 300 K	0.2% 7 K	0.2% 300 K	0.9% 7 K	0.9% 300 K	2.0% 7 K	2.0% 300 K
$\hbar\omega_{TO,1}$	2.27	11.5	2.63	11.5	6.01	12.1	8.51	13.0
$\hbar\omega_{LO,1}$	21.2	21.2	21.2	21.2	21.2	21.2	21.2	21.2
α_1	0.021	0.013	0.021	0.013	0.017	0.013	0.017	0.013
$\hbar\omega_{TO,2}$	21.2	21.8	21.2	21.8	21.2	21.8	21.2	21.8
$\hbar\omega_{LO,2}$	58.4	58.4	58.4	58.4	58.4	58.4	58.4	58.4
α_2	0.457	0.414	0.457	0.414	0.452	0.414	0.447	0.409
$\hbar\omega_{TO,3}$	67.6	67.1	67.6	67.1	67.6	67.1	67.6	67.1
$\hbar\omega_{LO,3}$	98.7	98.7	98.7	98.7	98.7	98.7	98.7	98.7
α_3	1.582	1.582	1.582	1.580	1.576	1.578	1.570	1.574
α_{eff}	2.06	2.01	2.06	2.01	2.05	2.01	2.03	2.01

The anisotropy of the electronic effective mass of the conduction band can be approximately taken into account in the following way. We use the averaged inverse band mass

$$\frac{1}{\bar{m}_b} = \frac{1}{3}\left(\frac{1}{m_x} + \frac{1}{m_y} + \frac{1}{m_z}\right) \tag{2.26}$$

and the density-of-states band mass

$$m_D = \left(m_x m_y m_z\right)^{1/3}. \tag{2.27}$$

This mass appears in the prefactor of the linear term of the specific heat. Comparing the experimental specific heat [54, 55] with the optical mass at 7 K (section 2.7.2) reveals the mass ratio of the heavy and light bands to be about 27. Eq. 2.26 replaces the bare mass m_b in the expressions of the optical conductivity. The band degeneracy is taken into account through the degeneracy factor equal to 3. As a particular result, a reduction of the polaron optical conductivity band due to screening is less significant with the band degeneracy than without the band degeneracy.

To calculate the optical conductivity of Nb doped SrTiO$_3$ within the framework of a gas of large polarons, we follow the procedure as outlined in Ref. [78]. The experimental parameters characterizing SrTi$_{1-x}$Nb$_x$O$_3$ that are necessary for the calculation are: the LO- and TO-phonon frequencies, the bare electron band mass, the electronic dielectric constant $\varepsilon_\infty \approx 5.4$, and the actual electron densities of the Nb doped SrTiO$_3$ samples considered in the experiments. The TO-phonon frequencies are determined in section 2.8.1, the LO phonon frequencies are taken from Ref. [13]. The averaged band mass (Eq. 2.26) is $\bar{m}_b = 0.81 m_e$. Using the before mentioned ratio of the heavy mass (m_z) to the light mass ($m_x = m_y$) $m_z/m_x = 27$ we find the density-of states band mass $m_D \approx 1.65 m_e$. The electron densities are based on the unit cell volume (59.5 Å^3) and the chemical composition (x is the doping level), determined from Hall effects measurements.

Following the procedure as described above using the mentioned material parameters, we obtain the theoretical large-polaron optical conductivity spectra of SrTi$_{1-x}$Nb$_x$O$_3$ as shown in Figs. 2.29 and 2.30 at 7 K and 300 K, respectively. For comparison, each graph also contains the experimental optical conductivity. *It should be stressed that in the present calculation, there is no fit of material constants for the polaron contribution to* Re $\sigma(\omega)$ *at all. Even the magnitude of the optical conductivity, which is often arbitrarily scaled by many authors* [79, 80, 81, 82]*, follows from first principles.*

At 7 K, the calculated optical conductivity based on the Fröhlich model and extended for a gas of large polarons shows a very convincing agreement with the experimental data. The correspondence is especially close for the high energy part of the spectra, i.e., $\hbar\omega \gtrapprox 200$ meV. We should mention here that the many-body approach turns out to be essential and that the optical conductivity calculated for the case of a *single* large-polaron absorption [27] fails agreement with the experimental data by shape (a single peak) and intensity (3-4 times bigger than the experimental curve, e.g. for $x = 0.1\,\%$). The small deviations between the experimental and calculated curves can be due to an inaccuracy of the charge carrier concentration deduced from the Hall constants.

At 300 K, we see in Fig. 2.30(a,b,d) at least a qualitative agreement between theory and experiment. Both show a maximum of the room-temperature optical conductivity spectra around $\hbar\omega \sim 250$ meV. For the doping level $x = 0.9\,\%$, there is some underestimation of the magnitude of the calculated optical conductivity spectrum with respect to the experimental data, as also observed at 7 K.

Many-body effects substantially influence the optical conductivity spectra of the polaron gas. First, features related to the emission of a plasmon together with a LO phonon [73] are clearly manifested in the optical conductivity spectra of the many-polaron gas at $T = 7$ K as distinctive peaks whose positions shift to higher energies with an increasing doping level. At room temperature, those peaks are strongly broadened and smoothed, and therefore hardly visible. Second, at

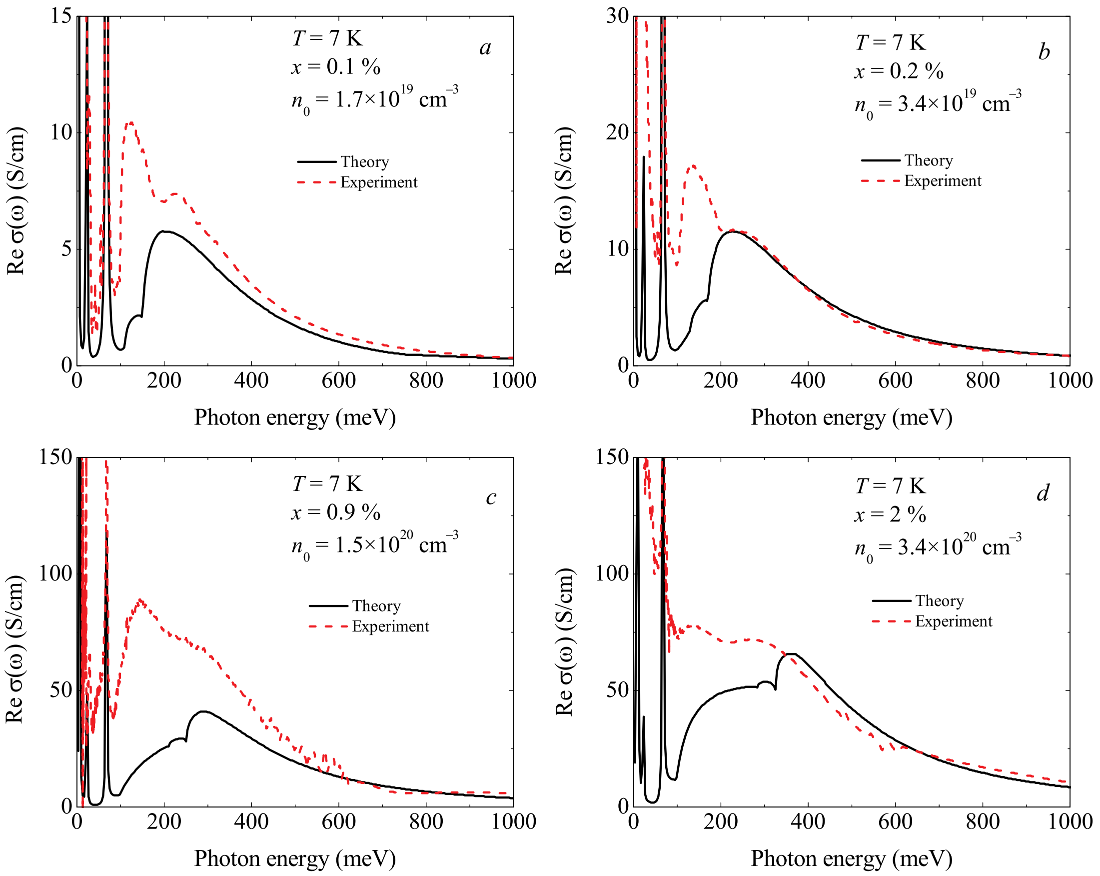

Figure 2.29: The many-large-polaron optical conductivity compared with the experiment (Fig. 2.16) at $T = 7$ K. The doping level is $x = 0.1\%$ (a), 0.2% (b), 0.9% (c) and 2% (d).

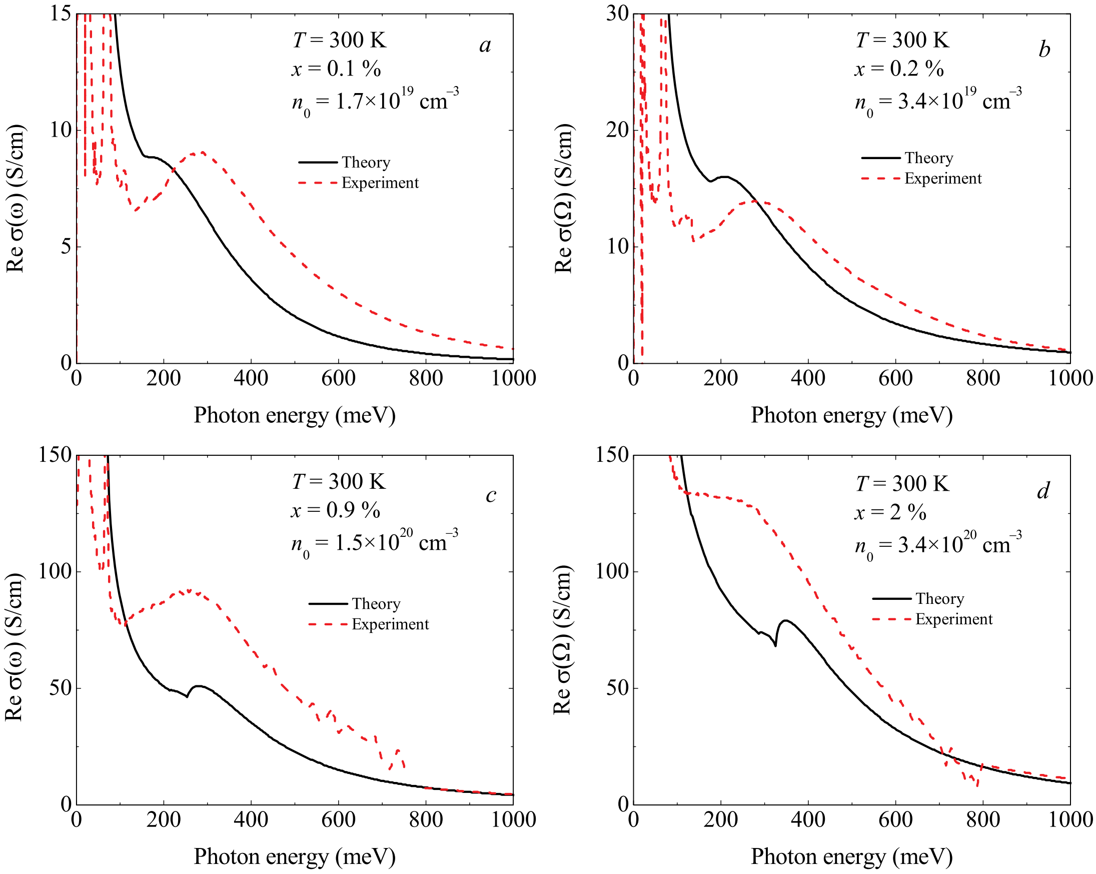

Figure 2.30: The many-large-polaron optical conductivity compared with the experiment (Fig 2.16) at $T = 300$ K. The doping level is $x = 0.1\%$ (a), 0.2% (b), 0.9% (c) and 2% (d).

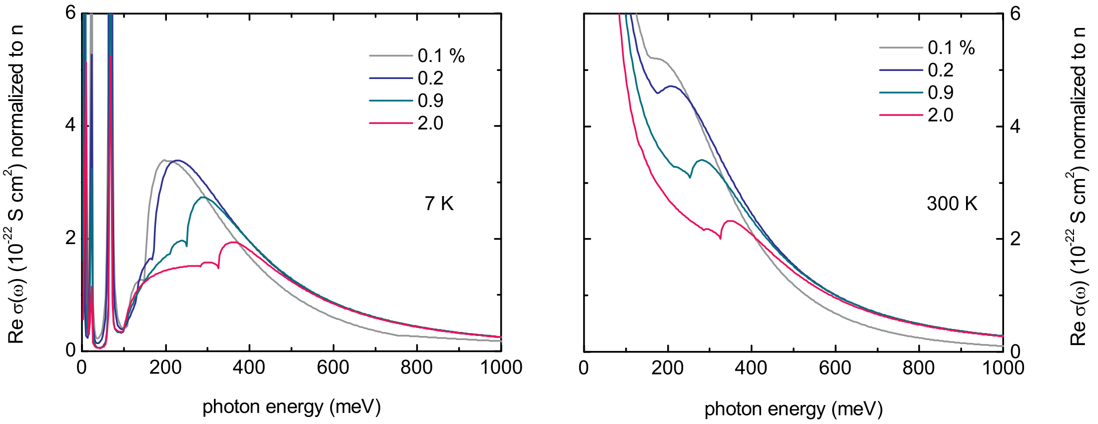

Figure 2.31: The calculated many-large-polaron optical conductivity at $T = 7$ K and $T = 300$ K divided by the charge carrier density x for doping levels 0.1%, 0.2%, 0.9% and 2%.

sufficiently high densities $n_0 \sim 10^{20}$ cm^{-3}, the many-polaron optical conductivity per particle is strongly (by about an order) reduced compared to the single-polaron optical conductivity. The reduction of the polaron optical conductivity band can be interpreted as a weakening of an effective electron-phonon coupling due to many-body effects (cf. Fig. 2.31).

The large-polaron theory of the optical absorption convincingly explains the main properties of the observed spectra of SrTi$_{1-x}$Nb$_x$O$_3$, including doping and and temperature dependence without the use of any adjustable parameter. Previous theoretical calculations of the (large) polaron optical conductivity always include a flexible parameter, as to adjust the intensity of the conductivity [79, 80, 81, 82]. However, some features of the experimental spectra remain to be explained. In particular, at $T = 7$ K, there is a distinctive peak at $\hbar\omega \sim 130$ meV in the experimental optical conductivity. In the theoretical spectra, there are peaks of smaller magnitudes at the same position. In the large-polaron theory, those peaks are provided by the interaction between electrons and the LO-phonon branch with the energy $\hbar\omega_{LO,2} \approx 58.4$ meV, accompanied by an emission of a plasmon as described in Ref. [73]. The magnitude of the aforementioned pronounced experimentally observed peak is substantially higher than described by the large-polaron theory. It thus appears to be so that upon approaching the zero density limit, the experimental data resemble more rapidly the single polaron limit [27] than the utilized theoretical model.

2.10 Conclusions

We have studied the optical and transport properties of Nb doped SrTiO$_3$ in the range $0.001 \leqslant x \leqslant 0.020$ for temperatures between 7 K and 300 K and for photon energies 0.3 meV $< \hbar\omega < 7\,\mathrm{eV}$ and interpreted them with the support of LDA and tight-binding band structure calculations. We observe an unusually narrow Drude peak in electron doped SrTiO$_3$ at 7 K for charge carrier concentrations between 0.1% and 2% per unit cell, which is less than 1 meV for the lowest dopings. The suppression of the Drude spectral weight reveals a mass enhancement which slightly decreases with doping from 2.5 to 1.5, caused by the electron-phonon coupling. The missing spectral weight is recovered in a series mid-infrared side-bands resulting from the electron-phonon coupling interaction, traditionally associated with the polaronic nature of the charge carriers. The low temperature optical effective mass yields an intermediate electron-phonon coupling strength, $2.5 < \alpha < 4$, thus suggesting that the charge transport in electron doped SrTiO$_3$ is carried by large polarons. This renormalization is in agreement with specific heat and thermopower measurements.

The experimental optical conductivity data are interpreted in terms of a gas of large polarons. The theoretical approach takes into account many-body effects, the electron-phonon interaction with multiple LO-phonon branches, and the degeneracy and the anisotropy of the Ti t$_{2g}$ conduction band. Based on the Fröhlich interaction, the many-body large-polaron theory provides an interpretation for the essential characteristics – except for the large intensity of a peak at $\sim$ 130 meV – of the observed optical conductivity spectra of SrTi$_{1-x}$Nb$_x$O$_3$ *without* any adjustment of material parameters.

As a function of temperature, for all doping concentrations, the mid-infrared spectral weight increases and the Drude weight decreases. The total spectral weight also marginally decreases which is very comparable with the decreasing carrier density measured by the DC Hall effect. The optical spectral weight analysis reveals an unusual mass *enhancement* with temperature which decreases with doping. A possible crossover from a low temperature situation with large polarons to a high temperature case with small polarons has been suggested. This mass enhancement together with the decreasing mobility, the decreasing scattering length and the T^2 behavior of the DC resistivity all support the crossover from a low temperature polaron liquid to a high temperature polaron gas.

Bibliography

[1] A. Lanzara *et al.*, Nature **412**, 510 (2001).

[2] A.S. Alexandrov, J. Phys.: Condens. Matter **19**, 125216 (2007).

[3] H.Y. Hwang, S.-W. Cheong, P.G. Radaelli, M. Marezio and B. Batlogg, Phys. Rev. Lett. **75**, 914 (1995).

[4] N. Mannella *et al.*, Nature **438**, 474 (2005).

[5] J.G. Bednorz and K.A. Müller, Rev. Mod. Phys. **60**, 585 (1988).

[6] C.S. Koonce, M.L. Cohen, J.F. Schooley, W.R. Hosler and E.R. Pfeiffer, Phys. Rev. **163**, 380 (1967).

[7] A.S. Barker Jr., *Optical Properties and Electronic Structure of Metals and Alloys*, 452-468 (ed. F. Abelès, North-Holland, Amsterdam, 1965).

[8] W.S. Baer, Phys. Rev **144**, 734 (1966).

[9] H.G. Reik and D. Heese, J. Phys. Chem. Solids **28**, 581 (1967).

[10] P. Rochon, J.L. Brebner and D. Matz, Solid State Comm. **29**, 63 (1979).

[11] J.L. Brebner, S. Jandl and Y. Lépine, Phys. Rev. B **23**, 3816 (1981).

[12] D.M. Eagles, *Physics of Disordered Materials*, edited by D. Adler, Plenium, New York, p. 357 (1985).

[13] F. Gervais, J.-L. Servoin, A. Baratoff, J.G. Bednorz and G. Binnig, Phys. Rev. B **47**, 8187 (1993).

[14] P. Calvani, M. Capizzi, F. Donato, S. Lupi, P. Maselli and D. Peschiaroli, Phys. Rev. B **47**, 8917 (1993).

[15] D.M. Eagles, M. Georgiev and P.C. Petrova, Phys. Rev. B **54**, 22 (1996).

[16] D.A. Crandles, Phys. Rev. B **59**, 12842 (1999).

[17] P. Calvani, Riv. Nuovo Cimento **24**, (2001).

[18] C.Z. Bi *et al.*, J. Phys.: Condens. Matter **18**, 2553 (2006).

[19] A.B. Kuzmenko, Rev. Sci. Instrum. **76**, 083108 (2005).

[20] A.B. Kuzmenko, D. van der Marel, F. Carbone and F. Marsiglio, New J. Phys. **9**, 229 (2007).

[21] J.-L. Servoin, Y. Luspin and F. Gervais, Phys. Rev. B **22**, 5501 (1980).

[22] G. Verbist, F.M. Peeters and J.T. Devreese, Ferroelectrics **130**, 27 (1992).

[23] R.P. Feynman, Phys. Rev. **97**, 660 (1955).

[24] G.D. Mahan, *Many-particle physics*, Plenum, New York, (1990).

[25] D. Emin, Phys. Rev. B **48**, 13691 (1993).

[26] E. Kartheuser, R. Evrard and J. Devreese, Phys. Rev. Lett. **22**, 94 (1969).

[27] J. Devreese, J. de Sitter and M. Goovaerts, Phys. Rev. B **5** 2367 (1972).

[28] L.F. Mattheiss, Phys. Rev. B **6**, 4740 (1972).

[29] B. Gregory, J. Arthur, and G. Seidel, Phys. Rev. B **19**, 1039 (1979).

[30] H.G. Reik, Solid State Comm. **1**, 67 (1963)

[31] S. Fratini and S. Ciuchi, Phys. Rev. B **74**, 075101 (2006).

[32] V.V. Kabanov and D.K. Ray, Phys. Rev. B **52**, 13021 (1995).

[33] S. Ciuchi, J. Lorenzana and C. Pierleoni, Phys. Rev. B **62**, 4426 (2000).

[34] L.J. van der Pauw, Philips Res. Rep. **13**, 1-9 (1958).

[35] WIEN2k, An Augmented Plane Wave + Local Orbitals Program for Calculating Crystal Properties, Karlheinz Schwarz, Techn. Universität Wien, Austria, (2001).

[36] J.P. Perdew, K. Burke and M. Ernzerhof, Phys. Rev. Lett. **77**, 3865-3868 (1996).

[37] P.A.J. Fleury, J.F. Scott and J.M. Worlock, Phys. Rev. Lett. **21**, 16 (1968).

[38] L.D. Landau, Sov. Phys. JETP, **3** 664 (1933).

[39] V.L. Gurevich, I.G. Lang and Y.A. Firsov, Sov. Phys. Solid State **4** 918 (1962).

[40] J. Tempere and J.T. Devreese, Phys. Rev. B **64**, 104504 (2001).

[41] J.T. Devreese, J. Phys.: Condensed Matter **19**, 255201 (2007).

[42] J.T. Devreese and A. Alexandrov, Rep. Prog. Phys. **72**, 066501 (2009).

[43] A.S. Alexandrov and N.F. Mott *Polarons and Bipolarons*, World Scientific, Singapore (1995).

[44] P. Calvani, Riv. Nuovo Cimento **24**, no.8 (2001).

[45] G. Iadonisi, Riv. Nuovo Cimento **7**, 1-116 (1984).

[46] H. Fröhlich *Polarons and Excitons*, ed. H. G. Kuper and G. D. Whitfield, Oliver & Boyd, Edinburgh (1962).

[47] K.A. Müller and H. Burkard, Phys. Rev. B **19**, 3593 (1976).

[48] Y. Toyozawa, *Optical Processes in Solids*, Cambridge University Press (2003).

[49] J.F. Scott, Rev. Mod. Phys **46**, 83 (1974).

[50] R. Micnas, J. Ranninger, S. Robaszkiewicz, Rev. Mod. Phys. **62**, 113 (1990).

[51] G. Binnig, A. Baratoff, H.E. Hoenig, J.G. Bednorz, Phys. Rev. Lett. **45**, 1352 (1980).

[52] A. Yamanaka, M. Kataoka, Y. Inaba, K. Inoue, B. Hehlen and E. Courtens, Europhys. Lett., **50**, 688 (2000).

[53] L.J. van der Pauw, Philips Res. Rep. **13**, 1 (1958).

[54] E. Ambler, J. H. Colwell, W. R. Hosler and J. F. Schooley, Phys. Rev. **148**, 280 (1966).

[55] N.E. Phillips, B.B. Triplett, R.D. Clear, H.E. Simon, J.K. Hulm, C.K. Jones and R. Mazelsky, Physica **55**, 571 (1971).

[56] S.I. Pekar, Sov. Phys. JETP **16**, 335 (1946).

[57] S.I. Pekar *Untersuchungen über die Elektronentheorie der Kristalle*, Akademie-Verlag, Berlin (1954).

[58] L.D. Landau and S.I. Pekar, Sov. Phys. JETP **18**, 419 (1948).

[59] H. Fröhlich, Adv. Phys. **3**, 325 (1954).

[60] H. Wu and W.Z. Shen, Appl. Phys. Lett **87**, 252906 (2005).

[61] H. Taniguchi, M. Itoh and T. Yagi, Phys. Rev. Lett **99**, 017602 (2007).

[62] T. Kolodiazhnyi, A. Petric, M. Niewczas, C. Bridges, A. Safa-Sefat and J. E. Greedan, Phys. Rev. B **68**, 085205 (2003).

[63] A. Damascelli, K. Schulte, D. van der Marel and A.A. Menovsky, Phys. Rev. B **55**, R4863 (1997).

[64] H.P.R. Frederikse, W.R. Thurber and W.R. Hosler, Phys. Rev. **134**, A442 (1964).

[65] H.P.R. Frederikse and W.R. Hosler, Phys. Rev. **161**, 822 (1967).

[66] N.W. Ashcroft and N.D. Mermin, *Solid State Physics*, Thomson Learning Inc. (1976).

[67] J.C. Slater and G.F. Koster, Phys. Rev. **94**, 1498 (1954).

[68] A. Bussmann, H. Bilz, R. Roenspiess and K. Schwarz, Ferroelectrics **25** 343 (1980).

[69] H. Bilz, A. Bussmann, G. Benedeck, H. Büttner and D. Strauch, Ferroelectrics **25** 339 (1980).

[70] D.M. Eagles, J. Phys. Chem. Solids **26**, 672 (1965).

[71] J. Hlinka, J. Petzelt, S. Kamba, D. Noujni and T. Ostapchuk, Phase Transitions **79**, 41 (2006).

[72] W. Meevasana, X.J. Zhou, B. Moritz, C-C. Chen, R.H. He, S.-I. Fujimori, D.H. Lu, S.-K. Mo, R.G. Moore, F. Baumberger, T.P. Devereaux, D. van der Marel, N. Nagaosa, J. Zaanen and Z.-X. Shen, New J. Phys. **12**, 023004 (2010).

[73] J. Tempere and J.T. Devreese, Phys. Rev. B **64**, 104504 (2001).

[74] S.N. Klimin, V.M. Fomin and J.T. Devreese, *to be published.*

[75] G. Verbist, F.M. Peeters, J.T. Devreese, Ferroelectrics **130**, 27 (1992).

[76] N. Choudhury, E.J. Walter, A.I. Kolesnikov and C.-K. Loong, Phys. Rev. B **77**, 134111 (2008).

[77] E. Kartheuser, R. Evrard and J. Devreese Phys. Rev. Lett. **22**, 94 (1969).

[78] J.T. Devreese, S.N. Klimin, J.L.M. van Mechelen and D. van der Marel, Phys. Rev. B **81**, 125119 (2010).

[79] X-X. Bi and P.C. Eklund, Phys. Rev. Lett., **70** (1993) 2625.

[80] P. Calvani, A. Paolone, P. Dore, S. Lupi, P. Maselli, P.G. Medaglia and S-W. Cheong, Phys. Rev. B, **54**, R9592 (1996).

[81] A.V. Puchkov, T. Timusk, M.A. Karlow, P.D. Han and D.A. Payne, Phys. Rev. B, **52**, R9855 (1995).

[82] H.G. Reik and R. Mühlstroh, Solid State Commun., **5**, 105 (1967).

Chapter 3

Electro-optics of $SrTiO_3$

Among the actual problems in modern physics are phase transitions that occur at zero temperature, so-called quantum phase transitions. These transitions, which can only be approached by a non-thermal parameter, are of a very different nature than the majority of physical phenomena. They are characterized by a universal behavior at all length scales and time scales and consequently scaling theories are often employed to judge about their presence. $SrTiO_3$ is an ideal candidate to study quantum criticality because of its proximity to a ferroelectric transition and the dominance of quantum fluctuations below 35 K [1]. In this chapter we present an optical study on pristine $SrTiO_3$ where we directly probe the relevant ferroelectric soft mode with an external static electric field as the tuning parameter. We use a simple harmonic oscillator model from which we can draw the potential landscape of the Ti atom in the three principal crystallographic directions. After the classical understanding of the problem, we touch the quantum critical aspect and show indications of universal behavior below 20 K.

3.1 Introduction to the theory of ferroelectricity

A ferroelectric is a material that without externally applied field has a permanent dipole moment giving rise to a permanent electric polarization. A true ferroelectric is characterized by a reversible swapping between two or more metastable states of different polarization using an electric field. The fact that an electric field influences the polarization can be seen from the material equations Eq. 1.6, where the macroscopic polarization $\mathbf{P}$ can be written as the sum of N molecular polarizations $\mathbf{p}$ defined by

$$\mathbf{P} = \sum_{N} \mathbf{p} \qquad \text{with} \qquad \mathbf{p} = \sum_{i} Q_i \mathbf{R}_i, \tag{3.1}$$

where Q_i is the point charge of atom i at position R_i.

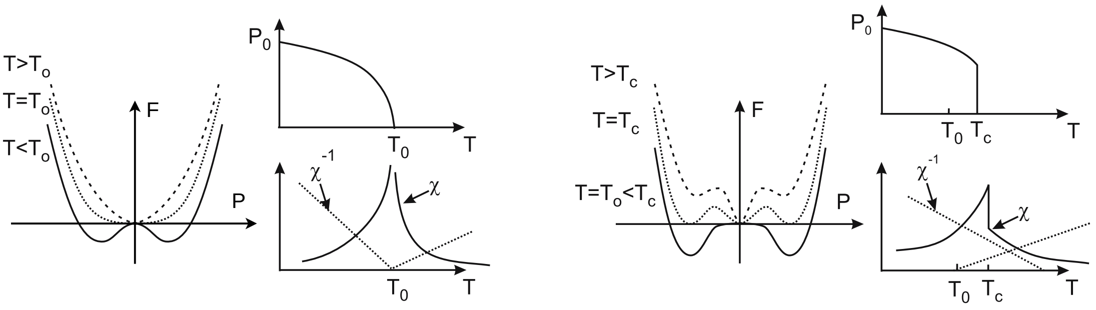

(a) (b)

Figure 3.1: Free energy $\mathcal{F}$ as a function of polarization P and temperature showing (a) a second-order phase transition where the polarization of the system continuously changes, and (b) a first-order phase transition where the polarization of the system abruptly changes below T_c, from Ref. [3].

A paraelectric material can become ferroelectric below a critical temperature which results from the competition between cooperative long-range forces which try to order the system and short-ranged fluctuations which favor disruption of the order [2]. Below this Curie temperature T_c, thermal fluctuations are frozen in and the system orders. If T_c is low other fluctuations come into play, so-called *quantum fluctuations* and it is not guaranteed that the long-range forces win from these zero-point motion fluctuations.

Ferroelectrics are traditionally described by the phenomenological Landau-Devonshire theory which expresses the system's free energy $\mathcal{F}$ as a function of the temperature T, the polarization P (three components), the electric field E, the strain η and the stress σ (six components) [3]. A fundamental postulate of thermodynamics is that away from the phase transition the free energy can be expanded in powers of the fields (like E and σ). The second important thermodynamic principle is that the values of the fields in thermal equilibrium are obtained at the minimum of the free energy. As an example we take the case where we expand the free energy in terms of a single component of the polarization and ignore the strain field, which might be appropriate for a uniaxial ferroelectric. Zero energy is obtained for a free unpolarized, unstrained crystal. The free energy density in the presence of an electric field E reads then

$$\mathcal{F}_P = \frac{1}{2}aP^2 + \frac{1}{4}bP^4 + \frac{1}{6}cP^6 + \ldots - EP. \tag{3.2}$$

where a, b and c are constants that determine the nature of the transition as will be discussed shortly. The equilibrium configuration is determined by finding the minima of $\mathcal{F}_P$ with respect to P, which gives

$$\frac{\partial \mathcal{F}}{\partial P} = aP + bP^3 + cP^4 - E = 0. \tag{3.3}$$

Since above the transition all coefficients are greater than zero, only the quadratic term in Eq. 3.2 is enough to describe the free energy and we obtain an expression for the susceptibility χ

$$\chi = \frac{P}{E} = \frac{1}{a}. \tag{3.4}$$

On crossing the transition a changes sign. The transition is characterized by an order parameter, here the polarization, which is a thermodynamic quantity that is zero in one phase (the disordered) and non-zero and non-unique in the other (the ordered) phase. We consider two different cases (i) $b > 0$ and (ii) $b < 0$, both with $c > 0$. The first case gives rise to a second-order transition at $T = T_c$ and the free energy evolves continuously with decreasing temperature from a paraelectric state of zero polarization above T_c to a ferroelectric state with $P = \pm P_0$ (see Fig. 3.1a). For the second case with $b < 0$ the free energy has already a minimum at zero polarization above T_c. On decreasing temperature two other minima develop at non-zero polarizations which become lower than the initial one for $T < T_c$. The polarization thus discontinuously changes at the transition to a finite value (Fig. 3.1b). At first-order transitions the two phases co-exist at the transition temperature, whereas at continuous transitions the two phases do not. The Landau-Devonshire theory further predicts the order parameter P and the soft mode frequency ω_0 to vary as

$$P = P_0 \left|T_c - T\right|^{\beta} \qquad\qquad \omega_0 = \Omega_0 \left|T_c - T\right|^{\beta} \tag{3.5}$$

where $\beta = \frac{1}{2}$ within a mean-field approach, as assumed to hold for ferroelectrics where forces are largely Coulomb-like and thus long-ranged[1].[6]

An important feature of ferroelectric materials is their great sensitivity to elastic stress. A cubic crystal for instance that undergoes a ferroelectric phase transition to a state where the polarization points along one of the six orthogonal cubic directions is no longer expected to remain cubic, but rather develops a tetragonal distortion due to the tetragonal strain. In the Landau theory the free energy expansion for η can be written as

$$\mathcal{F}_{\eta} = \frac{1}{2}K\eta^2 + L\eta P^2 + \ldots - \eta\sigma, \tag{3.6}$$

where the first term represents Hooke's law and the second term is the coupling between elastic strain and the polarization. The strain in a solid is measured by how the displacement $\mathbf{u}$ of a point in the solid varies with position $\mathbf{r}$.

In real materials the macroscopic polarization is due to a displacement of positive charge relative to negative charge which leaves the surface with an uncompensated charge density. This means that the surface charges themselves generate electric fields, the depolarization field. The response of the material to

---

[1] Strictly speaking, the mean-field approximation assumes that the force between particles is independent of distance r, although the Coulomb force does vary like $1/r$. [6]

this field is to form domains which are oriented such as to minimize the system's energy. In a thin film the orientation of the domains will thus be in-plane, whereas for a thick bulk crystal domains will be introduced which have the polarization always oriented parallel to the surfaces.

Soft mode theory

A structural phase transition is accompanied by a lattice instability of one of the three different types of lattice deformations: zone-center acoustic modes, zone-center optical modes and zone-boundary modes. The stability of a system is guaranteed as long as the frequency of the modes is real and finite, but ceases when any mode decreases and eventually approaches zero. At this point, once the atoms are displaced there is no restoring force to return them to their original equilibrium positions and they obtain thus a new equilibrium position determined by the symmetry of the mode, and the structure of the crystal changes [2]. Around the 1960s Cochran [4] found that ferroelectric transitions are driven by an instability of the crystal lattice against a soft optical phonon mode due to the anharmonic lattice potential. The softening of the mode is caused by the competition of short-range and long-range Coulomb forces and can be influenced by tuning parameters such as pressure, composition, temperature and external fields. The transition in high T_c materials is governed by thermal fluctuations, and the dielectric susceptibility χ follows a Curie-Weiss behavior,

$$\chi = \frac{C}{T - T_c}, \tag{3.7}$$

where C is a constant. From the Drude-Lorentz relation (Eq. 1.19) in the long wavelength limit and for zero damping we obtain a relationship between the soft mode frequency ω_0 and the dielectric susceptibility,

$$\epsilon = \chi + 1 \approx \frac{\omega_p^2}{\omega_0^2}, \tag{3.8}$$

which is valid since the static dielectric constant $\epsilon_0 \gg \epsilon_\infty$. For low T_c materials, quantum fluctuations stabilize the system and the soft mode saturates at a given frequency, as observed in KTaO$_3$ and SrTiO$_3$ [1]. These systems are barely stable against their ferroelectric soft modes at 0 K and are thus referred to as *incipient ferroelectrics*. At high temperatures the dielectric susceptibility is still described by the Curie-Weiss law (Eq. 3.7) which of course fails to describe the saturation of ϵ_1. Below the temperature T_1 where quantum fluctuations becomes discernible, ϵ_1 can be well described by the Barrett formula [5] which stems from a model based on a mean-field quantum-statistical ensemble of anharmonic oscillators,

$$\epsilon_1(T) = A + \frac{B}{\frac{1}{2}T_1 \coth\left(\frac{1}{2}T_1/T\right) - T_c^{cl}}, \tag{3.9}$$

where kT_1 is the energy of the lowest quantum level of an ion moving in an anharmonic lattice potential, and T_c^{cl} is the classical Curie-Weiss temperature. Consequently the theory predicts that $\epsilon_1(T)$ is constant for $T < T_1$, as experimentally observed for the above mentioned perovskites. Materials with a large and temperature independent ϵ_1 at low temperatures are called *quantum paraelectrics* [1]. The large ϵ_1 implies by the fluctuation-dissipation theorem large ferroelectric (soft-mode) fluctuations of wave vector $q = 0$ which are quantum mechanically stabilized in the paraelectric state [2]. With the use of Eq. 3.8 one can formulate the Barrett formula for the soft mode frequency, which can then be transformed into the generalized quantum Curie-Weiss law [7]

$$\omega_0(T) = \left| A \left[\frac{T_1}{2} \coth\left(\frac{T_1}{2T}\right) - T_c^{cl} \right] \right|^{\gamma/2} \tag{3.10}$$

where

$$\omega_0(T_c^q) = 0, \qquad T_c^{cl} = \frac{T_1}{2} \coth\left(\frac{T_1}{2T_c^q}\right), \tag{3.11}$$

with γ the critical exponent which is 1 for classical Landau-type behavior and 2 for quantum critical behavior. In the latter case $\gamma = \nu z$, where ν is the correlation length critical exponent and z the dynamical critical exponent.[8]

The paraelectric-ferroelectric transition can be either *displacive* or *order-disorder*. The first category calls transitions where the lattice displacements corresponding to the electronic polarization are equally uniform, and zero above T_c. The second can be compared to local moment magnetism where the local moment still persists above the transition temperature, although the order is destroyed. The spontaneous development of a ferroelectric moment is always associated with an atomic displacement and thus a broken-symmetry. It is often pictured as an essentially rigid displacement of charge, which is not entirely true since ferroelectricity arises from interactions in the electron system.[3] The electronic rigidity for an optical mode is equal to the transverse electric charge Z_T, which measures the average electrical dipole moment p per unit cell generated by the corresponding relative ionic displacement u,

$$p = Z_T \, q \, u, \tag{3.12}$$

where q is the electron charge.[3] If a phonon becomes entirely soft, it acquires a frozen displacement u_0, and $Z_T q u_0$ gives (to linear order) the ferroelectric moment per unit cell. Values of Z_T which are well beyond the rigid ion value indicate a largely delocalized electron cloud, eventually leading to an insulator-to-metal transition.[3]

3.2 Introduction to quantum critical phenomena

We give here a short introduction on quantum critical phenomena, which is principally based on Ref. [8] for systems near a continuous phase transition. While the thermodynamic average of the order parameter is zero in the disordered phase, its fluctuations are non-zero. When the critical point is approached, the spatial correlations of the order parameter fluctuations become long-ranged. Close to the critical point their typical length scale, the correlation length, ξ, diverges as

$$\xi \propto |t|^{-\nu} \tag{3.13}$$

where ν is the correlation length critical exponent and t is some dimensionless measure of the distance from the critical point. If the transition occurs at a non-zero temperature T_c, it can be defined as $t = |T - T_c|/T_c$. In addition to the long-range correlations in space there are analogous long-range correlations of the order parameter fluctuations in time. The typical timescale for a decay of the fluctuations is the correlation (or equilibration) time, τ_c. As the critical point is approached the correlation time diverges as

$$\tau_c \propto \xi^z \propto |t|^{-\nu z}, \tag{3.14}$$

where z is the dynamic critical exponent. Close to the critical point there is no characteristic length scale other than ξ and no characteristic timescale other than τ_c. At the phase transition point the correlation length and time are infinite, fluctuations occur on all length scales and time scales and the system is said to be scale invariant. As a consequence, all observables depend via power laws on the external parameters. If we observe the system at a scale x or λx, scale invariance states that the correlation functions are described by the same function F, apart from an overall constant, indicating that $F(\lambda x) = cF(x)$. Functions with this property are power laws, $F(x) = ax^\eta$.

As the transition point is approached the time scale τ_c diverges and consequently the corresponding frequency scale ω_c goes to zero, and thus also the energy scale

$$\hbar\omega_c \propto |t|^{\nu z}. \tag{3.15}$$

At finite temperature this has to be compared with the energy scale of the thermal fluctuations, k_BT. For a quantum mechanical system the character of the order parameter fluctuations crosses over from quantum to classical when $\hbar\omega_c$ becomes smaller then k_BT, indicating that classical thermal fluctuations are dominant. Therefore, close enough to the critical point any quantum mechanical system at finite temperature can be described with a classical (field) theory, see Fig. 3.2. Consequently, if we probe the system on a timescale larger than $1/\tau$ (or with a frequency $\hbar\omega < k_BT$) we are in the classical regime.

Now, for any transition occurring at some finite temperature T_c, quantum mechanics will become unimportant for $|t| < T_c^{1/\nu z}$; in other words, the critical behavior asymptotically close to the transition is entirely classical. This justifies calling all finite-temperature phase transitions ‘classical’. Quantum mechanics can still be important on microscopic scales, but classical thermal fluctuations

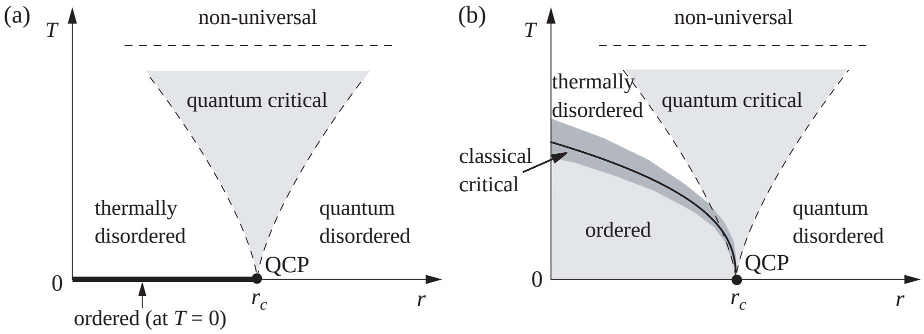

Figure 3.2: Two possible phase diagrams of the temperature vs. control parameter r in the vicinity of a QCP. (a) Order is only present at zero temperature. (b) Order can also exist at finite temperature. The solid line marks the finite-temperature boundary between the ordered and disordered phases. Close to this line, the critical behavior is classical, from Ref. [8].

dominate on the macroscopic scales that control the critical behavior. If, however, the transition occurs at zero temperature as a function of a non-thermal parameter, r, like pressure or magnetic field, the behavior is always dominated by quantum fluctuations. Consequently, transitions at zero temperature are called 'quantum' phase transitions.

3.3 Tuning $SrTiO_3$ towards ferroelectricity

Materials which naturally are on the verge to become ordered, magnetically or electrically for instance, can sometimes be pushed into the ordered state by using some non-thermal control parameter like pressure, chemical substitution, or a field, as mentioned before. A recent study reports on the metallic ruthenate $Sr_3Ru_2O_7$ which shows a metamagnetic transition with applied magnetic field around 8 T towards an ordered state.[9] Among the ABO_3 perovskites, $SrTiO_3$ is in the closest proximity to a ferroelectric phase transition as demonstrated by its huge static dielectric constant which typically attains 10^4 at liquid helium temperatures. It has been shown that both oxygen isotope substitution [10] and epitaxial strain [11] turn $SrTiO_3$ to a true ferroelectric. First principles theory [12] has demonstrated that this is due to the hybridization between the O $2p$ and Ti $3d$ orbitals in the Ti-O chain.[2] For $SrTi^{18}O_3$ Raman spectra show the presence of a quantum critical point (QCP) together with a phase separation nearby [13]. For both tensile strain and compressive strain in $SrTiO_3$ a ferroelectric phase has

---

[2] This is reflected in the Born effective charges (Eq. 3.12) of the individual atoms, which are anomalous at zero electric field and show a strong dependence on strain. Both compressive and tensile strain increases the effective charge on the Ti atom and decreases by almost the same amount on the O atoms.[12]

been predicted, although the phase transition happens at smaller values of the former compared to the latter [12, 11]. Measurements of the dielectric constant at 10 GHz confirm this prediction by showing ferroelectricity for $SrTiO_3$ on $DyScO_3$ ($a = 3.944\,\text{Å}$), and not for $SrTiO_3$ on LSAT ($a = 3.869\,\text{Å}$).[11] Hydrostatic pressure, on the contrary, drives both $SrTi^{16}O_3$ [14] and $SrTi^{18}O_3$ [15] away from the ferroelectric state, for pressures values below 1.6 GPa and 100 kPa, respectively.

The disadvantage of control parameters like isotope substitution is that disorder is introduced in the system – which is also true for thin films – to which quantum critical phenomena are very sensitive. A pure single crystal which consists of a single domain and is freely suspended without external strain is thus preferred. Ferroelectric phase transitions in the class of titanium perovskites are of the displacive type which makes it logical to expect a shift of the position of the Ti atom relative to the surrounding oxygens with an applied electric field. If the induced displacement is large enough, the crystal may eventually show a transition towards a (meta)ferroelectric state, and any deformation of the unit cell is only due to this transition. Since the mid-1950s the effect of an electric field on the static and dynamic properties of $SrTiO_3$ has been investigated with various techniques, like quasi-dc capacitance measurements [16, 17, 18, 19, 20], Raman spectroscopy [21], and mechanical strain measurements [22, 23, 24]. It should be mentioned that the ferroelectric soft mode is Raman inactive in zero field, and a finite electric field has to be applied to break the space inversion symmetry which makes the mode Raman active. The results unanimously show an overall decrease of the dielectric constant with field and temperature, which implies via the Lyddane-Sachs-Teller relationship a hardening of the soft mode frequency. In addition, as a function of temperature, for a fixed electric field value, $\epsilon_1(T)$ shows a shallow maximum which is strongly field dependent [21, 19, 25]. It has been suggested that this maximum corresponds to the crossover from the (quantum) paraelectric to the induced ferroelectric state. The fact that ϵ_1 never diverges (and consequently ω_0 never becomes zero) has been associated with a possible coupling of the zone-center ferroelectric optical mode with a zone-boundary acoustical mode [26, 27].

It has recently been suggested that the line of relative maxima of $\epsilon_1(T)$ of $SrTiO_3$ could end in a conventional quantum critical point in case we deal with a second-order transition line [27, 28] or in a quantum critical end point similar to $Sr_3Ru_2O_7$ for a first-order phase transition (as motivated by Ref. [29]). The presence of order at finite temperatures itself further implies classical behavior in the phase space close to the transition line and quantum critical behavior at higher and lower temperatures (see Fig. 3.2b).

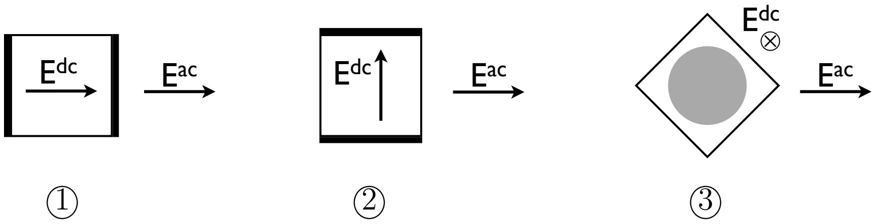

Figure 3.3: Cartoons illustrating three different experimental configurations with the orientation of the static electric field E^{dc} relative to the electric field polarization of the THz radiation, E^{ac}. The unit cells are aligned parallel to the crystal edges. ① E^{dc} is parallel to E^{ac}, both in-plane, ② E^{dc} is perpendicular to E^{ac}, both in-plane, ③ E^{dc} out-of-plane is perpendicular to E^{ac} in-plane. Black bars are solid Ag electrodes, gray surfaces are THz transparent Au electrodes.

3.4 Experiment

In the last section, previous work has been presented which reports on the electric field effect on $\mathrm{SrTiO_3}$. In order to study the soft mode behavior at a paraelectric to ferroelectric phase transition which is possibly accompanied by quantum critical effects, a measurement is required which directly measures the relevant parameter on a stress-free and pure sample. Hereto we have measured the electric field dependent transmission of pristine $\mathrm{SrTiO_3}$ for photon energies $\hbar\omega < 3.5$ meV, between 2.75 K and 60 K and for static electric fields E^{dc} up to 25 kV/cm by time-domain THz spectroscopy (see also section 1.8). As explained in detail in the next section, the ferroelectric soft mode frequency – which is the relevant parameter to look at – is directly obtained from the frequency dependent complex transmission.

It is now in order to discuss two important issues of the experiment which in previous literature have been overlooked or simply never reported. The first concerns the question whether the sample consists of one single domain or several randomly oriented domains, which is essential to orientation sensitive measurement techniques. $\mathrm{SrTiO_3}$ manifests an antiferrodistortive structural phase transition at 105 K where neighboring oxygen octahedra rotate oppositely, thereby doubling the unit cell and thus adopting the tetragonal structure. When no precaution is taken during the cool down of the sample different domains may be formed which have either the c-axis in-plane or out-of-plane. The soft mode has different frequencies in these directions ($\omega_a = 7.8$ cm^{-1}, $\omega_c = 16.5$ cm^{-1} at 7 K [30]) and probably also a different electric field effect. In order to obtain mono-domain samples one can apply a uniaxial compressive stress or pressure to the (110) faces while passing extremely slow (5 mK/min) the structural phase transition.[31, 30] It has however also been shown that crystals below ~ 0.3 mm thick always have their c-axis in-plane [32]. Due to the very large $\epsilon(\omega)$ of $\mathrm{SrTiO_3}$ in the THz range, the reflectivity is close to unity and a detectable transmission in the THz range can only be obtained for samples below 60 μm. We will show further on that all our measurements show a single domain response, probably because this thickness is well below 0.3 mm. The second issue is about the relative orientation of E^{dc} to the electric field of the probe direction which in our case is the polarization of the electric field of the THz beam, E^{ac}. We have considered different geometries as sketched in Fig. 3.3: two in-plane configurations where ① $\mathbf{E}^{\mathrm{dc}} \parallel \mathbf{E}^{\mathrm{ac}}$ with $\mathbf{E}^{\mathrm{dc}} \perp \mathbf{k}$ and ② $\mathbf{E}^{\mathrm{dc}} \perp \mathbf{E}^{\mathrm{ac}}$ with $\mathbf{E}^{\mathrm{dc}} \perp \mathbf{k}$ and one out-of plane configuration ③ with $\mathbf{E}^{\mathrm{dc}} \perp \mathbf{E}^{\mathrm{ac}}$ and $\mathbf{E}^{\mathrm{dc}} \parallel \mathbf{k}$, where $\mathbf{k}$ is the light propagation vector. Giving a look ahead on our experimental results compared to the past literature, we presume that previous work always considers the parallel configuration ①.

For the two in-plane configurations ① and ② (Fig. 3.3), silver paste electrodes (DuPont) have been painted onto two opposing sides of the sample which are 10.0 mm apart from each other. It is essential to attach the electrodes onto the sample such that the electric field inside the sample $E = V/d$, where V is the applied voltage and d the distance between the electrodes. An electric field created by distant electrodes becomes screened by the sample's depolarization field, and therefore $E = V/(\epsilon d)$, which is $\epsilon \sim 10^4$ lower. For the out-of-plane configuration ③ (Fig. 3.3) typically 5 nm thin Au electrodes[3] have been sputtered onto the two principal surfaces of a 55 μm thin sample. The resistance on a distance of 10 mm is about 500 kΩ such that the total RC time never exceeds 0.2 s. Their structure consists probably of very small gold islands just above the percolation threshold, although scanning electron microscopy (at 10 nm resolution) showed a homogeneous layer. The two electrodes have together a THz transmission of roughly 50 %.

For the in-plane experiments, the sample has been cooled down without any static electric field applied in 2 hours from room temperature down to 60 K with E^{ac} switched on. For the out-of-plane experiment, a distant electric field of 8 kV/cm parallel to the direction of E^{ac} (which was switched off) has been applied during the extremely slow cooling down: 100 hours across the structural phase transition from 115 K to 89 K and then in 24 hours down to 50 K. Rapid cooling down always caused multi-domain formation for this latter situation. It should be mentioned as an afterthought that the static electric field was probably completely screened by the depolarization field of the sample, and it was merely the gentle cooling down which made single domain formation possible.

3.5 Optical measurements and analysis

The raw THz transmission data are presented in Figs. 3.4–3.6 for the three experiment geometries. At zero applied voltage the figures 3.4 and 3.5 show a very

---

[3] The thickness of these transparent gold layers has been measured by Rutherford Backscattering Spectrometry at AMOLF (Amsterdam) thanks to J.H. Rector (Vrije Universiteit Amsterdam).

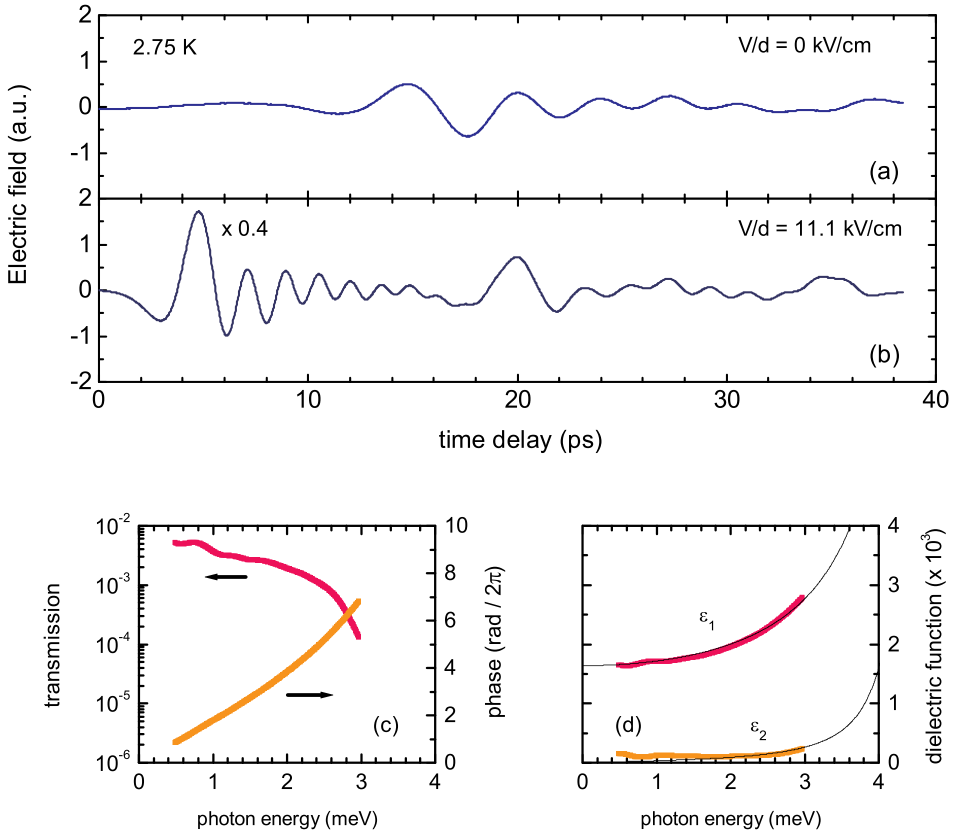

Figure 3.4: Time-domain transmission spectra for geometry ① at (a) 0 kV/cm and (b) 11.1 kV/cm. Note the first and second echo in (b) around 20 ps and 35 ps, respectively. Zero delay time has been chosen arbitrarily. (c) Fourier transformation of the straight transmission pulse at 11.1 kV/cm: transmission (red) and phase (orange). (d) Real (red) and imaginary (orange) part of the dielectric function. Black solid lines is a fit to the Drude-Lorentz model.

similar transmission signal, which is due to the straight transmission up to about 34 ps. When an external electric field is switched on, the transmission pulse shifts to earlier times and grows in intensity and for ① the first and second internal reflection become visible at 20 ps and 35 ps, respectively. For the perpendicular geometry ②, an electric field also causes a shift of the main pulse towards earlier times, but in addition a second response which is faster than the main one appears in the spectrum. Fig. 3.5b shows this second response between 2–6 ps followed by the main response starting around 8 ps. Note that the second response appears at the same time as the main pulse in geometry ①. The first internal reflection of the main response is visible around 36 ps. The transmission of geometry ③ is shown in Fig. 3.6. At zero bias the signal is very low, and grows with an electric field to a clearly recognizable peak.

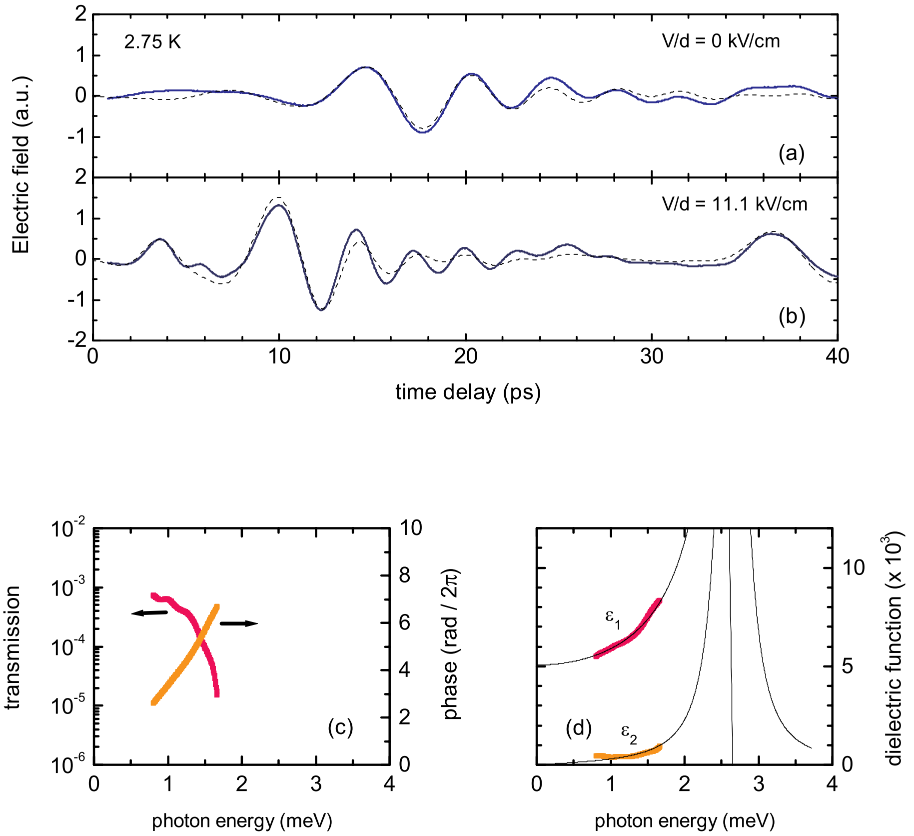

Figure 3.5: Time-domain transmission spectra for geometry ② at (a) 0 kV/cm and (b) 11.1 kV/cm. Note the first echo in (b) around 36 ps. In (b) the main transmission pulse is preceded by a faster response appearing around 2–6 ps. Zero delay time has been chosen arbitrarily. Black dashed lines are time-domain fits to a Drude-Lorentz model. (c) Fourier transformation of the slower straight transmission pulse starting from 8 ps at 11.1 kV/cm: transmission (red) and phase (orange). (d) Real (red) and imaginary part (orange) of the dielectric function. Black solid lines is a fit to a Drude-Lorentz model.

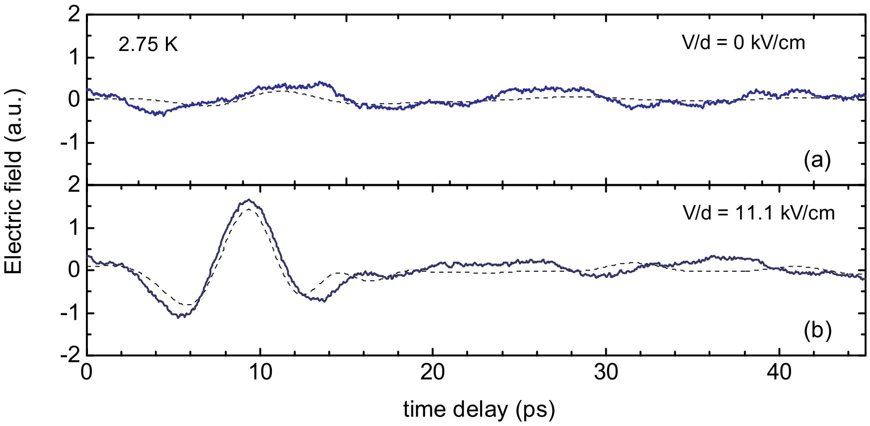

Figure 3.6: Time-domain transmission spectra for geometry ③ at (a) 0 kV/cm and (b) 11.1 kV/cm. Note the first echo in (b) around 36 ps. In (b) the main transmission pulse is preceded by a faster response appearing around 2–6 ps. Zero delay time has been chosen arbitrarily. Black dashed lines are time-domain fits to a Drude-Lorentz model.

The time-dependent transmission data have been Fourier transformed to obtain the frequency dependent transmission for each temperature and electric field value for geometry ① (see Fig. 3.4c). The frequency dependent complex transmission has been directly inverted using the iterative method as outlined in section 1.7.1 into the complex dielectric function $\epsilon(\omega)$, which has subsequently been fitted to a Drude-Lorentz model (cf. Eq. 1.19) with no Drude and 1 Lorentz oscillator corresponding to the ferroelectric soft mode (see Fig. 3.4d). Although experimental data are only available on the low energy side of the phonon frequency ω_0 (above ω_0 the transmission is below the detection limit) it can perfectly be described by a Lorentzian line shape. Measuring the complex THz transmission is thus equivalent to directly measuring the ferroelectric soft mode frequency.

The Fourier transformation of a transmission spectrum that comprises two individual responses as depicted in Fig. 3.5, does not provide any meaningful result. These spectra have thus been fitted in the time-domain to a Drude-Lorentz model which takes into account the response of 2 optically distinct domains (see Fig. 3.5b). As a verification, the slower response has separately been directly inverted (cf. section 1.7.1) into the complex dielectric function (see Fig. 3.5d). Both methods give the same result.

The faster second response for geometry ② is a strong signal which is easily recognizable in a time-domain spectrum. It is probably due to domains that have a different orientation than the main part of the sample. In that case, it is also expected that such a second response would be present in the spectra of geometry ①. However, the main pulse in the latter geometry is very strong, and the addition of 10 % of a slower signal would imply a slight distortion of the tail of the main pulse, which is hard to observe experimentally.

Due to the small signal, the data taken in experiment geometry ③ have also been fitted in the time-domain to a Drude-Lorentz model with 1 Lorentz oscillator (see Fig. 3.6).

3.6 Electric field dependence of the soft mode

Figs. 3.7 − 3.10 show the soft phonon frequency ω_0 as a function of temperature and applied dc voltage for the experimental configurations as illustrated in Fig. 3.3. As described before the soft mode frequency has been analytically deduced from the measured time-domain transmission. For the in-plane, parallel measurement configuration Fig. 3.7 shows that at 2.8 K and zero voltage, the observed mode frequency is about 17.3 cm^{-1}, which is very close to the c-axis ferroelectric soft mode frequency of 16.5 cm^{-1} as seen by hyper-Raman spectroscopy [30]. This together with the fact that we observe a mono-domain behavior lead to the conclusion that for configuration ① the c-axis is in-plane and parallel to $\mathbf{E}^{\text{ac}}$. The plasma frequency of the mode $\omega_p = 188.5$ meV is independent of electric field and temperature in the investigated ranges. The mode frequency is globally increasing with temperature and electric field, but for elevated fields a shallow minimum can be observed in $\omega_0(T)$. Notice that the range of the experimental curves is limited by the breakdown voltage. The dielectric constant and mode frequency of all previous reports [18, 21, 19, 20] strongly resemble our results of this configuration, which suggests those to concern also this in-plane, parallel geometry.

Fig. 3.8 shows the mode frequency of the in-plane, perpendicular experiment configuration, extracted from the main transmission pulse (i.e., $t > 8$ ps in Fig. 3.5b). The second response (between 2–6 ps) will be discussed below. At 2.8 K and zero field the observed frequency is again very close to $\omega_c = 16.5\,\text{cm}^{-1}$, which evinces that also for this configuration the tetragonal c-axis is oriented parallel to $\mathbf{E}^{\text{ac}}$. It is maybe because of the force exerted on the Ti atom by the electric field of the THz light $E^{\text{ac}} = 30$ V/cm that we always find $\hat{c} \parallel \mathbf{E}^{\text{ac}}$. The field effect of the mode frequency for this geometry is different from the former. There is still an overall increase with temperature and applied voltage, but the hardening as a function of the latter is much smaller. Also different is the absence of the shallow minimum in $\omega_0(T)$. Fig. 3.11 shows an overview of the mode frequency for the two in-plane measurement geometries ① and ②, where the light is always parallel to $\hat{c}$, but the direction of the applied bias voltage changes from parallel (left panel) to perpendicular (right panel).

The electric field effect on the soft mode phonon frequency in the out-of-

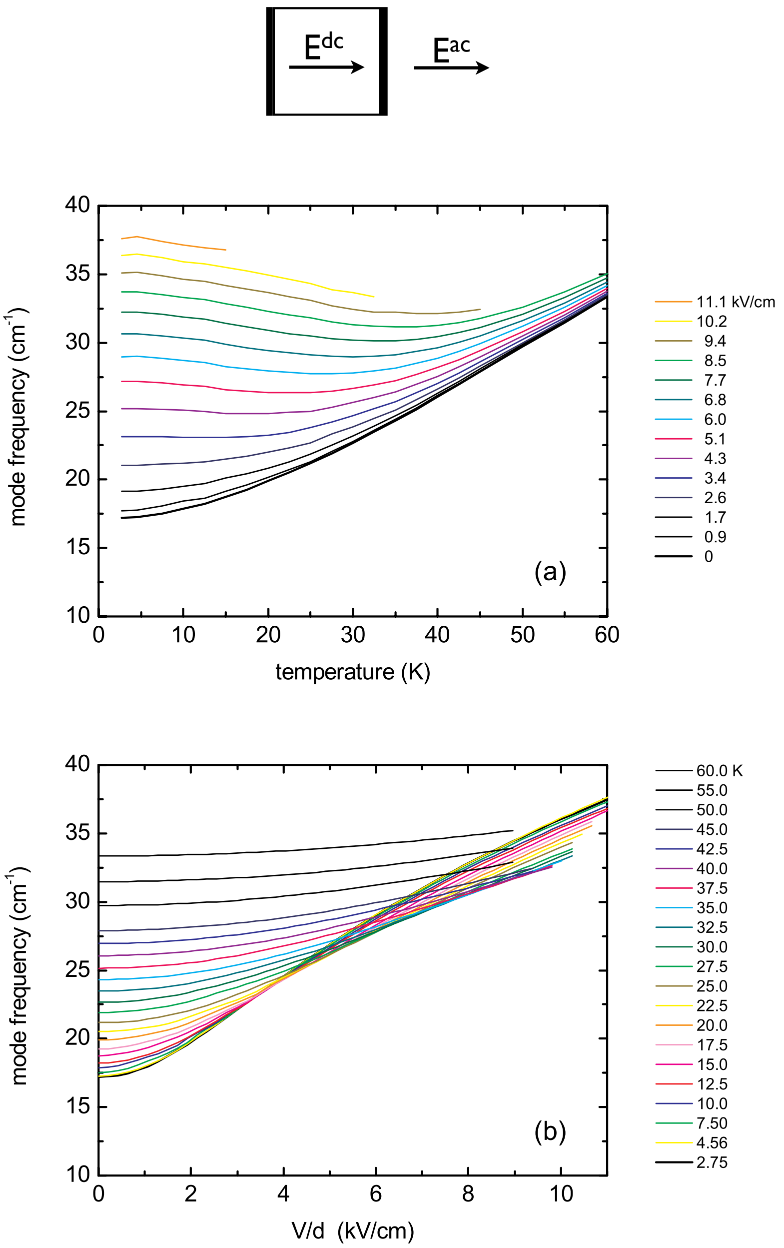

Figure 3.7: Soft mode frequency for the in-plane geometry ① of Fig. 3.3 where $\mathbf{E}^{dc} \parallel \mathbf{E}^{ac}$ with $\mathbf{E}^{dc} \perp \mathbf{k}$ (a) as a function of temperature for selected applied voltages and (b) as a function of applied voltage V for selected temperatures.

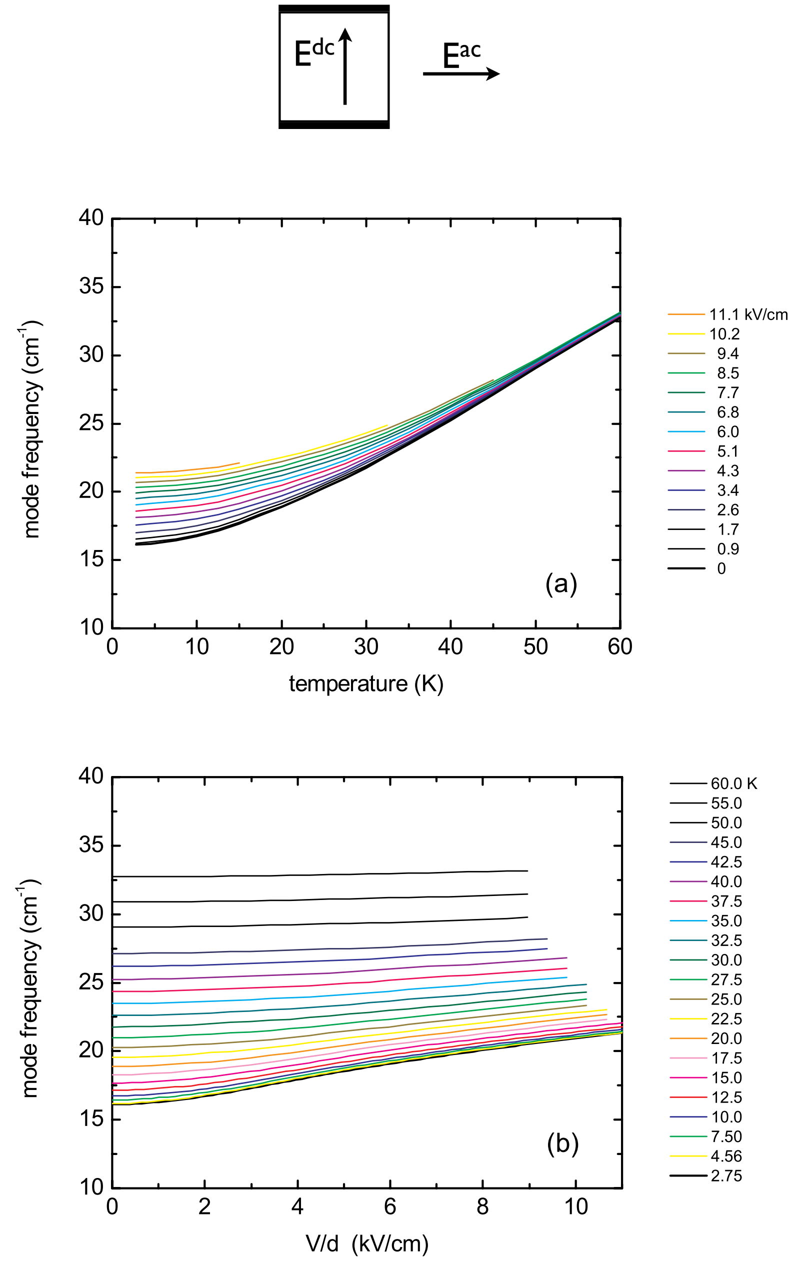

Figure 3.8: Soft mode frequency for the in-plane geometry ② of Fig. 3.3 where $\mathbf{E}^{\rm dc} \perp \mathbf{E}^{\rm ac}$ with $\mathbf{E}^{\rm dc} \perp \mathbf{k}$ (a) as a function of temperature for selected applied voltages and (b) as a function of applied voltage V for selected temperatures. The frequency is extracted from the major pulse in the time-domain (see Fig. 3.4), without the second (faster) response that appears in a limited part of phase space.

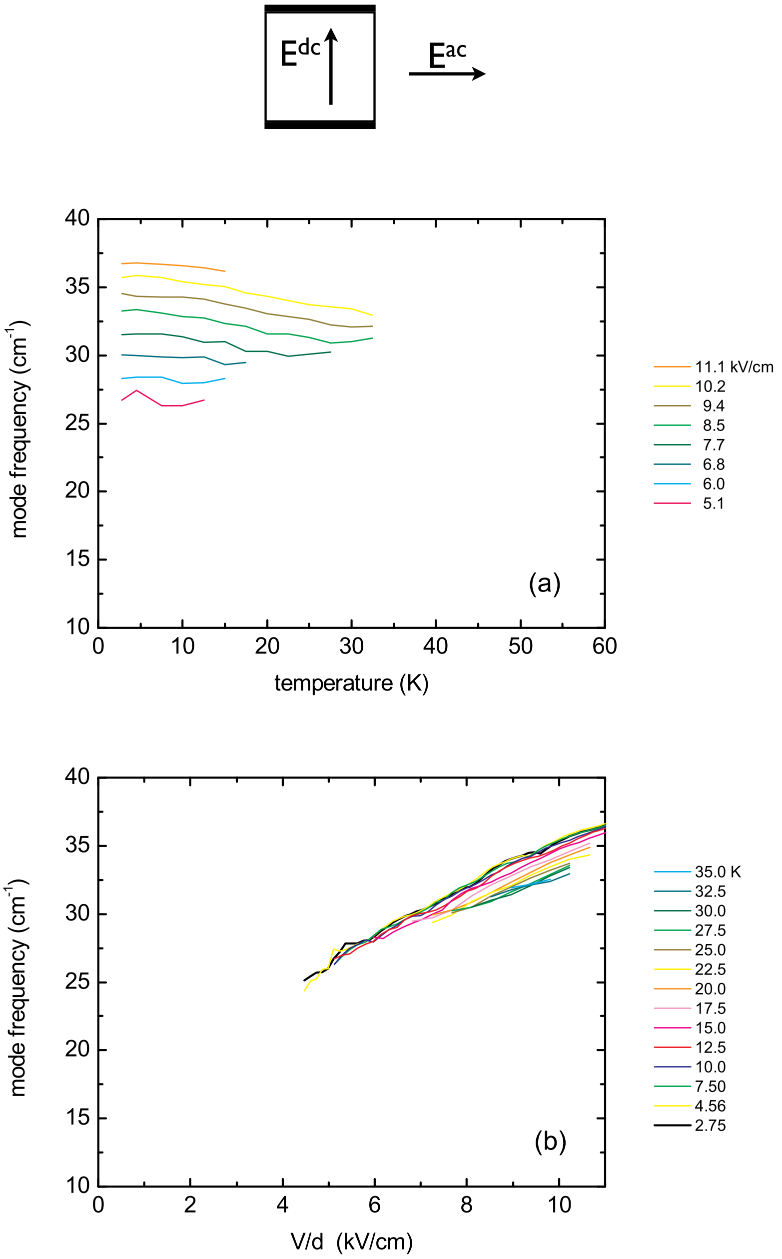

Figure 3.9: Soft mode frequency for the in-plane geometry ② of Fig. 3.3 where $\mathbf{E}^{dc} \perp \mathbf{E}^{ac}$ with $\mathbf{E}^{dc} \perp \mathbf{k}$ (a) as a function of temperature for selected applied voltages and (b) as a function of applied voltage V for selected temperatures. The frequency is extracted from solely the fast response which is present in Fig. 3.4b between 2–6 ps. This response is only visible in a very limited region of phase space.

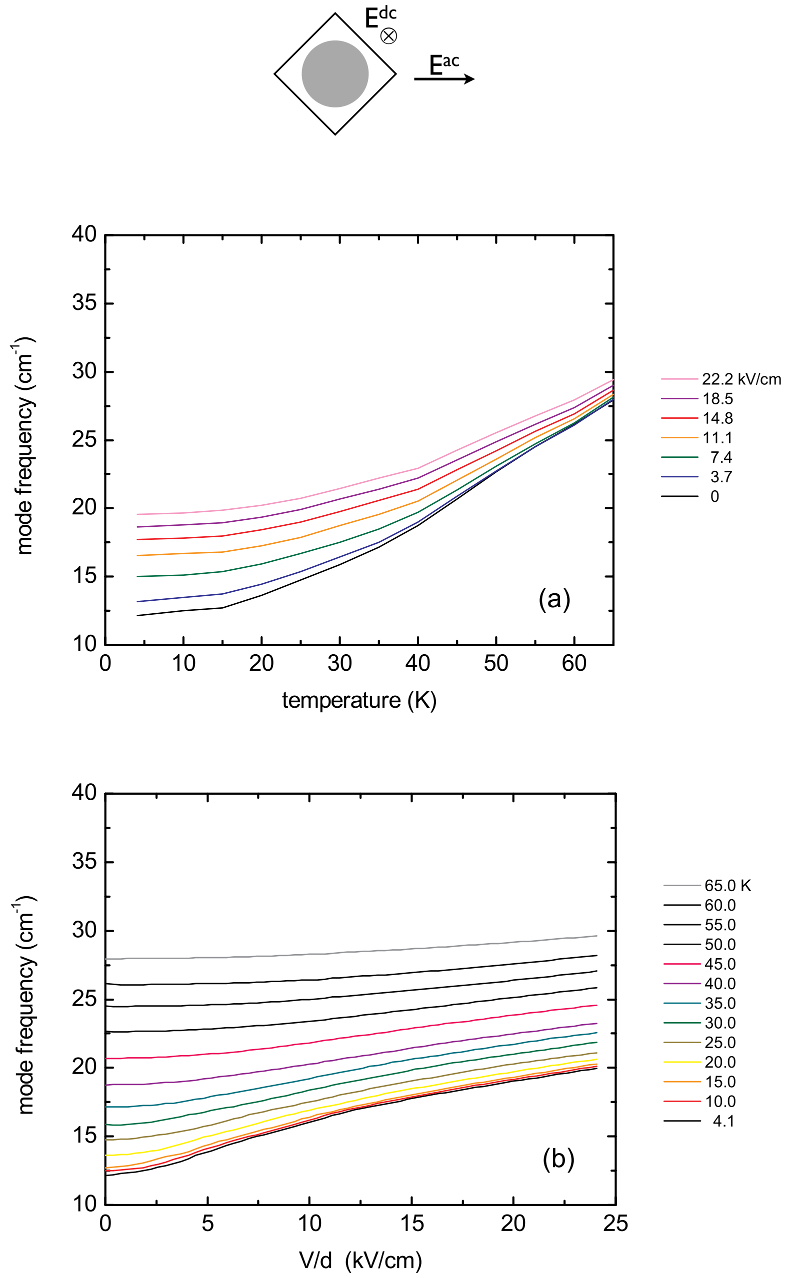

Figure 3.10: Soft mode frequency for the out-of-plane geometry ③ of Fig. 3.3 where $\mathbf{E}^{\mathrm{dc}} \perp \mathbf{E}^{\mathrm{ac}}$ and $\mathbf{E}^{\mathrm{dc}} \parallel \mathbf{k}$ (a) as a function of temperature for selected applied voltages and (b) as a function of applied voltage V for selected temperatures.

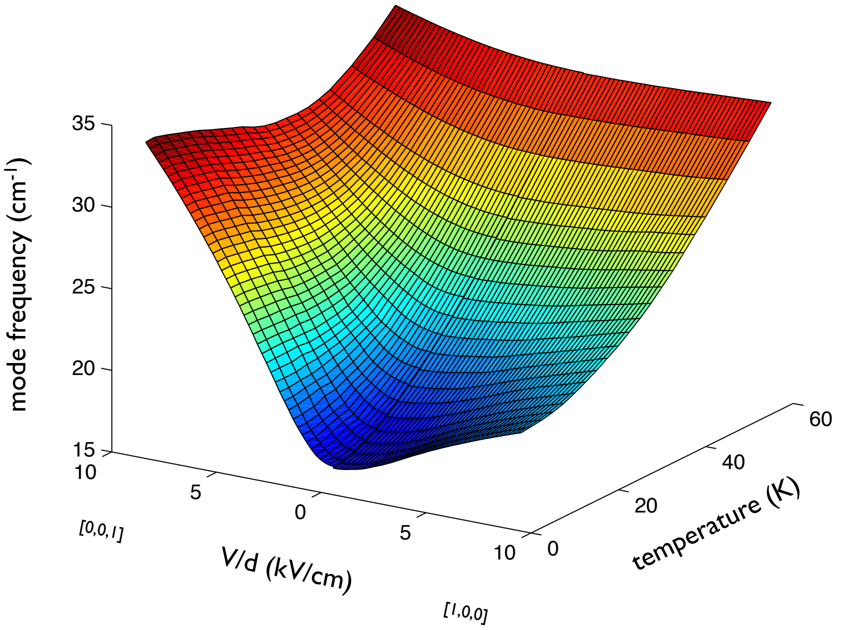

Figure 3.11: Soft mode frequency for the in-plane geometries ① along [0,0,1] and ② along [1,0,0] as a function of temperature and voltage. As will be shown further, this graph basically shows ω_c for a Ti displacement in the c-direction (left part) and in the a-direction (right part) together.

plane configuration ③ (Fig. 3.3) is depicted in Fig. 3.10. Due to the orientation of the sample edges (and thus of the alignment of the unit cells) relative to E^{ac} the c-axis can never lie parallel to it. This is directly observed from the mode frequency at 4 K and zero voltage which is about 12.2 cm^{-1}, exactly the average value of ω_a = 7.8 cm^{-1} and ω_c = 16.5 cm^{-1}. The experiment probes thus a combined response of on the one hand side the field effect in the c-direction of the in-plane, perpendicular geometry ① and on the other the field effect in the a, b-direction of the in-plane, perpendicular geometry. The fact that there is no contribution from a configuration similar to the in-plane, parallel situation can be seen from the data which resemble much more Fig. 3.8 than Fig. 3.7. The measured plasma frequency ω_p for this mode is 171 meV. For this out-of-plane geometry much larger voltages could be applied before breakdown, which occurs only above external field values of the order of 150 kV/cm.

The ferroelectric response

As said before, all measurements manifest single domain behavior, except for the in-plane, perpendicular configuration ② which shows the sudden appearance of a second response (see Fig. 3.5b between 2–6 ps) in a narrow part of the phase space. Since spectra with more than one optical response can not be Fourier transformed

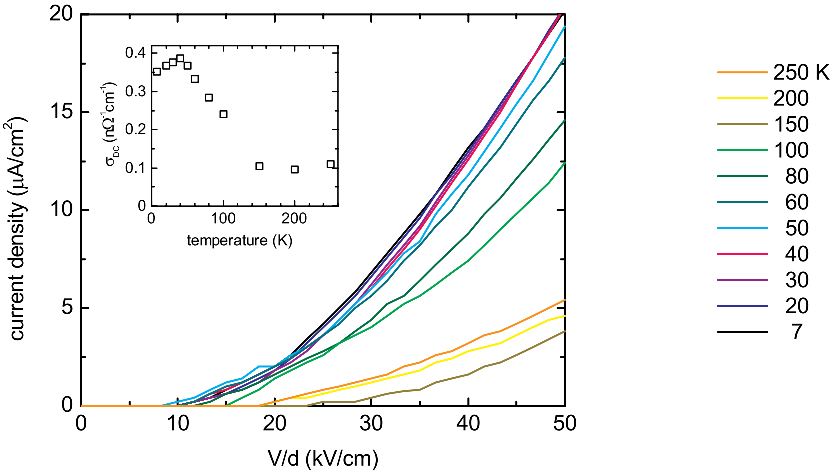

Figure 3.12: Current density J vs. the external electric field $E = V/d$ for the out-of-plane geometry ③ at selected temperatures. The inset shows $\sigma = dJ/dE$ above 38 kV/cm as a function of temperature.

nor inverted, a variational fitting routine [36] directly in the time-domain has been used which takes into account the time-domain transmission of two optically different domains, as mentioned before. Independently of the field strength and temperature, we always found 10 % (volumetric) of the second response and 90 % of the main response. The phonon frequency extracted from the second response is shown in Fig. 3.9. It resembles closely the soft mode frequency for the in-plane, parallel configuration of Fig. 3.7 in the phase space region for T smaller than the relative minimum of $\omega_0(T)$. In previous reports [17, 19, 20], this is precisely the region where remanent polarization has been observed and the phase of the material is assumed to be (induced) ferroelectric. A plausible explanation of the appearance of this faster response could be that Weiss domains are formed, which do not necessarily have their polarization oriented parallel to the applied electric field. Instead, in a ferroelectric (like for a ferromagnet) domains are oriented along the sample edges as to minimize the system's energy. The reason why we observe domains that are oriented perpendicular to the applied field in geometry ② and not in ①, is probably due to the size of the main signal in the latter geometry which is too large (caused by the lower dielectric constant) and thus completely overwhelming the 10 % of the slower response. It should be pointed out that the presence of a response that corresponds to domains of a different orientation is a strong indication of ferroelectric behavior, and thus of the presence of a phase transition from paraelectric to ferroelectric, in spite of the fact that the mode frequency never reaches zero.

3.6.1 Electrical conduction in pristine $SrTiO_3$

It is worth mentioning here that for the out-of-plane geometry large external electric fields generate an electrical current through the sample. This current is completely reversible with applied voltage and temperature and it is thus unlikely to be an onset of breakdown. Fig. 3.12 shows the current density J, which is the measured current I divided by the surface area of one electrode (0.5 cm^2) as a function of the applied voltage. It is only in the a-direction that we detected a current above 10 kV/cm. Along the c-direction no detectable current has been observed up to break down. All the optical data are thus taken in the fully insulating limit. The inset of Fig. 3.12 shows the static conductivity $\sigma = dJ/dE$ (cf. Eq. 1.6) as a function of temperature in the region which manifests Ohmic behavior, i.e., for $V/d \gtrsim 38$ kV/cm. This demonstrates a metallic behavior below 150 K down to ~ 40 K, close to the temperature where quantum fluctuations start dominating [1].This metallic behavior, and in particular the finite conductivity itself could be due to either ionic or electronic conduction. The first one requires large ionic displacements of the order of the lattice size, and we will show later that experimental values are smaller than 0.1 Å at 11 kV/cm. However, electronic conduction by impurities can explain the effect, since the largest observed conductivity corresponds to roughly 10^7 charge carriers per cm^{-3}, which is far below the impurity level of 10^{13} as reported for one of the purest materials like silicon.

3.7 Mapping of the soft mode potential well

After having presented the electric field dependent soft mode data in the preceding section, it is in order at this stage to discuss the influence of an electric field on an insulator like $SrTiO_3$ on a microscopic level. Putting $SrTiO_3$ in a static electric field is not the same as the effect of an external (negative or positive) pressure which deforms the entire unit cell in a given direction. It mainly acts as a force on the loosely attached Ti atom, while leaving the rest of the atoms more or less untouched [12]. We present below a 1-dimensional harmonic oscillator model applied to the soft mode motion of $SrTiO_3$.

3.7.1 A 1-dimensional harmonic oscillator approach

We start from the assumption that the amplitude of the soft mode resulting from a perturbation with THz light is small and that the motion of the Ti atom due to this ac field can be considered as harmonic. We furthermore treat the problem as a classical motion, which amounts to assuming that at $T = 0$ the zero-point fluctuations are negligible compared to the field-induced and thermal fluctuations.

Hooke's law relates the force F of a spring with spring constant k to its displacement z, $\mathbf{F} = k\mathbf{z}$. The potential energy stored in the spring system is

$U = \frac{1}{2}kz^2$ and thus

$$F = \frac{\partial U}{\partial z}. \tag{3.16}$$

The frequency ω_0 of the system is

$$m\omega_0^2 = \frac{\partial^2 U}{\partial z^2} = \frac{\partial F}{\partial z}. \tag{3.17}$$

where m is the relevant mass. Eq. 3.17 demonstrates that on measuring a phonon frequency we exactly know the second derivative of the potential energy landscape relative to the displacement.

Putting a static voltage V on an insulator is the same as charging a capacitor with capacitance C up to a charge Q, and thus $C = Q/V$. In order to calculate the electric field E *inside* the dielectric, it is essential to know the exact configuration of the capacitor and the electrodes. If the electrodes are *attached* to the dielectric, there is no depolarization field since the potential on the surface of the dielectric is determined by the metal, and thus by the applied voltage V. Consequently the electric field for this configuration inside the dielectric is

$$E = \frac{V}{d}, \tag{3.18}$$

where d is the distance between the electrodes.[37] If there is a (vacuum) gap in between the electrodes and the dielectric, the depolarization field decreases E by the static dielectric permittivity ϵ and therefore [37]

$$E = \frac{V}{\epsilon d}, \tag{3.19}$$

where ϵ is given by Eq. 3.8. In all our experiments, the electrodes are attached to the sample surface, and the electric field is thus always given by Eq. 3.18. Since the force on an ionic charge q_i due to an electric field is $F = q_i E$, we obtain the force due to a voltage V,

$$F = \frac{\partial U}{\partial z} = \frac{q_i V}{d}. \tag{3.20}$$

Up to here we can summarize the situation as follows. An optical measurement of the electric field effect on SrTiO$_3$ moves the Ti atom (relative to the oxygen atoms) in the direction of the applied dc bias (Eq. 3.20) where the light probes the curvature of the potential landscape experienced by the Ti atom (Eq. 3.17). The latter is mainly determined by the oxygen octahedron and is sketched for the (a, c)-plane in Fig. 3.13. For tetragonal SrTiO$_3$, the c-axis is the ferroelectric axis which is 0.056 % longer than a and b [34, 35]. It is thus easier to move the Ti atom in the direction of the Ti-O chain (i.e., along $\hat{c}$) than perpendicular to it. Fig. 3.13 shows the microscopic picture of the three different experiment geometries that were presented before (Fig. 3.3). In the in-plane, parallel experimental geometry

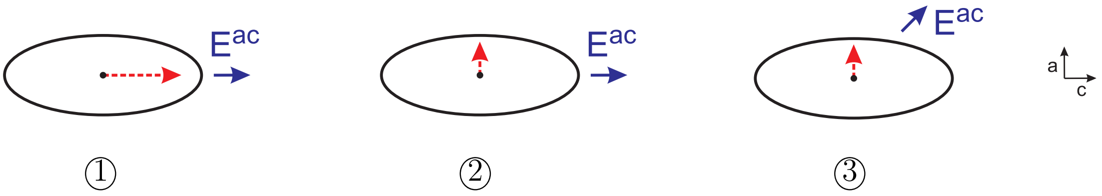

Figure 3.13: Equipotential line cartoons of the potential well created by the oxygen octahedron in tetragonal $SrTiO_3$ depicting the three different measurement geometries (cf. Fig. 3.3). The (zero bias) equilibrium position of the Ti atom is indicated by the dot. The red arrow indicates the direction of E^{dc}, the blue arrow the polarization direction of E^{ac}.

① E^{dc} moves the Ti atom along $\hat{c}$. E^{ac} is in the same direction and measures thus the curvature of the potential along $\hat{c}$. The in-plane, perpendicular geometry ② is slightly different. E^{dc} is along $\hat{a}$ but E^{ac} along $\hat{c}$, which means that the Ti atom is displaced along $\hat{a}$ while measuring the curvature in the $\hat{c}$ direction. Finally, for the out-of-plane geometry ③ E^{ac} probes on the diagonal between $\hat{a}$ and $\hat{c}$ while the Ti displacement is along $\hat{b}$ (which is equivalent to $\hat{a}$).

Note that the large ϵ is very convenient in these experiments, since it provides a low reluctance[4] path for electric flux which results in the fact that the field lines are 'sucked' into the material, just like a mu-metal[5] for magnetic fields.

It can now be seen that the field dependent soft mode frequencies as displayed in Figs. 3.7 – 3.10 provide the potential landscape of the Ti atom along different high symmetry directions. We will first consider the situation where the static external field is parallel to the probe direction (geometry ①), both in the c-direction. The displacement in this direction, z, can be calculated with Eq. 3.17 and Eq. 3.20 substituted with Eq. 3.8

$$z(V) = \int_0^F \frac{\partial z}{dF'}\, dF' = \int_0^F \frac{1}{m\omega_0^2}\, dF' = \frac{q_i}{md}\int_0^V \frac{1}{\omega_0^2}\, dV', \tag{3.21}$$

where $\omega_0 = \omega_0(V)$. Once we know the displacement z, we can also calculate the potential energy U from Eq. 3.16 substituted by Eqs. 3.20 and 3.8

$$U = \int_0^z F\, dz' = \frac{q_i}{d}\int_0^z V\, dz'. \tag{3.22}$$

In this way we obtain from the voltage dependent soft mode frequency $\omega_0(V)$ the functions $V(z)$, $F(z)$ and $U(z)$ through Eqs. 3.20, 3.21 and 3.22, respectively, provided that $E^{\mathrm{dc}} \parallel E^{\mathrm{ac}}$.

From the field dependence of the soft mode frequency we can also calculate the polarization P. The dielectric susceptibility χ probed in optics (in SI units)

---

[4] The electric reluctance is given by $R_e = \ell/(\epsilon_0\epsilon S)$, where ℓ is the length of the system and S the cross-section, similar to the magnetic reluctance $R_m = \ell/(\mu_0\mu S)$.[38]

[5] A mu-metal is a paramagnet with a magnetic permeability μ between $10^4 - 10^6$.

is equal to

$$\chi = \frac{1}{\epsilon_0}\frac{\partial P}{\partial E}, \tag{3.23}$$

with $\chi = \epsilon - 1$ and Eq. 3.18 this yields

$$P = \frac{\epsilon_0}{d}\int_0^V (\epsilon - 1)\ dV' \tag{3.24}$$

which gives with Eq. 3.8

$$P = \frac{\epsilon_0}{d}\int_0^V \left(\frac{\omega_p^2}{\omega_0^2} - 1\right) dV' \tag{3.25}$$

Further on, we will apply the preceding relationships to the soft phonon in the c-direction and the a-direction. However, up to here we did not specify the relevant charge and mass of the system. We can estimate the effective charge corresponding to this mode by looking at Eq. 3.12. The total polarization due to all (optical) lattice vibrations is

$$P = \frac{1}{V_u}\sum_j u_j Z_j q, \tag{3.26}$$

with q the elemental charge and V_u the unit cell volume. Since the ferroelectric soft mode is by far the dominant optical lattice vibration, we argue as if this were the only mode. The motion involved in this vibration is mainly the Ti^{4+} ion against the two oxygen atoms that are perpendicular to the Ti-O chain. Sr and the apical O are assumed to remain static under an electric field. This is true because the spring constants between Sr and apical O are much stiffer than between Ti and the planar oxygens. In this way we obtain

$$P = \frac{q}{V_u}\left(4|z_{\mathrm{Ti}}| + 2\cdot 2|z_{\mathrm{O,p}}|\right) \tag{3.27}$$

which tells us that for a relative displacement $z_{\mathrm{Ti}} - z_{\mathrm{O,p}}$ (of principal importance for the ferroelectric soft mode), the charge involved is $4q$. The reduced mass m for this motion is analogously

$$\frac{1}{m} = \frac{1}{2m_{\mathrm{O}}} + \frac{1}{m_{\mathrm{Ti}}}, \tag{3.28}$$

and thus $m = 19.2m_p$, with m_p the proton mass.

We can thus calculate the displacement of the Ti relative to the oxygens in two different ways: (i) from Eq. 3.21 using $q_i = 4q$ and $m = 19.2m_p$ and (ii) similar to Eq. 3.26 from the ionic polarization. In section 2.8.1 we concluded that the total ionic spectral weight of SrTiO$_3$ was 464/143 times bigger than the spectral weight based on the rigid ion model. We explained this as due to an

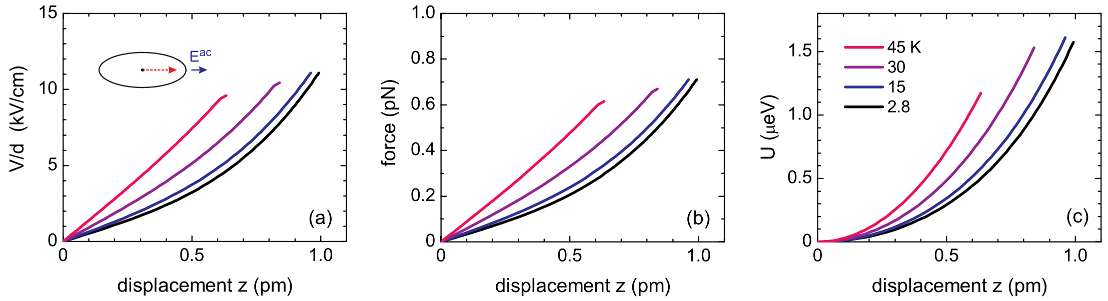

Figure 3.14: (a) displacement z due to an applied voltage V on a distance d in the c-direction; (b) the force exerted on the Ti atom vs. z; (c) the potential energy U vs. z. The cartoon indicates the displacement (dotted red arrow) and the probe direction (blue arrow) in the potential landscape.

addition of electronic spectral weight to ionic transitions. This factor is exactly the ratio of the Born effective charge Z_{eff} on the ions and the bare ionic charge Z. The plasma frequency ω_p of the ferroelectric soft mode that we obtained from the experimental data is thus not entirely due to ionic degrees of freedom. In order to obtain the displacement from the polarization, we thus have to consider only the *ionic* polarization P_i which we get through dividing the experimental ω_p^2 by Z_{eff}/Z and thus

$$P_i = P\frac{Z}{Z_{\text{eff}}} \tag{3.29}$$

and thus

$$P_i = \frac{q_i}{V_u}\left|z_{\text{Ti}} - z_{\text{O,p}}\right| \tag{3.30}$$

where $q_i = 4q$ as before. Here we also need the unit cell volume $V_u = 3.895$ Å^3 but no assumption is made about the relevant mass.

3.7.2 The potential well in the c-direction

We will first consider the situation where the static external field is parallel to the probe direction, both in the c-direction (geometry ①). We obtain the displacement z, the force F, the potential energy U and the polarization P from Eqs. 3.21, 3.20, 3.22 and 3.25, respectively. Fig. 3.14 shows these functions for some selected temperatures. Looking at the $V(z)$ characteristics, it is obvious that an external voltage moves the Ti atom, as expected. With increasing voltage, the slope of $V(z)$ increases at the lowest temperatures, which means that an increasing electric field is unable to move the Ti atom much more. This barrier is the signature of the Ti atom approach to the O atom along the Ti-O chain.

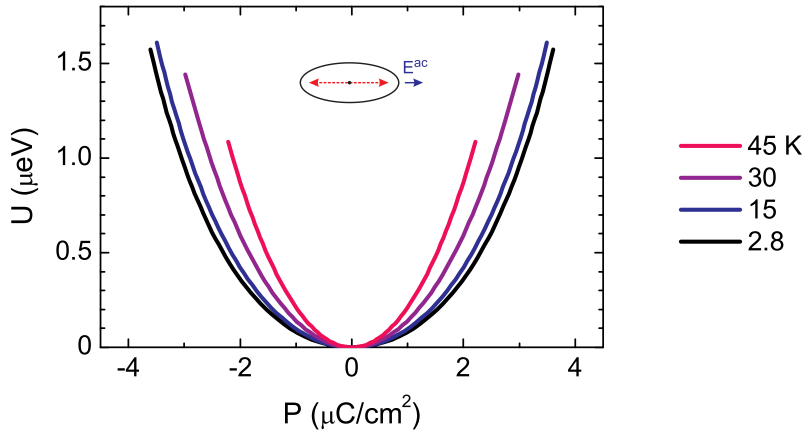

Figure 3.15: Potential energy U vs. the polarization P of for a displacement in the c-direction.

It demonstrates that the potential well which is experienced by the Ti atom becomes anharmonic at large external electric fields. This can also be seen by the force $F(z)$ which deviates from linearity at large voltages. Fig. 3.14c shows the potential energy U as a function of the displacement. With increasing temperature, all three functions show that the potential well becomes steeper which is consistent with an increasing mode frequency as experimentally observed. As mentioned before, the range of the curves in Fig. 3.14 is determined by the break down voltage.

The potential well imagined by the potential energy U vs. the polarization P is shown for the parallel geometry ① in Fig. 3.15.[6] The well is steep and narrow at 45 K and becomes wider with decreasing temperature, indicating a less well-defined Ti atom. Fig. 3.15 seems to show a quite harmonic potential, however, deviations from harmonicity are hard to observe in this representation, and we recommend the reader to look at $F(z)$ of Fig. 3.14b which gives direct evidence of the anharmonicity. The value of the polarization at the lowest temperatures is in the same range as earlier reported values, i.e., 4–5 μC/cm^2 for fields between 4–8 kV/cm below 10 K [17, 19]. This confirms the validity of using the harmonic oscillator model for the soft mode behavior in SrTiO$_3$.

As mentioned before, the displacement can also be calculated from the ionic polarization with Eqs. 3.25 and 3.30. However, since both the integrants of Eq. 3.21 and Eq. 3.25 are to a good approximation identical, the curves have the same shape and are just scaled with respect to each other by the prefactors. This makes that a displacement calculated from P is roughly 3 % bigger as compared

---

[6] Note that P is calculated from Eq. 3.25 without any correction on ω_p stemming from intermixing of electronic degrees of freedom, since it is the total polarization which is relevant.

to the one calculated from Eq. 3.21, which confirms the agreement of the mutual approaches.

In this section we interpreted the measured phonon frequencies as solely due to a classical motion of the ions, ignoring the zero-point fluctuations which are known to be increasingly important towards low temperatures for $SrTiO_3$. The maximum displacement that we obtained is of the order of 0.01 Å and the potential energy not larger than 1.5 μeV (i.e., 17 mK). In order to estimate their reliability, these numbers should be contrasted with the zero-point motion and the actual temperature, respectively. The zero-point energy of the Ti atom $E_{zp} = \frac{1}{2}\hbar\omega_0$. If we compare this energy to the potential U of the harmonic oscillator we obtain the zero-point motion which is 0.8 Å at $\omega_0 = 16.5\,\text{cm}^{-1}$, which is about two orders of magnitude bigger than the field induced shift. To explain this discrepancy, we assume for the moment that the actual potential well of the Ti atom is W shaped with two minima at non-zero polarization, in agreement with Ref. [33]. Then a scenario of the actual situation is that zero-point fluctuations prevent the Ti from a well-determined position in the well (see the gray shaded area in Fig. 3.16). The speed of the Ti atom at the bottom of the well (where ϵ is the biggest) is the biggest and at the turning points on the walls the smallest. Therefore, on average the Ti atom spends more time in regions of a lower ϵ, and the measured displacement is a *time averaged* displacement, which is small due to this reason. We treated the problem as a classical motion, which amounts to assuming that at $T = 0$ the zero-point fluctuations are negligible compared to the field-induced and thermal fluctuations. While the latter is nearly satisfied for some of the considered temperatures, the field induced displacement turns out to be small compared to the zero-point motion. Consequently a correction will be needed to "unfold" the zero-point fluctuations, which is subject of future studies.

Another comment that we should make about the anharmonicity of the well is the following. In a harmonic potential well all phonon excitation levels are equidistant in energy, but as soon as anharmonic terms are involved these levels are further spaced from each other the steeper the well becomes. This means that we should not observe a single phonon frequency, but an entire set of frequencies. However, since data is only available below the lowest transition, it is left for future studies to map out the actual phonon spectrum.

3.7.3 The potential well in the a-direction

A similar analysis where we calculate the potential energy vs. the polarization from the soft mode behavior in an electric field can not be applied for the other geometries ② and ③ separately, since the probe direction is different from the displacement direction and consequently a 1-dimensional oscillator model does not apply. However, we have enough information to perform a similar analysis for a displacement in the a-direction. The experimental geometry ③ probes the soft mode both along $\hat{c}$ and $\hat{a}$ for a displacement along $\hat{a}$. We mentioned before

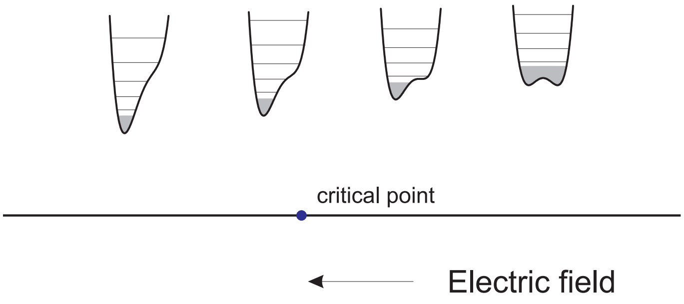

Figure 3.16: The approach and crossing of a second order phase transition as a function of the electric field as control parameter. The shaded area indicates the phase space occupied due to the zero-point motion. The horizontal lines indicate phonon excitation states inside the well.

that the corresponding deduced frequency ω_3 at zero field is exactly the average of the frequencies in both directions $\frac{1}{2}(\omega_a + \omega_c)$, as revealed from hyper-Raman data. In geometry ② we measure $\omega_2 = \omega_c$ for a displacement in the a-direction. Therefore we can determine ω_a for a displacement along $\hat{a}$ by $\omega_a = 2\omega_3 - \omega_2$. The temperature and electric field dependence of ω_a (Fig. 3.17) resemble Figs. 3.9-3.10, as expected. The plasma frequency $\omega_{p,a}$ of the soft mode along the a-direction is given by a subtraction of spectral weights $\omega_{p,a}^2 = 2\omega_{p,3}^2 - \omega_{p,2}^2$. With $\omega_{p,3} = 171$ meV and $\omega_{p,2} = 188.5$ meV, as mentioned before, we get $\omega_{p,a} = 151.5$ meV. The ratio of the optical spectral weights of the mode in the a-direction and the one in the c-direction is thus 65 %.

Fig. 3.18 shows $V(y), F(y)$ and $U(y)$ as a function of the displacement y which is in the a-direction. At low temperatures, $V(y)$ is less steep than $V(z)$, which means that the displacement in the a-direction is much easier than in the c-direction, which is also reflected by the fact that $\omega_a < \omega_c$. At large voltages, also in the a-direction the Ti atom experiences a barrier due to the proximity of an oxygen atom, although this one is relatively shallow. Notice the temperature dependence of the three functions which is more pronounced than for a displacement along $\hat{c}$: a movement along $\hat{a}$ at 45 K leads only to 38 % of the displacement at 4 K, whereas this is 66 % in the c-direction. Fig. 3.19 shows the potential well for a displacement along $\hat{a}$ which is more harmonic than for the c-direction (compare $F(z)$ and $F(y)$). Also here the large temperature dependence is evident. Note the value of the polarization P which is more than four times bigger than in the c-direction.

When we calculate y from the polarization with Eq. 3.30, we find a displacement which is only 65 % of the displacement calculated with Eq. 3.21 (Fig. 3.18). Qualitatively this does not change the picture: a voltage in the a-direction always induces a much larger displacement than the same voltage in the c-direction. The difference is possibly due to a slightly different mass m which is involved in the

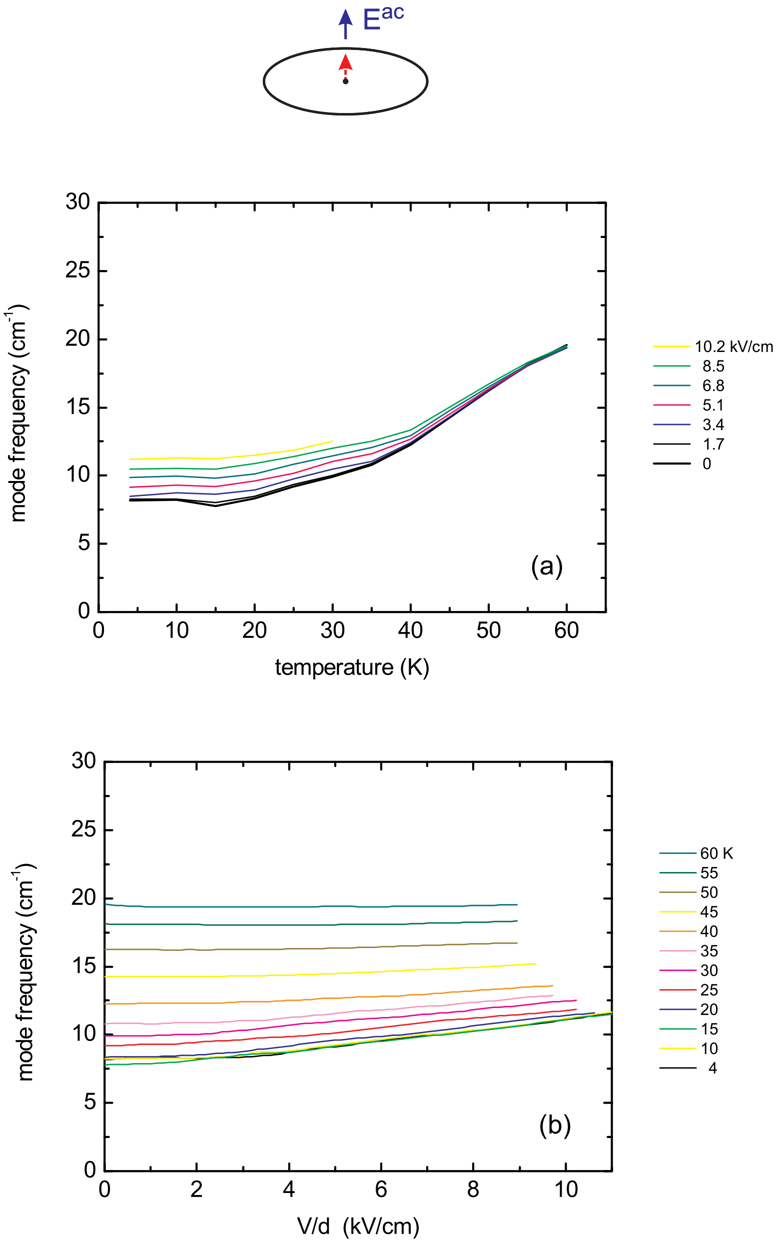

Figure 3.17: Soft mode frequency ω_a calculated (see text for details) from the mode frequencies of experiment geometries ② and ③ (a) as a function of temperature for selected applied voltages and (b) as a function of applied voltage V for selected temperatures.

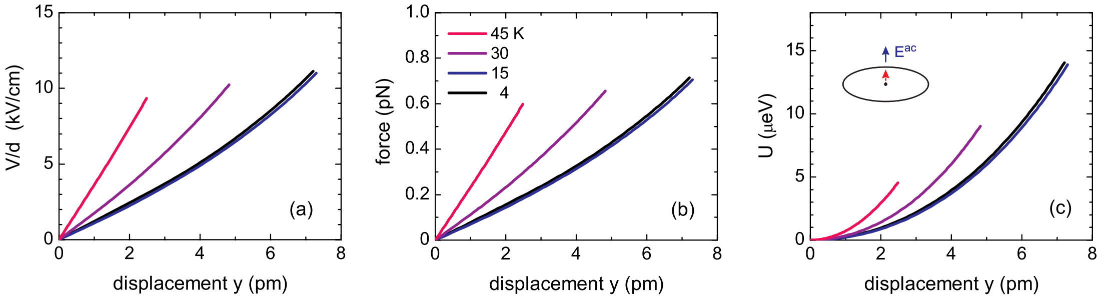

Figure 3.18: (a) displacement y due to an applied voltage V on a distance d in the a-direction; (b) the force exerted on the Ti atom vs. y; (c) the potential energy U vs. y. The cartoon indicates the displacement (red arrow) and the probe direction (blue arrow) in the potential landscape.

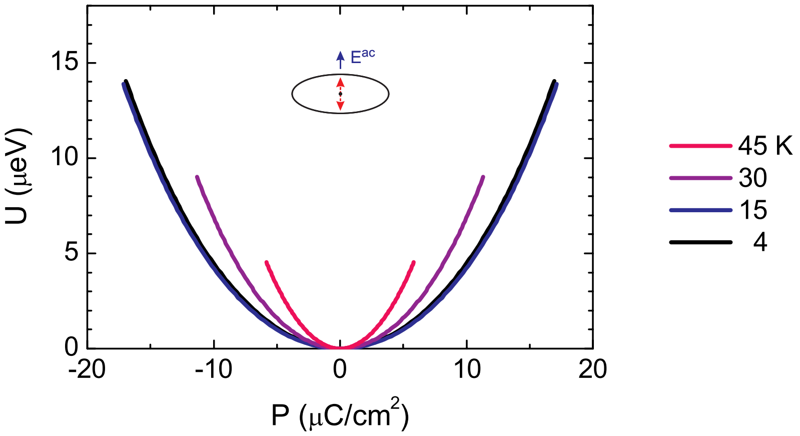

Figure 3.19: Potential energy U vs. the polarization P for a displacement in the a-direction.

phonon motion along $\hat{a}$.

3.7.4 Where is the phase transition?

In none of the two directions ($\hat{a}$ and $\hat{c}$) the potential well (Figs. 3.15 and 3.19) shows a behavior as expected from the classical Landau-Devonshire theory, as presented in section 3.1. The constant $a > 0$ in the free energy expansion (Eq. 3.2) decreases towards T_c and changes to negative values for a second order phase transition. Our potential energy curves are very harmonic, and the constant a decreases but saturates with decreasing temperature. The only indication of the anharmonicity is in $F(z)$, which clearly deviates from linearity. This nonlinearity becomes much less visible in $U(z)$ and thus in $U(P)$ due to the integration, $U = \int F dz$.

We discussed before that our treatment is purely classical and does not account for the presence of zero-point fluctuations. Due to this reason, the calculated displacement and the potential energy turn out to be too small to be realistic, as are the *time averaged* values. We assume that the potential well of the Ti atom is in reality W shaped, but quantum fluctuations hinder a true phase transition towards a non-zero polarization state. When an electric field is applied the potential well is tilted to one direction (see Fig. 3.16). For a large enough field, the well is on one side deeper than the zero-point energy and a non-zero polarization is adopted. There would be no true phase transition if the electric field were directly the control parameter and the polarization the order parameter, since any electric field induces a finite polarization. However, the presence of a remanent polarization and the sudden domain orientation perpendicular to the applied electric field in a narrow part of the $T-E$ phase space do indicate the presence of ferroelectricity. There should thus also be a phase transition, since the material is paraelectric at ambient conditions. An important feature of ferroelectric materials is their great sensitivity to elastic stress.[3] Electric-field induced strain measurements by Grupp and Goldman [22] have shown a large piezoelectric effect in $SrTiO_3$ at cryogenic temperatures. The electric field thus probably leads to a strain field which causes the electrical polarization. The control parameter (strain) is different from the order parameter (polarization), which allows for a second order phase transition.

The next question is why the mode frequency does not entirely soften to zero frequency at the phase transition. From Fig. 3.7 we have seen that the frequency of the ferroelectric soft mode along $\hat{c}$ has a minimum as a function of temperature for $E > 3.4$ kV/cm, but never reaches truly zero which is required for a proper second order phase transition from the paraelectric to the ferroelectric state. Here we refer to past literature [26, 40, 27, 28], where a coupling between a low lying zone-boundary acoustic phonon and the ferroelectric soft mode has been proposed. The coupling between an acoustical and optical mode is generally not possible due to symmetry reasons, but can happen in absence of inversion symmetry as caused by an electric field. At liquid helium temperatures, both modes have very comparable energies [39] which would lead to a mixing of both. One branch of the coupled mode becomes zero at the critical point while the other branch goes through a minimum but always remains finite.

3.8 Quantum criticality in SrTiO$_3$

In the previous section we have seen that zero-point fluctuations become very large for $T \rightarrow 0$ and $E \rightarrow 0$, which highlights the importance of quantum fluctuations. In particular we have seen that zero-point fluctuations drive SrTiO$_3$ away from static polarization. Traditionally, a quantum critical point (QCP) is the end-point at 0 K of a line of second order phase transitions at which both the correlation length and the correlation time diverge. At the QCP there is no characteristic length or time scale anymore, and fluctuations of both phases are coexisting. Among the early findings are the magnetic phase transition in LiHoF$_4$ which becomes suppressed in a transverse magnetic field [47]. In case we deal with a first-order phase transition, the system does not break any symmetry at the transition and per definition there can not be a QCP. Despite, a line of first-order transitions can have an end-point, like in the temperature-pressure phase diagram of water where liquid and vapor coexist. At this so-called critical opalescence point the density between both phases is equal and there is no latent heat associated with the transition. Recently, it has been suggested that such a critical point can be varied in temperature with some tuning parameter. Eventually, when $T_c = 0$ this would imply a QCP at the end of a line of first-order transitions [9, 48].

SrTiO$_3$ tuned with an external electric field E^{dc} is not expected to show a second order phase transition with E^{dc} since no symmetry is broken when the polarization is the order parameter and the electric field the control parameter. However, we expect the electric field to induce a strain field, as mentioned before, which is the control parameter that induces a finite polarization. There should thus be a second-order phase transition which is presumable smoothed due to the coupling between the optical ferroelectric mode and an acoustic mode.

The experimental indication of a phase transition point where $d\chi/dT = 0$ is the minimum in $\omega_c(T)$ at electric fields above 3.4 kV/cm (see Fig. 3.7). These points are plotted in Fig. 3.20 and fit very well to a power law $T_{\mathrm{c}} = 6.3(E^2 - 3.7)^{0.41}$, indicating a critical exponent $\gamma = \nu z = 0.41$ and possibly a QCP around 1.7 kV/cm. The critical exponent is close to the mean field value $\nu = \frac{1}{2}$ and the dynamical exponent $z = 1$. The phase diagram shows T vs. E^2 instead of E since we expect that the strain is the control parameter which is an even function of the electric field.

On decreasing temperature the importance of quantum fluctuations increases in SrTiO$_3$ due to the smallness of the gap energy (the soft mode energy) compared

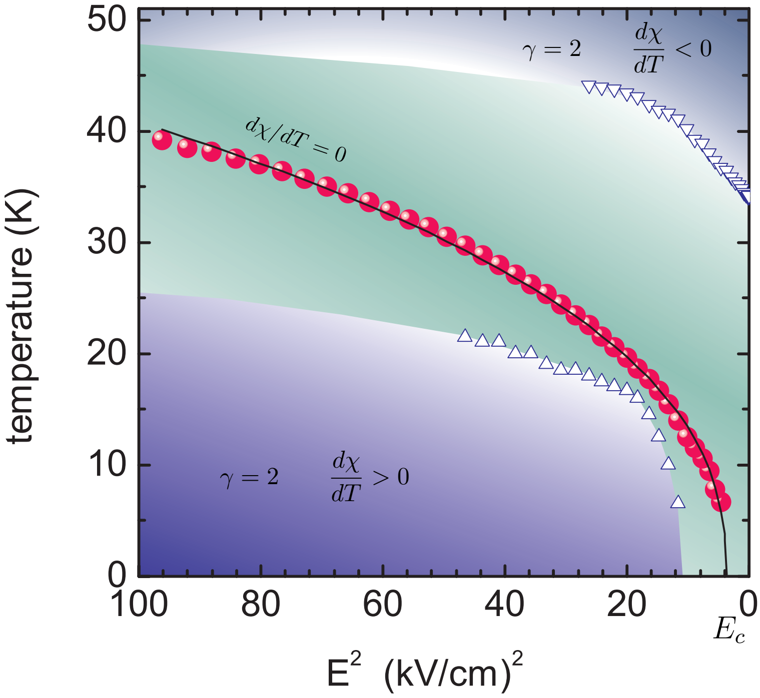

Figure 3.20: $E^2 - T$ phase diagram of $SrTiO_3$ in the $\hat{c}$ direction. The slope of $\chi(T)$ changes from the high temperature side to the low temperature side from negative to positive, passing through zero at the minimum of $\omega_c(T)$ (red dots). The blue regions are the ones where there is a linear relationship between ω_c and T, which implies $\gamma = 2$. The black solid line is a power law fit (see text for details).

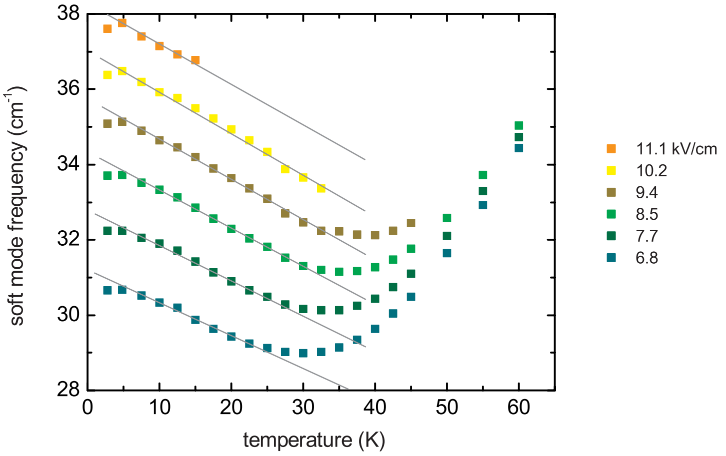

Figure 3.21: Blow up of Fig. 3.7 which shows the linear relationship between the soft mode frequency ω_0 and T for selected values of the applied voltage.

to $1/k_BT$. Although the classical Curie-Weiss behavior does not account for quantum fluctuations, the quantum Curie-Weiss (or Barrett) law does (cf. Eq. 3.10). Quantum critical behavior corresponds to a critical exponent $\gamma = 2$ [41, 8], which implies $\omega_0(T) \propto T$ for low T. A self-consistent phonon treatment of the soft transverse-optical phonon branch that leads to ferroelectricity also predicts such a linear behavior for $k_BT < \hbar\omega_0$.[28] A close inspection to the electric field dependent mode frequency ω_c reveals two regions which satisfy this criterion. The high temperature linear region can be seen from Fig. 3.7, the low temperature linear region is shown in detail in Fig. 3.21. For both regions, the extent of the linear part is strongly field dependent. Fig. 3.20 displays the upper bound of linearity of the first (down triangles), and the highest temperature of linearity of the second (up triangles). The former boundary indicates the region outside of which quantum fluctuations are important. Classical fluctuations dominate above the latter boundary.

The region enclosed by the two boundaries is predicted in the theory of quantum critical phase transitions, and shown in the hypothetical phase diagram of Fig. 3.2b by Vojta [8]. The main difference between Fig. 3.20 and the latter is the upper critical boundary which does not decrease down to zero temperature, but saturates at 35 K. This value is remarkable since it is equal to the temperature scale reported by Müller and Bukhard [1] below which the quantum paraelectric phase sets in. They determined it as the temperature for which $1/\epsilon = 0$ from the extrapolated classical Curie-Weiss behavior. Note that the lower blue region in the phase diagram of Fig. 3.20 corresponds exactly to the region of Fig. 3.9 where a second response has been observed for the perpendicular, in-plane geometry ②. We therefore indicate this region as being ferroelectric.

Referring back to the beginning of this section, it is unclear whether the min-

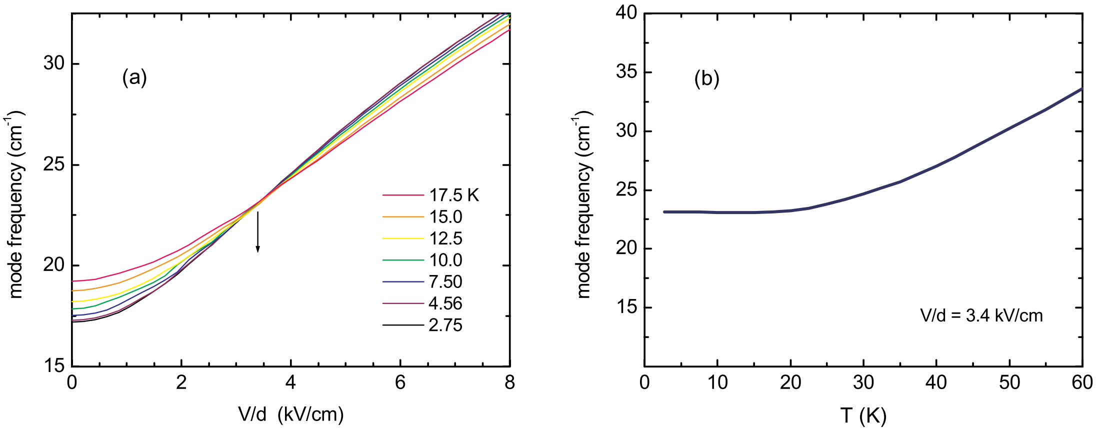

Figure 3.22: (a) ω_c vs. V/d of experiment geometry ① showing a common frequency point at 3.4 kV/cm for $T < 20\,\mathrm{K}$; (b) ω_c vs. T at 3.4 kV/cm.

imum in $\omega_c(T)$ is a first-order or second-order phase transition. However, in both cases a possible scenario would be that the line which connects the minima (red dots in Fig. 3.20) ends in a QCP. We will not tempt to perform any scaling analysis here, since the absence of an adequate scaling model could lead to unjustified conclusions. Something which is directly present in the data, and which suggests the presence of a QCP is the scale invariant point in $\omega_c(V)$ (see Fig. 3.22a). Below 20 K all curves have a common (ω_c, V) point which indicates universal behavior. In order words, the mode frequency at 3.4 kV/cm is completely temperature invariant (Fig. 3.22b). Systems which show evidence for a QCP often have such a universal point [41, 42, 43, 44, 45].

The behavior of ω_c for a displacement in the a-direction (geometry ②) is partially different from the displacement along $\hat{c}$. Also in these data there is a region in phase space with a linear relationship $\omega(T) \propto T$ for the higher temperatures, which gives an upper critical boundary idential as for a displacement in the c-direction (see Fig. 3.20). There is no minimum in $\omega(T)$ and also no linear part of $\omega(T)$ at low temperatures. This means that a displacement in the a-direction does thus not provoke a quantum ferroelectric state, although there is critical behavior at high temperatures.

3.9 Conclusions

We have performed an optical study of the influence of a static electric field on the soft mode of pristine $SrTiO_3$ at temperatures between 2.8 K and 60 K and for external electric fields below 25 kV/cm. A static electric field E^{dc} causes a displacement of the Ti atom relative to the oxygen octahedron, which can be parallel and perpendicular to the ferroelectric axis (along the Ti-O chain).

Linearly polarized THz light subsequently probes the curvature of the potential landscape in both directions. Within the approximation that the motion of the soft mode is small, a 1-dimensional harmonic oscillator model has been used to calculate the displacement z of Ti relative to O, the force F on the Ti atom, the potential energy U and the polarization P. The behavior of $V(z)$ at 2.8 K shows that at large voltages, the Ti atom experiences a barrier due to the presence of a neighboring O atom. The anharmonicity of the potential landscape is clearly demonstrated by $F(z)$ which deviates from linearity at large fields. We have determined the potential well $U(P)$ which in first order seems harmonic and which becomes wider with decreasing temperature, indicating the growing importance of the fluctuations. The movement along the a-direction (perpendicular to the Ti-O chain) is easier than along the c-direction: an identical external electric field gives a larger displacement and induces a larger polarization.

The harmonic oscillator analysis did not take into account the importance of zero-point fluctuations. We assume that the potential well is in reality W shaped, and that zero-point fluctuations prevent the system from adopting a static polarization. Experimentally, we observe for a displacement along the c-direction, a minimum in $\omega_c(T)$ which is most probably related to a paraelectric to ferroelectric phase transition. This transition is driven by the electric field induced strain which induces a static polarization. For temperatures smaller than this minimum, the optical spectra show an additional response of domains that have their polarization perpendicular to the applied electric field. We interpret this as due to Weiss domain formation and consider it as a signature of ferroelectricity.

The temperature points that connect the minima of $\omega_c(T)$ at different external fields describe a power law with a critical exponent $\gamma = 0.41$, which is close to the mean-field value of $\frac{1}{2}$. Both above and below this crossover line, for $k_B T < \hbar\omega_c$, we observe regions of $\omega_c \propto T$, which is interrupted in a sizable region around this line. The linear behavior indicates the presence of quantum criticality and thus the importance of quantum fluctuations, whereas the latter region where linearity is absent seems to point to a classical critical area.

It could be that the crossover line ends in a quantum critical point, although in absence of the adequate theory no scaling arguments are being made in this work. An indication of such a point is the scale invariance of $\omega_c(V)$ which manifests universal behavior below 20 K.

Bibliography

[1] K.A. Müller and H. Burkard, Phys. Rev. B **19**, 3593 (1976).

[2] G.A. Samara in *Solid State Physics* vol. 56, *Ferroelectricity Revisited – Advances in Materials and Physics*, H. Ehrenreich and F. Spaepen (Eds.) Academic Press (2001).

[3] K. Rabe, Ch. H. Ahn and J.-M. Triscone (Eds.) *Physics of Ferroelectrics, A Modern Perspective*, Springer-Verlag Berlin Heidelberg (2007).

[4] W. Cochran, Phys. Rev. Lett. **3**, 412 (1959).

[5] J.H. Barrett, Phys. Rev. **86**, 118 (1952).

[6] J.F. Scott, Rev. Mod. Phys. **46**, 83 (1974).

[7] J. Dec and W. Kleemann, Solid State Comm. **106**, 695 (1998).

[8] M. Vojta, Rep. Prog. Phys. **66**, 2069 (2003).

[9] S.A. Grigera, R.S. Perry, A.J. Schofield, M. Chiao, S.R. Julian, G.G. Lonzarich, S.I. Ikeda, Y. Maeno, A.J. Millis, A.P. Mackenzie, Science **294**, 329 (2001).

[10] M. Itoh, R. Wang, Y. Inaguma, T. Yamaguchi, Y.-J. Shan, and T. Nakamura, Phys. Rev. Lett. **82**, 3540 (1999); M. Itoh and R. Wang, Appl. Phys. Lett. **76**, 221 (2000).

[11] J.H. Haeni, P. Irvin, W. Chang, R. Uecker, P. Reiche, Y.L. Li, S. Choudhury, W. Tian, M.E. Hawley, B. Craigo, A.K. Tagantsev, X.Q. Pan, S.K. Streiffer, L.Q. Chen, S.W. Kirchoefer, J. Levy and D.G. Schlom, Nature **430**, 758 (2004).

[12] A. Antons, J. B. Neaton, K.M. Rabe and D. Vanderbilt, Phys. Rev. B **71**, 024102 (2005)

[13] H. Taniguchi, M. Itoh and T. Yagi, Phys. Rev. Lett. **99**, 017602 (2007).

[14] G.A. Samara, Phys. Rev. **151**, 378 (1966).

[15] E.L. Venturini and G.A. Samara, M. Itoh and R. Wang, Phys. Rev. B **69**, 184105 (2004).

[16] J.F. Youngblood, Phys. Rev. **98**, 1201 (1955).

[17] H. Gränicher, Helv. Phys. Acta **29**, 210 (1956).

[18] E. Hegenbarth, Phys. Stat. Sol. **6**, 333 (1964).

[19] J. Hemberger, P. Lunkenheimer, R. Viana, R. Böhmer, and A. Loidl, Phys. Rev. B **52**, 13159 (1995).

[20] J. Hemberger, M. Nicklas, R. Viana, P. Lunkenheimer, A. Loidl and R. Böhmer, J. Phys.: Condens. Matter **8**, 4673 (1996).

[21] J.M. Worlock and P.A. Fleury, Phys. Rev. Lett. **19**, 1176 (1967).

[22] D.E. Grupp and A.M. Goldman, Science **276**, 392 (1997).

[23] D.E. Grupp and A.M. Goldman, Phys. Rev. Lett. **78**, 3511 (1997).

[24] D.E. Grupp and A.M. Goldman, Phys. Rev. Lett. **82**, 3001 (1999).

[25] M. Maglione, Phys. Rev. Lett. **81**, 3299 (1998).

[26] D. E. Khmelnitskii and V. L. Shneerson, Sov. Phys. Solid State **13**, 687 (1971); Sov. Phys. JETP **37**, 164 (1973).

[27] L. Pálová, P. Chandra and P. Coleman, Phys. Rev. B **79**, 075101 (2009).

[28] S.E. Rowley, L.J. Spalek, R.P. Smith, M.P.M. Dean, G.G. Lonzarich, J.F. Scott and S.S. Saxena, arXiv:0903.1445v1 (2009).

[29] N. Das and S.G. Mishra, arXiv:0906.0944v3 (2009).

[30] A. Yamanaka, M. Kataoka, Y. Inaba, K. Inoue, B. Hehlen and E. Courtens, Europhys. Lett. **50**, 688 (2000).

[31] T.S. Chang, J.F. Holzrichter, G.F. Imbusch and A.L. Schawlow, Appl. Phys. Lett. **17**, 254 (1970).

[32] K.A. Müller, W. Berlinger, M. Capizzi and H. Gränicher, Solid State Comm. **8**, 549 (1970).

[33] E. Tosatti and R. Martoňák, Solid State Comm. **92**, 167 (1994).

[34] F.W. Lytle, J. Appl. Phys. **35**, 2212 (1964).

[35] H. Unoki and T. Sakudo, J. Phys. Soc. Jpn. **23**, 546 (1967).

[36] A. B. Kuzmenko, Rev. Sci. Instrum. **76**, 083108 (2005).

[37] D.J. Griffiths, *Introduction to Electrodynamics*, 3^{rd} ed., Prentice-Hall, Inc. (New Jersey, USA), pp. 182-185 (1999).

[38] A.R. von Hippel, *Dielectrics and waves*, Chapman and Hall (London), (1959).

[39] W.G. Stirling, J. Phys. C : Solid State Phys. **5** 2711 (1972).

[40] V.L. Gurevich and A.K. Tagantsev, Zh.Eksp.Teor.Fiz. **94**, 370 (1988) [Sov. Phys. JETP **67**, 206 (1988)].

[41] S.L. Sondhi, S.M. Girvin, J. P. Carini and D. Shahar, Rev. Mod. Phys. **69**, 315 (1997).

[42] D. Shahar, D.C. Tsui, M. Shayegan, R.N. Bhatt and J.E. Cunningham, Phys. Rev. Lett. **74**, 4511 (1995).

[43] S.V. Kravchenko, W.E. Mason, G.E. Bowker, J.E. Furneaux, V.M. Pudalov and M. D'Iorio, Phys. Rev. B **51**, 7038 (1995).

[44] D. Popović, A.B. Fowler and S. Washburn, Phys. Rev. Lett. **79**, 1543 (1997).

[45] H. Aubin, C.A. Marrache-Kikuchi, A. Pourret, K. Behnia, L. Bergé, L. Dumoulin and J. Lesueur, Phys. Rev. B **73** 094521 (2006).

[46] S. Sachdev, *Quantum Phase Transitions*, Cambridge Univ. Press (1999).

[47] D. Bitko, T.F. Rosenbaum and G. Aeppli, Phys. Rev. Lett. **77**, 940 (1996).

[48] A.J. Millis, A.J. Schofield, G.G. Lonzarich and S.A. Grigera, Phys. Rev. Lett. **88**, 217204 (2002).

Chapter 4

Magneto-optics of $EuTiO_3$

The phenomena of ferromagnetic and antiferromagnetic spin resonance are discovered in 1911 [1, 2, 3] and ever since many early studies have been performed on materials like ferrites and garnets that provide understanding of the spin dynamics in solids.[4, 5, 6] However, despite these efforts, most experimental studies concern magnetic field dependent absorption for a single photon energy. In addition, almost all materials with a finite magnetization have a non-zero orbital momentum which makes the dichroic transition not purely spin-like, but mixed. We have studied the magneto-optical properties of insulating $EuTiO_3$ in the THz range by time-domain ellipsometry. Due to its spin-only character, a strong magnetic dichroism shows up only in the magnetic permeability function for one specific chirality. The effect manifests itself as a gigantic broad band Faraday rotation of linearly polarized THz light of 170 deg $mm^{-1}T^{-1}$.

4.1 Theoretical background on Spin Resonance

The phenomenon of ferromagnetic resonance has first been observed by Arkad'Yev [1] in 1911 and later theoretically described by Landau and Lifshitz [3]. It results from the interaction of electromagnetic radiation and spin-waves (magnons) and is widely used to probe the ac magnetization properties of materials. In order to understand the microscopic behavior of a magnetic material we first shortly review the basic principles of magnetic resonance. Electrons have both charge and spin degrees of freedom. These spins represent little magnetic dipoles that each have a magnetic moment $\boldsymbol{\mu}$ which is parallel to the angular momentum $\mathbf{L}$, and is related to it by

$$\boldsymbol{\mu} = \gamma \mathbf{L}, \tag{4.1}$$

with (in SI units) the gyromagnetic ratio $\gamma = ge/2m$, e is the absolute value of the electronic charge, m is the mass of the electron, c is the speed of light and g is the Landé g factor.

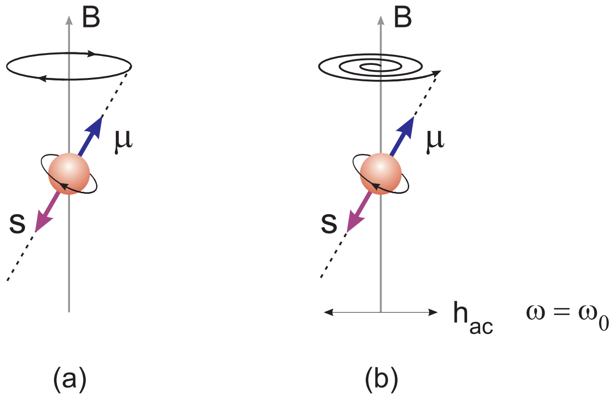

Figure 4.1: (a) Precessional motion of a spinning electron with angular momentum **s** and magnetic moment μ in a static magnetic field B. (b) When the frequency of the rf field is close to the natural precession frequency ω_0 the magnetization vector increases in amplitude.

In a magnetic field **B**, the situation of minimum energy is obtained when the magnetic moment is aligned along the magnetic field. However, since spin possesses angular momentum there will be a torque exerted on the angular momentum which forces the spin to precess around **B**. The rate of change of the angular momentum of the electron spin can be written with Eq. 4.1 as

$$\frac{d\boldsymbol{\mu}}{dt} = \gamma \boldsymbol{\mu} \times \mathbf{B}. \tag{4.2}$$

The frequency of the gyromagnetic precession

$$\omega_0 = \gamma \mathbf{B}, \tag{4.3}$$

is called the Larmor frequency and describes the natural resonance frequency of the electron in an effective magnetic field **B**.

The total magnetization of a solid is determined by the magnetic moment per unit volume, $M = \mu N$, where N is the number of magnetic dipoles per unit volume. In the absence of damping, this leads to the macroscopic equation of motion for the magnetization

$$\frac{d\mathbf{M}}{dt} = \gamma \mathbf{M} \times \mathbf{B}. \tag{4.4}$$

The magnetic field **B** as mentioned above is in fact the vector sum of all magnetic fields[1] present in the solid which is experienced by the electron spin. In order to drive the system into resonance, an ac electromagnetic field has to be applied perpendicularly to the static magnetic field. When the frequency of the ac field

---

[1] As will be explained later in this chapter, the total magnetic field consists of e.g. the external field, the anisotropy field and the demagnetization field.

is equal to the Larmor frequency, the system absorbs very efficiently the energy from the ac field and the precession amplitude will grow. Quantum mechanically this can be seen by realizing that both an electron and a photon carry angular momentum. In a one-electron picture, a photon can be absorbed by the system when Eq. 4.3 is satisfied, which will transfer an angular momentum quantum to the electron. In case the transition is purely magnetic, a spin angular momentum quantum alters its spin state if the selection rules permit. In this way the system shows to be selective upon the chirality of the light which is also called magnetic circular dichroism (see also section 1.5). Upon absorption of the photon's angular momentum the total magnetization of the system changes. When the electron relaxes back to the ground state, also the magnetization returns to its original value. These so-called Rabi oscillations can be imagined by the nutation movement of the spin.

In order to describe realistic ferromagnetic media, a dissipative term has to be added to the undamped dynamical equation of motion (Eq. 4.4). Landau and Lifshitz did this in a phenomenological way by adding an additional torque term that directs the magnetization towards the effective magnetic field **B**.[3] The Landau-Lifshitz form of the equation of motion is

$$\frac{d\mathbf{M}}{dt} = \gamma \mathbf{M} \times \mathbf{B} - \frac{\lambda}{|M|}\mathbf{M} \times (\mathbf{M} \times \mathbf{B}), \tag{4.5}$$

where λ is a damping factor having the dimensions of frequency. It is the inverse of the relaxation time. It is important to note that the phenomenological damping term influences the precession angle of the magnetization but not its magnitude. A different phenomenological approach to add the dissipative term to Eq. 4.4 due to Gilbert [7] adds a kind of 'viscous' force by considering the field

$$\mathbf{B}_{\text{viscous}} = \frac{\alpha}{\gamma |M|}\frac{d\mathbf{M}}{dt} \tag{4.6}$$

where $\alpha > 0$ is the Gilbert damping constant[2]. Gilbert damping is understood to be a nonlinear spin relaxation phenomenon and it controls the rate at which magnetization spins reach equilibrium.[8] The Landau-Lifshitz-Gilbert equation of motion of the magnetization then becomes

$$\frac{d\mathbf{M}}{dt} = \gamma \mathbf{M} \times \mathbf{B} - \frac{\alpha}{|M|}\mathbf{M} \times \frac{d\mathbf{M}}{dt}. \tag{4.7}$$

Although the Landau-Lifshitz and the Landau-Lifshitz-Gilbert equations seem mathematically very similar, the limit of infinite damping clearly distinguishes

---

[2] The Gilbert damping can be split into extrinsic and intrinsic contributions. The extrinsic one is due to nonlocal spin relaxation processes and disorder broadening (e.g. sample quality), the intrinsic term is mainly determined by the spin-orbit interaction, as recently demonstrated by Hickey and Moodera [8]. Typical values are between 10^{-3} and 10^{-2}, although it has been shown that also large values on the order of unity can occur as for instance in $SrRuO_3$ [9].

them : $d\mathbf{M}/dt \to \infty$ and $d\mathbf{M}/dt \to 0$, respectively. A very large damping corresponds to an almost static behavior of the magnetization, which pleads for the use of the Landau-Lifshitz-Gilbert form. From Eq. 4.7 we obtain the magnetic susceptibility by substituting $\mathbf{B} = \mathbf{H}_0 + \mathbf{h}e^{i\omega t}$ and $\mathbf{M} = \mathbf{M}_0 + \mathbf{m}e^{i\omega t}$, which is sum of the static (external) contribution and the alternating ac component. Within the linear approximation (small ac power) this provides the components of the magnetic permeability tensor $\mu(\omega)$

$$\mu_{xx} = \frac{\omega_M(\omega_0 + i\Gamma)}{(\omega_0 + i\Gamma)^2 - \omega^2} + 1 \qquad \mu_{xy} = -\frac{i\omega\omega_M}{(\omega_0 + i\Gamma)^2 - \omega^2} \tag{4.8}$$

In circular representation, through $\mu^{\pm} = \mu_{xx} \pm i\mu_{xy}$, this becomes [11]

$$\mu^{\pm} = 1 + \frac{\omega_M}{(\omega_0 + i\Gamma) \mp \omega} = 1 + \frac{\omega_M(\omega_0 \mp \omega)}{(\omega_0 \mp \omega)^2 + \Gamma^2} - i\frac{\omega_M\Gamma}{(\omega_0 \mp \omega)^2 + \Gamma^2} \tag{4.9}$$

where $\omega_M = \mu_0\gamma M$ and Γ the damping constant. When damping is neglected ($\Gamma = 0$) this reduces to the so-called Polder susceptibility [10]. It should be noticed that magnetic transitions expressed by the magnetic permeability (Eq. 4.8) have thus a fundamentally different origin than electric transitions that are described by a harmonic oscillator model resulting in the Drude-Lorentz formalism (cf. section 1.2).

Up to now we considered a *total* magnetic field $\mathbf{B}$ as-experienced by the electron. In the following we will decompose this field in the external magnetic field $\mathbf{H}_0$, the demagnetization field $\mathbf{H}_d$ and the anisotropy field $\mathbf{H}_a$ and derive the permeability tensor in terms of these partial magnetic fields.

(i) The demagnetization effects come into play when considering samples of finite dimensions. The demagnetization effect can be seen as follows. Magnetic dipoles in a ferromagnetic substance cancel inside but give a net contribution on the surfaces, which creates a field opposing the applied field. The strength of this demagnetization field depends on the distance between the opposing surfaces, and can be written as

$$\mathbf{H}_\mathrm{d} = -\mathsf{N}\mu_0\mathbf{M} \tag{4.10}$$

where N is the demagnetization tensor. In case the magnetization $\mathbf{M}$ is parallel to one of the principal axis of the sample, N can be diagonalized, satisfying $\mathrm{Tr}\,\mathsf{N} = N_x + N_y + N_z = 1$. The internal static and ac magnetic fields for a parallel plate magnetized perpendicular to the surface, for which $N_x = N_y = 0, N_z = 1$ are given by, respectively,

$$\mathbf{B}_0 = \mathbf{H}_0 - \mu_0\mathbf{M}, \qquad \mathbf{b}_0 = \mathbf{h}_0 - \mu_0\mathbf{m} \tag{4.11}$$

The introduction of the demagnetization field permits to give a more explicit relationship (as compared to Eq. 4.3) for the ferromagnetic resonance condition,

$$\omega_0 = \gamma B = \gamma(H_0 - H_d). \tag{4.12}$$

Substitution of Eq. 4.11 into Eq. 4.7 provides the permeability including demagnetization effects due to a parallel plate shape

$$\mu_{xx} = \frac{\omega_M(\Omega_0 + i\Gamma)}{\omega_0^2 - \omega^2 + 2i\Gamma(\Omega_0 + \omega_M)} + 1 \qquad \mu_{xy} = -\frac{i\omega\omega_M}{\omega_0^2 - \omega^2 + 2i\Gamma(\Omega_0 + \omega_M)} \tag{4.13}$$

with $\Omega_0 = \gamma H_0$ the bare Larmor frequency. We do not show the circular representation since these are lengthly expressions and can be easily formed from Eq. 4.13.

(ii) The magnetic anisotropy field describes the preferred direction of the effective spontaneous magnetization for a ferromagnetic or ferrimagnetic substance. It consists of the intrinsic crystalline anisotropy and the (much smaller) magnetostrictive anisotropy.[11] The intrinsic anisotropy in a solid can be thought of as an internal magnetic field which is due to spin-orbit interaction and which creates an *easy axis* in the crystal along which magnetic saturation can be achieved with the smallest magnetic field. The intrinsic anisotropy is caused by the (anisotropic) orbital motion which is determined by the crystal field. Taking into account only the intrinsic anisotropy Eq. 4.12 can be written as [11]

$$\omega_0 = \gamma B = \sqrt{\left(\gamma H_0 - \gamma H_d + \frac{\omega_M}{\mu_0 M_{\text{sat}}} H_a\right)(\gamma H_0 - \gamma H_d)}, \tag{4.14}$$

where $H_a = 2K_1/M_{\text{sat}}$ is the anisotropy field with K_1 the first-order anisotropy constant and M_{sat} the saturation magnetization. Typical values of K_1 for ferrites are between -0.01 and 0.4 J/cm^3.

The resonance phenomenon described up to now is purely valid for ferromagnets. When the resonance condition is satisfied, the ac electromagnetic field is uniform over the sample and perpendicular to $\mathbf{B}$, then all spins will precess in phase. This uniform precession is called a *spin wave* with wave vector $k = 0$, and is the magnetic analog of a phonon. The dispersion relation for a ferromagnetic magnon in a cubic lattice at small $\mathbf{k}$ in an external magnetic field is[12],

$$\hbar\omega_k = \gamma H_0 + 4JSa^2k^2, \tag{4.15}$$

where S is the total spin on site, J is the exchange constant and a is the lattice parameter. The ferromagnetic magnon dispersion is quadratic, which implies that the spin wave has an *effective mass.*

The situation for an antiferromagnet is slightly different. At finite temperatures, an antiferromagnet can be regarded as a ferrimagnet which consists of two magnetic sublattices with magnetization $\mathbf{M}_1, \mathbf{M}_2$, respectively, that are equal and oppositely directed to each other at $T = 0$. The dispersion relation for a 3-dimensional antiferromagnet is in the limit of $\mathbf{k} \to 0$ [13],

$$\hbar|\omega_{\mathbf{k}}^{\pm}| \propto \sqrt{(2JzS)^2k^2 + (9 + 12z|J|)S^2} \;\pm\; \gamma\hbar H_0, \tag{4.16}$$

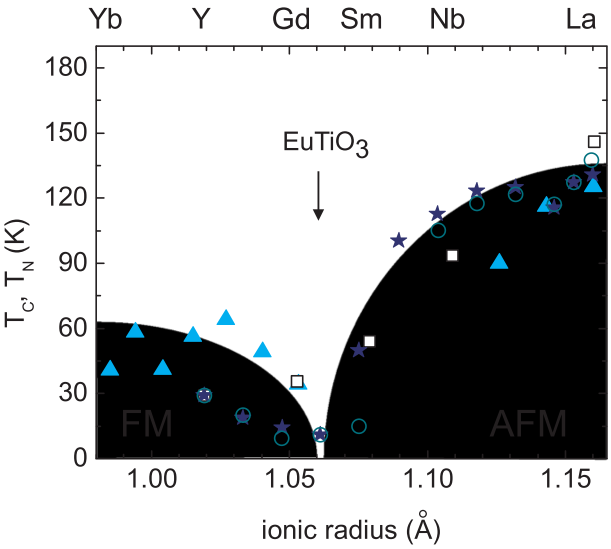

Figure 4.2: Magnetic phase diagram of rare-earth titanates. Adapted after ref. [28]. EuTiO$_3$ is close to the FM and AFM phase boundary.

and thus [14]

$$\omega_0 = \gamma\sqrt{H_a^2 + 2H_aH_E} \pm \gamma H_0, \tag{4.17}$$

where $H_E = 2|J|zS/g\mu_B$ is the exchange field. At $H_0 = 0$ the dispersion relation of an antiferromagnet is thus gapped and double degenerate at $T = 0$ due to the fact that there is a clockwise and anti-clockwise precession, each belonging to a sublattice. In case the external field and the anisotropy field are zero, $\hbar|\omega_{\mathbf{k}}^{\pm}|$ vanishes as a function of $|\mathbf{k}|$ [13].

4.2 Introduction to EuTiO$_3$

Quantum paraelectric EuTiO$_3$ recently received attention due to the possibility to possess magneto-electrical coupling without excluding the presence of multiferroicity. [19, 20] The system is of interest since besides the proximity to a *ferroelectric* instability, like the other quantum paraelectric compounds (SrTiO$_3$, KTaO$_3$, CaTiO$_3$), it also has a magnetic instability towards a *ferromagnetic* ordering, which can be achieved in a modest external magnetic field of 1.5 T. The fact that EuTiO$_3$ is a band insulator with a small effective gap of about 1 eV [32], which can become easily ferromagnetic and probably also ferroelectric makes it of particular interest for the field of spintronics. The narrow, almost unhybridized Eu 4f band lies in the fundamental gap and if this band comes into play it is mostly sufficient to consider atomic europium. A recent study on different rare-earth titanates shows the position of EuTiO$_3$ in the magnetic phase diagram (Fig. 4.2), which is localized at the point where both T_N and T_C of the lighter

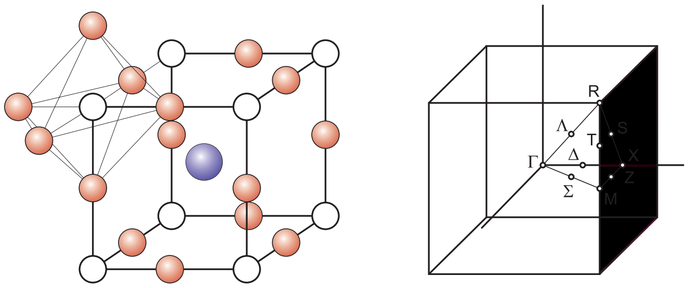

Figure 4.3: (a) Simple cubic ABO_3 perovskite crystal structure with around each corner Ti atom an octahedron of oxygen atoms. (b) First Brillouin zone for the simple cubic lattice.

and heavier rare earths vanishes, respectively. This demonstrates the instability between the formation of a FM and AFM phase.

$EuTiO_3$ can be considered as the magnetic relative of $SrTiO_3$. They both have a simple cubic perovskite structure at room temperature with a lattice constant of 3.905 Å. On cooling down, as far as is known, $EuTiO_3$ does not have the antiferrodistortive phase transition characterized by rotating oxygen octahedra and it remains presumably cubic down to the lowest temperatures. Like $SrTiO_3$ it possesses an instability towards a ferroelectric state which for very low temperatures gets hindered by quantum fluctuations [15]. The proximity to this transition is demonstrated by the static dielectric constant, which for $EuTiO_3$ is very large compared to typical AFM insulators (around 400) [17] but relatively small compared to $SrTiO_3$ (10^4), which is almost ferroelectric. The main difference with $SrTiO_3$ is that $EuTiO_3$ is magnetic due to the seven parallel spins on the Eu site which form a $4f^7$ state and thus $S = 7/2$ and $L = 0$ and the Landé factor $g = 2$. Because of the spin-only character, the anisotropy field is expected to be very small. Neutron diffraction at low temperatures has shown that $EuTiO_3$ orders antiferromagnetically below $T_N = 5.5$ K in a G-type structure [22]. The dc magnetic susceptibility shows a Curie-Weiss behavior with a positive characteristic Weiss temperature of $\Theta = 3.8$ K, which is remarkable for an AFM. With the molecular field theory one can calculate from T_N and Θ the nearest neighbor and next-nearest neighbor exchange constants, $J_1/k = -0.014$ K and $J_2/k = +0.037$ K, respectively. The two dominant interactions are the superexchange between two Eu ions through the oxygen and the indirect exchange via the Eu 5d orbitals. The first one is a 180° bond which is antiferromagnetic, the second a 90° bond which is ferromagnetic. Since there are no 180 degree bonds in $EuTiO_3$, the ferromagnetic interaction should prevail below 5.5 K, which is apparently not the case. Most probably, because of the small exchange constants, the little exchange field and the small critical temperature push the system close to a magnetic instability and a prediction of the magnetic state with these kind of simple arguments is not adequate. Application of a small external magnetic field aligns the Eu spins and at $1-1.5$ T the material becomes ferromagnetically ordered.

The low energy dielectric properties of EuTiO$_3$ are determined by a TO phonon, similarly to SrTiO$_3$. This triply degenerated F$_{1u}$ mode is the movement of the Ti cation against the oxygen octahedra, which induces an electric polarization and is thus optically active. At room temperature the triply degenerate mode is around 13.6 ± 0.6 meV and decreases down to 9.5 meV at T_N.[18] Previous studies of EuTiO$_3$ also reported a change of the quasi static dielectric constant ϵ_1 with magnetic field. In zero field, ϵ_1 decreases below T_N by 3.5 % and at 2 K it increases by 7 % in a magnetic field of 1.5 T. Therefore it is tempting to conclude that the soft mode follows the magnetic order in this compound. The authors suggested that the changes in ϵ_1 were related to the magneto-electrical coupling via the pair correlation function of neighboring Eu spins and thus to the soft phonon mode. They further conclude that the hybridization between the Eu orbitals and the O 2p orbital is varied depending on the configuration of the Eu spins, which modifies the frequency of the F_{1u} mode that contains Eu-O stretching motion.[17] It should be mentioned that invoking a behavior of the soft mode based on quasi dc data can be misleading when other phenomena are observed on an energy scale between the two. Susceptibility data of Katsufuji *et al.* [17] and dielectric permittivity data of Kamba *et al.* [18] show the presence of Maxwell-Wagner effects[3] which makes the validity of using the Lyddane-Sachs-Teller relationship questionable.

EuTiO$_3$ can be electron doped by introducting La^{3+} on the Eu^{2+} site [23], Nb^{5+} on the Ti^{4+} site [24] or by creating oxygen vacancies [25]. Elemental Eu becomes superconducting at 2.8 K at 142 GPa because of a valence change of Eu from divalent to trivalent [26]. It is however unknown if EuTiO$_3$ also becomes superconducting upon pressure or doping.

4.3 Band structure

For the AFM structure, Dr. Igor I. Mazin (Naval Research Laboratory, Washington D.C., USA) has performed first-principles density-functional calculations using the linear augmented plane wave method as implemented in the WIEN2K code and the generalized gradient approximation for the exchange-correlation potential in the form proposed by J.P. Perdew *et al* [29]. Fermi-surface integrals were evaluated using the k-point meshes up to $28 \times 28 \times 28$. The LDA+U calculation has been performed by taking into account the on-site Coulomb repulsion on the 4f site, $U = 6.8$ eV, the crystal field splitting and spin-orbit splitting. The

---

[3] The Maxwell-Wagner effect is an interfacial relaxation process occurring in systems where the electric current must pass an interface between two different dielectrics, e.g. between grains. The dispersion in ϵ (often in the kHz to GHz range) is due to a conductance in parallel with a capacitance for each dielectric, so that the interface can be charged by the conductivity [27].

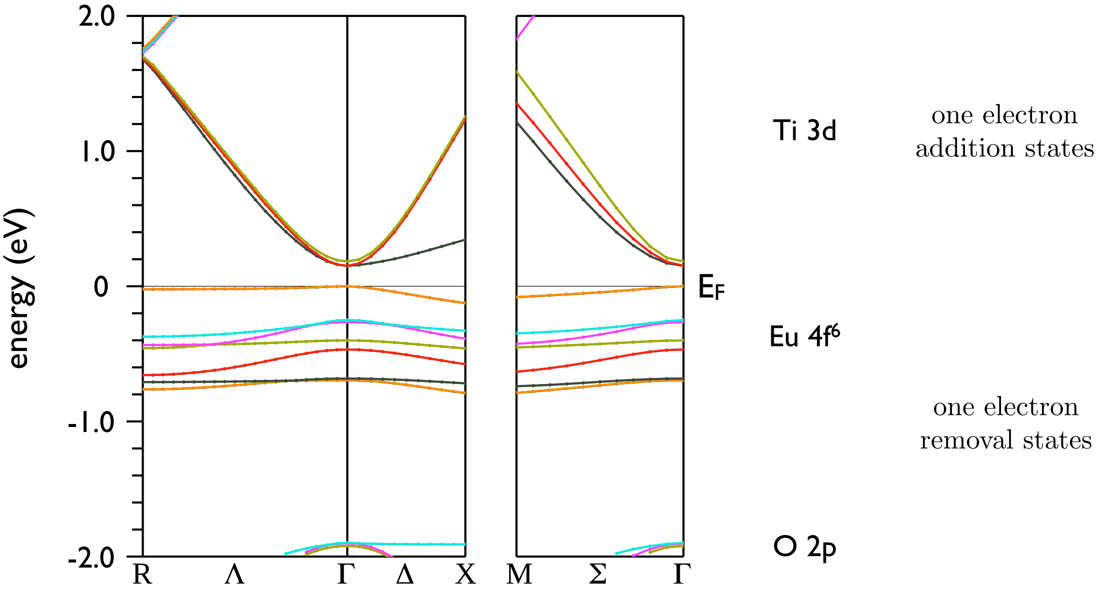

Figure 4.4: LDA+U band structure of AFM insulating $EuTiO_3$ in the excited state. Visible are the one electron removal states (O 2p and Eu $4f^6$) and the one electron addition states (Ti 3d).

exchange interaction $J = 0.82$ eV. Fig. 4.4 shows the band structure of insulating $EuTiO_3$ in the AFM state. Just visible is the low lying valence band, mainly formed by the O 2p states, above it the three slightly degenerate (empty) Ti t_{2g} conduction bands and in between the $4f^6$ levels. These very localized states each contain a spin-up electron and their mutual splitting is due to the crystal field and the spin-orbit interaction. Notice that the conduction band is very similar to the one of $SrTiO_3$. Further evidence for this is the effective mass on electron doping, which for Nb doped $SrTiO_3$ is $m^*/m_b = 3.0 \pm 0.4$ (see Chapter 2) and for oxygen depleted $EuTiO_3$ $m^*/m_b = 3.1 \pm 0.4$ (cf. section 4.5).

4.4 Sample preparation and characterization

Sample preparation

Polycrystalline $EuTiO_3$ pellets have been synthesized by Dr. Taras Kolodiazhnyi at the National Institute for Material Science (NIMS) in Tsukuba, Japan. Stoichiometric amounts of the raw products of Eu_2O_3 (Kanto Chemicals, Japan) and TiO_2 (Wako, Japan) have been mixed in ethanol using stabilized zirconia balls. The mixtures were compacted and heat-treated at 1100 − 1200 °C in flowing hydrogen at 100 cm^3/min. This procedure leads to reduction of TiO_2 to Ti_2O_3 and its subsequent reaction with Eu_2O_3 to form $EuTiO_3$. The phase purity was confirmed by the powder X-ray diffraction (XRD) analysis. Several alternative

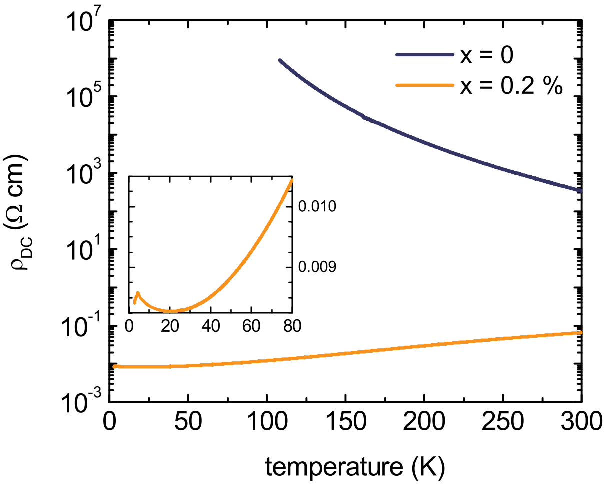

Figure 4.5: DC resistivity ρ_{DC} of pristine polycrystalline EuTiO$_3$ (blue curve) and oxygen depleted EuTiO$_{3-x/2}$ with $x = 0.2\,\%$ (orange curve) as a function of temperature. The inset shows the ρ_{DC} for $x = 0.2\,\%$ at low temperatures.

methods have been explored to sinter EuTiO$_3$ into dense polycrystalline bodies. Conventional pressureless sintering at 1360 °C resulted in poor density of around 80 %. To increase the density, several samples have been sintered in a Belt-type high-pressure high-temperature (HPHT) apparatus (Kobelco, Japan) at 6 GPa and T = 900–1000 °C. The samples prepared this way contained 5-10 % of Eu$_2$Ti$_2$O$_7$ pyrochlore impurity as revealed by the powder x-ray diffraction. To remove the pyrochlore phase, the as-sintered samples were treated in flowing hydrogen at 1300 °C for 20 hours. Although the relative density was improved to around 95 %, the disadvantage of the HTHP method is a limited diameter of the samples of maximum 6 mm. Later on, we adopted another method – spark plasma sintering – that allowed both very high density of the samples (of 97-98 %) and large sample diameter of $\geqslant$10 mm. Using the spark plasma sintering, the polycrystalline samples were prepared in the high-density graphite pressing dies under 100-130 MPa at 1350 °C. Short sintering time of 3-5 min ensured low concentration of the pyrochlore secondary phase that were further eliminated by the post-sintering annealing in hydrogen at 1200-1300 °C. The cylindrical pellets of 1-2 mm thick and 6-10 mm diameter were then sawn into disks of typically 300 μm thick and finished by optical polishing. The typical density of the utilized samples is around 96 %. This large value implies [18] that the static dielectric constant should be close to single crystal EuTiO$_3$, which is indeed the case [17]. The visual appearance is deep black with almost single crystal like shiny surfaces.

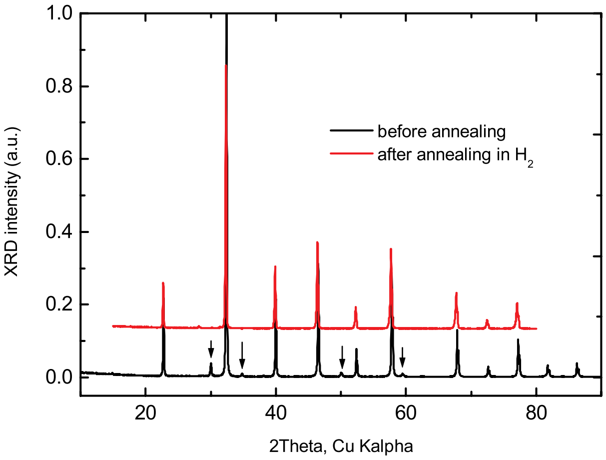

Figure 4.6: XRD 2θ scan of polycrystalline $EuTiO_3$ before and after annealing. Black arrows indicate the impurity phases before annealing.

DC resistivity

$EuTiO_{3-x/2}$ samples with $x = 0$ have a dc resistivity of typically $350\,\Omega$cm at 300 K which strongly increases and eventually seems to diverge below 100 K, as usual for an insulator (Fig. 4.5). Down to $\sim$ 160 K ρ_{DC} follows an Arrhenius behavior with activation energy of 95 meV. Metallic $EuTiO_{3-x/2}$ has been formed by oxygen depletion due to a longer exposure in an hydrogen atmosphere. The metallic sample has $x = 0.2\,\%$ electrons per unit cell as determined from Hall effect measurements at 6.0 K, i.e., in the paramagnetic phase. At 300 K, the resistivity (Fig. 4.5) is more than three orders of magnitude smaller than that of the insulating sample. ρ_{DC} slowly decreases with decreasing temperature, demonstrating that this sample is just on the metallic side of the insulator to metal transition. Below 20 K the resistivity increases again until the antiferromagnetic phase transition at 5 K. In this temperature region, ρ_{DC} follows an activated Arrhenius behavior with a very low characteristic energy of about 20 μeV.

X-ray diffraction

Fig. 4.6 shows two rocking curves (2θ scans) measured with standard X-ray diffraction spectroscopy (XRD). Before the annealing process traces of impurity phases are visible, but after annealing in an hydrogen environment, the XRD data show the $EuTiO_3$ diffraction peaks and demonstrate that less than 1% parasitic phases like pyrochlore $Eu_2Ti_2O_7$ are present.

Magnetometry

Fig. 4.7 shows the dc magnetization M of polycrystalline insulating $EuTiO_3$ as a function of temperature for applied magnetic fields between 1 mT and 1 T

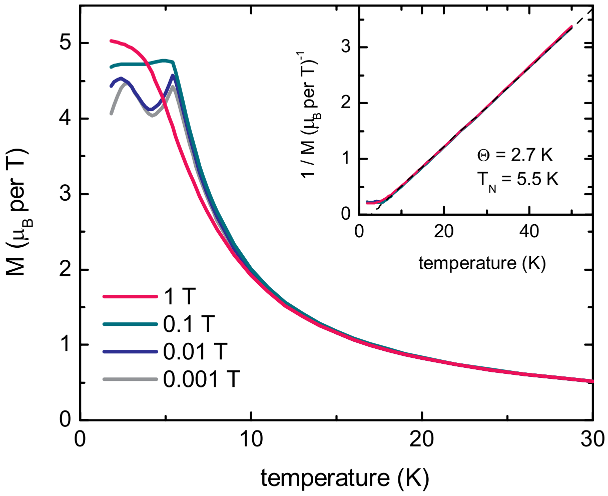

Figure 4.7: DC magnetization of polycrystalline EuTiO$_3$ as a function of temperature for some selected magnetic fields.

measured with a SQUID magnetometer by Ms. Corine Reibel (Université de Montpellier II, France). With decreasing temperature, the magnetization monotonically increases down to the Néel temperature which is characterized by a sharp change of the slope for low fields. The fact that M increases again below 4 K suggests that another ordering sets in, possibly a ferromagnetic one or a frustrated state like a spin glass[4]. At 1.8 K the magnetization reaches a value of $6.6\,\mu_B$ at 1.6 T which slowly increases up to $6.92\,\mu_B$ at 7.0 T. From the latter value one can conclude that the samples contain at least 98.9% Eu^{2+}. The inset of Fig 4.7 shows the inverse of the magnetization, which clearly demonstrates the Curie-Weiss behavior with Weiss temperature $\Theta = 2.7\,\mathrm{K}$ and $T_N = 5.5\,\mathrm{K}$.

Fig. 4.8 shows the magnetization as a function of applied field. The inset displays the hysteresis at selected temperatures, which is small but clearly present and thus indicates the ferromagnetic character. Fig. 4.9 shows the temperature dependence of the ac magnetic permeability for photon energies between 1 and 1000 Hz. A signature of the presence of a glassy state would be that the cusp in $\mu_1(T)$ increases with frequency, as observed for Mn:Cu [33]. Closer inspection to the inset of Fig. 4.9 shows indeed a positive shift of about 0.1-0.15 K. This means that below the antiferromagnetic phase transition at 5.5 K, there is a transition to a spin glass state around 3 K.

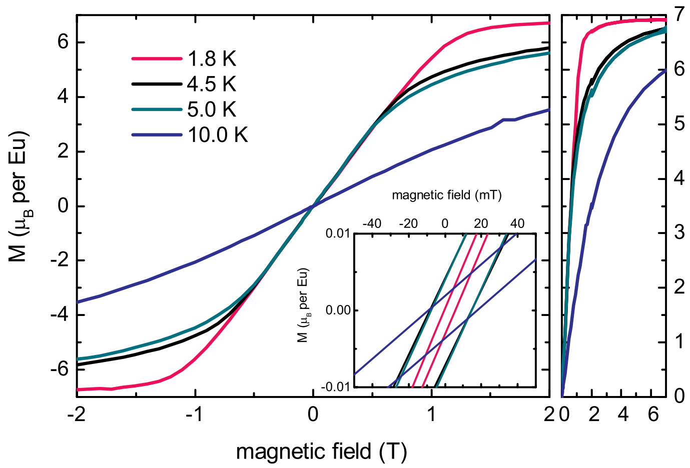

Figure 4.8: DC magnetization hysteresis loops of polycrystalline $EuTiO_3$ as function of applied magnetic field at 1.8 K, 4.5 K, 5.0 K and 10.0 K.

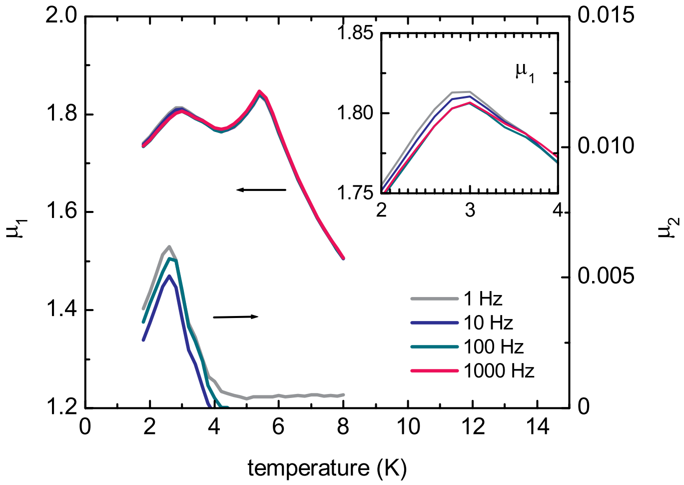

Figure 4.9: AC magnetic permeability $\mu = \mu_1 + i\mu_2$ of polycrystalline $EuTiO_3$ as a function of temperature for some selected frequencies. The inset shows μ_1 zoomed in onto the cusp at 3 K.

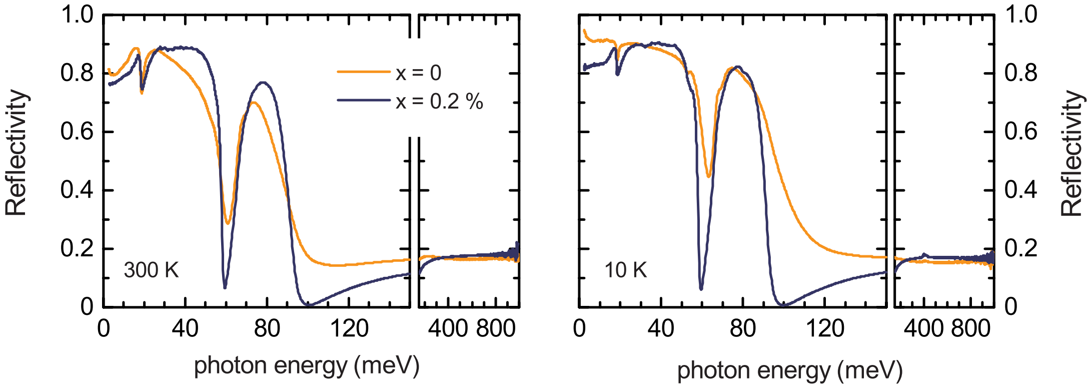

Figure 4.10: The infrared reflectivity of EuTiO$_{3-x/2}$ for $x = 0$ and $x = 0.002$ at 300 K (left panel) and 10 K.

4.5 Optical conductivity

The optical reflectivity of EuTiO$_{3-x/2}$ has been measured in the range between 2.5 meV and 1 eV for temperatures between 10 K and 300 K on a Bruker 113 and 66v Fourier Transform Infrared Spectrometer (Fig. 4.10). Visible ellipsometry in reflection has been measured between 0.75 and 6 eV with a Woollam VASE 32 ellipsometer. The sample has been cooled down in a home-built helium flow cryostat that minimizes the sample movement due to e.g. shrinkage of the cold finger. For the reflectivity measurements a gold reference coating has been evaporated on the sample at 300 K. For insulating EuTiO$_3$ THz spectroscopy (TPI 1000, Teraview Ltd.) could be done and provides the complex transmission of linearly polarized light between 0.12 and 3.7 meV. The optical conductivity is obtained from Kramers-Kronig analyses of the reflectivity spectra with Drude-Lorentz fits to the reflectivity, visible ellipsometric data and complex THz transmission. At 300 K, the optical conductivity for $x = 0$ (Fig. 4.11) shows three TO phonons at 12.8 meV, 22 meV and 68.2 meV, similar to SrTiO$_3$ (section 2.6.1) and in agreement with Ref. [18]. Notice the very asymmetric shape of the first one which is known to be the three fold degenerate ferroelectric F_{1u} soft mode. Above the phonons, $\sigma_1(\omega)$ increases for photon energies $\hbar\omega > 0.2$ eV and gets significant above 0.6–0.7 eV. This is probably due to excitations inside the crystal field split 4f band and excitations from the 4f to the 3d band. The strong increase of $\sigma_1(\omega)$ at higher energies reveals the fundamental gap (the onset of transitions of O 2p to Ti t$_{2g}$) to be roughly 3.4 eV, which is also very comparable to 3.25 eV of SrTiO$_3$. The main effect with lowering temperature is the soft mode which decreases down to about 9.1 meV.

Metallic, oxygen depleted EuTiO$_{3-x/2}$ with 0.2% charge carriers per unit cell

---

[4] The increase of M below the AFM phase transition is observed for insulating (and also metallic for $x < 0.01$) EuTiO$_3$ samples that have slightly lower values of ρ_{DC} at 300 K than pristine EuTiO$_3$.[24]

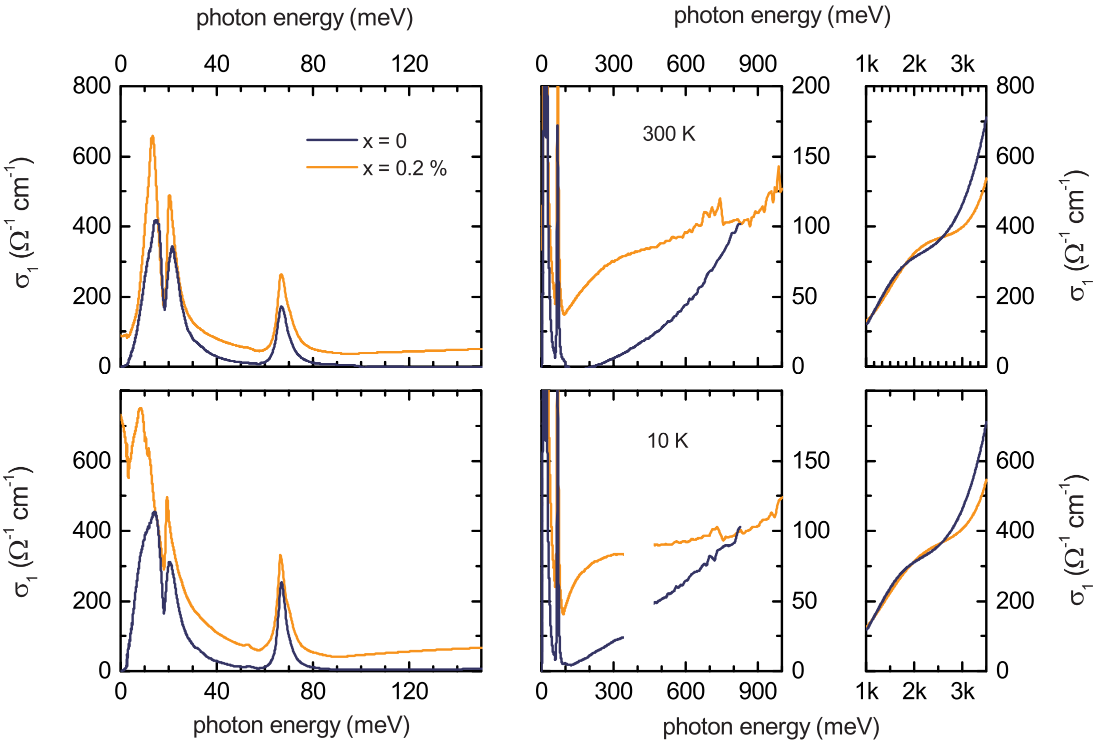

Figure 4.11: The real part of the optical conductivity $\sigma_1(\omega)$ of EuTiO$_{3-x/2}$ for $x = 0$ and $x = 0.002$ at 10 K and 300 K.

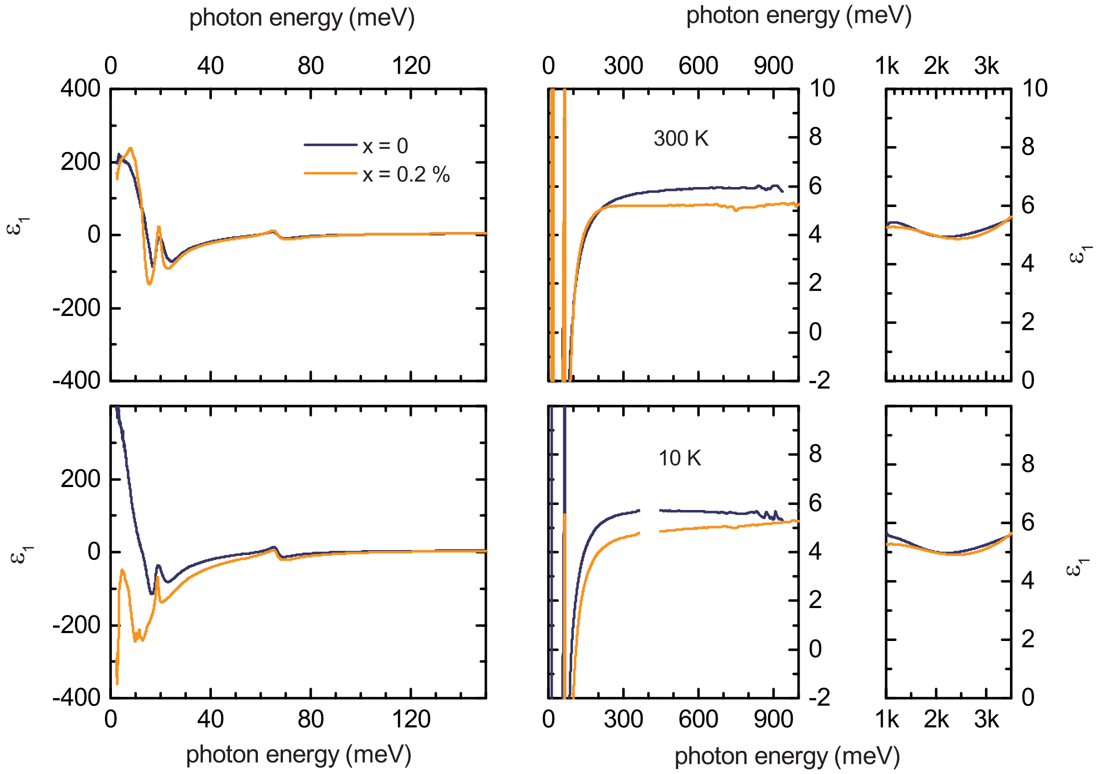

Figure 4.12: The real part of the dielectric permittivity $\epsilon_1(\omega)$ of EuTiO$_{3-x/2}$ for $x = 0$ and $x = 0.002$ at 10 K and 300 K.

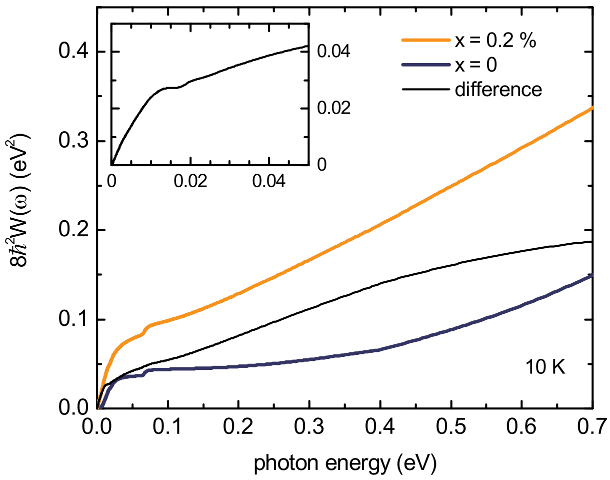

Figure 4.13: The integrated optical spectral weight of $\mathrm{EuTiO}_{3-x/2}$ for $x = 0$ and 0.002 as a function of photon energy at 10 K. The electronic spectral weight of metallic EuTiO_3 (black curve) is obtained by subtraction of the spectral weight of the insulating compound from the metallic one. The inset shows the low energy electronic spectral weight.

resembles the undoped case a lot: the optical phonons are roughly at the same energy, and the fundamental gap changes only slightly. The highest LO-mode (obtained from the zero-crossing of $\epsilon_1(\omega)$) is for $x = 0$ at 93 meV and shifts for $x = 0.2\,\%$ to 110 meV, very similar as for $\mathrm{SrTi}_{1-x}\mathrm{Nb}_x\mathrm{O}_3$: from 99 meV to 116 meV. A significant difference with the undoped sample is the strongly enhanced mid-infrared conductivity and a clear narrow Drude peak which becomes visible with decreasing temperature. Similar as for Nb doped SrTiO_3 we perform a spectral weight analysis using the f sum rule (cf. section 1.6.1). Integration up to a cutoff frequency ω_c then yields

$$W(\omega_c) = \int_0^{\omega_c} \sigma_1(\omega)\, d\omega \tag{4.18}$$

which is shown in Fig. 4.13. The electronic contribution $8W(\infty) = \omega_p^2 = 4\pi n e^2/m$ where e and m are the free electron charge and mass, and n is the electron density (in cgs units). The contribution of the infrared phonons manifests itself in $W(\omega)$ as steps, e.g. at 68 meV. When we apply the partial sum rule (Eq. 4.18) with $\omega_c = 15$ meV, which is larger than the Drude relaxation rate but below the soft phonon we obtain $\hbar\omega_p = 0.16 \pm 0.01$ eV. LDA calculations of the Drude plasma frequency of electron doped SrTiO_3 yield $\hbar\omega_{p,\mathrm{LDA}} = 0.28$ eV for $x = 0.002$. From this follows that the effective mass $m^*/m = 3.1 \pm 0.4$, very similar to Nb doped SrTiO_3 [30]. A clear mid-infrared polaronic band is probably not visible here because of the overwhelming spectral weight due to interband transitions inside the 4f multiplet. The observation of a mid-infrared band in e.g. the manganites or the cuprates raised the question if the origin of this band was due to spin-lattice or charge-lattice interactions. For a material without any spin degrees of freedom like SrTiO$_3$ chapter 2 evinced a clear manifestation of a charge-lattice interaction. In summary, despite the fact that we increase the material degrees of freedom by adding a nonzero magnetic moment on one of the ions, like EuTiO$_3$, the effective mass is largely the same in the paramagnetic phase (at 10 K).

4.6 Magneto-optics of EuTiO$_3$

4.6.1 Experimental setup

We briefly outline the experimental setup used for the magneto-optical measurements on EuTiO$_3$ which are reported and discussed further on in this section. We concentrate on the very low energy optical properties and study insulating EuTiO$_3$ in its only subgap transparency window. The main experimental technique that has been utilized is THz time-domain spectroscopy, as earlier discussed in section 1.8. Since an isotropic material placed in a magnetic field has polarization eigenstates which are circular (section 1.5.1) it is much more convenient for the interpretation of the experimental data to have the transmission measured for each chirality. We have therefore adapted the standard THz setup as described in chapter 2 with a home-built magnet (described below) and a set of remotely rotatable THz polarizers as outlined in section 1.5. The 2 inch polarizers (Microtech Instruments, USA) are made of free standing 10 μm thin tungsten wires mutually spaced by 25 μm. The reproducibility of their rotation is verified *in-situ* with a ccd camera by optical comparison.

The ultra compact superconducting magnet

Since magneto-optical measurements need an external magnetic field, and a conventional split-coil magnet does geometrically not fit into the sample compartment of the utilized THz spectrometer, an ultra compact superconducting 1.6 tesla magnet with a THz wavelength optical aperture has been developed for usage in a liquid helium flow cryostat. As depicted in Fig. 4.14 the magnet is attached to the copper block of a liquid helium flow cryostat and operates between 2.5 K and 7.5 K. In contrast to conventional bath cryostat magnets, there is no helium contact gas but a 10^{-7} mbar vacuum surrounding the sample compartment. Temperatures below 10 K are reached due to a novel thermal shielding which consists of both a multi-layer super-insulation blanket wrapped around the cold finger and specially designed thermally opaque but THz transparent screens mounted in the optical feedthrough of the aluminum thermal radiation shield. The coil of the superconducting magnet consists of an oxygen-free copper spindle with length of 22 mm and diameter of 31 mm. It has a concentrical hole with a diameter of 15 mm (and behind the sample 9 mm) which allows transmission of long-wavelength radiation. A 500 m long 115 micron thin isolated single filament

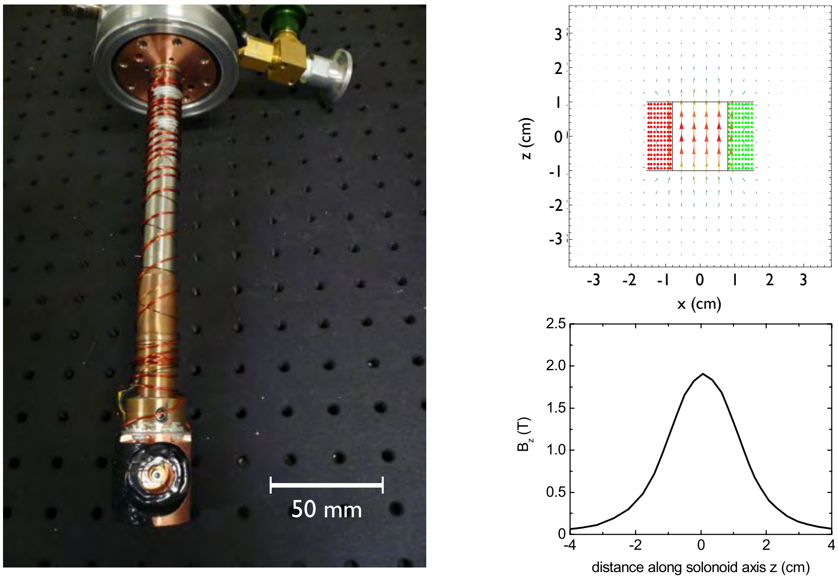

Figure 4.14: Photograph of the cold finger of the helium flow cryostat. The ultra compact superconducting magnet fixed with black Stycast^{TM} glue into a hollow cylinder that is attached to the bottom part of the cold finger. On the right: theoretical field distribution inside and outside the coil (courtesy to J. Hancock).

Cu/ NbTi (Cu:NbTi = 3:2) wire is regularly wound around the spindle. Thermal contact is assured by embedding each of the 50 layers in Stycast 2850^{TM} non-magnetic glue, which also fixes the wires and prohibits vibration. The spindle is housed in an oxygen-free copper cylinder, which is attached to the copper block of a Janis ST-100^{TM} liquid helium optical flow cryostat. The thermal heat shielding consists of the following parts: (i) a blanket of multi-layer super-insulation with two opposite 15 mm holes for optical feedthrough is wrapped around the cold finger including the coil, (ii) an aluminum radiation shield which is thermally attached to the top of the cold finger. Inside each optical feedthrough hole of this shield, (iii) a 150 μm thick glass window absorbs all the heat radiation and transfers it to the aluminum radiation shield. For temperatures below the critical current of NbTi (i.e., ~ 10 K) a dc current through the coil induces a very stable and (at the sample position) homogenous magnetic field inside the optical access which is 1.6 tesla for a relatively small current of 5.5 A at 1 V below 6 K. Fig. 4.14 shows the theoretical field distribution around the coil, which corresponds very well with the experimental situation. The off-axis stray field is less than 5 mT at 4 cm distance. The remanence of the magnet is too small to be measured, i.e. < 0.1 mT. Due to its tiny power consumption, quenching the ultra compact superconducting coil raises the temperature only by several degrees and operating conditions are gained back in a few seconds. The optical feedthrough in the ultra compact superconducting magnet allows transmission and reflection of frequencies down to the THz range for incidence angles between normal and 25°.

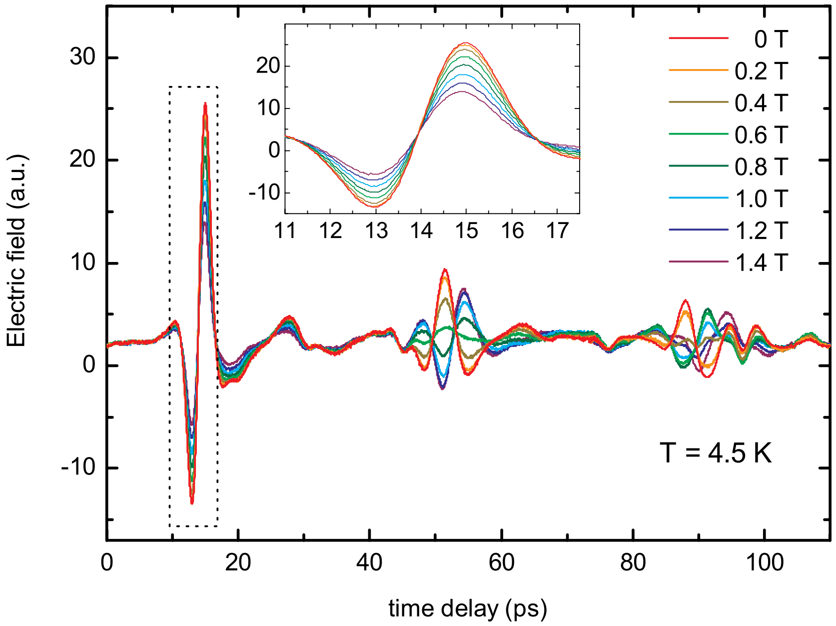

Figure 4.15: THz transmission of 315 μm thick undoped EuTiO$_3$ as a function of time delay and for several magnetic fields at 4.5 K for linearly polarized light. The inset shows the pulse only due to the straight transmission.

A particular advantage of the vacuum guard around the sample is the stability of the transmission/reflection signal contrary to conventional bath cryostat magnets where the sample is surrounded by boiling liquid helium (for $T > 1.9$ K).

4.6.2 Faraday rotation

Fig. 4.15 shows the THz transmission of 315 μm thick undoped EuTiO$_3$ as a function of delay time and external magnetic field. The polarizer and analyzer are both parallel to the light polarization. With increasing delay time the figure shows first the straight transmission, then the first internal reflection (first echo) and the second internal reflection. With increasing magnetic field the electric field decreases for the straight transmission, whereas for the first echo it eventually also flips sign. Since the electric field change of the first echo is close to three times the one of the straight transmission the observed magneto-optical effect suggests to be a rotation of the light polarization.

To check this idea, we rotated the analyzer which is placed behind the sample by an angle α and recorded time-domain spectra for each analyzer position. In this way, not only the rotation of the incident linearly polarized light can be measured, but also possible changes of the polarization from linear to e.g. elliptical. Fig. 4.16 shows the extrema of the straight transmission pulse as a function of the analyzer angle for a 265 μm thick EuTiO$_3$ platelet and a reference hole of 8 mm diameter. The precision of the setup can be read off from the perfect gonio-

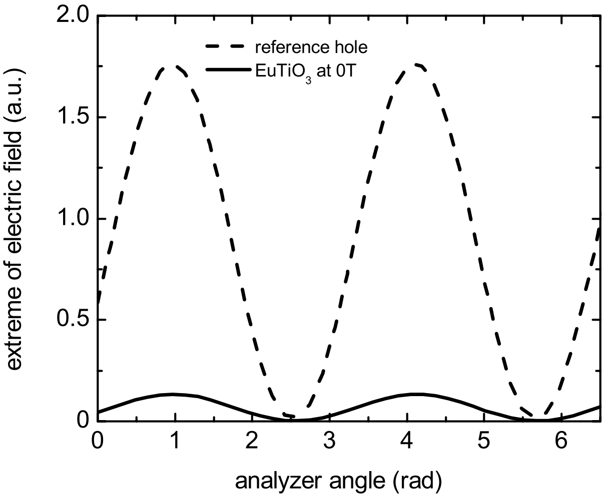

Figure 4.16: Extrema of the time-domain electric field spectra as a function of analyzer angle of the reference hole (dashed curve) and of a 265 micron thick $EuTiO_3$ sample at 4.5 K (solid curve).

metric shape and from the reproducible signal level when the analyzer rotates by 180°. When an external magnetic field is switched on, as in Fig. 4.15, and we let the analyzer scan we obtain Fig. 4.17. The maxima in this figure correspond to the situation where the main polarization axis of the THz light is parallel to the analyzer. With decreasing magnetic field the maximum intensity shifts to larger angles, which means a rotation of the polarization. An indication of the finite ellipticity of the polarization is given by the signal offset compared to the zero field offset, which increases with the applied magnetic field.

In order to follow the procedure as described in secion 1.7.2 to obtain the dielectric permittivity and magnetic permeability from the complex transmission of right and left handed circular polarized light, we proceed as follows. The time-domain spectra of the sample and the reference are fitted to the relationship $\mathcal{E}(\alpha) = \mathcal{E}_{xx}\cos^2\alpha - \mathcal{E}_{xy}\cos\alpha\sin\alpha$. Since the $EuTiO_3$ time-domain spectra allow for a clear separation of the straight transmission pulse and for the first internal reflection pulse, this procedure has been followed for both pulses separately. This provides time-domain spectra for left and right handed circular polarized light (hereafter LCP and RCP, respectively) by the relation

$$\mathcal{E}_{\pm} = \mathcal{E}_{xx} \pm i\mathcal{E}_{xy}, \tag{4.19}$$

which yields for the straight transmission and for the first echo. Subsequently all the as-obtained RCP and LCP time-domain spectra are Fourier transformed to obtain their frequency dependence. Division by the frequency dependent electric field of the reference hole provides the complex transmission of circularly polarized THz light. As described in section 1.7.2 this is in principle enough to obtain analytically $\epsilon(\omega)$ and $\mu(\omega)$. However, it turns out that in case of $EuTiO_3$

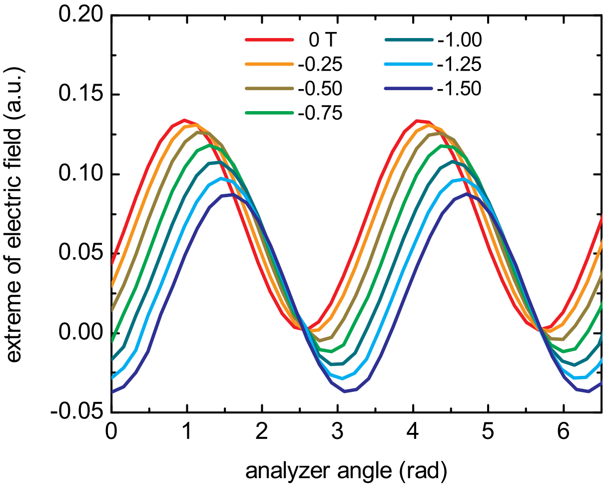

Figure 4.17: Extrema of the time-domain electric field spectra as a function of analyzer angle for some selected magnetic fields at 4.5 K.

the straight transmission is fundamentally different from the first echo and the described procedure gives mainly unphysical results. A reason for this could be that nonlinear effects come into play for which the linear Fresnel equations do not account, as has been reported [31] and predicted [8] before in case of ferromagnetic resonance. For this reason, in the following only the straight transmission will be considered.

Fig. 4.18 shows the amplitude and phase of the straight transmission at THz photon energies for LCP and RCP separately. The main trend is a decreasing transmission amplitude and a rapidly increasing phase with photon energy which is due to the proximity of the ferroelectric soft mode. At very low energies a sharp absorption can be observed in the amplitude for both LCP and RCP which increases in strength with increasing magnetic field, as clearly demonstrated by the detail view of Fig. 4.20. Notice that at 0 T the energy of the absorption is about the same for LCP and RCP light, but the magnetic field behavior for both chiralities is quite distinct. For LCP the absorption becomes stronger but remains at quasi the same energy, whereas for RCP the transmission minimum shifts with the applied magnetic field and also changes strength. The shift is about linear with H above $\sim$1.2 T. The feature shows up in the phase as a step of about π radians[5] which is in general only caused by some typical processes which will be reviewed later. Please notice that on reversal of the magnetic field direction, the behavior for LCP and RCP light also reverses, pointing to a fully symmetrical magneto-optical phenomenon.

From the LCP and RCP transmission we obtain the polarization state of the

---

[5] As a comparison, please notice that a resonance described by a Lorentzian shows up in the phase closely to the lineshape of $\epsilon_1(\omega)$ superposed on a straight line which increases with the photon energy.

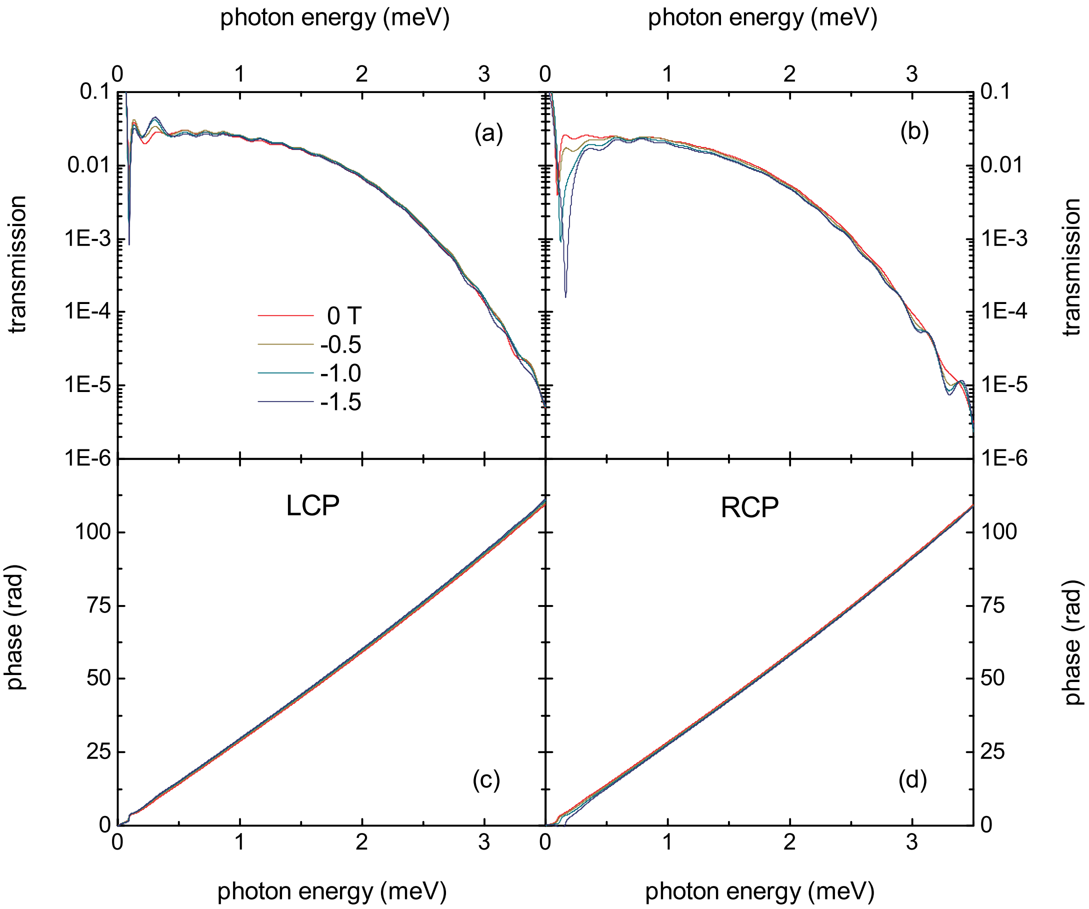

Figure 4.18: Complex transmission of 265 μm thick $EuTiO_3$ as a function of photon energy in the THz range and for several external magnetic fields at 4.5 K. Panels (a) and (b) display the transmission amplitude for LCP and RCP, respectively. Panels (c) and (d) display the phase for LCP and RCP, respectively.

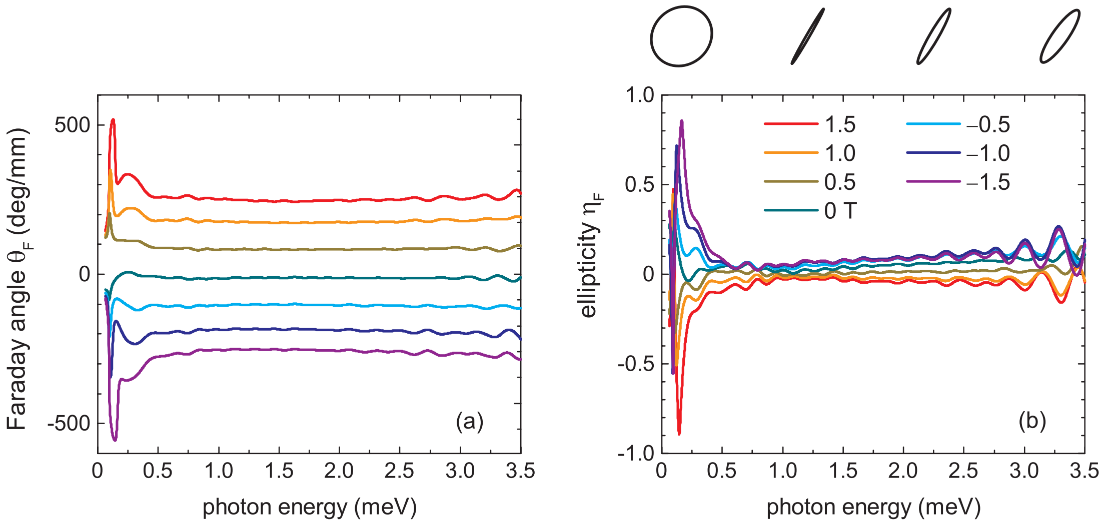

Figure 4.19: (a) Faraday angle θ_F and (b) ellipticity η_F of the transmitted light polarization as a function of photon energy for some selected magnetic fields at 4.5 K. The oscillations above 2.5 meV are artificial and due to the very low transmission level. The cartoons above panel (b) show the evolution of the polarization state at four selected photon energies.

light after transmission through the sample which is characterized by the rotation angle θ_F and the ellipticity η_F by Eq. 1.57. Fig. 4.19 shows both quantities as a function of photon energy for some selected magnetic fields. The rotation in a magnetic field, generally called *Faraday rotation*, increases in a magnetic field up to values of 170 $\mathrm{deg\,mm^{-1}T^{-1}}$ in a broad frequency range, which attains even values up to 340 $\mathrm{deg\,mm^{-1}T^{-1}}$ between 0.10 – 0.15 meV. These are very large rotations, and to the best of our knowledge by far the largest at THz energies[6]. At the same photon energies where θ_F is maximum, also the ellipticity increases and almost approaches 1, which implies fully circularly polarized light. At this photon energy there is thus just one polarization state that is transmitted, whereas the other is entirely absorbed. This demonstrates the presence of a very pure magnetic circular dichroism in EuTiO$_3$, which is fully symmetrical in the magnetic field (Fig. 4.19). The origin of such a phenomenon can be the following processes: (*i*) a purely electric dipole transition from the Eu 4f levels to the Ti t_{2g} conduction band, (*ii*) a purely magnetic dipole transition inside the Eu 4f levels or (*iii*) a transition of a mixed electric dipole and magnetic dipole character. The first and the third option imply transitions at energies of the order of the effective band gap energy of 1 eV [32] which means that the Faraday rotation at THz wavelengths

---

[6] Materials which also have large Faraday angles in the THz range are molecular magnets like the Mn$_{12}$Ac [35] which has a maximum rotation of about 130 $\mathrm{deg\,mm^{-1}T^{-1}}$ at the resonance energy of 1.25 meV which rapidly falls of to zero ±0.07 meV away from the transition. Others are the ferrites and garnets which have typical maximum rotations of 10 deg/mm in the microwave X band (around 0.04 meV) [11].

is negligible. The only plausible option is a magnetic dipole transition inside the Zeeman split 4f levels. As discussed before (cf. section 1.5) upon absorption of a photon its angular momentum is transferred to the system. For a purely magnetic dipole transition it is the spin angular momentum, and thus the total magnetization of the system, that alters. In the FM state, the $4f^7$ configuration has seven parallel spins up and only photons that decrease the total spin angular momentum can be absorbed, i.e. only RCP light will be absorbed in case the light propagation vector is antiparallel to the external magnetic field direction. For a $g = 2$ system the Zeeman energy is about 0.12 meV per tesla which is *a priori* compatible with a polarization rotation below 4 meV, as observed. A material which is AFM ordered, like $EuTiO_3$ in zero field, has two sublattices which each have an equally large but opposite magnetic moment. Such a material absorbs thus both chiralities with equal probability. The energy of the spin resonance is given by the exchange field and anisotropy field (cf. Eq. 4.17). A priori this energy is expected to be small due to the spin-only character of $EuTiO_3$, which implies a very small anisotropy field due to the negligible spin-orbital mixing. On the other hand, when the magnetic field (antiparallel to the light propagation vector) increases, the Larmor frequency for LCP light should decrease whereas it should increase for RCP. The experimental transmission data (Fig. 4.20) show that the absorption which increases with magnetic field indeed only occurs for RCP which is compatible with a magnetic dipole transition between the Zeeman split 4f levels as just discussed. However, the peak in LCP is static with the magnetic field which can not be reconciled with an AFM resonance. Above we shortly mentioned that this feature shows up in the phase as a step of about π radians. Phase changes of this size occur only at rather unique situations, namely at (*i*) reflection of light at an interface (as seen for thin $SrTiO_3$ where the frequency dependent transmission takes various echos into account, cf. Fig. 2.15) or at (*ii*) a so-called geometrical resonance. A geometrical resonance is a resonance of an electromagnetic wave which occurs when it transmits through an obstacle which is at the diffraction limit and which allows for resonance. A simple hole does not, but a small box with the size of the wavelength placed behind the hole does allow for resonance.[36] The first possibility of an internal reflection is rejected by the fact that only the straight transmission is taken into account. To verify the presence of the second we measured the transmission of 475 μm thick $SrTiO_3$ at 300 K in front of the same 8 mm hole. The dielectric constant of $SrTiO_3$ at 300 K is about 300, which makes the product $d\sqrt{\epsilon}$ comparable to 265 μm thick $EuTiO_3$ at 4.5 K. Figure 4.21 shows the transmission amplitude and phase of both $EuTiO_3$ and $SrTiO_3$ for *linearly* polarized light. Remarkably, the transmission amplitude of $SrTiO_3$ also shows a minimum at approximately the same photon energy and the phase has an equally large step of about π rad at this energy. Since $SrTiO_3$ has no magnetic moments, an AFM or FM resonance is excluded for this compound. We thus conclude that the origin of the low energy peak at zero field for both LCP and RCP light in $EuTiO_3$ is not magnetic but simply a

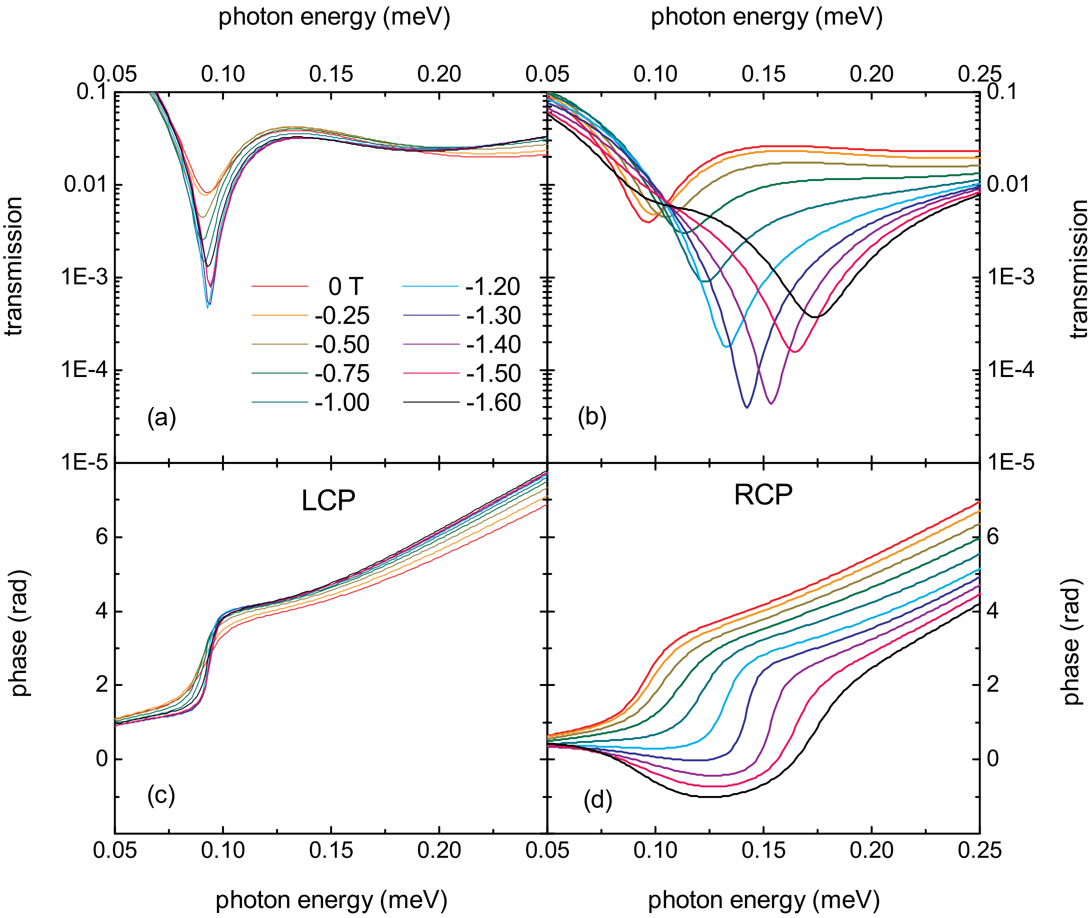

Figure 4.20: Detail views of the amplitude and phase of Fig. 4.18 of 265 μm thick EuTiO$_3$ as a function of photon energy in the THz range and for several external magnetic fields at 4.5 K. Panels (a) and (b) display the transmission amplitude for LCP and RCP, respectively. Panels (c) and (d) display the phase for LCP and RCP, respectively.

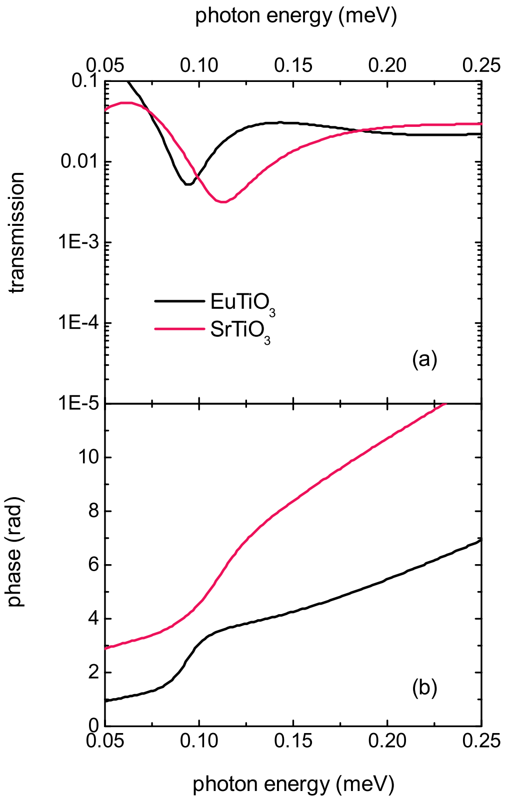

Figure 4.21: Transmission (a) and phase (b) of 265 μm thick EuTiO$_3$ at 4.5 K (black) and of 475 μm thick SrTiO$_3$ at 300 K (red) for *linearly* polarized light.

geometrical resonance effect. At relatively large magnetic fields, above 1 T, the ferromagnetic resonance has been shifted far enough away from the geometrical resonance to be well separated from it. The reason behind the unusually large Faraday rotation is that EuTiO$_3$ has a very high density of magnetic moments per unit volume, which results in a strong dichroism.

4.6.3 Determination of $\epsilon(\omega)$ and $\mu(\omega)$

As argued in the preceding section, the observed absorption around $0.1-0.2$ meV for RCP light above 1 T is due to ferromagnetic spin resonance. This resonance is provoked by a purely magnetic dipole transition between the Zeeman split Eu 4f levels, and should show up solely in the magnetic permeability function $\mu(\omega)$. The procedure that we will follow to obtain $\mu(\omega)$ is as follows. The complex transmission data as shown in Fig. 4.18 have been inverted into the dielectric permittivity function $\epsilon(\omega)$ by the procedure expounded in section 1.7.1. The result is shown in Fig. 4.22. To obtain the unperturbed low energy part of $\epsilon(\omega)$, a Drude-Lorentz fit has been made to $\epsilon(\omega)$ between 1.25 meV and 3.7 meV using only a single oscillator which represents the ferroelectric soft mode. The as-obtained $\epsilon(\omega)$ has been

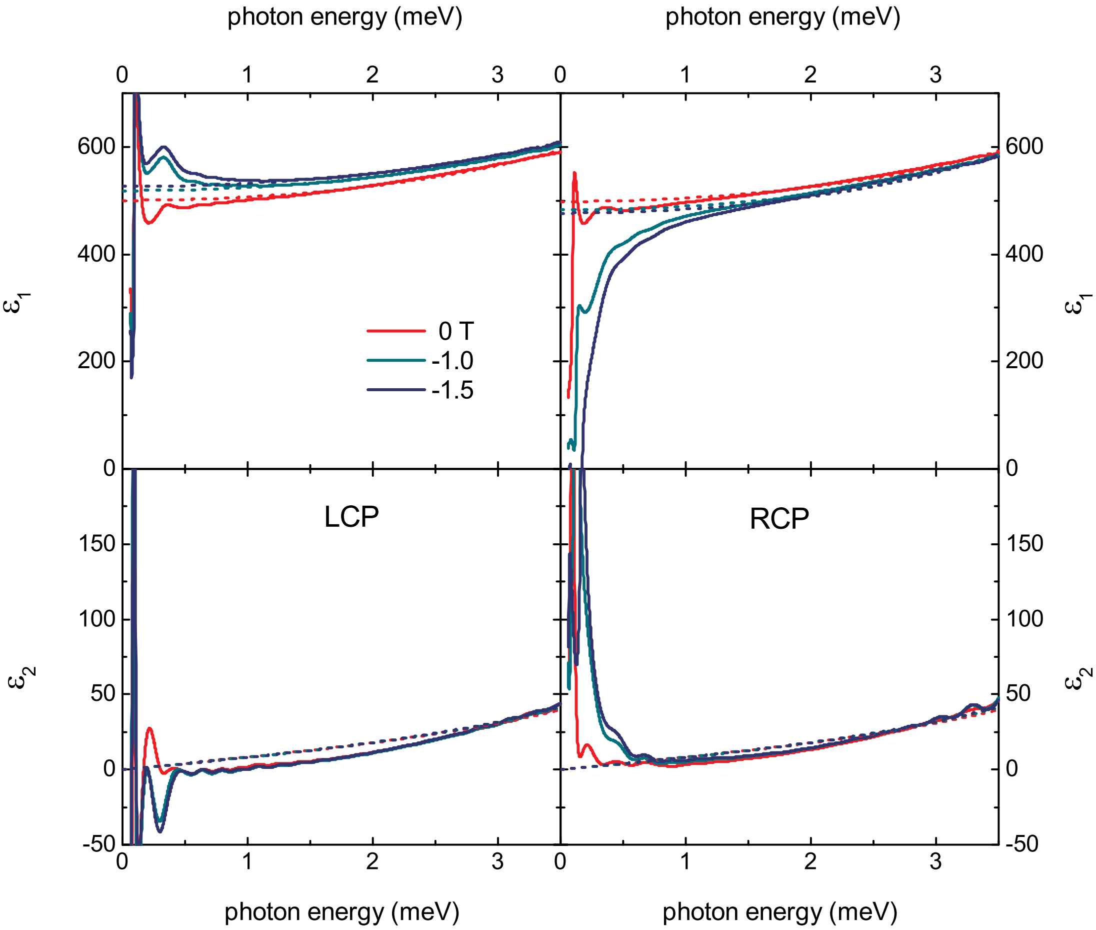

Figure 4.22: Real and imaginary part of the dielectric function $\epsilon^{\pm}(\omega) = \epsilon_1^{\pm}(\omega) + i\epsilon_2^{\pm}(\omega)$ for LCP and RCP light for some selected magnetic fields. Inverted data are represented by solid lines, Drude-Lorentz fits above 1.25 meV are shown by dotted lines.

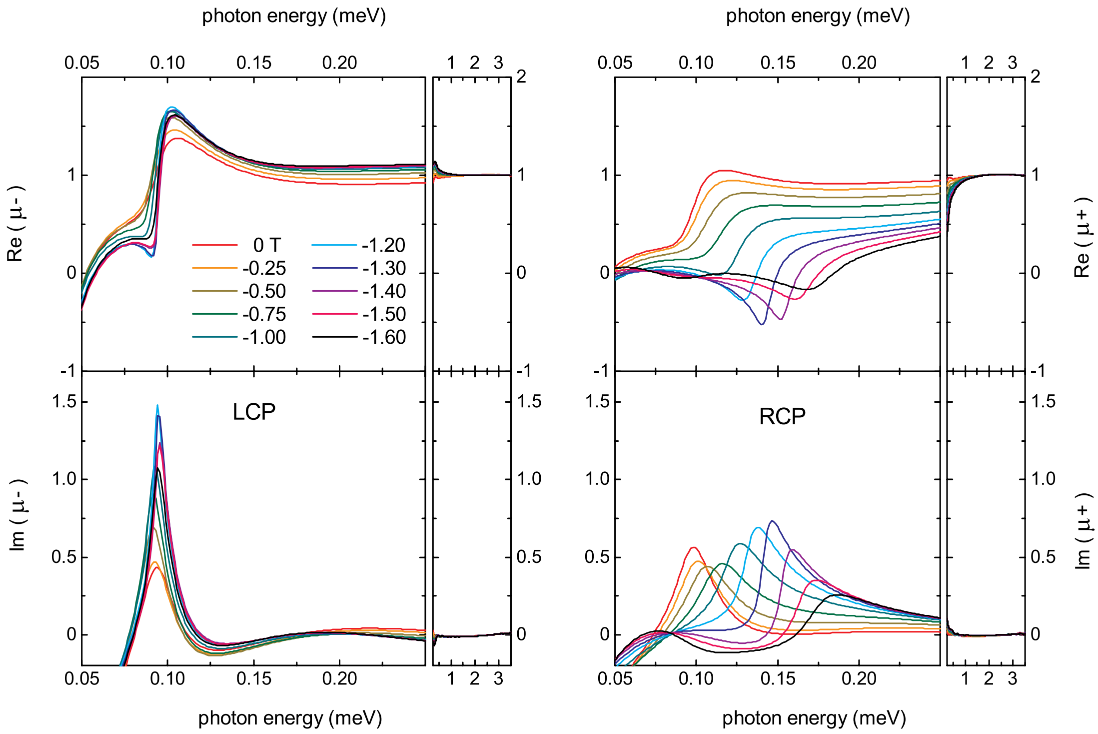

Figure 4.23: Real and imaginary part of the magnetic permeability function $\mu^{\pm}(\omega) = \mu_1^{\pm}(\omega) + i\mu_2^{\pm}(\omega)$ as a function of photon energy and magnetic field.

used for the direct inversion of the original complex transmission data in order to obtain $\mu(\omega)$, as shown in Fig. 4.23. At low energies the imaginary part of $\mu^+(\omega)$ shows a peak which is coming from the ferromagnetic resonance, as motivated before. The real part of $\mu^+(\omega)$, however, has for low magnetic fields a lineshape which is different from a standard Lorentz-like behavior of $\epsilon_1(\omega)$. This is most probably due to the fact that the geometrical resonance (which provokes the peak at zero and low magnetic fields) is not described by the Fresnel equations used to calculate $\mu(\omega)$ and $\epsilon(\omega)$ from the transmission coefficients. At energies above the resonance, Fig. 4.23 shows that $\mu_1 \rightarrow 1$ and $\mu_2 \rightarrow 0$ for both LCP and RCP light, which is physically expected and equal to the high energy behavior of $\epsilon(\omega)$. The fact that the low energy excitation is present in $\mu(\omega)$ and not in $\epsilon(\omega)$ is also evinced by experimental data of the quasi static dielectric constant as measured by Katsufuji *et al.* [17] which show a change of only 7 % in a magnetic field of ~ 1.6 T. In case the excitation would be present in $\epsilon(\omega)$ this would induce huge changes of ϵ_0, which are not observed.

4.6.4 Ferromagnetic spin resonance in EuTiO$_3$

Fig. 4.23 shows the magnetic permeability of EuTiO$_3$, a system which evolves from an AFM ground state to a magnetic field induced FM state. It is for the

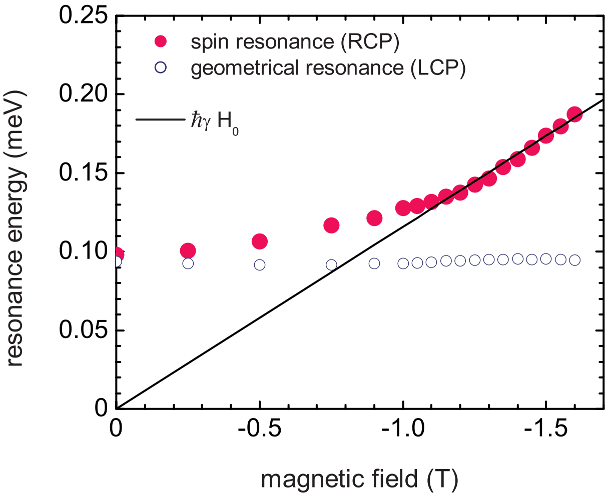

Figure 4.24: Resonance energy of the spin resonance from RCP light and the geometrical resonance from LCP light. The solid line shows the bare Larmor energy $\hbar\omega_0 = \hbar\gamma H_0$ for $g = 2$.

first time that the magnetic permeability of a ferromagnetic resonance which is purely due to magnetic dipole transitions has been measured. The magnetic permeability (Fig. 4.23) shows a peak at the ferromagnetic resonance which shifts with the magnetic field. The slightly negative values of $\mu_2(\omega)$ below the resonance are not described by the linear response theory which prescribes $\mu_2(\omega)$ to be positive definite, but have nevertheless also recently been observed for SrRuO$_3$ [9]. Also $\mu_1(\omega)$ shows a line shape which is not described by the Landau-Lifshitz-Gilbert equations. It may therefore be that either the geometrical resonance influences the $\mu(\omega)$ landscape for low photon energies or that there is indeed an emission of light as predicted by Ref. [8] caused by the FM resonance.

When we plot the maxima of dynamical permeability $\mu_2^{\pm}(\omega)$ as a function of magnetic field we get Fig. 4.24, which shows the magnetic field dependence of the ferromagnetic resonance (+) and the geometrical resonance (−). It is clear that at higher fields, where the spin resonance energy exceeds the geometrical resonance energy, the behavior is linear and agrees well with the bare Larmor energy $\hbar\omega_0 = \hbar\gamma H_0$ for a system with Landé factor $g = 2$, which is the case for EuTiO$_3$. In the used geometry, where the magnetic field is directed perpendicular to the sample surface, the demagnetization field is zero. The data match well with the bare Larmor energy which proves that the anisotropy field is negligibly small and as far as the 4f multiplet is concerned, the spin-orbit interaction is absent. This confirms the presumption that EuTiO$_3$ is a spin-only material and that the spin resonance is of purely magnetic character.

Another interesting quantity to look at is the electronic spectral weight of $\mu_2(\omega)$ and to compare it to the spectral weight expected for a ferromagnetic

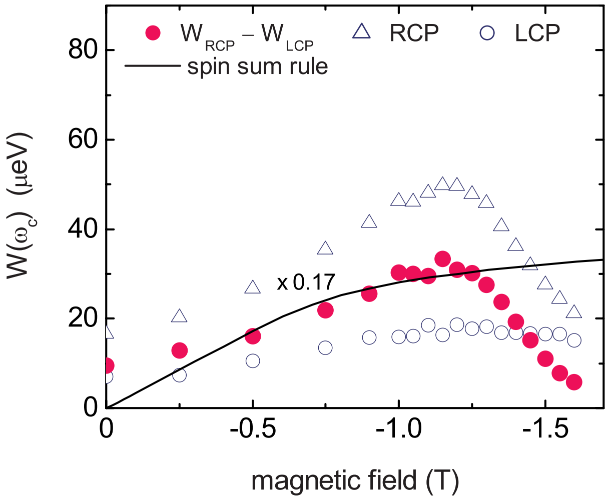

Figure 4.25: Integrated experimental spectral weight $W(\omega_c)$ as a function of magnetic field for LCP and RCP light compared to the spin sum rule of Eq. 4.21 (black line, for clarity multiplied by a factor 0.4). The difference between the spectral spectral weight of the ferromagnetic resonance (RCP) and of the geometrical resonance (LCP) is shown by red dots.

resonance in EuTiO$_3$. We define the integrated spectral weight $W(\omega_c)$ as

$$W(\omega_c) = \int_{\omega_0}^{\omega_c} \mu_2(\omega)\, d\omega \tag{4.20}$$

where $\hbar\omega_0 = 0.06$ meV and $\hbar\omega_c = 3.7$ meV, the lowest and the highest limit of the THz transmission spectrum, respectively, and is plotted in Fig. 4.25 for both chiralities. This experimentally obtained spectral weight should satisfy the *spin sum rule* as derived in section 1.6.2, which yields the *total* electronic spectral weight due to magnetic dipole excitations

$$W = \int_{0}^{\infty} \mu_2(\omega)\, d\omega = \frac{\pi}{2}\mu_0\gamma M, \tag{4.21}$$

where γ is the gyromagnetic ratio and M the magnetization. The magnetization has been obtained from the experimentally determined dc magnetic susceptibility (cf. Fig. 4.8). Fig. 4.25 shows the experimentally obtained spectral weight of LCP and RCP light and the difference between them. The spectral weight of LCP light is purely due to the geometrical resonance and is of course not included in the derivation of Eq. 4.21. Since the geometrical resonance is also present in RCP light, W_{LCP} has been subtracted from W_{RCP} to obtain the total spectral weight due to the ferromagnetic spin resonance. The black line in Fig. 4.25 shows the last term of Eq. 4.21 multiplied by a factor $\frac{1}{6}$. Like the magnetization, the theoretical spectral weight almost linearly increases and levels off for larger magnetic fields. It is immediately clear that the theoretical spectral weight is about a factor 6

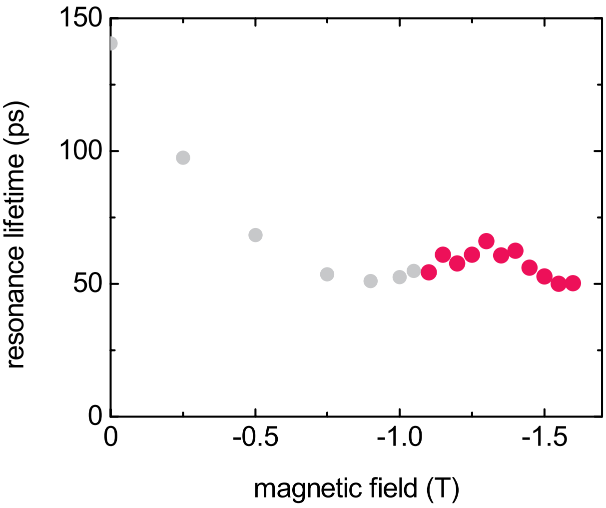

Figure 4.26: Indication of the spin lifetime τ obtained by taking the ratio of the maximum value of $\mu^{+}(\omega)$ and the integral of $\mu^{+}(\omega)$. Values of τ which are obtained in the magnetic field range where the ferromagnetic resonance and the geometrical resonance (partially) overlap are indicated by gray dots.

larger than the experimental one for fields below 1.2 T. An explanation for the missing spectral weight may be that not all magnetic dipole transitions are at exactly the Zeeman energy, as shown in Fig. 4.24. In the experimental data this hypothesis is supported by the constant Faraday angle θ_F and the increasing ellipticity η_F as a function of photon energy. The only situation which gives a Faraday angle which is independent of photon energy is when the photon energy is in between two dichroic transitions. On the other hand, an increase of the ellipticity as a function of photon energy always means the approach towards a dichroic transition. An example of the opposite case of a single dichroic transition has been observed for Mn$_{12}$Ac, where θ_F and η_F rapidly change between 1.08 and 1.15 meV [35]. Apart from the missing spectral weight, a large discrepancy between the experimental spectral weight and the spin sum rule is the decrease of $W(H)$ above 1.2 T. Although the exact origin is unknown, it could be due to strong exchange interactions between the neighboring Eu spins, which takes away spectral weight from the resonance phenomenon.

The peaks in $\mu_2(\omega)$ show up as being asymmetric, probably due to the fact that the geometrical resonance is mixed with the spin resonance. A fit to these peaks to obtain the spin lifetime is therefore *a priori* questionable and would possibly induce large errorbars which are hard to estimate. However, in order to get any idea of the spin lifetime τ we crudely took the ratio of the maximum of $\mu^{+}(\omega)$ and the integral of $\mu^{+}(\omega)$, as is shown in Fig. 4.26. We concentrate only on magnetic fields above 1.1 T where the ferromagnetic resonance and the geometrical resonance are clearly separable. τ first slightly increases up to ~ 1.3 T and then decreases. It is remarkable that this decrease occurs at the same field

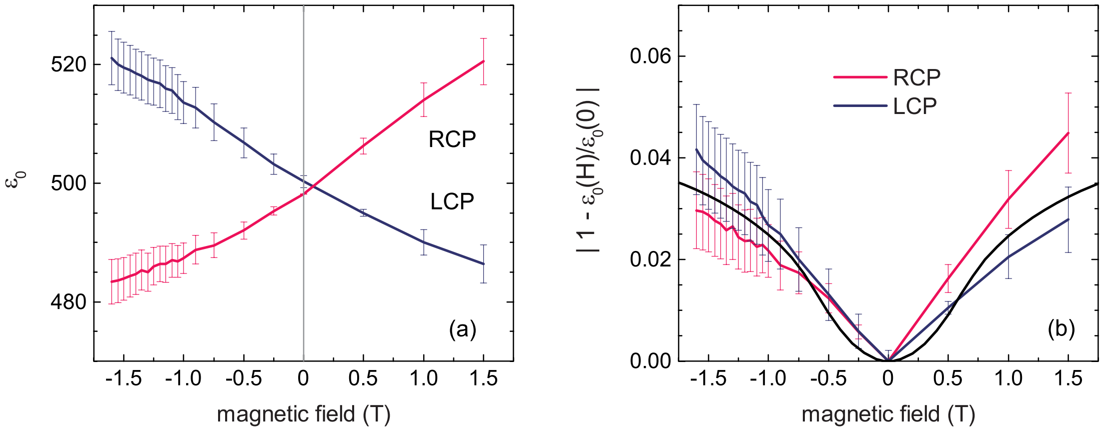

Figure 4.27: (a) Static dielectric constant ϵ_0 as a function of magnetic field for LCP and RCP light at 4.5 K. (b) Relative change of ϵ_0 versus magnetic field for LCP and RCP light at 4.5 K. The black line is $[M(H)]^2$ at 4.5 K.

as the decrease of the spectral weight.

It may be the right moment to motivate the rejection of the transmission data of the first internal reflection. Fig. 4.26 shows that the lifetime is about 50-65 ps, which is longer then the time difference between the straight transmission and the first echo (cf. Fig. 4.15). This means that the system is not yet fully relaxed from the straight transmission pulse when the internally reflected pulse goes through the sample. A system which is close to displaying non-linear effects will thus definitely cease to behave linearly when it gets excited from its excited state instead of from the relaxed ground state.

4.6.5 An antiferromagnetic vs. ferromagnetic ground state

As mentioned in section 4.2, Katsufuji *et al.* [17] suggested the presence of spin-lattice coupling in EuTiO$_3$ which involves a magnetic field dependent hybridization between the Eu orbitals and the O 2p orbitals and thus a magnetic field dependent soft mode frequency. They predict a change of the soft mode frequency of 3.5% in a magnetic field > 1.5 T at 2 K. Our Drude-Lorentz fits to the complex transmission data as described in the previous subsection provide the phonon frequency ω_0, the plasma frequency ω_p and the scattering rate γ. However, the highest photon energy which still permitted a detectable transmission is about 3.7 meV, well below the soft mode energy of $8.5 - 9$ meV. This makes it hard to estimate the errorbars of the fit parameters individually. However, the static dielectric constant ϵ_0 on the other hand can be obtained with a quite good accuracy, and is depicted in Fig. 4.27. The errorbars are determined by making different Drude-Lorentz fits where each time one of the three parameters is fixed to the zero-field value. Panel (b) shows the relative change of ϵ_0 in a magnetic field, and is about $3 - 4\%$ at 4.5 K. Notice the sharp behavior at small fields which has also been observed for the ferromagnetic insulator SeCuO$_3$ [34]. As mentioned in Ref. [34], for a ferromagnet M is a strongly nonlinear function of H due to the switching of domains. This means that based on ϵ_0 EuTiO$_3$ would be ferromagnetic instead of the previously claimed antiferromagnetic [22]. However, the DC magnetization squared shows a behavior different from Fig 4.27. At small fields its dependence on H is smooth which points to an AFM behavior, like the AFM insulator TeCuO$_3$ for instance [34]. This reveals an interesting situation where the static response on low magnetic fields suggests an AFM ordering while the ac response is FM. For large magnetic fields, both the dc and ac behavior show an almost linear dependence on H, which is characteristic for a ferromagnet, as expected for EuTiO$_3$.

4.7 Conclusions

A time-domain study in the THz range on insulating EuTiO$_3$ has revealed the existence of a strong magnetic circular dichroism which manifests itself as a gigantic Faraday rotation of THz light up to 340 deg mm^{-1}T^{-1}. We have performed ellipsometric transmission measurements at low temperatures in a magnetic field up to 1.6 T, from which we deduced the dielectric permittivity and the magnetic permeability for right and left handed circularly polarized light. Due to the spin-only character of EuTiO$_3$ the dichroism is present for *purely* magnetic dipole transitions inside the Zeeman split Eu 4f levels and shows up as a ferromagnetic spin resonance absorption for only one chirality. To the best of our knowledge it is for the first time that such a spin resonance has been studied as a function of photon energy and applied magnetic field. It therefore serves as an experimental verification of the well-established theories including e.g. the Landau-Lifshitz-Gilbert equations, which have proven their validity in magnetic field space but rarely in frequency space. The ferromagnetic resonance energy is well described by the bare Zeeman energy without any corrections like demagnetization effects. The spectral weight of the resonance below 3.7 meV is only about a sixth of the expected spectral weight as described by the spin sum rule. It is very likely that magnetic dipole transitions between the crystal field split 4f levels are situated at higher energies, which could not be detected by the present measurement technique. Indications for this are the Faraday angle which is large and energy independent above the spin resonance and the ellipticity which increases towards higher energies. Both phenomena require the presence of a higher energy excitation which is dichroic.

Infrared reflectivity measurements on oxygen depleted EuTiO$_3$ show a clear free carrier Drude absorption which is well separated from the lowest ferroelectric soft mode. A spectral weight analysis of $\sigma_1(\omega)$ has shown that the effective electron mass in EuTiO$_{3-x/2}$ with $x = 0.2\,\%$ is 3.1 ± 0.4 which is very similar to Nb doped SrTiO$_3$. This suggests that in the paramagnetic state, the charge carriers in $EuTiO_{3-x}$ are coupled in the same manner to the phonons as they are in $SrTi_{1-x}Nb_xO_3$.

The magnetic ground state of $EuTiO_3$ remains an open question. While old neutron diffraction data of the 1960s concluded an AFM ordering below 5.5 K, which is confirmed by our dc magnetic susceptibility data, the magnetic field dependence of ϵ_0 invoked from THz transmission data suggest a FM ground state, which in turn is supported by simple exchange interaction arguments. The frequency dependence of $\mu_1(T)$ as measured by ac magnetometry gives us the impression that the true ground state is a spin glass. From this it may be clear that insulating $EuTiO_3$ is extremely close to a magnetic instability where the AFM, the FM and the spin glass states closely compete. It would therefore also be a perfect toy material to study quantum critical phenomena by applying small magnetic or electric fields.

Bibliography

[1] V.K. Arkad'Yev, J. Russ. Phys. Chem. Soc. **44**, 165 (1912).

[2] Ya.G. Dorfman, Z. f. Phys. **17**, 98 (1923).

[3] L.D. Landau and E.M. Lifshitz, Phys. Z. Sowietunion **8**, 153 (1935).

[4] J.L. Snoek, Philips. Tech. Rev. **8**, 353 (1946).

[5] J.L. Snoek, Nature **160**, 90 (1947).

[6] J.H.E. Griffiths, Nature **158**, 670 (1946).

[7] T.L. Gilbert, Phys. Rev. **100**, 1243 (1955), T.L. Gilbert, IEEE Trans. Mag. **40**, 3443 (2004).

[8] M.C. Hickey and J.S. Moodera, Phys. Rev. Lett. **102**, 137601 (2009).

[9] M.C. Langner, C.L.S. Kantner, Y.H. Chu, L.M. Martin, P. Yu, J. Seidel, R. Ramesh and J. Orenstein, Phys. Rev. Lett **102**, 177601 (2009).

[10] D. Polder, Phil. Mag. **40**, 99 (1949).

[11] B. Lax and K.J. Button, *Microwave Ferrites and Ferrimagnets*, McGraw-Hill book company, Inc (1962).

[12] D.D. Stancil and A. Prabhakar, *Spin Waves, theory and applications*, Springer (2009).

[13] K. Yosida, *Theory of Magnetism*, Springer (1996).

[14] C. Kittel, Phys. Rev. **82**, 565 (1951).

[15] A. Bussmann, H. Bilz, R. Roenspiess and K. Schwarz, Ferroelectrics **25** 343 (1980).

[16] T. Katsufuji and Y. Tokura, Phys. Rev. B **60**, R15021 (1999).

[17] T. Katsufuji and H. Takagi, Phys. Rev. B **64**, 054415 (2001).

[18] S. Kamba, D. Nuzhnyy, P. Vaněk, M. Savinov, K. Knížek, Z. Shen, E. Šantavá, K. Maca, M. Sadowski and J. Petzelt, Europhys. Lett. **80**, 27002 (2007).

[19] S.J. Gong and Q. Jiang, Phys. Stat. Sol. (b) **241** 3033 (2004).

[20] C.J. Fennie and K.M. Rabe, Phys. Rev. Lett **97**, 267602 (2006).

[21] C.-L. Chien, S. DeBenedetti and F. de S. Barros, Phys. Rev. B **10**, 3913 (1974).

[22] T.R. McGuire, M.W. Shafer, R.J. Joenk, H.A. Alperin and S.J. Pickart, J. Appl. Phys. **37**, 981 (1966).

[23] K.S. Takahashi, M. Onoda, M. Kawasaki, N. Nagaosa, and Y. Tokura, Phys. Rev. Lett. **103**, 057204 (2009).

[24] T. Kolodiazhnyi, private communication.

[25] K. Kugimiya, K. Fujita, K. Tanaka, K. Hirao, J. Magn. Magn. Mater. **310** 2268 (2007).

[26] M. Debessai, T. Matsuoka, J. J. Hamlin, J. S. Schilling and K. Shimizu, Phys. Rev. Lett. **102** 197002 (2009).

[27] S. Grimnes and Ø.G. Martinsen, *Bioimpedance and bioelectricity basics*, Academic Press (2000).

[28] A.C. Komarek, H. Roth, M. Cwik, W.-D. Stein, J. Baier, M. Kriener, F. Bourée, T. Lorenz and M. Braden, Phys. Rev. B **75**, 224402 (2007).

[29] J. P. Perdew, K. Burke and M. Ernzerhof, Phys. Rev. Lett. **77**, 3865 (1996).

[30] J.L.M. van Mechelen, D. van der Marel, C. Grimaldi, A.B. Kuzmenko, N.P. Armitage, N. Reyren, H. Hagemann and I.I. Mazin, Phys. Rev. Lett **100**, 226403 (2008).

[31] P.E. Wigen (ed.), *Nonlinear phenomena and chaos in magnetic materials*, World Scientific Publishing Co. Pte. Ltd., Singapore (1994).

[32] J. H. Lee, X. Ke, N.J. Podraza, L. Fitting Kourkoutis, T. Heeg, M. Roeckerath, J.W. Freeland, C.J. Fennie, J. Schubert, D.A. Muller, P. Schiffer and D.G. Schlom, Appl. Phys. Lett **94**, 212509 (2009).

[33] C.A.M. Mulder, A.J. van Duyneveldt and J.A. Mydosh, Phys. Rev. B **23**, 1384 (1981).

[34] G. Lawes, A.P. Ramirez, C.M. Varma and M.A. Subramanian, Phys. Rev. Lett **91**, 257208 (2003).

[35] J. van Slageren, S. Vongtragool, A. Mukhin, B. Gorshunov and M. Dressel, Phys. Rev. B **72**, 020401(R) (2005).

[36] D. van der Marel, Nanostructures Physics and Fabrication, 149 (1989).

Acknowledgements

The actual basis of this Thesis was in May 2004 when Dirk decided to have a student on a still unexplored project, on a subject different from usual. Soon afterwards a novel time-domain spectrometer for measuring in the THz range was bought, at that time the fourth in the world. From the moment that data could be taken, Dirk was always in to have a never-very-short discussion on the physics behind the measurements resulting in banal but understandable to fairly exotic ideas. Dirk, you have taught me how to think in condensed matter physics while doing very interesting basic research. I am very pleased with your guidance which was sometimes tight but always left room for self-initiative, even for choosing the subject of Chapter 3 and 4. You really 'saved' Chapter 4 by once turning on one of the tens of adjustment screws in the THz spectrometer, just the one to let reappear the signal to an unequalled level. Dirk I admire your passion and ingenuity which made these five years a very pleasant time for me. Thanks a lot!

I wish to thank Prof. Jean-Marc Triscone, Prof. Paul van Loosdrecht, Prof. José Lorenzana and Prof. Christoph Renner for being member of this thesis committee. Thank you for very carefully reading the manuscript, for your comments and questions.

A great appreciation goes to Prof. Jozef Devreese, who I met in summer 2007. I knew about your work before, but this period made it clear to me that you are one of the wold's greatest expert on polarons. I learned a lot from the discussions we had during your visits in Geneva. I also have to thank you especially for section 2.9 and for thoroughly reading the thesis.

Many thanks to Alexey, with whom I shared the office for more than five years, and who was very helpful to introduce me to the measurements in the beginning of the thesis work. After this begun the almost endless time of data fitting, which I had also done before but never to this extent. Fitting data from 0.1 meV to 7 eV in 6 different ranges, for 8 different quantities at 75 temperature points and for 5 doping concentrations seemed to be desperate, but you made time to help me and gave me insight in the procedure how to tackle this ostensibly impossible task.

I am moreover sincerely grateful to Claudio Grimaldi and Peter Armitage, who helped me finding my way in condensed matter physics. Claudio you always explained the theory with a very practical and pedagogical touch, such that it suddenly becomes much more comprehensible for an experimentalist. You even prepared me for my first group meeting on SrTiO$_3$. I admire your enthusiasm, always in for a coffee at the EPFL while explaining me the real physics behind the 3ème cycle lecture, which was then just finished. Peter, I enjoyed the time we were together in the group. You were always there, at the most crazy times when I came in the building, and always up for a little chat. I will never forget that one night in winter 2006 when we were together in the lab during the first field-effect experiment. Unbelievable to see a phonon moving when turning on a knob!

I liked the time we spend with the Italian gang: Riccardo, Fabrizio, Francesco and Joachim (although not officially Italian, I'm sure his blood is). We had a great time, did a lot together and I still admire the change from the Science II cafeteria to UniMail, where the lunch became sometimes very Burgundian. Ricci, I am more than obliged to thank you especially. Without you there was no good working Bruker 66 spectrometer, no BlackOctopus, nor the Pink or the Green :) and you were of essential help during the organization of the Swiss Physical Society conference in 2008 when you programmed the participation web site and thought about a sustainable backup against various earth catastrophes. Grazie mille!

Jason, I liked the scientific discussions we had. You were always willing to hear about new results and often had a clear vision on the subject that I still had to study. Thanks a lot and I hope that you will enjoy your experiments on the THz machine.

Merci beaucoup à toi Roland et tout ton équipe de l'atelier méchanique. C'était un grand plaisir de travailler avec un tel groupe qui est toujours enthousiaste de construire une pièce solide, quoique il m'ait fallu du temps de m'habituer à vos horaires très différents des miens. Roland, j'ai apprécié les discussions sur mes dessins de construction et toutes tes vérifications techniques. Grâce à la bobine miniature dont tu as fait le châssis j'ai pu effectuer les mesures magnétiques du Chapitre 4.

I wish also to thank Hans Hagemann and Andreas Hauser who made it possible to do measurements up to 7 eV with their newly acquired spectrometer, and later also EPR. Hans, being a chemist you always saw different aspects of a spectrum then me, and I like that we were able to mutually help each other.

Un grand remerciement à Corine Reibel qui a fait une grande partie des mesures de la susceptibilité magnetique statique avec le SQUID de l'Université de Montpellier II. J'ai bien aimé de travailler avec toi, toujours là et jamais de soucis pour une mesure additionnelle.

Je veux aussi exprimer mes reconnaissances pour le service d'hélium de Spiros Zanos avec qui c'était toujours possible de négocier pour avoir un dewar plein d'hélium tout de suite. Merci Spiros, sans toi beaucoup des mesures pendant le weekend n'auraient pas eu lieu.

Cor and Mehdi, I'm grateful to your technical assistance during these years. Cor, you always surprised me how many very useful details of the lab and the instruments you knew. Mehdi, we often had our own ideas of approaching a specific problem, but at the end we always agreed. Thanks to the both of you.

Of major importance for the social support was the Afro-Persian team, 'The Group'. It started knowing some people, and then suddenly we were a tight group: Niloufar, Sareh, Asmaa, Amir, Bahareh, Parisa, Hela, Hanane, Nesrine, Maryam, Sadegh, Mona and Mojdeh. I think that the food at Sciences II was honestly not very healthy, but the better was it to be together at lunch.

I also have to thank my good friend with whom we started in Amsterdam. Robin, you introduced me to the swiss culture and showed me how good life in Switzerland can be. During our regular mountain hikes we always exchanged our physics projects and I'm sure we will write a nice paper together about the old Amsterdam results.

I should not forget the social support of the theoretical 'Giamarchi' group: Gladys, Aníbal, Sebastian, Vivien, Alejandro, Piotr, Elisabeth and Pierre. I enjoyed the coffee breaks with you which were often accompanied with some good swiss chocolate. Especially with you Gladys we had a lot of fun for about four years. I will never forget the bike trips we had together. Especially to Evian, you in rose like a Mars woman, and me in normal jeans on a Dutch bike even without a helmet.

Further I would like to thank Alexander, Violeta, Fabrizio, Erik, Hajo, Romain, Natalia, Florance, Jérémie, Mohamadou, Iman, Verner, Michael, Julien, Alberto, Jack and Enrico for the time we were together in the group.

Diemer and Iris, you were my first two undergraduate students from whom I learned a lot by supervising you. I hope you enjoyed as much as I did.

And then not to forget at all my most valuable family, my parents and sister Ymke who were living at quite some distance away, but were always there for any advise or help. My mother who taught me about life, my father who after months of repeated setbacks of the field-effect experiments on $SrTiO_3$ advised to paint the electrodes directly *onto* the sample and my sweet sister with whom I had a lot of fun on Skype. Thanks a lot to all of you.

Dook van Mechelen
Genève, April 2010

Index